

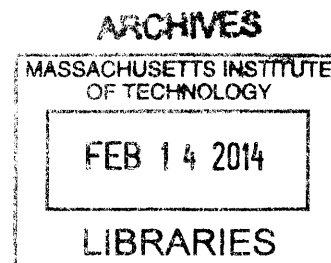
High Field DNP and Cryogenic MAS NMR. Novel Instrumentation and Applications

by

Evgeny Markhasin

B.S., Chemistry (2003)
University of Nizhny Novgorod

M.S., Chemistry (2005)
University of Nizhny Novgorod



Submitted to the Department of Chemistry
in Partial Fulfillment of the Requirements for the Degree of

Doctor of Philosophy in Chemistry

at the

Massachusetts Institute of Technology

February 2014

© 2013 Massachusetts Institute of Technology. All rights reserved

Signature of Author

Department of Chemistry
May 31, 2013

Certified by

Robert G. Griffin
Professor of Chemistry
Thesis Supervisor

Accepted by

Robert W. Field
Chairman, Departmental Committee on Graduate Students

This Doctoral thesis has been examined by a Committee of the Department of Chemistry as follows:

Professor Mounji G. Bawendi.....
Chairman

Professor Robert G. Griffin.....
Thesis Supervisor

Professor Keith A. Nelson

High Field DNP and Cryogenic MAS NMR. Novel Instrumentation and Applications

by
Evgeny Markhasin

Submitted to the Department of Chemistry on October 14, 2013
in Partial Fulfillment of the Requirements for the
Degree of Doctor of Philosophy in Chemistry

Abstract

Solid State Nuclear Magnetic Resonance (ssNMR) spectroscopy has blossomed over the last two decades. As ssNMR is progressively applied to more challenging systems, the sensitivity remains one of its major limiting factors. Gyrotron based high-field dynamic nuclear polarization (DNP) permits increasing the sensitivity of ssNMR by 1-2 orders magnitude, significantly extending the reach of ssNMR. Successful application of ssNMR/DNP at 5T and 9.4T stimulated interest to extending this technique to higher fields and new applications. Here, the progress toward this goal is presented. It has involved completion of the world highest field magic angle spinning (MAS) DNP spectrometer and a probe for 16.4T, initial DNP experiments on ^{17}O nuclei, variable temperature studies of a model tripeptide, and a systematic analysis of a novel approach to high efficiency RF circuit design.

The extension of DNP-NMR to 16.4T has required the development of probe technology, cryogenics, gyrotrons, and microwave transmission lines. A novel DNP probe and cryogenic instrumentation permit extended operation at 85-90K and 10kHz MAS. Initial enhancements $\epsilon=40$ and further optimization of experimental conditions is underway.

^{17}O detected DNP-NMR of a water/glycerol glass at 5T enabled an 80-fold enhancement of signal intensities at 82K permitting ^{17}O - ^1H distance measurements and heteronuclear correlation experiments.

Variable temperature MAS NMR studies of a model tripeptide APG in combination with cryogenic calorimetry and XRD revealed a first-order phase transition and severe attenuation of the cross polarization MAS signal in a wide temperature range due to interference between decoupling and 3-fold hopping of the Ala- CH_3 and Ala- NH_3^+ groups.

A new, efficient strategy for designing balanced transmission line RF circuits for MAS NMR probes based on back propagation of a common impedance node (BPCIN) is presented. In this approach, the impedance node is the sole means of achieving mutual RF isolation and balance in all channels. BPCIN is illustrated using a custom double resonance MAS probe operating at 11.7T.

Thesis Supervisor: Robert G. Griffin
Title: Professor of Chemistry

Dedicated to my Grandparents, Mom and Dad

Acknowledgments

Over the years, I have learned a lot from different people, and it is difficult to mention the names of all of them. Their support and advice have been essential for me to get to where I am now. I cannot be thankful enough for the numerous opportunities to interact with them not only in formal but also in informal settings.

I would like to thank my advisor, Robert Griffin, and his collaborator, Judith Herzfeld, for the opportunity to learn and work in this laboratory. This has been a very challenging and instructive program and intellectually stimulating environment with plenty opportunities to learn beyond of what I expected.

Alexander Barnes has introduced me to design and engineering and taught me the design of a MAS DNP spectrometer. He has been a helpful mentor, and it has been a pleasure working with him.

I am grateful to Anthony Bielecki for his help with RF circuit design for NMR probes. While I have been watching Jianping Hu building his probes, I have learned about the difficulties associated with building high quality electrical circuits.

Expertise and experience of Ajay Thakkar have proved to be invaluable and crucial for building and troubleshooting 700 DNP probe in particular and RF instrumentation in general. From him, I have learned a good deal about troubleshooting spectrometer issues.

I have enjoyed advising and spending time with Rebecca Mayrhofer, Qing Zhe Ni, and Thach Can.

Our DNP experiments would not be possible without the expertise and support provided by the members of Richard Temkin's group, including Jagadishwar Sirigiri, Emilio Nanni, Michael Shapiro, Ivan Mastovsky, Antonio Torrezan, Sudheer Jawla, and Paul Woskov.

I am thankful to Yongchao Su, Björn Corzilius, Galia Debelouchina, Patrick van de Wel, Yoh Matsuki, Melody Mak-Jurkauskas, Józef Lewandowski, Gaël De Paëpe, Mikhail Veshtort, Marc Caporini, Marvin Bayro, Thorsten Maly, Matthew Eddy, and Loren Andreas for guidance, advice, and stimulating discussions.

Advice and support of Jeffrey Bryant, Michael Mullins, Ron DeRocher, Chris Turner, and Dave Ruben are essential for keeping the Bitter running.

Excellent classes on professional communications in English taught by Jane Dunphy have thoroughly demonstrated the scientific aspects of communications. This understanding has helped me greatly in improving my communication skills not only in English, but also in my native language, as I realized that this knowledge is largely applicable there too.

I have been very lucky to have numerous opportunities to learn from many talented teachers and scientists from Lobachevsky University of Nizhny Novgorod (UNN) and Nizhny Novgorod Physics and Mathematics Lyceum 40, who have introduced me to the fascinating world of mathematics, physics, chemistry, and information technologies and helped acquire a vast body of scientific knowledge and develop my skills. I am indebted to my high school teachers, Vladimir Yu. Kovalev, Valentina F. Krevskaya, and David A. Erenkrants; my undergraduate advisors, Nikolay V. Karyakin and Aleksandr M. Kutysin; UNN professors, Aleksey A. Sibirkin, Albert A. Kalugin, Olga P. Bolotova, Aleksey Yu. Fedorov, Aleksey V. Kalinkin, Vladimir D. Lelukh, and many others.

I am grateful to all my friends Anatoly Khilo, Marina Khankhalaeva, Sergey Nikolenko, Maksim Imakaev, Nikolay Kryukov, Ekaterina Brilts, Mikhail Dorf, Grigory Kagan, Maksim Kuznetsov, Anton Pirogov, Anna Pirogova, Sergey Makarov, Aleksandr Pikulin, Anna Mensova,

Anna Krevskaya, Olga Markelova, Oksana Kapustina, Victoria Fayzullina, Sergey Makarov, Tatyana Serova, Ksenia Serova, and Anastasia Sidorova.

I would like to thank Mounqi Bawendi and Keith Nelson for serving on thesis committee.

I would not be able to achieve these results without the support from my family, grandparents, and parents, and it is to them that this work is dedicated.

Table of Contents

Abstract	5
Acknowledgments	9
Table of Contents	11
Table of Figures	14
Table of Tables	16
1. Introduction	17
1.1. NMR Hamiltonian	18
1.1.1. <i>Static Hamiltonian</i>	18
1.1.2. <i>The Magic behind Magic Angle Spinning NMR</i>	19
1.2. Violation of the High Field Approximation	20
1.2.1. <i>Quadrupolar Interaction</i>	20
1.2.2. <i>Local Dynamics on Larmor Frequency Scale</i>	21
References	25
2. Dynamic Nuclear Polarization Spectrometer for DNP at 700 MHz/460 GHz	35
Abstract	35
2.1. Introduction	36
2.2. Spectrometer Design	36
2.2.1. <i>700 MHz MAS DNP Probe</i>	37
2.2.2. <i>Metal Composite Transfer Lines</i>	39
2.2.3. <i>Dewar</i>	40
2.2.4. <i>3.2 mm Cryogenic Sample Exchange</i>	40
2.2.5. <i>Nitrogen Generation for MAS</i>	41
2.2.6. <i>Heat Exchanger</i>	41
2.2.7. <i>460 GHz Microwave Transmission</i>	43
2.3. Results	44
2.4. Conclusions and Outlook	45
Acknowledgments	46
References	46
3. Structural Dynamics and Transformations of Alanyl-Prolyl-Glycine Investigated by Low-Temperature MAS NMR	51
3.1. Introduction	51
3.2. Experimental Procedures	52
3.2.1. <i>Sample preparation</i>	52
3.2.2. <i>Instrumentation</i>	52
3.2.3. <i>Data processing</i>	54
3.3. Results and Discussion	54
3.3.1. <i>Temperature dependent shift</i>	55
3.3.2. <i>Polymorphic phase transition</i>	56

3.3.3. <i>Low temperature dynamics</i>	57
3.3.4. <i>Activation energy of methyl group reorientation</i>	60
References	62
Program 1. PyMOL Script Generating Figure 17	68
Program 2. PyMOL Script Generating Figure 20	69
Program 3. PyMOL Script Generating Figure 21	70
4. Dynamic Nuclear Polarization Enhanced SSNMR of Oxygen-17	71
Abstract	71
4.1. Introduction	72
4.2. CPMG Experiment. Sensitivity Enhancement	73
4.3. NMR Experiments	75
4.3.1. <i>¹H Mediated and Direct Polarization. Sensitivity Limit</i>	75
4.3.2. <i>Effect of ¹H Decoupling on ¹⁷O NMR Spectra</i>	77
4.3.3. <i>¹⁷O Correlation Spectra</i>	78
4.4. Conclusions and Outlook	80
Acknowledgments	81
References	81
Program 4. SIMMOL Setup File Water.mol for Water.spinsys	87
Program 5. Water.spinsys	89
5. Efficient, Balanced, Transmission Line RF Circuits by Back Propagation of Common Impedance Nodes	91
Abstract	91
5.1. Introduction	92
5.2. RF circuit design and implementation	92
5.2.1. <i>Circuit overview</i>	92
5.2.2. <i>Circuit design based on impedance nodes</i>	92
5.2.3. <i>Back propagation of common impedance node</i>	94
5.2.4. <i>Tuning elements</i>	97
5.3. Experimental verification	98
5.3.1. <i>Static optimized circuit</i>	98
5.3.2. <i>MAS tests</i>	99
5.4. Conclusions and Outlook	100
Acknowledgments	100
References	101
6. Analysis of Probe RF Circuitry Using Analytical Expressions and SPICE-like Simulators	107
Abstract	107
6.1. Introduction	108
6.2. Basics of RF Circuits	108
6.2.1. <i>AC Circuit Analysis. Phasor Domain</i>	109
6.2.2. <i>Waves in Time and Phasor Domains. Impedance Waves and Nodes</i>	111
6.3. RF Circuit Simulations	115
6.3.1. <i>Simulation Approaches</i>	115
6.3.2. <i>SPICE-like Circuit Simulations</i>	116

6.4. Resonant Phenomena and Circuit Efficiency	119
6.4.1. <i>Coil Leads Effect</i>	120
6.4.2. <i>Efficiency Limit due to Power Dissipation</i>	121
6.4.3. <i>Power Transfer Efficiency in Transmission Line RF Circuit</i>	122
6.5. Conclusions	123
6.6. Questions and Answers	124
Acknowledgments	126
References	127
7. Precision Calorimetry of Tripeptides Ala-Pro-Gly•H₂O, N-formyl-Met-Leu-Phe-OH, and N-formyl-Met-Leu-Phe-OMe	135
Abstract	135
7.1. Introduction	136
7.2. Experimental Section	136
7.2.1. <i>Samples</i>	136
7.2.2. <i>Adiabatic Calorimeter</i>	136
7.2.3. <i>Heat Capacity Measurements</i>	137
7.3. Results and Discussion	137
7.3.1. <i>Heat Capacity Measurements</i>	137
7.3.2. <i>Standard Thermodynamic Functions of Tripeptides</i>	139
7.4. Conclusions	139
References	147

Table of Figures

Figure 1. Schematic showing successive transformations of the dipolar tensor.....	22
Figure 2. DNP at 700 MHz / 460 GHz.	35
Figure 3. MAS DNP spectrometer structure.....	36
Figure 4. 700 MHz DNP instrumentation.....	37
Figure 5. 700 MHz MAS DNP probe.	38
Figure 6. Upper assembly of the 700 MHz MAS DNP probe.....	38
Figure 7. Cryogenic isolation strategies.....	39
Figure 8. Nitrogen gas generation and cryocooling apparatus.....	42
Figure 9. 460 GHz microwave transmission and beam quality.....	43
Figure 10. DNP at 700 MHz.	44
Figure 11. ^{13}C - ^{13}C Correlation spectra at 700 MHz.....	45
Figure 12. Temperature dependent ^{13}C CP MAS NMR spectra of 10%-U- ^{13}C , ^{15}N -APG.....	53
Figure 13. ^{13}C CP MAS NMR spectrum of 10%-U- ^{13}C , ^{15}N -APG at 78 K.	54
Figure 14. Aligned temperature dependent ^{13}C CP MAS NMR spectra of 10%-U- ^{13}C , ^{15}N -APG.	54
Figure 15. Temperature dependence of Gly- C_O isotropic chemical shift in APG.	55
Figure 16. Aliphatic region of ^{13}C CP MAS NMR spectra of 10%-U- ^{13}C , ^{15}N -APG around the polymorphic phase transition region collected in the heating direction.	55
Figure 17. Crystal structure of APG.	56
Figure 18. Isobaric heat capacity of APG.	56
Figure 19. Photographs showing a single crystal of APG at 208 K (left) and 207 K (right).....	57
Figure 20. Fragment of crystal structure of APG showing five methyl groups (green balls) located within 4 Å of the molecule.	58
Figure 21. Fragment of crystal structure of APG showing six oxygen nuclei (red balls) located within 3.5 Å of Ala-N (blue ball).....	58
Figure 22. Temperature dependence of integrated intensity of Ala- C_β	58
Figure 23. Temperature dependence of integrated intensity of select lines in CP MAS NMR spectra of APG corrected for loss of Boltzmann polarization.	59
Figure 24. Same as Figure 23, except direct ^{13}C	59
Figure 25. Same as Figure 23, with ^{15}N CP MAS NMR trace for Ala-N.....	59
Figure 26. ^1H spin-lattice relaxation times measured via indirect detection of ^{13}C signal after CP transfer.	59
Figure 27. ^{13}C spin-lattice relaxation times.	60
Figure 28. ^{13}C and ^1H spin-lattice relaxation times for Ala- C_β overlaid on top of its intensity trace. See details in text.	60
Figure 29. Homogeneous linewidth (FWHM) of the Ala- C_β resonance in uniformly ^{13}C , ^{15}N - labeled APG.....	61
Figure 30. DNP enhanced NMR of oxygen-17.....	71
Figure 31. ^{17}O echo in a frozen water-glycerol matrix.	73
Figure 32. ^{17}O echo train in a frozen water-glycerol matrix.....	73
Figure 33. Model CPMG echo train.....	74
Figure 34. Dependence of the f_p gain factor on the length of echo train.	75
Figure 35. Pulse sequences of ^{17}O DNP/NMR experiments.....	75
Figure 36. Static solid state NMR spectra of ^{17}O labeled water (^1H mediated polarization).....	76

Figure 37. Static solid state NMR spectra of ^{17}O labeled water (direct polarization).	76
Figure 38. DNP enhanced MAS NMR spectrum of ^{17}O labeled water.	77
Figure 39. DNP enhanced static ssNMR spectrum of natural abundance ^{17}O sample.	77
Figure 40. Effect of ^1H decoupling on T_2 , signal intensity and lineshape in ^{17}O SSNMR.	78
Figure 41. Central transition ^{17}O - ^1H HETCOR-CPMG spectrum of H_2^{17}O with DNP.	79
Figure 42. Central transition ^{17}O - ^1H SEDOR experiment.	80
Figure 43. Back propagation of a common impedance node.	91
Figure 44. Schematic of a RF circuit with a common mode input (a) and balanced input (b). ...	92
Figure 45. Simplified schematic (a) and block diagram (b) of a balanced double resonance RF circuit.	93
Figure 46. Mutual isolation of multiple RF channels by means of a common impedance node.	94
Figure 47. Stepwise propagation of common impedance nodes along the circuit.	95
Figure 48. Implementation of ^1H (500 MHz), ^{13}C (125 MHz) fully balanced, transmission line probe.	96
Figure 49. Schematic indicating the function of the tuning elements that form the common (black) blocks in Figure 45b.	97
Figure 50. ^1H and ^{13}C nutation curves.	98
Figure 51. ^1H and ^{13}C balance ball shift test.	98
Figure 52. ^1H and ^{13}C γB_1 dependence on input RF power.	98
Figure 53. Broadband RFDR spectra of uniformly ^{13}C and ^{15}N labeled peptide and protein samples.	100
Figure 54. Illustration of impedance waves in the phasor domain.	113
Figure 55. Typical contributions of the real and imaginary parts to impedance of high Q components used in resonant circuits.	114
Figure 56. Single resonance transmission line circuit model.	117
Figure 57. Tuned circuit for coil leads effect modeling.	120
Figure 58. Simplified model of a lossy single resonance circuit.	121
Figure 59. Experimental temperature dependence of heat capacity of N- <i>f</i> -MLF-OH and N- <i>f</i> -MLF-OMe.	138
Figure 60. Experimental temperature dependence of heat capacity of APG.	138
Figure 61. DSC curves for small samples of APG.	138

Table of Tables

Table 1. Typical sizes of NMR Hamiltonian terms for a modern high field spectrometer.....	18
Table 2. Matching conditions and recoupled terms in the first order dipolar Hamiltonian.	24
Table 3. Experimental Molar Heat Capacity of Crystalline N-f-MLF-OH.	140
Table 4. Experimental Molar Heat Capacity of Crystalline N-f-MLF-OMe.....	141
Table 5. Experimental Molar Heat Capacity of Crystalline APG•H ₂ O.....	142
Table 6. Smoothed Molar Heat Capacity and Thermodynamic Functions of Crystalline N-f-MLF-OH ($M = 437.56$ g/mol, $p^\circ = 0.1$ MPa).	144
Table 7. Smoothed Molar Heat Capacity and Thermodynamic Functions of Crystalline N-f-MLF-OMe ($M = 451.59$ g/mol, $p^\circ = 0.1$ MPa).	145
Table 8. Smoothed Molar Heat Capacity and Thermodynamic Functions of Crystalline APG•H ₂ O ($M = 261.28$ g/mol, $p^\circ = 0.1$ MPa).	146

1. Introduction

Solid State Nuclear Magnetic Resonance (ssNMR) spectroscopy has blossomed over the last two decades. With advances in instrumentation [1-25], methodology [26-42], and isotopic labeling techniques [43-49], ssNMR is now used to study a wide range of systems, including biomolecules [50-52], polymers [53-55], glasses [56-58], surface materials and catalysts [59-62]. Despite the ever expanding scope of ssNMR, the inherently low sensitivity of this technique remains the most limiting factors.

The sensitivity of an NMR signal is proportional to the magnetization M_0 , which is, in turn, inversely proportional to absolute temperature $M_0 \sim 1/T$ [63]. Thus low temperatures and to a larger extent, cryogenic temperatures provide a means to increase sensitivity. For this reason, several research groups continue to pursue research in cryogenic ssNMR [64-74]. Furthermore, an additional sensitivity enhancement can be achieved by combining cryogenic ssNMR with dynamic nuclear polarization (DNP [75-76]). Initial research efforts in gyrotron based high field DNP, which began more than 20 years ago in Professor Robert Griffin's laboratory in collaboration with the research groups of Professor Judith Herzfeld and Doctor Richard Temkin, clearly demonstrated the power of combining cryogenic ssNMR with DNP. The first generation gyrotron DNP spectrometer, which operated at 5 T [77] and was subsequently extended to a higher field second generation system operated at 9 T [78], provided a means of increasing the sensitivity of ssNMR by $\geq 1-2$ orders magnitude without the necessity for a μ wave cavity and was compatible with magic angle spinning NMR experiments. Furthermore this experimental set-up could be combined with other routinely used sensitivity enhancement techniques, such as cross polarization [79].

Designing and constructing the complex instrumentation required for DNP experiments has been a primary research goal of Griffin and coworkers for the last two decades. The technology developed in pursuit of this goal has resulted in the first commercial DNP spectrometer offered by the Bruker Corporation, which was modeled after Griffin's second generation system [80] several years ago. This spectrometer attracted wide interest from the magnetic resonance community worldwide. It has also stimulated interest to extend this technique to higher fields, where the majority of modern biological NMR research is conducted. Development of such a system, as well as associated methodology, was, therefore, an acute research problem with high immediate impact on a large scale, and it constitutes a large portion of the present work.

The required experimental setting, as well as the advantages afforded by DNP, have stimulated research in several key areas. First, DNP experiments in the solid state typically require cryogenic temperatures, which in turn requires special instrumentation [81-82]. Second, the signal enhancement provided by DNP enables new experiments that would otherwise be prohibitively insensitive, and these new application areas need to be explored and investigated [83-84]. Third, many systems of interest, such as biological molecular systems, operate at ambient temperature conditions. Therefore, it is important to understand the dynamics of the system as it is cooled down to cryogenic temperatures and it is equally important to establish whether the experimental information obtained at cryogenic temperatures is relevant to the system at ambient conditions. Finally, DNP experiments require presence of special polarizing agents, stable radicals [85], a source of μ wave power [86-93], and investigation of DNP mechanisms [85,94].

Accordingly, after a brief review of the relevant NMR Hamiltonians in Chapter 1, a DNP-NMR spectrometer is presented in Chapter 2, which at the time of writing, was the highest field instrument of this variety [95-98]. This instrumentation is then applied to variable temperature ssNMR studies of a model tripeptide, highlighting a variety of structural and related spectroscopic phenomena (Chapter 3). Chapter 4 discusses the initial applications of DNP to ssNMR of ^{17}O [99-100], which will be eventually extended to biologically relevant systems. Chapter 5 presents a detailed analysis of a recently developed approach to design probe radiofrequency circuits [101-103] and a probe based on this design, which demonstrated outstanding performance [95,104]. Chapter 6 revisits the basics of AC circuits analysis and simulations in a format intended for students and other members of the NMR community. Finally, cryogenic calorimetry [105] is used in Chapter 7 to complement NMR and X-ray data and elucidate the transformations of model systems as they are cryocooled.

1.1. NMR Hamiltonian

Detailed descriptions of various interactions contributing to the NMR Hamiltonian are readily available elsewhere [63]. Here, we will include some general remarks and discuss the role of the static magnetic field in high field magic angle spinning (MAS) NMR.

1.1.1. Static Hamiltonian

The nuclear NMR Hamiltonian includes a number of terms, which describe the interaction of nuclear spins with the static magnetic field, spin-spin interaction, as well as the interaction of spins with the “control” magnetic radiofrequency (RF) field. In the laboratory frame the Hamiltonian is given by

$$H = H_Z + H_Q + H_{RF} + H_D + H_{CS} + H_J, \quad (1)$$

where H , H_Z , H_Q , H_{RF} , H_D , H_{CS} , and H_J are the total, Zeeman, quadrupolar, RF, dipolar, chemical shift, and J-coupling Hamiltonians, respectively. The terms in Equation (1) are ordered based on their typical size as illustrated in Table 1. The dominating Zeeman term defines the so-called rotating frame of reference, in which it has no further effect on the evolution of the spin system. The second largest term in the Hamiltonian describes the quadrupolar interaction, which vanishes for spins $I=1/2$. In this case, the “control” RF term is the dominating relevant contribution to the NMR Hamiltonian, which puts NMR in the unique position by allowing the NMR spectroscopist to exert a high level of control of the evolution of spin systems.

The terms in Equation (1) describe different spin-spin and spin-field interactions, and, in general, may have *isotropic* (orientation independent) and *anisotropic* (orientation dependent) contributions. While the role of H_Z is usually limited in a sense that the evolution of spin systems

Table 1. Typical sizes of NMR Hamiltonian terms for a modern high field spectrometer.

Term	Size, Hz
H_Z	10^7 - 10^9
H_Q	10^6 - 10^{8*}
H_{RF}	10^4 - 10^5
H_D	10^2 - 10^4
H_{CS}	10^2 - 10^3
H_J	1 - 10^2

* H_Q varies greatly. It can be as small as 10^3 - 10^4 Hz for an imperfect crystal and as high as $3 \cdot 10^9$ Hz for ^{127}I in solid ICl [106].

due to H_Z is trivial, H_{RF} makes it possible to control the overall evolution of the system. The isotropic part of H_{CS} is the primary basis of high resolution NMR at high fields (though, it can also be used a source of structural information [107-108]). The terms H_D and H_J arise from direct and indirect spin-spin couplings, respectively, rather than spin-field couplings, and make NMR a powerful source of structural information. Finally, the anisotropic part of H_{CS} and H_Q also contain structural information.

1.1.2. *The Magic behind Magic Angle Spinning NMR*

Both spin operators and magnetic fields can be represented by Cartesian 3D vectors (1st rank tensors) and the interactions contributing to NMR Hamiltonian in Equation (1) can be represented by 2nd rank tensors [40,109-113]:

$$\mathcal{H}_X = \overset{\rightarrow}{\mathbf{A}} \mathbf{M} \mathbf{C}, \quad (2)$$

where \mathbf{A} is a vector spin operator, \mathbf{C} is either a vector spin operator or a vector representing a field, and \mathbf{M} is a 2nd rank Cartesian tensor corresponding to interaction X. The same relation can also be expressed using spherical tensor formalism [40,110,114-118], which is usually more convenient for ssNMR. When cast in spherical tensors, each NMR interaction is represented by a scalar product of a spatial tensor and a spin space tensor, with isotropic interactions represented by a spatial tensor of rank 0 and anisotropic interactions normally represented by tensors of rank 2:

$$\mathcal{H}_X = \sum_{l=0}^2 \Lambda_l \cdot \mathcal{T}_l = \sum_{l=0}^2 \sum_{q=-l}^l (-1)^q \Lambda_{l,q} \mathcal{T}_{l,-q}, \quad (3)$$

where $\Lambda_{l,q}$ is a q -component of a spatial irreducible spherical tensor of rank l , and $\mathcal{T}_{l,q}$ is q -component of a spin-space irreducible spherical tensor of rank l . Since energy of anisotropic interactions and associated shifts of energy levels depend on orientation of the molecule (due to orientational dependence of Λ in Equation (3)), in polycrystalline solids containing a mixture of different orientations, such interactions “broaden” energy levels, corresponding transitions, and spectral lines. For this reason, anisotropic interactions are generally incompatible with high resolution NMR and must be removed from the Hamiltonian. In liquid, rapid molecular tumbling usually averages spatial tensors of rank higher than 0 and, therefore, the corresponding contributions. In solids, this is not the case; however, high resolution spectra can often be recovered using approach that relies on the very same orientational dependence of spatial tensors Λ . The basic idea is to modulate Λ by making orientation of the sample time dependent, and under certain conditions, the anisotropic part disappears from the effective Λ . A common example of such an approach is magic angle spinning NMR, which involves rapid sample spinning about an axis inclined at the so called magic angle with respect to the static magnetic field [119-120]. In order to understand the mechanism of this approach, it is necessary to consider explicit expressions for Λ . These expressions can be obtained by transforming interactions from their principle axis system (PAS), where Λ is diagonal, into the laboratory frame (Lab), which is static and has its positive z axis aligned with the static magnetic field. This transformation usually performed via some intermediate steps. In the case of MAS, the last step involves transformation from the time independent tensors of the rotor fixed frame (RFF) to the time dependent tensors of the Lab frame:

$$\Lambda_{l,q} = \sum_{m=-l}^l \mathcal{D}_{m,q}^l(-\omega_r t, -\theta_r, 0) R_{l,m} = \sum_{m=-l}^l e^{im\omega_r t} d_{m,q}^l(-\theta_r) R_{l,m}, \quad (4)$$

where R are spherical tensor components expressed in the RFF, \mathcal{D} and d are Wigner matrices, θ_r is the angle between the rotor axis and static magnetic field, ω_r is rotor spinning frequency, and t is time. Therefore,

$$\mathcal{H}_X^{Lab} = \sum_{l=0}^2 \sum_{q=-l}^l \sum_{m=-l}^l (-1)^q e^{im\omega_r t} d_{m,q}^l(-\theta_r) R_{l,m} \mathcal{J}_{l,-q}. \quad (5)$$

It is important to note that Equation (4) expresses full, rather than truncated Hamiltonian. An additional step, which needs to be done, is the transformation of Equation (4) into the rotating frame (RF), which involves the rotation of the spin component of the Hamiltonian about the laboratory z axis. This transformation will be slightly different depending on the type of the interaction. In the case of homonuclear spin-spin interactions, we obtain

$$\begin{aligned} \mathcal{H}_X^{RF} &= \sum_{l=0}^2 \sum_{q=-l}^l (-1)^q \Lambda_{l,q} \sum_{s=-l}^l \mathcal{D}_{s,-q}^l(\omega_o t, 0, 0) \mathcal{J}_{l,s} = \sum_{l=0}^2 \sum_{q=-l}^l (-1)^q \Lambda_{l,q} \sum_{s=-l}^l e^{-is\omega_o t} d_{s,-q}^l(0) \mathcal{J}_{l,s} = \\ &= \sum_{l=0}^2 \sum_{q=-l}^l \sum_{s=-l}^l (-1)^q d_{s,-q}^l(0) \Lambda_{l,q} e^{-is\omega_o t} \mathcal{J}_{l,s}, \\ \mathcal{H}_X^{RF} &= \sum_{l=0}^2 \sum_{q=-l}^l \sum_{s=-l}^l \sum_{m=-l}^l (-1)^q d_{s,-q}^l(0) e^{im\omega_r t} d_{m,q}^l(\theta_r) R_{l,m} \Lambda_{l,q} e^{-is\omega_o t} \mathcal{J}_{l,s}, \end{aligned} \quad (6)$$

where ω_o is the Larmor frequency. Equation (6) contains three groups of terms:

- 1) terms that are modulated due to the second exponential;
- 2) terms that are modulated due to sample spinning
- 3) time independent terms corresponding to $q=m=s=0$.

The first group contains the so-called non-secular terms and are usually neglected to first order in the high field approximation. Similarly, to first order terms in the second group average to zero. Since the rank 0 term is isotropic and there is no contribution from $\mathcal{J}_{l,0}$ to the NMR Hamiltonian [110], there is only one time independent anisotropic term from the third group proportional to $d_{0,0}^2(\theta_r)$. This Wigner element becomes zero when its argument – the angle between the rotor axis and static magnetic field – is set to magic angle. In other words, there is no special magic associated with the direction of static magnetic field; both MAS and static magnetic field play similar roles averaging several term in the Hamiltonian through either spatial or spin space rotation.

1.2. Violation of the High Field Approximation

1.2.1. Quadrupolar Interaction

Any nucleus with spin greater than one-half has a nonspherical charge distribution and, as a result, an electrical quadrupolar moment. A quadrupolar moment couples to electric field gradi-

ent (EFG) at the nucleus and gives rise to the quadrupolar Hamiltonian [63,121], which can be expressed in a laboratory axis frame (LAB) as follows [122]:

$$H_Q = \omega_Q \sum_{m=-2}^2 (-1)^m R_{2,-m} T_{2,m}, \quad (7)$$

where ω_Q is quadrupole frequency, R and T are spatial and spin tensor operators, respectively. Equation (7) can be truncated in high field approximation, and, to first order, only the part commuting with the Zeeman interaction is kept:

$$H_Q^{(1)} = \omega_Q R_{2,0} T_{2,0}. \quad (8)$$

The spin tensor operator in Equation (8) can be recast in terms of conventional spin operators:

$$T_{2,0} = \frac{1}{\sqrt{6}} (3I_z^2 - I(I+1)), \quad (9)$$

while the spatial tensor operator can be obtained from the tensor components of the principal axis system (PAS) using Wigner rotation matrices:[115]

$$R_{2,0} = \sqrt{\frac{3}{2}} \left(\frac{3\cos^2(\beta) - 1}{2} + \frac{\eta}{2} \cos(2\alpha) \sin^2(\beta) \right), \quad (10)$$

where α and β are two of the three Euler angles relating PAS and the LAB frames. In case of quadrupolar Hamiltonian, the first order term is often insufficient, and the second order term must be taken into account:

$$H_Q^{(2)} = \frac{\omega_Q^2}{\omega_0} \sum_{l=0,2,4} C_l(I, I_z) A_{l,0}, \quad (11)$$

where, ω_0 is the Larmor frequency, $C_l(I, I_z)$ are coefficients that are functions of only the spin and magnetic quantum number, $A_{l,0}$ are space tensors. It is the last term in Equation (11) proportional to a 4th rank tensor, $A_{4,0}$, which is responsible for failure of conventional MAS to produce high resolution spectra. The same term is also responsible for substantial degradation of sensitivity, which is the direct consequence of severe line broadening.

A number of different techniques have been developed to improve the resolution and / or sensitivity. Most of the sensitivity enhancement techniques applied to quadrupolar nuclei are focused on preparation of a state with increased polarization. CPMG experiment [123-127], on the other hand, is applied during the acquisition, and can often be combined with other experiments to optimize utilization of the available signal. The gain in sensitivity due to CPMG may be substantial, as demonstrated in Chapter 4.

1.2.2. Local Dynamics on Larmor Frequency Scale

Local dynamics, such as 3-fold hopping of a CH₃ group, plays an important role for NMR. In this section, we demonstrate that when the rate of such motion is comparable to the Larmor frequency, it can interfere with truncation of the nuclear Hamiltonian by the Zeeman field rendering heteronuclear decoupling inefficient.

Let us consider a heteronuclear dipolar Hamiltonian $\mathcal{H}_D^{(k,n)}$ of a simplified model system consisting of an isolated ^1H - ^{13}C spin pair coherently rotating at frequency ω_h about an axis forming angle φ with the internuclear vector (the C3 symmetry axis, where k and n refer to ^{13}C and ^1H , respectively). Using the spherical tensor formalism, the dipolar tensor can be expressed in its principal axis system (PAS) with the only non-zero component

$$\rho_{2,0}^{(k,n)} = \sqrt{\frac{3}{2}} \delta_D^{(k,n)},$$

where $\delta_D^{(k,n)}$ is the dipolar coupling. We will now transform it into the lab frame following the steps schematically shown in Figure 1, starting from the PAS followed by the ‘‘crystal fixed frame’’ (CFF), which in this case is a frame aligned with and fixed to the spinning axis (the C₃ symmetry axis of the methyl group), then the tensor is transformed into the rotor fixed frame (RFF) and the laboratory frame (Lab). Finally, we will transform spherical tensor operators from the Lab frame into the doubly rotating frame (RF). The top line in Figure 1 indicates appropriate Wigner rotation matrix elements necessary to perform these transformations, and the bottom line indicates notation for spherical tensor components that we will use in the corresponding frames. Therefore,

$$\begin{aligned} \Lambda_{l,m} &= \sum_{m'=-l}^l R_{l,m'} \mathcal{D}_{m',m}^l(-\omega_r t, -\theta, 0) = \\ &= \sum_{m'=-l}^l R_{l,m'} d_{m',m}^l(-\theta) e^{-i(-m'\omega_r t)} = \\ &= \sum_{m'=-l}^l \sum_{m''=-l}^l C_{l,m''} \mathcal{D}_{m'',m'}^l(\alpha, \beta, \gamma) d_{m',m}^l(-\theta) e^{-i(-m'\omega_r t)} = \\ &= \sum_{m'=-l}^l \sum_{m''=-l}^l C_{l,m''} d_{m'',m'}^l(\beta) d_{m',m}^l(-\theta) e^{-i(m''\alpha + m'\gamma - m'\omega_r t)} = \\ &= \sum_{m'=-l}^l \sum_{m''=-l}^l \sum_{m'''=-l}^l \rho_{l,m''} \mathcal{D}_{m'',m'''}^l(0, \varphi, \omega_h) d_{m'',m'}^l(\beta) d_{m',m}^l(-\theta) e^{-i(m''\omega_h t + m''\alpha + m'\gamma - m'\omega_r t)} = \\ &= \sum_{m'=-l}^l \sum_{m''=-l}^l \sum_{m'''=-l}^l \rho_{l,m''} d_{m'',m'''}^l(\varphi) d_{m'',m'}^l(\beta) d_{m',m}^l(-\theta) e^{-i(m''\omega_h t + m''\alpha + m'\gamma - m'\omega_r t)}, \end{aligned}$$

where θ is the magic angle and ω_r is rotor spinning frequency.

$$\Lambda_{2,m} = \sum_{m'=-2}^2 \sum_{m''=-2}^2 \rho_{2,0} d_{m'',m'}^2(\varphi) d_{m'',m'}^2(\beta) d_{m',m}^2(-\theta) e^{-i(m''\omega_h t + m''\alpha + m'\gamma - m'\omega_r t)}.$$

Here we define a shortcut

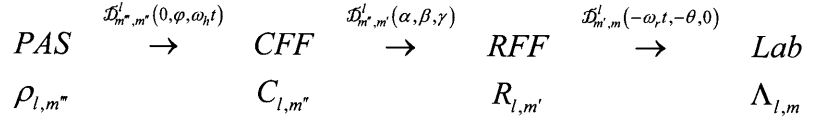


Figure 1. Schematic showing successive transformations of the dipolar tensor.

$$A_p = \rho_{2,0} d_{0,m^*}^2(\varphi) d_{m^*,m'}^2(\beta) d_{m',p}^2(-\theta) e^{-i(m^*\alpha + m'\gamma)}. \quad (12)$$

then

$$\Lambda_{2,m} = \sum_{m'=-2}^2 \sum_{m''=-2}^2 A_m e^{-i(m^*\omega_h - m'\omega_r)t}. \quad (13)$$

We now convert the spin tensor operators into the doubly rotating frame. Single spin-1/2 tensor operators

$$T_{1,0}^{(j)} = I_{jz},$$

$$T_{1,\pm 1}^{(j)} = \mp \frac{1}{\sqrt{2}} I_j^\pm$$

and tensor components of the dipolar Hamiltonian

$$\mathcal{J}_{2,0}^{(k,n)} = \frac{1}{\sqrt{6}} \left(2T_{1,0}^{(k)} T_{1,0}^{(n)} + T_{1,1}^{(k)} T_{1,-1}^{(n)} + T_{1,-1}^{(k)} T_{1,1}^{(n)} \right),$$

$$\mathcal{J}_{2,\pm 1}^{(k,n)} = \frac{1}{\sqrt{2}} \left(T_{1,\pm 1}^{(k)} T_{1,0}^{(n)} + T_{1,0}^{(k)} T_{1,\pm 1}^{(n)} \right),$$

$$\mathcal{J}_{2,\pm 2}^{(k,n)} = T_{1,\pm 1}^{(k)} T_{1,\pm 1}^{(n)}$$

can be converted into the rotating frame as follows:

$$T_{1,0}^{(j)RF} = T_{1,0}^{(j)},$$

$$T_{1,\pm 1}^{(j)RF} = \sum_{q'=-1}^1 T_{1,q'}^{(j)} \mathcal{D}_{q',\pm 1}^1(\omega_0^{(j)}t, 0, 0) = \sum_{q'=-1}^1 T_{1,q'}^{(j)} d_{q',\pm 1}^1(0) e^{-iq'\omega_0^{(j)}t} = T_{1,\pm 1}^{(j)} e^{\mp i\omega_0^{(j)}t},$$

$$\mathcal{J}_{2,0}^{(k,n)RF} = \frac{1}{\sqrt{6}} \left(2T_{1,0}^{(k)} T_{1,0}^{(n)} + T_{1,1}^{(k)} T_{1,-1}^{(n)} e^{-i(\omega_0^{(k)} - \omega_0^{(n)})t} + T_{1,-1}^{(k)} T_{1,1}^{(n)} e^{i(\omega_0^{(k)} - \omega_0^{(n)})t} \right),$$

$$\mathcal{J}_{2,\pm 1}^{(k,n)RF} = \frac{1}{\sqrt{2}} \left(T_{1,\pm 1}^{(k)} T_{1,0}^{(n)} e^{-i(\pm\omega_0^{(k)})t} + T_{1,0}^{(k)} T_{1,\pm 1}^{(n)} e^{-i(\pm\omega_0^{(n)})t} \right), \quad (14)$$

$$\mathcal{J}_{2,\pm 2}^{(k,n)RF} = T_{1,\pm 1}^{(k)} T_{1,\pm 1}^{(n)} e^{\mp i(\omega_0^{(k)} + \omega_0^{(n)})t}.$$

The time dependent terms in Equation (14) are non-secular and usually ignored. We, however, will keep the full Hamiltonian. Combining Equation (13) and (14), we can now express the full dipolar Hamiltonian

$$\mathcal{H}_D^{(k,n)RF} = \sum_{q=-2}^2 (-1)^q \Lambda_{2,q} \mathcal{J}_{2,-q}^{(k,n)RF} = \sum_{q=-2}^2 \mathcal{H}_{D,q}^{(k,n)RF},$$

with components

$$\begin{aligned}
\mathcal{H}_{D,0}^{(k,n)RF} &= \frac{1}{\sqrt{6}} \sum_{m'=-2}^2 \sum_{m''=-2}^2 A_0 \left(2T_{1,0}^{(k)}T_{1,0}^{(n)} + T_{1,1}^{(k)}T_{1,-1}^{(n)} e^{-i(\omega_0^{(k)}-\omega_0^{(n)})t} + T_{1,-1}^{(k)}T_{1,1}^{(n)} e^{i(\omega_0^{(k)}-\omega_0^{(n)})t} \right) e^{-i(m'\omega_h-m'\omega_r)t}, \\
\mathcal{H}_{D,\pm 1}^{(k,n)RF} &= \frac{1}{\sqrt{2}} \sum_{m'=-2}^2 \sum_{m''=-2}^2 A_{\pm 1} \left(T_{1,\pm 1}^{(k)}T_{1,0}^{(n)} e^{-i(\pm\omega_0^{(k)})t} + T_{1,0}^{(k)}T_{1,\pm 1}^{(n)} e^{-i(\pm\omega_0^{(n)})t} \right) e^{-i(m'\omega_h-m'\omega_r)t}, \\
\mathcal{H}_{D,\pm 2}^{(k,n)RF} &= \sum_{m'=-2}^2 \sum_{m''=-2}^2 A_{\pm 2} T_{1,\pm 1}^{(k)}T_{1,\pm 1}^{(n)} e^{\mp i(\omega_0^{(k)}+\omega_0^{(n)})t} e^{-i(m'\omega_h-m'\omega_r)t}.
\end{aligned} \tag{15}$$

Ignoring for the moment contributions from rotor spinning frequency, we can identify matching conditions for the frequency of the internal motion and corresponding recoupled terms as summarized in Table 2.

Clearly, sample spinning creates recoupling sidebands. Similarly, if a continuous wave decoupling field is applied, it will create another set of recoupling sidebands.

In case of ^1H spins, the truncated CSA terms will be recoupled in a similar fashion, while truncated terms of the quadrupolar Hamiltonian will be recoupled in the case of ^2H .

If a threefold jump is considered instead of rotational diffusion model treated above, the matching conditions for the zeroth order average Hamiltonian will be unaffected as in case of the just treated rotational diffusion model.

Lastly we did not take into account the stochastic nature of the motion. When included, it will scale down the magnitude of the recoupled terms.

Table 2. Matching conditions and recoupled terms in the first order dipolar Hamiltonian.

ω_h	$\overline{\mathcal{H}_D^{(k,n)RF}}^{(1)}$
$\pm(\omega_0^{(k)} - \omega_0^{(n)}), \pm(\omega_0^{(k)} - \omega_0^{(n)})/2$	$I_k^+ I_n^- + I_k^- I_n^+$
$\pm\omega_0^{(k)}, \pm\omega_0^{(k)}/2$	$I_k^+ I_{nz} + I_k^- I_{nz}$
$\pm\omega_0^{(n)}, \pm\omega_0^{(n)}/2$	$I_{kz} I_n^+ + I_{kz} I_n^-$
$\pm(\omega_0^{(k)} + \omega_0^{(n)}), \pm(\omega_0^{(k)} + \omega_0^{(n)})/2$	$I_k^+ I_n^+ + I_k^- I_n^-$

References

- [1] Cross, V. R.; Hester, R. K.; Waugh, J. S. Single coil probe with transmission-line tuning for nuclear magnetic double resonance. *Rev. Sci. Instrum.* **1976**, *47*, 1486. DOI: 10.1063/1.1134560
- [2] Stoll, M. E.; Vega, A. J.; Vaughn, R. W. Simple single-coil double resonance NMR probe for solid state studies. *Rev. Sci. Instrum.* **1977**, *48*, 800. DOI: 10.1063/1.1135159
- [3] Hoult, D. I. Fast recovery, high sensitivity NMR probe and preamplifier for low frequencies. *Rev. Sci. Instrum.* **1979**, *50*, 193. DOI: 10.1063/1.1135786
- [4] Doty, F. D.; Inners, R. R.; Ellis, P. D. A multinuclear double-tuned probe for applications with solids or liquids utilizing lumped tuning elements. *J. Magn. Reson.* **1981**, *43*, 399. DOI: 10.1016/0022-2364(81)90051-2
- [5] Idziak, S.; Haeberlen, U. Design and construction of a high homogeneity rf coil for solid-state multiple-pulse NMR. *J. Magn. Reson.* **1982**, *50*, 281. DOI: 10.1016/0022-2364(82)90058-0
- [6] Sullivan, N. S.; Deschamps, P.; Neel, P.; Vaissiere, J. M. Efficient fast-recovery scheme for NMR pulse spectrometers. *Revue de Physique Appliquee* **1983**, *18*, 253. DOI: 10.1051/rphysap:01983001804025300
- [7] Carduner, K.; Villa, M.; White, D. Variable-temperature solid-state nuclear-magnetic-resonance probe for superconducting magnets operating in the range 3-350 K. *Rev. Sci. Instrum.* **1984**, *55*, 68. DOI: 10.1063/1.1137592
- [8] McKay, R. A. Double-tuned single coil probe for nuclear magnetic resonance spectrometer. Patent #4446431, 1984.
- [9] Dubro, D. W.; Nuij, T. H.; Pope, J. M. An automated pulse programmer for NMR experiments. *J. Phys. E* **1987**, *20*, 413. DOI: 10.1088/0022-3735/20/4/013
- [10] Doty, D. F. Doubly broadband triple resonance or quad resonance NMR probe circuit. Patent #5424645, 1995.
- [11] Doty, F. D. Solid State NMR Probe Design. In *Encyclopedia of Magnetic Resonance*; John Wiley & Sons, Ltd: 2007. DOI: 10.1002/9780470034590.emrstm1001
- [12] Hill, H. D. W. Probes for High Resolution. In *Encyclopedia of Magnetic Resonance*; John Wiley & Sons, Ltd: 2007. DOI: 10.1002/9780470034590.emrstm0415
- [13] McKay, R. A. Probes for Special Purposes. In *Encyclopedia of Magnetic Resonance*; John Wiley & Sons, Ltd: 2007. DOI: 10.1002/9780470034590.emrstm0416
- [14] Doty, F. D. Probe Design and Construction. In *Encyclopedia of Magnetic Resonance*; John Wiley & Sons, Ltd: 2007. DOI: 10.1002/9780470034590.emrstm1000
- [15] Privalov, A. F.; Dvinskikh, S. V.; Vieth, H. M. Coil Design for Large-Volume High-B1 Homogeneity for Solid-State NMR Applications. *J. Magn. Reson. A* **1996**, *123*, 157. DOI: 10.1006/jmra.1996.0229

- [16] Schaefer, J.; McKay, R. A. Multi-tuned single coil transmission line probe for nuclear magnetic resonance spectrometer. Patent #5861748, 1999.
- [17] Marek, D. Cooled NMR probe head with thermal insulation of the sample. Patent #6441617, 2002.
- [18] Stringer, J.; Bronnimann, C. E. Balanced mode operation of a high frequency NMR probe. Patent #6380742, 2002.
- [19] Paulson, E. K.; Martin, R. W.; Zilm, K. W. Cross polarization, radio frequency field homogeneity, and circuit balancing in high field solid state NMR probes. *J. Magn. Reson.* **2004**, *171*, 314. DOI: 10.1016/j.jmr.2004.09.009
- [20] Fu, R.; Brey, W. W.; Shetty, K.; Gor'kov, P.; Saha, S.; Long, J. R.; Grant, S. C.; Chekmenev, E. Y.; Hu, J.; Gan, Z.; Sharma, M.; Zhang, F.; Logan, T. M.; Bruschweller, R.; Edison, A.; Blue, A.; Dixon, I. R.; Markiewicz, W. D.; Cross, T. A. Ultra-wide bore 900 MHz high-resolution NMR at the National High Magnetic Field Laboratory. *J. Magn. Reson.* **2005**, *177*, 1. DOI: 10.1016/j.jmr.2005.07.013
- [21] Shevgoor, S.; Spitzmesser, J. B.; Kulkarni, J.; Staab, J. P.; Entzminger, G.; Doty, F. D. Development of a CryoMASTM HR-MAS-MAG NMR Probe for High-field WB Magnets. ENC; 2005.
- [22] Stringer, J. A.; Bronnimann, C. E.; Mullen, C. G.; Zhou, D. H.; Stellfox, S. A.; Li, Y.; Williams, E. H.; Rienstra, C. M. Reduction of RF-induced sample heating with a scroll coil resonator structure for solid-state NMR probes. *J. Magn. Reson.* **2005**, *173*, 40. DOI: 10.1016/j.jmr.2004.11.015
- [23] Dillmann, B.; Elbayed, K.; Zeiger, H.; Weingertner, M.-C.; Piotto, M.; Engelke, F. A novel low-E field coil to minimize heating of biological samples in solid-state multinuclear NMR experiments. *J. Magn. Reson.* **2007**, *187*, 10. DOI: 10.1016/j.jmr.2007.02.018
- [24] Gor'kov, P. L.; Brey, W. W.; Long, J. R. Probe Development for Biosolids NMR Spectroscopy. In *Encyclopedia of Magnetic Resonance*; John Wiley & Sons, Ltd: 2007. DOI: 10.1002/9780470034590.emrstm1149
- [25] Krahn, A.; Priller, U.; Emsley, L.; Engelke, F. Resonator with reduced sample heating and increased homogeneity for solid-state NMR. *J. Magn. Reson.* **2008**, *191*, 78. DOI: 10.1016/j.jmr.2007.12.004
- [26] Griffin, R. G. Dipolar recoupling in MAS spectra of biological solids. *Nat. Struct. Biol.* **1998**, *5*, 508. DOI: 10.1038/749
- [27] Brinkmann, A. Dipolar recoupling in magic-angle-spinning nuclear magnetic resonance. Ph.D. Thesis, Stockholms Universitet, 2001. <http://search.proquest.com/docview/304780453/>
- [28] De Paepe, G. Dipolar recoupling in magic angle spinning solid-state nuclear magnetic resonance. *Annu. Rev. Phys. Chem.* **2012**, *63*, 661. DOI: 10.1146/annurev-physchem-032511-143726
- [29] Ladizhansky, V. Dipolar-Based Torsion Angle Measurements for Protein Structure Determination. In *Encyclopedia of Magnetic Resonance*; John Wiley & Sons, Ltd: 2007. DOI: 10.1002/9780470034590.emrstm1153

- [30] Rienstra, C. M. Magic-angle spinning recoupling techniques for distance determinations among spin-1/2 nuclei in solid peptides and proteins. *NMR Spectrosc. Biol. Solids* **2006**, 1. DOI: 10.1201/9781420027617.ch1
- [31] Schnell, I. Dipolar recoupling in fast-MAS solid-state NMR spectroscopy. *Prog. Nucl. Magn. Reson. Spectrosc.* **2004**, 45, 145. DOI: 10.1016/j.pnmrs.2004.06.003
- [32] Ernst, M.; Meier, B. H. Adiabatic Polarization-Transfer Methods in MAS Spectroscopy. In *Encyclopedia of Magnetic Resonance*; John Wiley & Sons, Ltd: 2007. DOI: 10.1002/9780470034590.emrstm0004.pub2
- [33] Bjerring, M.; Rasmussen, J. T.; Krogshave, R. S.; Nielsen, N. C. Heteronuclear coherence transfer in solid-state nuclear magnetic resonance using a gamma -encoded transferred echo experiment. *J. Chem. Phys.* **2003**, 119, 8916. DOI: 10.1063/1.1613933
- [34] Ernst, M. Heteronuclear spin decoupling in solid-state NMR under magic-angle sample spinning. *J. Magn. Reson.* **2003**, 162, 1. DOI: 10.1016/S1090-7807(03)00074-0
- [35] Mithu, V. S.; Pratihari, S.; Paul, S.; Madhu, P. K. Efficiency of heteronuclear dipolar decoupling schemes in solid-state NMR: Investigation of effective transverse relaxation times. *J. Magn. Reson.* **2012**, 220, 8. DOI: 10.1016/j.jmr.2012.04.005
- [36] Mithu, V. S.; Paul, S.; Kurur, N. D.; Madhu, P. K. Heteronuclear dipolar decoupling in solid-state nuclear magnetic resonance under ultra-high magic-angle spinning. *J. Magn. Reson.* **2011**, 209, 359. DOI: 10.1016/j.jmr.2011.01.028
- [37] Brinkmann, A.; Levitt, M. H. Symmetry principles in the nuclear magnetic resonance of spinning solids. Heteronuclear recoupling by generalized Hartmann-Hahn sequences. *J. Chem. Phys.* **2001**, 115, 357. DOI: 10.1063/1.1377031
- [38] Carravetta, M.; Eden, M.; Zhao, X.; Brinkmann, A.; Levitt, M. H. Symmetry principles for the design of radiofrequency pulse sequences in the nuclear magnetic resonance of rotating solids. *Chem. Phys. Lett.* **2000**, 321, 205. DOI: 10.1016/s0009-2614(00)00340-7
- [39] Levitt, M. H. Symmetry-based pulse sequences in magic-angle spinning solid-state NMR. In *Encyclopedia of Magnetic Resonance*; Grant, D. M., Harris, R. K., Eds.; Wiley: 2002; Vol. 9, p 165. DOI: 10.1002/9780470034590.emrstm0551
- [40] van Beek, J. D.; Carravetta, M.; Antonioli, G. C.; Levitt, M. H. Spherical tensor analysis of nuclear magnetic resonance signals. *J. Chem. Phys.* **2005**, 122, 244510/1. DOI: 10.1063/1.1943947
- [41] Zhao, X.; Hoffbauer, W.; Schmedt auf der Gunne, J.; Levitt, M. H. Heteronuclear polarization transfer by symmetry-based recoupling sequences in solid-state NMR. *Solid State Nucl. Magn. Reson.* **2004**, 26, 57. DOI: 10.1016/j.ssnmr.2003.11.001
- [42] Drobny, G. P.; Long, J. R.; Karlsson, T.; Shaw, W.; Popham, J.; Oyler, N.; Bower, P.; Stringer, J.; Gregory, D.; Mehta, M.; Stayton, P. S. Structural studies of biomaterials using double-quantum solid-state NMR spectroscopy. *Annu. Rev. Phys. Chem.* **2003**, 54, 531. DOI: 10.1146/annurev.physchem.54.011002.103903
- [43] LeMaster, D. M.; Kushlan, D. M. Dynamical Mapping of E. coli Thioredoxin via ¹³C NMR Relaxation Analysis. *J. Am. Chem. Soc.* **1996**, 118, 9255. DOI: 10.1021/ja960877r

- [44] Hong, M. Determination of Multiple ϕ -Torsion Angles in Proteins by Selective and Extensive ^{13}C Labeling and Two-Dimensional Solid-State NMR. *J. Magn. Reson.* **1999**, *139*, 389. DOI: 10.1006/jmre.1999.1805
- [45] Castellani, F.; van Rossum, B.; Diehl, A.; Schubert, M.; Rehbein, K.; Oschkinat, H. Structure of a protein determined by solid-state magic-angle-spinning NMR spectroscopy. *Nature* **2002**, *420*, 98. DOI: 10.1038/nature01070
- [46] Ellman, J. A.; Volkman, B. F.; Mendel, D.; Schulz, P. G.; Wemmer, D. E. Site-specific isotopic labeling of proteins for NMR studies. *J. Am. Chem. Soc.* **1992**, *114*, 7959. DOI: 10.1021/ja00046a080
- [47] Samuel-Landtiser, M.; Zachariah, C.; Williams, C. R.; Edison, A. S.; Long, J. R. Incorporation of Isotopically Enriched Amino Acids. In *Current Protocols in Protein Science*; John Wiley & Sons, Inc.: 2001. DOI: 10.1002/0471140864.ps2603s47
- [48] Jones, D. H.; Cellitti, S. E.; Hao, X.; Zhang, Q.; Jahnz, M.; Summerer, D.; Schultz, P. G.; Uno, T.; Geierstanger, B. H. Site-specific labeling of proteins with NMR-active unnatural amino acids. *J. Biomol. NMR* **2010**, *46*, 89. DOI: 10.1007/s10858-009-9365-4
- [49] Davis, L.; Chin, J. W. Designer proteins: applications of genetic code expansion in cell biology. *Nat. Rev. Mol. Cell Biol.* **2012**, *13*, 168. DOI: 10.1038/nrm3286
- [50] Renault, M.; Cukkemane, A.; Baldus, M. Solid-State NMR Spectroscopy on Complex Biomolecules. *Angew. Chem., Int. Ed.* **2010**, *49*, 8346. DOI: 10.1002/anie.201002823
- [51] McDermott, A. Solid state NMR studies of uniformly isotopically enriched proteins. *Biol. Magn. Reson.* **2003**, *20*, 103. DOI: 10.1007/0-306-47936-2_5
- [52] Tycko, R. Biomolecular solid state NMR: advances in structural methodology and applications to peptide and protein fibrils. *Annu. Rev. Phys. Chem.* **2001**, *52*, 575. DOI: 10.1146/annurev.physchem.52.1.575
- [53] Schmidt-Rohr, K.; Spiess, H. W. *Multidimensional Solid-state NMR and Polymers*; Academic Press: London; San Diego, 1994.
- [54] Yamanobe, T.; Uehara, H.; Kakiage, M. Practical NMR analysis of morphology and structure of polymers. *Annu. Rep. NMR Spectrosc.* **2010**, *70*, 203. DOI: 10.1016/s0066-4103(10)70003-x
- [55] Borisov, A. S.; Hazendonk, P.; Hayes, P. G. Solid-State Nuclear Magnetic Resonance Spectroscopy: A Review of Modern Techniques and Applications for Inorganic Polymers. *J. Inorg. Organomet. Polym. Mater.* **2010**, *20*, 183. DOI: 10.1007/s10904-010-9358-5
- [56] Michaelis, V. K.; Aguiar, P. M.; Kroeker, S. Probing alkali coordination environments in alkali borate glasses by multinuclear magnetic resonance. *J. Non-Cryst. Solids* **2007**, *353*, 2582. DOI: 10.1016/j.jnoncrysol.2007.04.029
- [57] van Wuelen, L.; Tricot, G.; Wegner, S. An advanced NMR protocol for the structural characterization of aluminophosphate glasses. *Solid State Nucl. Magn. Reson.* **2007**, *32*, 44. DOI: 10.1016/j.ssnmr.2007.07.004

- [58] Deschamps, M.; Roiland, C.; Bureau, B.; Yang, G.; Le Polles, L.; Massiot, D. ^{77}Se solid-state NMR investigations on $\text{As}_x\text{Se}_{1-x}$ glasses using CPMG acquisition under MAS. *Solid State Nucl. Magn. Reson.* **2011**, *40*, 72. DOI: 10.1016/j.ssnmr.2011.06.001
- [59] Fitzgerald, J. J. Solid-state ^1H , ^{17}O , and ^{27}Al NMR studies of the surface chemistry of alumina materials. *ACS Symp. Ser.* **1999**, *717*, 182. DOI: 10.1021/bk-1999-0717.ch005
- [60] Blasco, T. Insights into reaction mechanisms in heterogeneous catalysis revealed by in situ NMR spectroscopy. *Chem. Soc. Rev.* **2010**, *39*, 4685. DOI: 10.1039/c0cs00033g
- [61] Hunger, M.; Wang, W. Characterization of solid catalysts in the functioning state by nuclear magnetic resonance spectroscopy. *Adv. Catal.* **2006**, *50*, 149. DOI: 10.1016/s0360-0564(06)50004-5
- [62] Blanc, F.; Coperet, C.; Lesage, A.; Emsley, L. High resolution solid state NMR spectroscopy in surface organometallic chemistry: access to molecular understanding of active sites of well-defined heterogeneous catalysts. *Chem. Soc. Rev.* **2008**, *37*, 518. DOI: 10.1039/b612793m
- [63] Abragam, A. *The principles of nuclear magnetism*; Clarendon Press: Oxford, 1961.
- [64] Hackmann, A.; Seidel, H.; Kendrick, R. D.; Myhre, P. C.; Yannoni, C. S. Magic-angle spinning NMR at near-liquid-helium temperatures. *J. Magn. Reson.* **1988**, *79*, 148. DOI: 10.1016/0022-2364(88)90331-9
- [65] Allen, P. J.; Creuzet, F.; De Groot, H. J. M.; Griffin, R. G. Apparatus for low-temperature magic-angle spinning NMR. *J. Magn. Reson.* **1991**, *92*, 614. DOI: 10.1016/0022-2364(91)90357-Y
- [66] Macho, V.; Kendrick, R.; Yannoni, C. S. Cross polarization magic-angle spinning NMR at cryogenic temperatures. *J. Magn. Reson.* **1983**, *52*, 450. DOI: 10.1016/0022-2364(83)90170-1
- [67] Concistre, M.; Johannessen, O. G.; Carignani, E.; Geppi, M.; Levitt, M. H. Magic-Angle Spinning NMR of Cold Samples. *Acc. Chem. Res.*, Ahead of Print. DOI: 10.1021/ar300323c
- [68] Yannoni, C. S.; Myhre, P. C.; Webb, G. G. Magic angle spinning nuclear magnetic resonance near liquid-helium temperatures. Variable-temperature CPMA spectra of the 2-norbornyl cation to 6 K. *J. Am. Chem. Soc.* **1990**, *112*, 8991. DOI: 10.1021/ja00180a060
- [69] Tycko, R. NMR at Low and Ultralow Temperatures. *Acc. Chem. Res.*, Ahead of Print. DOI: 10.1021/ar300358z
- [70] De Groot, H. J. M.; Smith, S. O.; Courtin, J.; Van den Berg, E.; Winkel, C.; Lugtenburg, J.; Griffin, R. G.; Herzfeld, J. Solid-state carbon-13 and nitrogen-15 NMR study of the low pH forms of bacteriorhodopsin. *Biochemistry* **1990**, *29*, 6873. DOI: 10.1021/bi00481a017
- [71] Lipton, A. S.; Heck, R. W.; Sears, J. A.; Ellis, P. D. Low temperature solid-state NMR experiments of half-integer quadrupolar nuclides: caveats and data analysis. *J. Magn. Reson.* **2004**, *168*, 66. DOI: 10.1016/j.jmr.2004.01.008

- [72] Samoson, A.; Heinmaa, I.; Tuherm, T.; Reinhold, A.; Past, J.; Stern, R.; Anupold, T. A high resolution low temperature solid-state nuclear magnetic resonance probe. Patent #WO2005101949, 04/18/05, 2005.
- [73] Matsuki, Y.; Ueda, K.; Idehara, T.; Ikeda, R.; Ogawa, I.; Nakamura, S.; Toda, M.; Anai, T.; Fujiwara, T. Helium-cooling and -spinning dynamic nuclear polarization for sensitivity-enhanced solid-state NMR at 14 T and 30 K. *J. Magn. Reson.* **2012**, *225*, 1. DOI: 10.1016/j.jmr.2012.09.008
- [74] Barnes, A. B.; Mak-Jurkauskas, M. L.; Matsuki, Y.; Bajaj, V. S.; van der Wel, P. C. A.; De Rocher, R.; Bryant, J.; Sirigiri, J. R.; Temkin, R. J.; Lugtenburg, J.; Herzfeld, J.; Griffin, R. G. Cryogenic sample exchange NMR probe for magic angle spinning dynamic nuclear polarization. *J. Magn. Reson.* **2009**, *198*, 261. DOI: 10.1016/j.jmr.2009.03.003
- [75] Overhauser, A. W. Polarization of nuclei in metals. *Phys. Rev.* **1953**, *92*, 411. DOI: 10.1103/PhysRev.92.411
- [76] Carver, T. R.; Slichter, C. P. Polarization of nuclear spins in metals. *Phys. Rev.* **1953**, *92*, 212. DOI: 10.1103/PhysRev.92.212.2
- [77] Becerra, L. R.; Gerfen, G. J.; Temkin, R. J.; Singel, D. J.; Griffin, R. G. Dynamic nuclear polarization with a cyclotron resonance maser at 5 T. *Phys. Rev. Lett.* **1993**, *71*, 3561. DOI: 10.1103/PhysRevLett.71.3561
- [78] Bajaj, V. S.; Farrar, C. T.; Hornstein, M. K.; Mastovsky, I.; Vieregg, J.; Bryant, J.; Elena, B.; Kreisler, K. E.; Temkin, R. J.; Griffin, R. G. Dynamic nuclear polarization at 9 T using a novel 250 GHz gyrotron microwave source. *J. Magn. Reson.* **2003**, *160*, 85. DOI: 10.1016/s1090-7807(02)00192-1
- [79] Hartmann, S. R.; Hahn, E. L. Nuclear double resonance in the rotating frame. *Phys. Rev.* **1962**, *128*, 2042. DOI: 10.1103/PhysRev.128.2042
- [80] Rosay, M.; Tometich, L.; Pawsey, S.; Bader, R.; Schauwecker, R.; Blank, M.; Borchard, P. M.; Cauffman, S. R.; Felch, K. L.; Weber, R. T.; Temkin, R. J.; Griffin, R. G.; Maas, W. E. Solid-state dynamic nuclear polarization at 263 GHz: spectrometer design and experimental results. *Phys. Chem. Chem. Phys.* **2010**, *12*, 5850. DOI: 10.1039/c003685b
- [81] Bajaj, V. S. Dynamic nuclear polarization in biomolecular solid state NMR : methods and applications in peptides and membrane proteins. Ph.D. Thesis, Massachusetts Institute of Technology, 2007. <http://hdl.handle.net/1721.1/40874>
- [82] Barnes, A. B. High-resolution high-frequency dynamic nuclear polarization for biomolecular solid state NMR. Ph.D. Thesis, Massachusetts Institute of Technology, 2010. <http://hdl.handle.net/1721.1/65263>
- [83] Hall, D. A. Dynamic nuclear polarization of biological systems at high magnetic fields. Ph.D. Thesis, Massachusetts Institute of Technology, 1998. <http://hdl.handle.net/1721.1/9635>
- [84] Inati, S. J. Dynamic nuclear polarization and electron spin resonance in paramagnetic solids at high field. Ph.D. Thesis, Massachusetts Institute of Technology, 1999. <http://hdl.handle.net/1721.1/17474>

- [85] Hu, K.-N. Polarizing agents for high-frequency Dynamic Nuclear Polarization: development and applications. Ph.D. Thesis, Massachusetts Institute of Technology, 2006. <http://hdl.handle.net/1721.1/37887>
- [86] Hornstein, M. K. Design of a 460 GHz second harmonic gyrotron oscillator for use in dynamic nuclear polarization. S.M. Thesis, Massachusetts Institute of Technology, 2001. <http://hdl.handle.net/1721.1/33939>
- [87] Vieregg, J. R. A CW 250 GHz gyrotron oscillator for use in dynamic nuclear polarization. S.B. Thesis, Massachusetts Institute of Technology, 2001.
- [88] Joye, C. D. Design of a wideband, 100 W, 140 GHz gyrotron amplifier. S.M. Thesis, Massachusetts Institute of Technology, 2004. <http://hdl.handle.net/1721.1/28723>
- [89] Hornstein, M. K. A continuous-wave second harmonic gyrotron oscillator at 460 GHz. Ph.D. Thesis, Massachusetts Institute of Technology, 2005. <http://hdl.handle.net/1721.1/33939>
- [90] Casey, A. Dynamic nuclear polarization for NMR: applications and hardware development. S.M. Thesis, Massachusetts Institute of Technology, 2008. <http://hdl.handle.net/1721.1/43813>
- [91] Joye, C. D. A novel wideband 140 GHz gyrotron amplifier. Ph.D. Thesis, Massachusetts Institute of Technology, 2008. <http://hdl.handle.net/1721.1/45617>
- [92] Nanni, E. A. Design of a 250 GHz gyrotron amplifier. S.M. Thesis, Massachusetts Institute of Technology, 2010. <http://hdl.handle.net/1721.1/62438>
- [93] Sousa, A. C. T. d. Frequency-tunable second-harmonic submillimeter-wave gyrotron oscillators. Ph.D. Thesis, Massachusetts Institute of Technology, 2010. <http://hdl.handle.net/1721.1/62463>
- [94] Smith, A. A. Investigation of DNP mechanisms: the solid effect. Ph.D. Thesis, Massachusetts Institute of Technology, 2012. <http://hdl.handle.net/1721.1/73180>
- [95] Markhasin, E.; Barnes, A. B.; Hu, J.; Herzfeld, J.; Griffin, R. G. In *Balanced Triple Resonance Probe for Cryogenic MAS NMR and Dynamic Nuclear Polarization at 700 MHz*. WWMR2010. Joint EUROMAR 2010 and 17th ISMAR Conference, Florence, Italy, July 4-9, 2010. (oral presentation and poster)
- [96] Barnes, A. B.; Markhasin, E.; Daviso, E.; Michaelis, V. K.; Nanni, E. A.; Jawla, S. K.; Mena, E. L.; DeRocher, R.; Thakkar, A.; Woskov, P. P.; Herzfeld, J.; Temkin, R. J.; Griffin, R. G. Dynamic Nuclear Polarization at 700 MHz / 460 GHz. *J. Magn. Reson.* **2012**, *224*, 1. DOI: 10.1016/j.jmr.2012.08.002
- [97] Markhasin, E.; Barnes, A. B.; Daviso, E.; Michaelis, V. K.; Nanni, E. A.; Jawla, S. K.; Woskov, P.; Thakkar, A.; DeRocher, R.; Herzfeld, J.; Temkin, R. J.; Griffin, R. G. In *Spectrometer for Dynamic Nuclear Polarization at 700 MHz / 460 GHz*. 53rd ENC, Miami, Florida, April 15-20, 2012. (poster)
- [98] Barnes, A. B.; Markhasin, E.; Nanni, E. A.; Daviso, E.; Michaelis, V. K.; Jawla, S.; Herzfeld, J.; Temkin, R. J.; Griffin, R. G. In *DNP at 16.4 and 8.9 Tesla with Tunable Gyrotrons and High-Resolution Cryogenic MAS Probes*. Third International Symposium on Dynamic Nuclear Polarization, EPFL Lausanne, Switzerland, September 7-10, 2011.

- [99] Markhasin, E.; Michaelis, V. K.; Daviso, E.; Corzilius, B.; Herzfeld, J.; Griffin, R. G. In *Dynamic Nuclear Polarization of ^{17}O at 212 MHz / 140 GHz*. VIII International Voevodsky Conference "Physics and Chemistry of Elementary Chemical Processes", Novosibirsk Akademgorodok, Russia, July 15-19, 2012. (poster)
- [100] Michaelis, V. K.; Markhasin, E.; Daviso, E.; Herzfeld, J.; Griffin, R. G. Dynamic Nuclear Polarization of Oxygen-17. *J. Phys. Chem. Lett.* **2012**, *3*, 2030. DOI: 10.1021/jz300742w
- [101] Hu, J.; Herzfeld, J. Baluns, a fine balance and impedance adjustment module, a multi-layer transmission line, and transmission line NMR probes using same. Patent #7936171, 2011.
- [102] Hu, J.; Bielecki, A.; Griffin, R. G.; Herzfeld, J. In *A Totally Balanced, Fully Transmission Line, Triple Resonance NMR Probe for High Frequencies*. 49th ENC, Pacific Grove, California, 2008.
- [103] Hu, J. Balanced multi-resonant transmission line nuclear magnetic resonance probes. Ph.D. Thesis, Brandeis University, 2010. <http://search.proquest.com/docview/305185343>
- [104] Markhasin, E.; Hu, J.; Su, Y.; Herzfeld, J.; Griffin, R. G. Efficient, balanced, transmission line RF circuits by back propagation of common impedance nodes. *J. Magn. Reson.* **2013**, *231C*, 32. DOI: 10.1016/j.jmr.2013.02.017
- [105] Markin, A. V.; Markhasin, E.; Sologubov, S. S.; Smirnova, N. N.; Griffin, R. G. Standard Thermodynamic Functions of Tripeptides N-formyl-Met-Pro-Phe-OH and N-formyl-Met-Pro-Phe-OMe.
- [106] Das, T. P.; Hahn, E. L. *Nuclear quadrupole resonance spectroscopy*; Academic Press: New York,, 1958.
- [107] Cavalli, A.; Salvatella, X.; Dobson, C. M.; Vendruscolo, M. Protein structure determination from NMR chemical shifts. *Proc. Natl. Acad. Sci. U.S.A.* **2007**, *104*, 9615. DOI: 10.1073/pnas.0610313104
- [108] Shen, Y.; Lange, O.; Delaglio, F.; Rossi, P.; Aramini, J. M.; Liu, G.; Eletsky, A.; Wu, Y.; Singarapu, K. K.; Lemak, A.; Ignatchenko, A.; Arrowsmith, C. H.; Szyperski, T.; Montelione, G. T.; Baker, D.; Bax, A. Consistent blind protein structure generation from NMR chemical shift data. *Proc. Natl. Acad. Sci. U.S.A.* **2008**, *105*, 4685. DOI: 10.1073/pnas.0800256105
- [109] Chandrashekar, S.; Jerschow, A. Tensors in NMR. In *Encyclopedia of Magnetic Resonance*; John Wiley & Sons, Ltd: 2007. DOI: 10.1002/9780470034590.emrstm1050
- [110] Ernst, M.; Meier, B. H. *Physical Chemistry VIII, 2003. High-Resolution Solid-State NMR: Principles and Applications*; Laboratorium fur Physikalische Chemie, ETH Zurich, 2003.
- [111] Mehring, M. *Principles of high-resolution NMR in solids*; 2nd, rev. and enl. ed.; Springer-Verlag: Berlin ; New York, 1983.
- [112] Mehring, M.; Waugh, J. S. Magic-angle NMR experiments in solids. *Phys. Rev. B* **1972**, *[3]5*, 3459. DOI: 10.1103/PhysRevB.5.3459

- [113] Mehring, M. Internal Spin Interactions and Rotations in Solids. In *Encyclopedia of Magnetic Resonance*; John Wiley & Sons, Ltd: 2007. DOI: 10.1002/9780470034590.emrstm0244
- [114] Brink, D. M.; Satchler, G. R. *Angular momentum*; Clarendon Press; Oxford University Press: Oxford; New York, 1993.
- [115] Rose, M. E. *Elementary theory of angular momentum*; Dover ed.; Dover: New York, 1995.
- [116] Sakurai, J. J.; Napolitano, J. *Modern quantum mechanics*; 2nd ed.; Addison-Wesley: Boston, 2011.
- [117] Eden, M. Computer simulations in solid-state NMR. I. Spin dynamics theory. *Concepts Magn. Reson. A* **2003**, *17A*, 117. DOI: 10.1002/cmr.a.10061
- [118] Maricq, M. M.; Waugh, J. S. NMR in rotating solids. *J. Chem. Phys.* **1979**, *70*, 3300. DOI: 10.1063/1.437915
- [119] Lowe, I. J. Free induction decay of rotating solids. *Phys. Rev. Lett.* **1959**, *2*, 285. DOI: 10.1103/PhysRevLett.2.285
- [120] Andrew, E. R.; Bradbury, A.; Eades, R. G. Nuclear magnetic resonance spectra from a crystal rotated at high speed. *Nature (London, U. K.)* **1958**, *182*, 1659. DOI: 10.1038/1821659a0
- [121] Slichter, C. P.; Fulde, P. *Principles of Magnetic Resonance*; Originally published by Harper and Row Publishers, New York, 1963, 3rd enlarged and updated 1990. Corr. 3rd printing ed.; Springer, 1996; Vol. 1.
- [122] Jerschow, A. From nuclear structure to the quadrupolar NMR interaction and high-resolution spectroscopy. *Prog. Nucl. Magn. Reson. Spectrosc.* **2005**, *46*, 63. DOI: 10.1016/j.pnmrs.2004.12.001
- [123] Larsen, F. H.; Jakobsen, H. J.; Ellis, P. D.; Nielsen, N. C. Sensitivity-Enhanced Quadrupolar-Echo NMR of Half-Integer Quadrupolar Nuclei. Magnitudes and Relative Orientation of Chemical Shielding and Quadrupolar Coupling Tensors. *J. Phys. Chem. A* **1997**, *101*, 8597. DOI: 10.1021/jp971547b
- [124] Larsen, F. H.; Jakobsen, H. J.; Ellis, P. D.; Nielsen, N. C. QCPMG-MAS NMR of half-integer quadrupolar nuclei. *J. Magn. Reson.* **1998**, *131*, 144. DOI: 10.1006/jmre.1997.1341
- [125] Larsen, F. H.; Jakobsen, H. J.; Ellis, P. D.; Nielsen, N. C. High-field QCPMG-MAS NMR of half-integer quadrupolar nuclei with large quadrupole couplings. *Mol. Phys.* **1998**, *95*, 1185. DOI: 10.1080/00268979809483250
- [126] Meiboom, S.; Gill, D. Modified spin-echo method for measuring nuclear relaxation times. *Rev. Sci. Instrum.* **1958**, *29*, 688. DOI: 10.1063/1.1716296
- [127] Carr, H. Y.; Purcell, E. M. Effects of diffusion on free precession in nuclear magnetic resonance experiments. *Phys. Rev.* **1954**, *94*, 630. DOI: 10.1103/PhysRev.94.630

2. Dynamic Nuclear Polarization Spectrometer for DNP at 700 MHz/460 GHz

Adapted from references [1-4].

Abstract

We describe the design and implementation of the instrumentation required to perform DNP-NMR at higher field strengths than previously demonstrated, and report the first magic-angle spinning (MAS) DNP-NMR experiments performed at $^1\text{H}/e^-$ frequencies of 700 MHz/460 GHz. The extension of DNP-NMR to 16.4 T has required the development of probe technology, cryogenics, gyrotrons, and microwave transmission lines. The probe contains a 460 GHz microwave channel, with corrugated waveguide, tapers, and miter-bends that couple microwave power to the sample. Experimental efficiency is increased by a cryogenic exchange system for 3.2 mm rotors within the 89 mm bore. Sample temperatures ≤ 85 K, resulting in improved DNP enhancements, are achieved by a novel heat exchanger design, stainless steel and brass vacuum jacketed transfer lines, and a bronze probe dewar. In addition, the heat exchanger is preceded with a nitrogen drying and generation system in series with a pre-cooling refrigerator. This reduces liquid nitrogen usage from >400 liters per day to <100 liters per day and allows for continuous (>7 days) cryogenic spinning without detrimental frost or ice formation. Initial enhancements, $\epsilon = -40$, and a strong microwave power dependence suggests the possibility for considerable improvement. Finally, two-dimensional spectra of a model system demonstrate that the higher field provides excellent resolution, even in a glassy, cryoprotecting matrix.

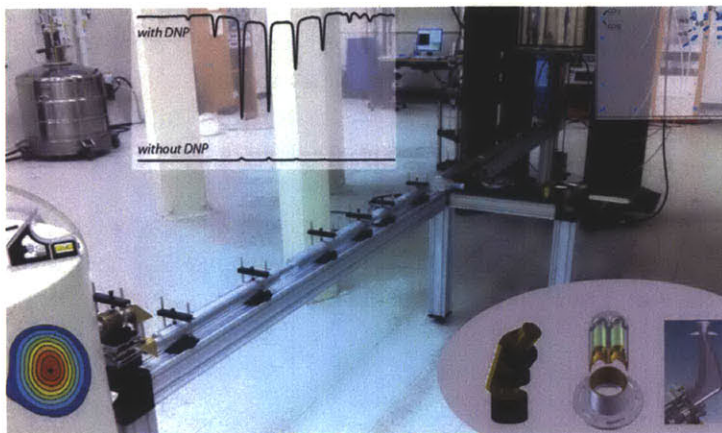


Figure 2. DNP at 700 MHz / 460 GHz.

The 460 gyrotron is on the left, and the transmission line couples microwaves to the probe in the 700 MHz wide bore magnet (upper right). The spectrometer is currently the highest field MAS DNP/NMR system in the world and is providing enhancements of ≥ 50 on standard samples and 25-30 on proteins in glassy media.

2.1. Introduction

Dynamic nuclear polarization (DNP) has emerged as a widely applicable technique to provide significant gains in sensitivity to NMR [5-10]. In a DNP experiment the sample is generally doped with an exogenous paramagnetic polarizing agent, and the large polarization present in the electron spin reservoir is transferred to the nuclear spins via microwave irradiation of transitions in the electron paramagnetic resonance (EPR) spectrum. In the early 1950's Carver and Slichter [11-12] performed the initial demonstration of DNP, but subsequent applications to high resolution, high field NMR have been limited. In particular, there was a dearth of microwave sources operating at electron Larmor frequencies (130-660 GHz) corresponding to the magnetic fields of the superconducting magnets (200-1000 MHz ^1H frequencies) used in contemporary NMR experiments. This barrier was broken in the early 1990's by gyrotrons [7-8] and subsequently by Gunn and Impatt diodes [8,13] resulting in the application of the method to a wide range of chemical and biochemical problems at fields up to 9 T [14-19] with one instrument operating at 14.1 T [20].

The recent availability of commercial DNP spectrometers operating at 9.4 T ($^1\text{H}/e^-$ frequencies of 400 MHz/263 GHz) [21] has greatly expanded access to DNP [22-24]. However, for many contemporary NMR experiments, 9.4 T is a relatively low field for optimal spectral resolution and it is therefore important to extend DNP to higher fields. Here, we describe the extension of magic-angle spinning (MAS) DNP to 16.4 T ($^1\text{H}/e^-$ frequencies of 700 MHz/460 GHz), a nearly two-fold increase in field over commonly available DNP instrumentation. Our initial experiments show that standard samples yield the expected enhancements and that the higher field provides increased resolution even for molecules embedded in glassy solvents such as glycerol/ H_2O .

2.2. Spectrometer Design

A MAS NMR / DNP spectrometer is a complex instrument, and its design can be conveniently rationalized within the following framework (Figure 3). From the "sample perspective" (the inner circle) the first device it sees is the probe (inner ring), consisting of several subsystems. In the order of increasing experimental complexity, basic NMR experiments require a radiofrequency (RF) circuit; MAS NMR also requires a pneumatic circuit; variable temperature and cryogenic MAS NMR also require a cryogenic circuit; finally, DNP enhanced MAS NMR experiments also require a microwave (MW) circuit. A MAS NMR / DNP probe integrates these subsystems, and each of them is further supported by peripheral instruments (the outer ring),

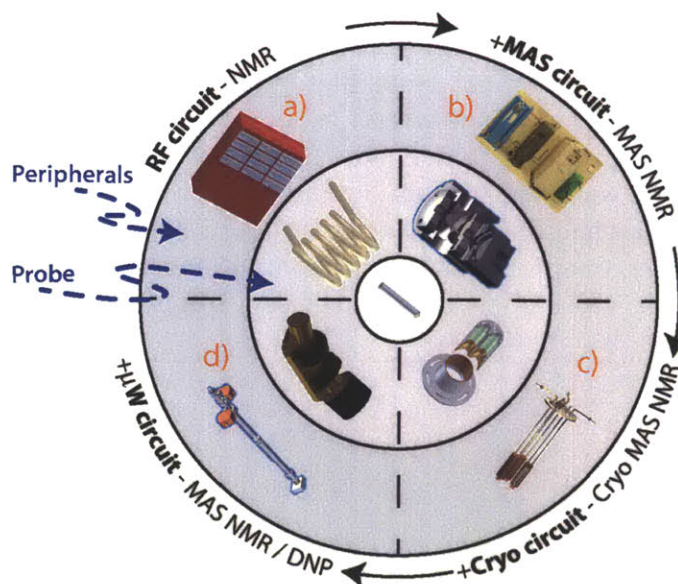


Figure 3. MAS DNP spectrometer structure. The middle circle represents a MAS DNP probe consisting of RF (a), pneumatic (b), cryogenic (c), and μW (d) circuits driven by corresponding peripheral instruments represented by the outer circle.

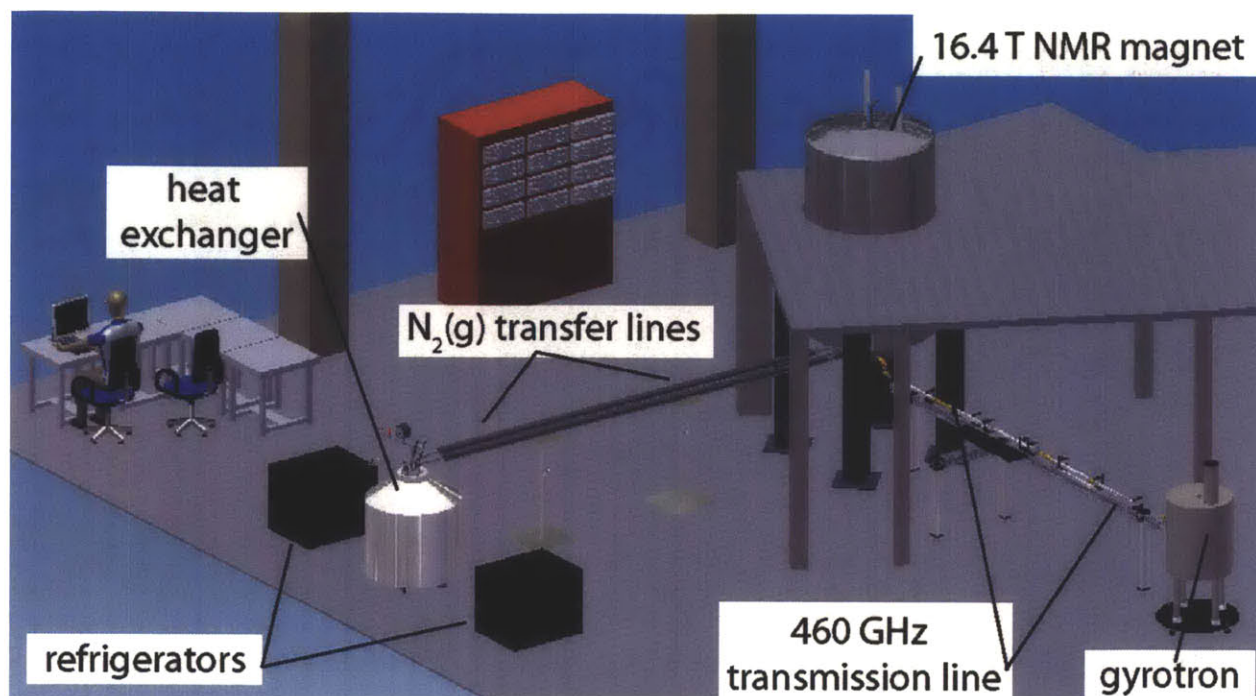


Figure 4. 700 MHz DNP instrumentation.

Schematic showing the physical layout of the NMR magnet, heat exchanger, gyrotron, microwave transmission lines, and Cambridge Instruments spectrometer console with RF power amplifiers from Ophir (Los Angeles, California) at 700 MHz and Herley Industries (Lancaster, Pennsylvania) at 175 MHz.

including NMR console (a) and magnet equipped with a sweep coil; high power microwave source, such as a gyrotron (d) and microwave waveguide; generator of neat nitrogen gas (b); heat exchanger (c), cryogenic sample exchange system and cryogenics transfer lines.

The architecture of custom build 700 MHz / 460 GHz DNP spectrometer is illustrated schematically in Figure 4. Shown are a 700 MHz / 89 mm magnet and a 460 GHz gyrotron. The microwave radiation from the gyrotron is coupled to the probe by a system of corrugated waveguides, tapers, and miter-bends. On the left of the figure are located the cryogenics for the system. It presently consists of a nitrogen generator in series with ballasts, pressure regulators, refrigerators, heat exchange coils, and vacuum jacketed transfer lines cool and deliver the dry ~80 K N₂ gas to the sample chamber. The spectrometer console, designed by Cambridge Instruments, is in the background. We now discuss each of these components in greater detail.

2.2.1. 700 MHz MAS DNP Probe

The custom designed probe, shown in Figure 5 and Figure 6, has over 11 ports for the diverse functions required of a DNP MAS probe. Fiber optic channels monitor the MAS frequency, the sample temperature, and provide a pathway for *in situ* illumination of the sample with visible light for photochemical experiments. The fiber optics in the sample chamber are shown in Figure 6a,b. In-situ irradiation of the sample with visible light, in conjunction with temperature control from 80–300 K, facilitates cryo-trapping of photoreaction intermediates as in bacteriorhodopsin. [25] The temperature is continually monitored at four points using fiber optic temperature sensors (Neoptix, Canada): a sensor several millimeters away from the sample (the yellow fiber optic in Figure 6a) provides a close measure of the sample temperature, one in the probe box near

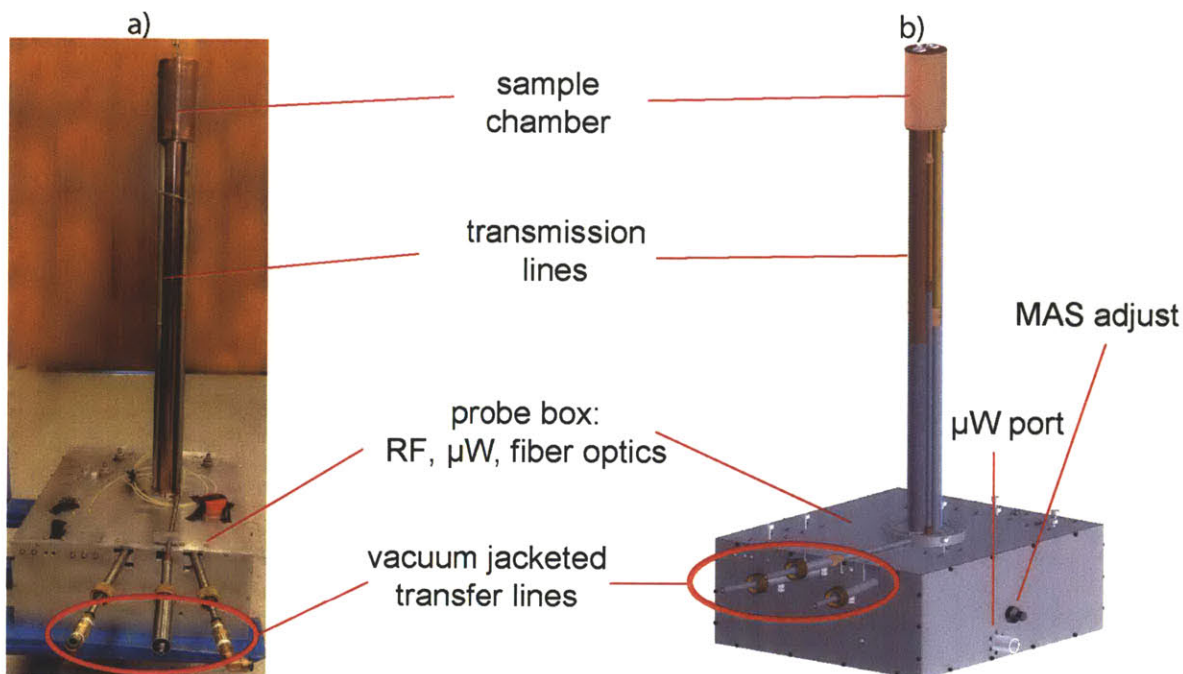


Figure 5. 700 MHz MAS DNP probe. a) Photograph. b) Solid CAD model.

the tuning elements is needed to maintain long-term radiofrequency tuning and stability, and sensors at the top and bottom of the magnet bore near the O-rings protect the superconducting magnet system.

Three vacuum jacketed composite metal transfer lines provide an insulated pathway for delivery of the cold bearing, drive, and variable temperature gas. A high-flow vacuum jacketed port at the top of the probe exhausts the cold cryogenics during operation, but is switched to input high pressure ejection gas during sample exchange (see below).

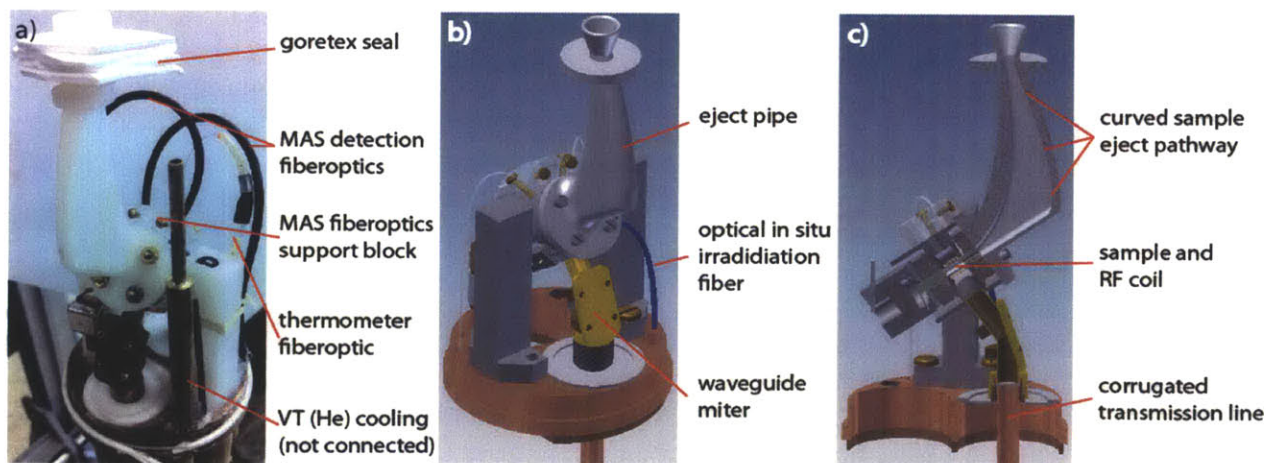


Figure 6. Upper assembly of the 700 MHz MAS DNP probe. a) Photograph of the fiber optics and the GORE-TEX® seal required for cryogenic sample exchange. b) Solid CAD model. c) Cut-away showing the microwaves being directed at the sample and surrounding RF coil. The sample eject pathway is curved to fit the assembly into the bore while still allowing for adjustment of the magic angle.

A Schaefer-McKay transmission line circuit [26-27] generates RF fields at the ^{13}C and ^1H Larmor frequencies of 175 MHz and 698 MHz, respectively. The Rabi frequencies are $\gamma B_1/2\pi=105$ kHz and 90 kHz for ^1H and ^{13}C , respectively. The transmission line (1.125" outer conductor, 0.25" inner conductor) allows the temperature sensitive and more bulky tuning and matching capacitors to be physically, and thermally, isolated from the cryogenic sample chamber, while providing efficient coupling to the 5-turn RF transmit/receive solenoid. The 460 GHz channel of the probe delivers the microwave power to the sample as a Gaussian beam (see below).

Spinning detection is performed on the rotor body with the detection fiber optics protruding into the stator housing as indicated in Figure 6a. A support block is attached to the stator housing and is required to lock the detection optics in place during cryogenic operation and extreme temperature cycling. Two PEEK screws, orthogonal to the holes in the Kel-F support block that guide the fiber optics, are threaded through the support block and gently pinch the spinning detection fiber optics to keep them securely in place. The support block also houses a pathway for a variable temperature gas-stream (nitrogen or helium) to blow directly on the rotor, although this is not yet fully implemented.

2.2.2. Metal Composite Transfer Lines

In large 127 mm bore magnets [28-29], it is possible to use fiberglass in the dewar and vacuum jacketed transfer lines to avoid magnetic materials. However, although fiberglass is an excellent thermal insulator, it must be thick for use in transfer lines and dewars. It also requires a

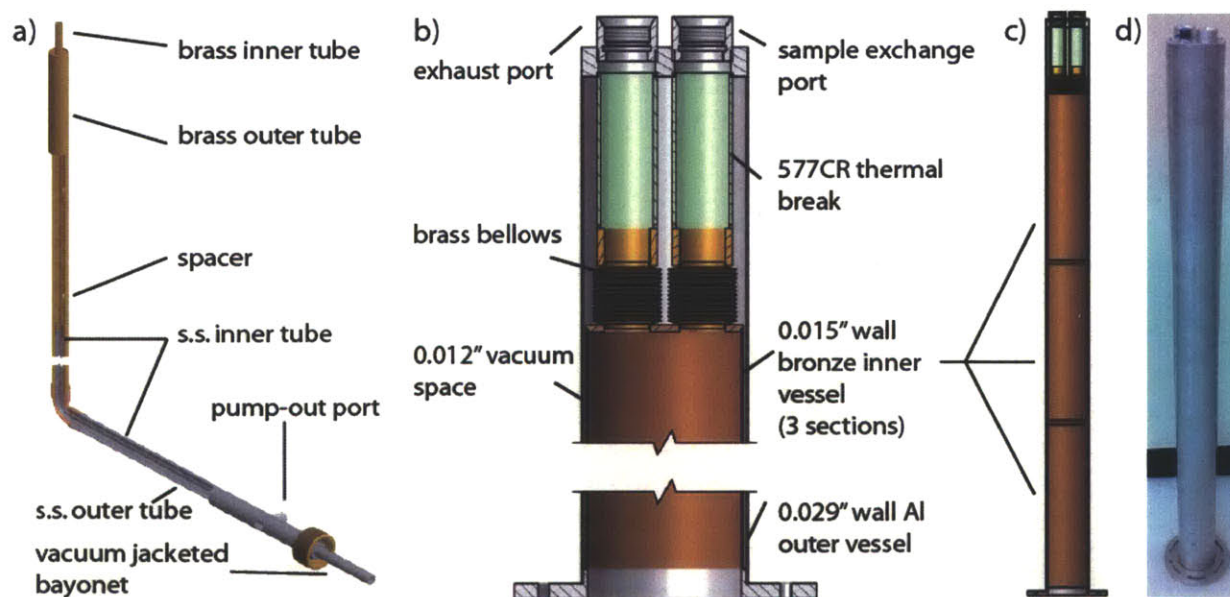


Figure 7. Cryogenic isolation strategies.

a) The vacuum jacketed transfer lines inside the probe employ brass tubing inside the bore of the magnet that can be soldered to the stainless steel (s.s.) components at the bottom of the assembly. **b)** The vacuum jacketed dewar features an inner bronze vessel and an aluminum outer vessel that are connected via a fiberglass thermal break and brass bellows to allow for transport of the cryogen exhaust and the rotor during sample exchange. **c)** CAD rendering show the three sections of the dewar inner vessel that are soldered together. **d)** Photograph of the dewar.

relatively large vacuum space between the inner and outer vessels, as its emissivity can otherwise lead to substantial radiative heat transfer to the inner vessel. Furthermore, the epoxy required to connect the fiberglass to other pieces of the assembly complicates fabrication and is prone to forming leaks that compromise the vacuum space. Meanwhile, gases (especially helium) can permeate the fiberglass itself.

To circumvent these issues the probe transfer lines shown in Figure 7 are made exclusively of non-magnetic brass and austenitic steel. This provides excellent insulation of the cryogenics while passively holding a vacuum for extended periods of operation. We emphasize that insulating the cryogenics until they enter the sample chamber is crucial for attaining the sample temperatures of ≤ 85 K that significantly increase DNP enhancements, as described in the results section.

2.2.3. Dewar

A vacuum jacketed dewar thermally isolates the cryogenic sample chamber from the magnet bore. Excellent insulation is required not only to establish ≤ 85 K at the sample, but also to protect the O-ring on the bore tube of the NMR magnet from freezing, compromising the insulating vacuum of the magnet, and leading to a quench. The inner vessel is machined from 2.25" i.d., 3" o.d. silicon bronze tubing (National Bronze, Lorain, OH). We elected to use bronze rather than stainless steel because the inner vessel of the dewar surrounds the sample in close proximity, and even a weakly ferromagnetic character can lead to a field inhomogeneity across the sample that cannot be effectively compensated for by shim coils. Although austenitic stainless steel (i.e., 316, 321 series) is commonly referred to as "non-magnetic", it actually becomes quite magnetic by NMR standards after mechanical work or thermal cycling due to martensite formation [29].

Because it is prohibitively difficult to machine the full 30" length of the inner surface to the final 0.015" wall thickness, the inner vessel is first cut into three sections to turn down the material, and then soldered together with vacuum tight joints (see Figure 7c).

There is a bellowed port on the top of the dewar to accommodate the sample exchange tube similar to that described previously. [29] In this dewar we also include a port to accept the cryogen exhaust line. Utilizing the space above the probe to exhaust the cryogenics out of the top of the system frees space at the bottom of the probe, making it easier to fit the fiber optics, magic-angle adjustment assembly, and transfer and transmission lines into the lower assembly.

2.2.4. 3.2 mm Cryogenic Sample Exchange

Previous DNP probe technology in our lab has been designed for use in 127 mm (5") bore magnets. Even with the longer 4 mm diameter rotors employed in those probes, there is sufficient space in the bore for the rotor to turn from the magic angle to vertical orientation for sample insertion and ejection. However, the smaller 89 mm bore magnets present a greater challenge. In order to implement a cryogenic sample exchange system, we optimized the ejection trajectory in the sample eject pipe, and maximized the space available in the dewar (Figure 6c).

After the rotor makes the turn in the sample eject pipe, it must couple to the long straight ejection tube leading to the top of the magnet. This is accomplished by two overlapped cones, which maintain the ability to adjust the magic angle [29]. However, the cone requires space that is difficult to accommodate in the 89 mm bore. Whereas previous designs simply mounted the cone on the vertical end of the sample eject pipe, the present design introduces a curved pathway to first bend the rotor trajectory back toward the center of the bore. This complicated geometry is fabricated by 3D printing (Accelerate Global Sourcing, Cedar Park, TX). Extrusions on the sur-

face of the eject pipe flush with the front bearing mount ensure proper alignment of the insertion pathway in the ejection pipe with the inner surface of the front bearing. Care is taken to ensure that the guiding pathway is well aligned and extremely smooth ($<0.2 \mu\text{m}$ roughness), to allow the rotor to slide into the front bearing of the stator. The robust plastic ejection pipe survives dozens of temperature cycles and hundreds of sample ejections.

2.2.5. Nitrogen Generation for MAS

To achieve operating temperatures down to $\sim 80 \text{ K}$, we and others have traditionally used dry N_2 produced from liquid boil-off to drive the MAS rotors. After evaporation, the N_2 is first warmed to ambient temperature, to allow precise control of the pressure, and then cooled directly to $\sim 80 \text{ K}$ with a custom pressurized can heat exchanger [29-30]. While boil-off N_2 has the advantage of very low H_2O vapor content, which prevents ice formation, this strategy leads to high operational costs, due not only to the $\text{N}_2(l)$ required for generation of the dry gas, but also the $\text{N}_2(l)$ needed to re-cool the gas from 300 K to 80 K . To reduce costs and allow for continuous long-term operation of the spectrometer, we now employ a N_2 generation and pre-cooling strategy similar to that described previously [20] and illustrated schematically in Figure 8a-b. Compressed air that initially has a dew point of 253 K is first processed through a series of two pressure swing activated (PSA) dryers (Parker-Balston, Haverhill, MA). The dry air then passes through a PSA nitrogen generator (Parker-Balston, Haverhill, MA) that removes oxygen and argon and further reduces the H_2O dew point to $<77 \text{ K}$, as is crucial to prevent ice formation in the heat exchange coils. The pressure of the dry N_2 gas is stabilized by a ballast and controlled precisely with pressure regulators. From there, it enters a Polycold PGC-152 gas chiller shown in Figure 8c for pre-cooling (Brooks Automation, MA) from 300 K to $\sim 150\text{-}200 \text{ K}$, depending on the flow rate. Bayoneted connectors and vacuum jacketed transfer lines connect the output of the refrigerators (one for bearing and one for drive) to the input of a custom pressurized-can heat exchanger [30] described below. This strategy allows for continuous operation for periods longer than one week without detrimental ice formation while reducing the nitrogen consumption rate from $\geq 400 \text{ L N}_2(l)$ per day to $\leq 200 \text{ L N}_2(l)$ per day. In addition, the liquid that was vaporized and used to drive the rotor is no longer used, saving an additional ≥ 100 liters/day. Therefore the system saves ≥ 4 in nitrogen cost.

2.2.6. Heat Exchanger

Following cooling to $T=150\text{-}200 \text{ K}$ by the Polycold chillers, the $\text{N}_2(g)$ is routed via vacuum jacketed transfer lines to the heat exchanger which further cools the gas to $\sim 85 \text{ K}$ (Figure 8). This device is designed in a manner similar to the one we described some time ago [29-30], but with several modifications. Specifically, it consists of two independent 7 turn, 7" cooling coils made of 0.375" o.d. nickel-plated copper tubing, which independently cool the drive and bearing gas and permit the two to be adjusted independently. The large cooling capacity of the coils allows a relatively low $\text{N}_2(l)$ level (resulting from condensation of $\text{N}_2(g)$ at $<5 \text{ psi}$ in the can) to effectively cool the spinning gases to $\sim 85 \text{ K}$, and yields stable, long-term cryogenic MAS without liquefaction of the spinning gases. Less than 1 K temperature stability over a period of days is achieved as described previously [28] with heating elements and Cernox temperature sensors that are engineered into the flexible transfer lines (Precision Cryogenics, Indianapolis, IN) near the probe interface and are controlled by 50 and 100 W heating units under PID feedback (Lakeshore Cryogenics, OH). A further modification of the heat exchanger that is under development

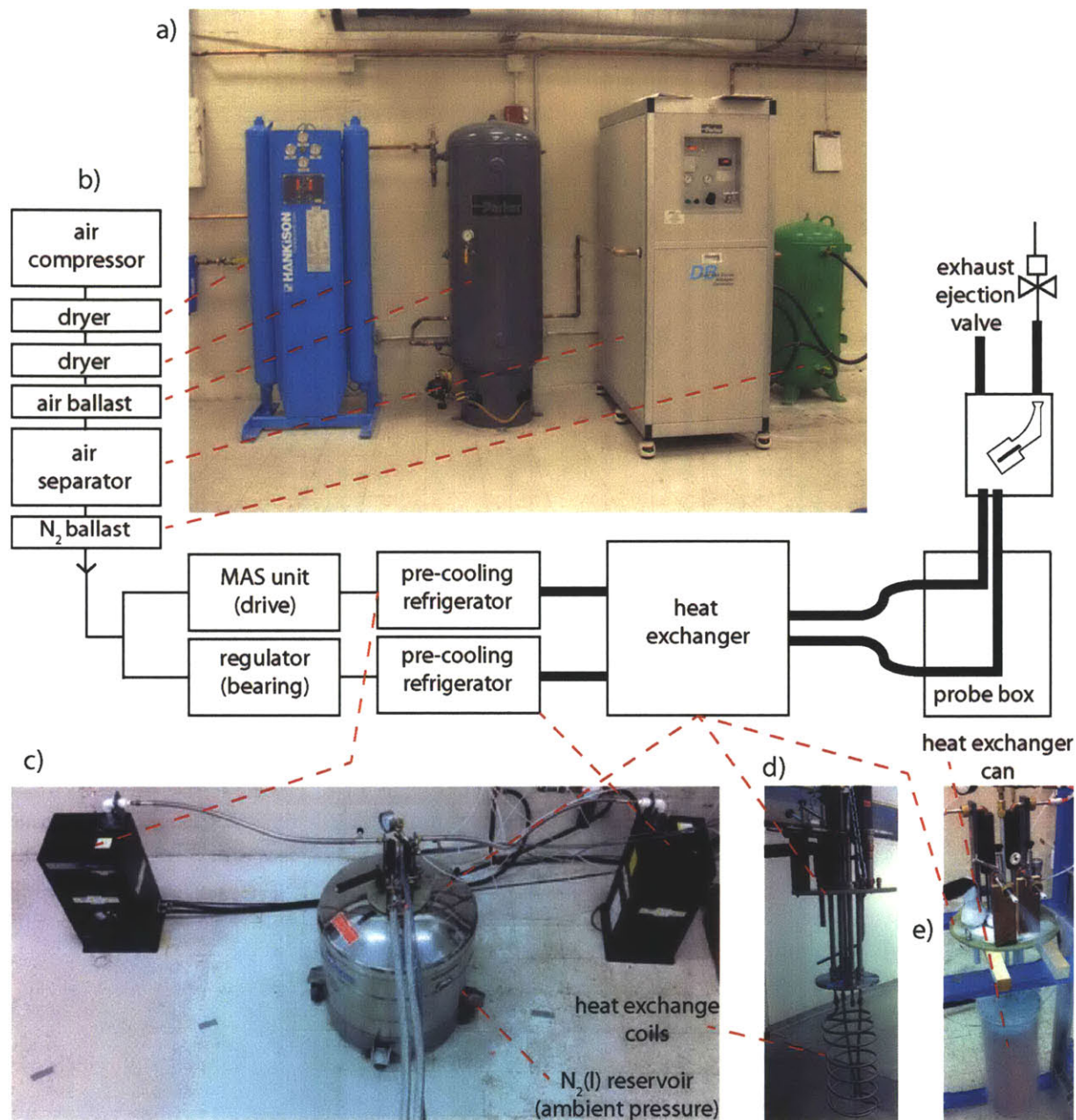


Figure 8. Nitrogen gas generation and cryocooling apparatus.

a) Photograph of nitrogen gas generation system. **b)** System architecture showing the serial and parallel layout of the nitrogen gas as it is purified, cooled, and transferred to the sample chamber. Cryogen exhaust and sample exchange lines are connected to the probe from the top of the magnet. **c)** The inlet ports of the refrigerators (black units in upper corners) are connected to the precisely controlled bearing and drive gas regulators. Vacuum jacketed lines connect the refrigerators, heat exchanger, and NMR probe. **d)** The nickel-plated copper coil of the heat exchanger with 7 turns. **e)** The cold heat exchange assembly showing the 8" copper can.

will use a third chamber and permit the drive and bearing to operate at higher temperatures while independently cooling the center of the rotor containing the sample.

2.2.7. 460 GHz Microwave Transmission

Substantial efforts in the development of microwave sources for DNP have resulted in the availability of robust, continuous wave gyrotrons with 10-35 W power levels capable of generating electron nutation frequencies of 1 MHz across microliters of lossy sample volume [22,31-35]. A gyrotron operating in the second cyclotron resonance harmonic with a TE_{11,2} whispering gallery interaction mode was specifically developed for DNP at 16.4 T. This design offers greater than 1 GHz of tuning range while maintaining 12 W of stable microwave power output for extended periods. [36-37]

The output beam of the gyrotron reflects off the last surface of the mode converter and into the corrugated waveguide that protrudes into the cross bore of the gyrotron magnet. Alignment of the output beam is crucial to maintaining a high purity HE₁₁ mode in the transmission line. After exiting the crossbore of the gyrotron magnet, the microwave power traverses 4.7 m to the probe in a 19 mm wide corrugated waveguide (see Figure 9a), and then travels 0.8 m up the magnet bore. Altogether the radiation travels 5.5 m passing through 6 miter-bends and two tapers,

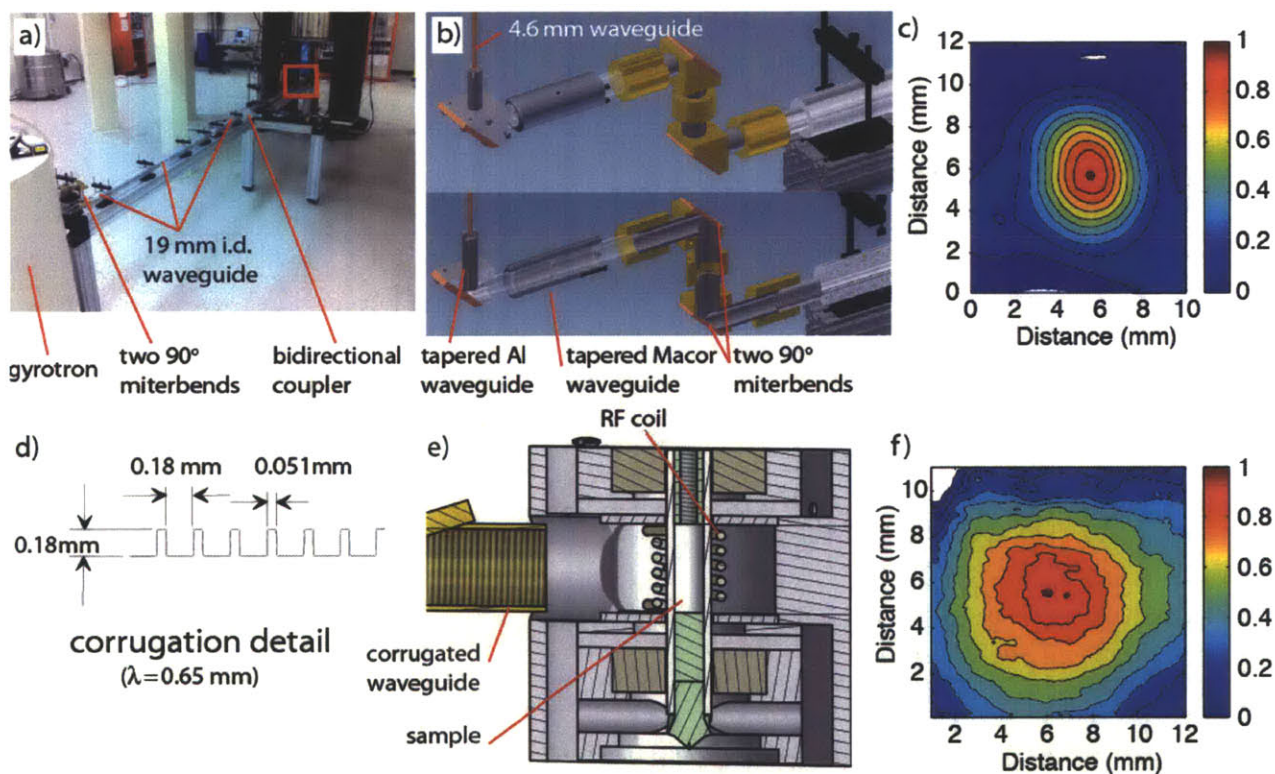


Figure 9. 460 GHz microwave transmission and beam quality.

a) The corrugated transmission line contains miter-bends, a bidirectional coupler for power monitoring and efficiently couples the microwave output of the gyrotron to the probe. **b)** The probe contains smooth-wall Macor and corrugated aluminum tapers to focus the microwave beam into the 4.6 mm i.d. vertical waveguide leading to the sample chamber. **c)** Thermal image recorded with a pyroelectric camera (Spiricon, Logan Utah) of the beam taken from the middle of the 3 m stretch of the 19 mm i.d. corrugated waveguide showing a high Gaussian content 10 cm from the waveguide aperture. **d)** Schematic showing the $1/4 \lambda$ depth and spacing of the corrugations. **e)** Cross-section of the stator with the rotor and waveguide. **f)** Image of the high-quality beam being launched from the end of the waveguide in panel e toward the sample 4 cm from the waveguide aperture.

so any distortion in the beam quality (in the form of the presence of higher order modes) leads to a cumulative loss of the microwave power and significant decrease in DNP performance.

To precisely align the output of the mode converter mirror with the probe inside the NMR magnet across the room, we utilize two sets of double 90° miter-bends. Each employs small gaps between the waveguide pieces connecting the miter-bends, as shown in Figure 9b. Generally, gaps in overmoded corrugated waveguides that are shorter than the i.d. of the guide have very low transmission loss. This allows us to add more degrees of freedom during the alignment process by implementing a “flexible” GHz transmission line. Evidence for the excellent coupling into the transmission line from the gyrotron and proper alignment of the system is shown in Figure 9c. The pyroelectric image of the beam recorded from the bidirectional coupler (Figure 9a) shows an excellent beam with $>90\%$ Gaussian content. The bidirectional coupler [38] permits continuous monitoring of the microwave power either with a calorimeter or a diode. The output can be fed back into the LabView control system of the gyrotron to stabilize the power output via PID control of the electron beam current.

The HE_{11} mode maintained in the 19 mm corrugated waveguide, whose cross section is illustrated in Figure 9d, is accepted by the 460 GHz channel of the probe. The microwave beam is then focused into a 12.7 mm i.d. tapered smooth-wall dielectric (Macor) waveguide. After a 90° miter-bend to direct the radiation up the bore of the magnet, the beam is further focused with a tapered corrugated Al waveguide that couples to the ~ 0.6 m long vertical helically corrugated (tapped) 4.6 mm i.d. copper waveguide. The radiation then reflects off of a final miter-bend at the inverse magic angle, travels through a short section of corrugated waveguide, and illuminates the sample as shown in Figure 9e. The beam quality is maintained through these tapers and miter-bends, as can be seen by the $>90\%$ Gaussian content of the experimental beam in Figure 9f.

2.3. Results

Figure 10a shows an enhancement of $\varepsilon = -40$ on ^{13}C -Urea dissolved in a 60/30/10 glycerol/ D_2O / H_2O glass forming matrix containing 10 mM of the biradical polarizing agent [39]

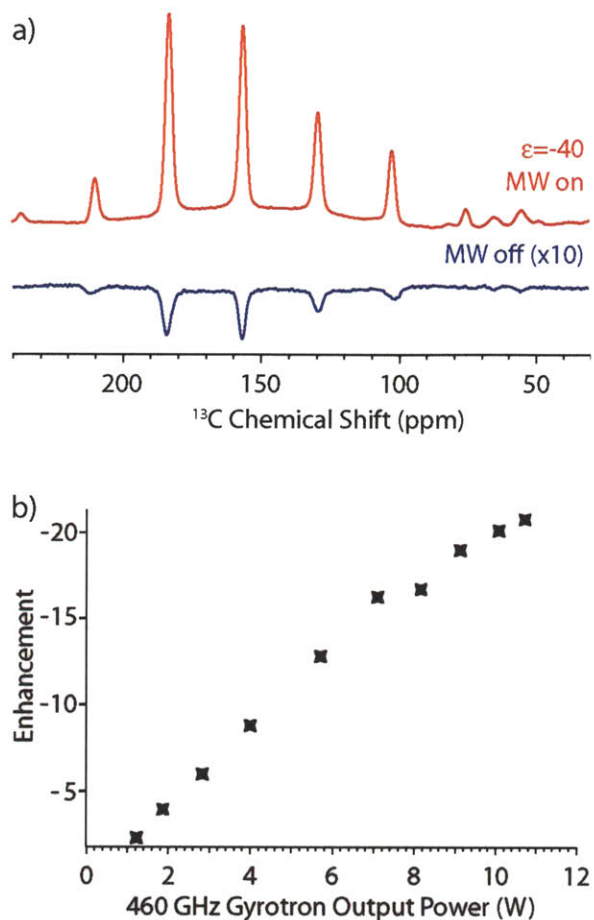


Figure 10. DNP at 700 MHz.

a) enhanced ^{13}C CPMAS spectrum of 1 M ^{13}C -Urea in 60/30/10 (d8-glycerol/ D_2O / H_2O , 10 mM TOTAPOL, showing an enhancement of -40 . The spinning frequency is $\omega_r/2\pi = 4.8$ kHz, the sample temperature is 80 K, and the gyrotron output power is 12 W. **b)** The DNP enhancement as a function of gyrotron output power. The spinning frequency is $\omega_r/2\pi = 6.7$ KHz, sample temperature is 90 K, the gyrotron cathode potential is 12.1 kV, the microwave output frequency is 460.5 GHz, and the ^1H NMR frequency is 697.8 MHz.

TOTAPOL [40]. As was the case at lower fields, the enhancements have a strong dependence on temperature [21]. Thus, we have found that it is important to operate at temperatures in the 80-85 K range to achieve enhancement values that agree well with the expected $\sim \omega_0^{-1}$ scaling of the cross effect. [29,41-44] The power dependence shown in Figure 10b, recorded at 6.7 kHz spinning frequency and $T = 90$ K, reaches -20 enhancement with 11 W output power, whereas the enhancement shown in Figure 10a increases to -40 by reducing the spinning frequency to 4.8 kHz, cooling the sample to 80 K, and using 12 W of output power. We note that there is still a linear dependence of the enhancement on microwave power, as shown in Figure 10b. Thus, further increases γB_1 will likely lead to further increases in ϵ .

Finally, it is essential that the system be sufficiently stable to record multidimensional spectra. Figure 11a shows one bond correlations recorded in a 2D fashion with RFDR ^{13}C - ^{13}C recoupling [45], and Figure 11b employs DARR mixing for short and long-range contacts [45-47]. Each of these two-dimensional spectra took 2.6 hours to record. The ability to record these 2D spectra demonstrates the long-term stability of the DNP instrumentation and spectrometer. We note that the resolution of the 2D spectrum is sufficient to assign all of the proline resonances.

2.4. Conclusions and Outlook

Significant DNP enhancements of $\epsilon = -40$ have been demonstrated at a field strength of 16.4 T (700 MHz for ^1H). If the gain in Boltzmann polarization due to the lower temperature ($300\text{ K}/85\text{ K} = 3.53$) is taken into account, then the total enhancement is $\epsilon^\dagger \sim -140$ which is a significant improvement in sensitivity. Thus, these experiments provide a convincing demonstration of the gains that DNP can provide at high magnetic fields. At present this is to our knowledge the highest frequency DNP spectrometer in operation, and importantly takes DNP to a regime of considerable significance for studies of biological samples.

The gyrotron frequency of 460.5 GHz presently irradiates the portion of the nitroxide line-shape leading to negative enhancements. Typically for CPMAS DNP experiments with nitroxide radicals, the magnitude of enhancement is smaller on the negative side of the enhancement profile, so we expect still higher magnitude positive enhancements when the NMR field is further optimized. The strong dependence of the DNP enhancement on microwave power suggests that

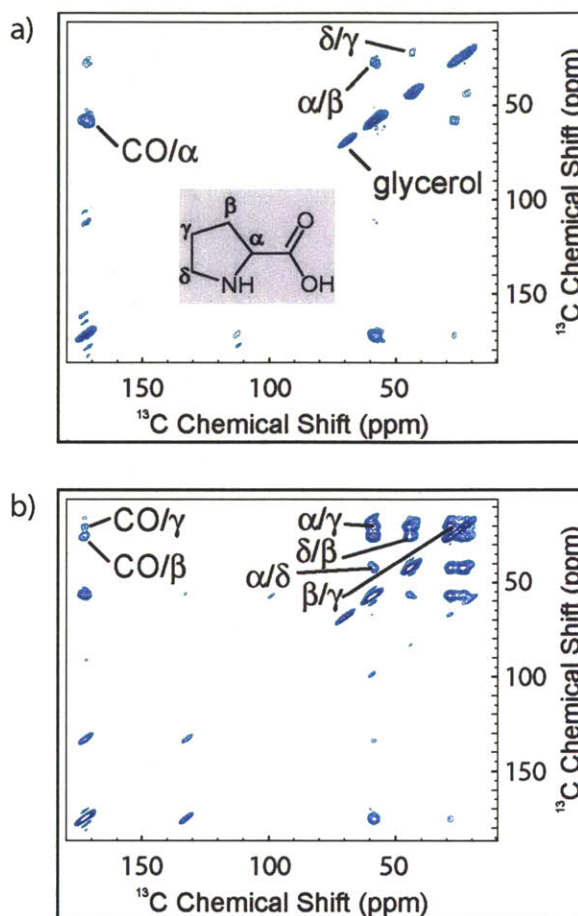


Figure 11. ^{13}C - ^{13}C Correlation spectra at 700 MHz. **a)** one-bond radio frequency driven recoupling (RFDR) correlation showing the one-bond cross-peak assignments. The spinning frequency is $\omega_r/2\pi = 9.8$ kHz, and the sample temperature is 85 K **b)** Short and long-range correlations with dipolar assisted rotary resonance (DARR) and long-range correlation assignments. The spinning frequency is $\omega_r/2\pi = 7.8$ kHz, and the sample temperature is 85 K.

improvements to the microwave transmission line, gyrotron output power, or both, could also lead to significant improvement in the enhancements.

Acknowledgments

The National Institutes of Health through grants EB002804, EB003151, EB002026, EB001960, EB001035, EB001965, and EB004866 supported this research. A.B.B. was partially supported by a graduate research fellowship from the National Science Foundation. V.K.M. thanks the Natural Sciences and Engineering Research Council of Canada for a Postdoctoral Fellowship. We thank Mr. Michael Mullins, Dr. David J. Ruben, Dr. Christopher Turner, and Mr. Ivan Mastovsky for crucial assistance constructing the spectrometer, Albert A. Smith, Loren B. Andreas, Bjorn Corzilius, Marvin Bayro, Galia Debelouchina, Matthew Eddy, and Dr. Michael Shapiro for helpful discussions and careful reading of the manuscript. We also gratefully acknowledge Sid Shevgoor, and David and Judy Doty (Doty Scientific) for introducing us to the bronze material used for the dewar.

References

- [1] Markhasin, E.; Barnes, A. B.; Hu, J.; Herzfeld, J.; Griffin, R. G. In *Balanced Triple Resonance Probe for Cryogenic MAS NMR and Dynamic Nuclear Polarization at 700 MHz*. WWMR2010. Joint EUROMAR 2010 and 17th ISMAR Conference, Florence, Italy, July 4-9, 2010. (oral presentation and poster)
- [2] Barnes, A. B.; Markhasin, E.; Daviso, E.; Michaelis, V. K.; Nanni, E. A.; Jawla, S. K.; Mena, E. L.; DeRocher, R.; Thakkar, A.; Woskov, P. P.; Herzfeld, J.; Temkin, R. J.; Griffin, R. G. *Dynamic Nuclear Polarization at 700 MHz / 460 GHz*. *J. Magn. Reson.* 2012, 224, 1. DOI: 10.1016/j.jmr.2012.08.002
- [3] Markhasin, E.; Barnes, A. B.; Daviso, E.; Michaelis, V. K.; Nanni, E. A.; Jawla, S. K.; Woskov, P.; Thakkar, A.; DeRocher, R.; Herzfeld, J.; Temkin, R. J.; Griffin, R. G. In *Spectrometer for Dynamic Nuclear Polarization at 700 MHz / 460 GHz*. 53rd ENC, Miami, Florida, April 15-20, 2012. (poster)
- [4] Barnes, A. B.; Markhasin, E.; Nanni, E. A.; Daviso, E.; Michaelis, V. K.; Jawla, S.; Herzfeld, J.; Temkin, R. J.; Griffin, R. G. In *DNP at 16.4 and 8.9 Tesla with Tunable Gyrotrons and High-Resolution Cryogenic MAS Probes*. Third International Symposium on Dynamic Nuclear Polarization, EPFL Lausanne, Switzerland, September 7-10, 2011.
- [5] Afeworki, M.; Vega, S.; Schaefer, J. *Direct electron-to-carbon polarization transfer in homogeneously doped polycarbonates*. *Macromolecules* 1992, 25, 4100. DOI: 10.1021/ma00042a009
- [6] Barnes, A. B.; Corzilius, B.; Mak-Jurkauskas, M. L.; Andreas, L. B.; Bajaj, V. S.; Matsuki, Y.; Belenky, M. L.; Lugtenburg, J.; Sirigiri, J. R.; Temkin, R. J.; Herzfeld, J.; Griffin, R. G. *Resolution and polarization distribution in cryogenic DNP/MAS experiments*. *Phys. Chem. Chem. Phys.* 2010, 12, 5861. DOI: 10.1039/c003763j
- [7] Becerra, L. R.; Gerfen, G. J.; Temkin, R. J.; Singel, D. J.; Griffin, R. G. *Dynamic nuclear polarization with a cyclotron resonance maser at 5 T*. *Phys. Rev. Lett.* 1993, 71, 3561. DOI: 10.1103/PhysRevLett.71.3561

- [8] Gerfen, G. J.; Becerra, L. R.; Hall, D. A.; Griffin, R. G.; Temkin, R. J.; Singel, D. J. High frequency (140 GHz) dynamic nuclear polarization: polarization transfer to a solute in frozen aqueous solution. *J. Chem. Phys.* 1995, 102, 9494. DOI: 10.1063/1.468818
- [9] Macho, V.; Kendrick, R.; Yannoni, C. S. Cross polarization magic-angle spinning NMR at cryogenic temperatures. *J. Magn. Reson.* 1983, 52, 450. DOI: 10.1016/0022-2364(83)90170-1
- [10] Wind, R. A.; Duijvestijn, M. J.; Van der Lugt, C.; Manenschijn, A.; Vriend, J. Applications of dynamic nuclear polarization in carbon-13 NMR in solids. *Prog. Nucl. Magn. Reson. Spectrosc.* 1985, 17, 33. DOI: 10.1016/0079-6565(85)80005-4
- [11] Carver, T. R.; Slichter, C. P. Polarization of nuclear spins in metals. *Phys. Rev.* 1953, 92, 212. DOI: 10.1103/PhysRev.92.212.2
- [12] Carver, T. R.; Slichter, C. P. Experimental verification of the Overhauser nuclear polarization effect. *Phys. Rev.* 1956, 102, 975. DOI: 10.1103/PhysRev.102.975
- [13] Weis, V.; Bennati, M.; Rosay, M.; Bryant, J. A.; Griffin, R. G. High-Field DNP and ENDOR with a Novel Multiple-Frequency Resonance Structure. *J. Magn. Reson.* 1999, 140, 293. DOI: 10.1006/jmre.1999.1841
- [14] Bajaj, V. S.; Mak-Jurkauskas, M. L.; Belenky, M.; Herzfeld, J.; Griffin, R. G. Functional and shunt states of bacteriorhodopsin resolved by 250 GHz dynamic nuclear polarization-enhanced solid-state NMR. *Proc. Natl. Acad. Sci. U.S.A.* 2009, 106, 9244. DOI: 10.1073/pnas.0900908106
- [15] Bajaj, V. S.; Farrar, C. T.; Hornstein, M. K.; Mastovsky, I.; Vieregg, J.; Bryant, J.; Elena, B.; Kreischer, K. E.; Temkin, R. J.; Griffin, R. G. Dynamic nuclear polarization at 9 T using a novel 250 GHz gyrotron microwave source. *J. Magn. Reson.* 2003, 160, 85. DOI: 10.1016/s1090-7807(02)00192-1
- [16] Bayro, M. J.; Maly, T.; Birkett, N. R.; MacPhee, C. E.; Dobson, C. M.; Griffin, R. G. High-Resolution MAS NMR Analysis of PI3-SH3 Amyloid Fibrils: Backbone Conformation and Implications for Protofilament Assembly and Structure. *Biochemistry* 2010, 49, 7474. DOI: 10.1021/bi100864t
- [17] Rosay, M.; Lansing, J. C.; Haddad, K. C.; Bachovchin, W. W.; Herzfeld, J.; Temkin, R. J.; Griffin, R. G. High-frequency dynamic nuclear polarization in MAS spectra of membrane and soluble proteins. *J. Am. Chem. Soc.* 2003, 125, 13626. DOI: 10.1021/ja036898k
- [18] Rosay, M.; Weis, V.; Kreischer, K. E.; Temkin, R. J.; Griffin, R. G. Two-Dimensional ¹³C-¹³C Correlation Spectroscopy with Magic Angle Spinning and Dynamic Nuclear Polarization. *J. Am. Chem. Soc.* 2002, 124, 3214. DOI: 10.1021/ja0176752
- [19] Debelouchina, G. T.; Bayro, M. J.; van der Wel, P. C. A.; Caporini, M. A.; Barnes, A. B.; Rosay, M.; Maas, W. E.; Griffin, R. G. Dynamic nuclear polarization-enhanced solid-state NMR spectroscopy of GNNQQNY nanocrystals and amyloid fibrils. *Phys. Chem. Chem. Phys.* 2010, 12, 5911. DOI: 10.1039/c003661g

- [20] Matsuki, Y.; Takahashi, H.; Ueda, K.; Idehara, T.; Ogawa, I.; Toda, M.; Akutsu, H.; Fujiwara, T. Dynamic nuclear polarization experiments at 14.1 T for solid-state NMR. *Phys. Chem. Chem. Phys.* 2010, 12, 5799. DOI: 10.1039/c002268c
- [21] Rosay, M.; Tometich, L.; Pawsey, S.; Bader, R.; Schauwecker, R.; Blank, M.; Borchard, P. M.; Cauffman, S. R.; Felch, K. L.; Weber, R. T.; Temkin, R. J.; Griffin, R. G.; Maas, W. E. Solid-state dynamic nuclear polarization at 263 GHz: spectrometer design and experimental results. *Phys. Chem. Chem. Phys.* 2010, 12, 5850. DOI: 10.1039/c003685b
- [22] Jacso, T.; Franks, W. T.; Rose, H.; Fink, U.; Broecker, J.; Keller, S.; Oschkinat, H.; Reif, B. Characterization of Membrane Proteins in Isolated Native Cellular Membranes by Dynamic Nuclear Polarization Solid-State NMR Spectroscopy without Purification and Reconstitution. *Angew. Chem., Int. Ed.* 2012, 51, 432. DOI: 10.1002/anie.201104987
- [23] Sergeev, I. V.; Day, L. A.; Goldbourt, A.; McDermott, A. E. Chemical Shifts for the Unusual DNA Structure in Pfl Bacteriophage from Dynamic-Nuclear-Polarization-Enhanced Solid-State NMR Spectroscopy. *J. Am. Chem. Soc.* 2011, 133, 20208. DOI: 10.1021/ja2043062
- [24] Vitzthum, V.; Caporini, M. A.; Bodenhausen, G. Solid-state nitrogen-14 nuclear magnetic resonance enhanced by dynamic nuclear polarization using a gyrotron. *J. Magn. Reson.* 2010, 205, 177. DOI: 10.1016/j.jmr.2010.04.014
- [25] Mak-Jurkauskas, M. L.; Bajaj, V. S.; Hornstein, M. K.; Belenky, M.; Griffin, R. G.; Herzfeld, J. Energy transformations early in the bacteriorhodopsin photocycle revealed by DNP-enhanced solid-state NMR. *Proc. Natl. Acad. Sci. U.S.A.* 2008, 105, 883. DOI: 10.1073/pnas.0706156105
- [26] McKay, R. A. Double-tuned single coil probe for nuclear magnetic resonance spectrometer. Patent #4446431, 1984.
- [27] McKay, R. A. Probes for Special Purposes. In *Encyclopedia of Magnetic Resonance*; John Wiley & Sons, Ltd: 2007. DOI: 10.1002/9780470034590.emrstm0416
- [28] Bajaj, V. S.; Hornstein, M. K.; Kreischer, K. E.; Sirigiri, J. R.; Woskov, P. P.; Mak-Jurkauskas, M. L.; Herzfeld, J.; Temkin, R. J.; Griffin, R. G. 250GHz CW gyrotron oscillator for dynamic nuclear polarization in biological solid state NMR. *J. Magn. Reson.* 2007, 189, 251. DOI: 10.1016/j.jmr.2007.09.013
- [29] Barnes, A. B.; Mak-Jurkauskas, M. L.; Matsuki, Y.; Bajaj, V. S.; van der Wel, P. C. A.; De Rocher, R.; Bryant, J.; Sirigiri, J. R.; Temkin, R. J.; Lugtenburg, J.; Herzfeld, J.; Griffin, R. G. Cryogenic sample exchange NMR probe for magic angle spinning dynamic nuclear polarization. *J. Magn. Reson.* 2009, 198, 261. DOI: 10.1016/j.jmr.2009.03.003
- [30] Allen, P. J.; Creuzet, F.; De Groot, H. J. M.; Griffin, R. G. Apparatus for low-temperature magic-angle spinning NMR. *J. Magn. Reson.* 1991, 92, 614. DOI: 10.1016/0022-2364(91)90357-Y
- [31] Melissa, K. H.; Vikram, S. B.; Robert, G. G.; Richard, J. T. Efficient Low-Voltage Operation of a CW Gyrotron Oscillator at 233 GHz. *IEEE T. Plasma Sci.* 2007, 35, 27. DOI: 10.1109/tps.2006.889295

- [32] Joye, C. D.; Griffin, R. G.; Hornstein, M. K.; Kan-Nian, H.; Kreischer, K. E.; Rosay, M.; Shapiro, M. A.; Sirigiri, J. R.; Temkin, R. J.; Woskov, P. P. Operational characteristics of a 14-W 140-GHz gyrotron for dynamic nuclear polarization. *IEEE T. Plasma Sci.* 2006, 34, 518. DOI: 10.1109/tps.2006.875776
- [33] Kreischer, K. E.; Farrar, C.; G., G. R.; Temkin, R. J.; Vieregg, J. In *Development of a 250 GHz CW Gyrotron for EPR and NMR Spectroscopy*. Proceedings of the 24th International Conference on Infrared and Millimeter Waves, Monterey, CA, 1999.
- [34] Nanni, E. A.; Barnes, A. B.; Griffin, R. G.; Temkin, R. J. THz Dynamic Nuclear Polarization NMR. *IEEE Trans. Terahertz Sci. Technol.* 2011, 1, 145. DOI: 10.1109/tthz.2011.2159546
- [35] Nanni, E. A.; Barnes, A. B.; Matsuki, Y.; Woskov, P. P.; Corzilius, B.; Griffin, R. G.; Temkin, R. J. Microwave field distribution in a magic angle spinning dynamic nuclear polarization NMR probe. *J. Magn. Reson.* 2011, 210, 16. DOI: 10.1016/j.jmr.2011.02.001
- [36] Hornstein, M. K.; Bajaj, V. S.; Griffin, R. G.; Kreischer, K. E.; Mastovsky, I.; Shapiro, M. A.; Sirigiri, J. R.; Temkin, R. J. Second harmonic operation at 460 GHz and broadband continuous frequency tuning of a gyrotron oscillator. *IEEE Trans. Elec. Dev.* 2005, 52, 798. DOI: 10.1109/TED.2005.845818
- [37] Torrezan, A. C.; Seong-Tae, H.; Mastovsky, I.; Shapiro, M. A.; Sirigiri, J. R.; Temkin, R. J.; Barnes, A. B.; Griffin, R. G. Continuous-Wave Operation of a Frequency-Tunable 460-GHz Second-Harmonic Gyrotron for Enhanced Nuclear Magnetic Resonance. *IEEE T. Plasma Sci.* 2010, 38, 1150. DOI: 10.1109/TPS.2010.2046617
- [38] Woskov, P. P.; Bajaj, V. S.; Hornstein, M. K.; Temkin, R. J.; Griffin, R. G. Corrugated waveguide and directional coupler for CW 250-GHz gyrotron DNP experiments. *IEEE T. Microw. Theory Tech.* 2005, 53, 1863. DOI: 10.1109/TMTT.2005.848097
- [39] Hu, K.-N.; Yu, H.-H.; Swager, T. M.; Griffin, R. G. Dynamic Nuclear Polarization with Biradicals. *J. Am. Chem. Soc.* 2004, 126, 10844. DOI: 10.1021/ja039749a
- [40] Song, C.; Hu, K.-N.; Joo, C.-G.; Swager, T. M.; Griffin, R. G. TOTAPOL: A Biradical Polarizing Agent for Dynamic Nuclear Polarization Experiments in Aqueous Media. *J. Am. Chem. Soc.* 2006, 128, 11385. DOI: 10.1021/ja061284b
- [41] Duijvestijn, M. J.; Wind, R. A.; Smidt, J. A quantitative investigation of the dynamic nuclear polarization effect of fixed paramagnetic centers of abundant and rare spins in solids at room temperature. *Physica B+C* 1986, 138, 147. DOI: 10.1016/0378-4363(86)90503-6
- [42] Hu, K.-N.; Song, C.; Yu, H.-h.; Swager, T. M.; Griffin, R. G. High-frequency dynamic nuclear polarization using biradicals: A multifrequency EPR lineshape analysis. *J. Chem. Phys.* 2008, 128, 052302/1. DOI: 10.1063/1.2816783
- [43] Hu, K.-N.; Debelouchina, G. T.; Smith, A. A.; Griffin, R. G. Quantum mechanical theory of dynamic nuclear polarization in solid dielectrics. *J. Chem. Phys.* 2011, 134, 125105/1. DOI: 10.1063/1.3564920

- [44] Maly, T.; Debelouchina, G. T.; Bajaj, V. S.; Hu, K.-N.; Joo, C.-G.; Mak-Jurkauskas, M. L.; Sirigiri, J. R.; van der Wel, P. C. A.; Herzfeld, J.; Temkin, R. J.; Griffin, R. G. Dynamic nuclear polarization at high magnetic fields. *J. Chem. Phys.* 2008, 128, 052211/1. DOI: 10.1063/1.2833582
- [45] Bennett, A. E.; Rienstra, C. M.; Griffiths, J. M.; Zhen, W.; Lansbury, P. T., Jr.; Griffin, R. G. Homonuclear radio frequency-driven recoupling in rotating solids. *J. Chem. Phys.* 1998, 108, 9463. DOI: 10.1063/1.476420
- [46] Morcombe, C. R.; Gaponenko, V.; Byrd, R. A.; Zilm, K. W. Diluting Abundant Spins by Isotope Edited Radio Frequency Field Assisted Diffusion. *J. Am. Chem. Soc.* 2004, 126, 7196. DOI: 10.1021/ja047919t
- [47] Takegoshi, K.; Nakamura, S.; Terao, T. ^{13}C - ^1H dipolar-assisted rotational resonance in magic-angle spinning NMR. *Chem. Phys. Lett.* 2001, 344, 631. DOI: 10.1016/s0009-2614(01)00791-6

3. Structural Dynamics and Transformations of Alanyl-Prolyl-Glycine Investigated by Low-Temperature MAS NMR

Adapted from references [1-3].

3.1. Introduction

Over the last two decades, magic angle spinning (MAS) NMR has grown into a powerful and versatile tool for many fields and particularly structural biology [4-18]. Due to multiple advancements in sample preparation, methodology [10,15,19-33], and labeling strategies [34-40], the resolution of MAS NMR of biological molecules often approaches that of solution NMR, thus making possible studies of large molecules and molecular complexes [41]. The inherently low sensitivity of NMR, therefore, is often the primary factor limiting the amount of structural information that can be extracted from correlation spectra.

Since the sensitivity of NMR experiment is proportional to magnetization M_0 , which is, in turn, inversely proportional to absolute temperature $M_0 \sim 1/T$ [42], low and, particularly, cryogenic temperatures provide a means to improve the sensitivity [43]. A further sensitivity gain can be achieved by combining cryogenic temperatures with gyrotron based dynamic nuclear polarization (DNP) [44].

Additionally, the ability to perform NMR experiments at variable and cryogenic temperatures provides access to useful information on dynamics [45-54] and a way to study biological processes by kinetic trapping of intermediate forms [55], as well as permits optimization of experimental conditions for certain experiments characterized by temperature dependent efficiency, such as correlation experiments aimed at aromatic spins.

At the same time, as the sample temperature decreases, a variety of dynamic and structural transformation may potentially occur. Knowledge whether any such transformation actually occur and how they affect the structure of the investigated system is important for relating the low temperature information to biologically relevant conditions. Isotropic chemical shift is a sensitive indicator of any structural changes. However, since chemical shift change may reflect on a variety of processes, including phase transitions, change of internal dynamics, temperature, etc., interpretation of chemical shift changes may not be straightforward.

Additional complications arise from the fact that organic molecules have relatively high number of internal degrees of freedom and mobility / conformational flexibility. Large size and flexibility makes it more difficult for the molecule to find the stablest accessible state in case of phase transitions, thus, often resulting in thermal history effects (hysteresis) and supercooled / superheated states [45,56-57]. Conformational changes may be part of a phase transition resulting in interesting thermodynamic transformations impossible for rigid molecules [56]. On the other hand, dynamical processes coupled to kinetically controlled first order phase transforma-

tions may result in the so called *dynamically driven nonequilibrium phase transitions* [58-61] continuously occurring within a certain range of thermodynamic parameters resembling, for example, a second order phase transition.

For these reasons, investigation of temperature dependent structural and dynamic processes may necessitate to combine several NMR approaches with complimentary data provided by other techniques, such as dynamic scanning calorimetry (DSC) and X-ray. Here, we combine ^{13}C and ^{15}N cross-polarization (CP) MAS NMR, ^{13}C MAS NMR, spin-lattice relaxation data, adiabatic calorimetry and X-ray. We apply these techniques to analyze the various phenomena observed in ^{13}C CP MAS NMR spectra of APG tripeptide (which has a published crystal structure [17] and assigned MAS NMR spectra [17,62]) and to understand the underline temperature dependent structural changes.

3.2. Experimental Procedures

3.2.1. Sample preparation

Uniformly ^{13}C , ^{15}N -labeled Alanyl-prolyl-glycine (APG) was diluted to 10 % with the corresponding natural abundance tripeptide by dissolving the two compounds in a minimal amount of water. The solubility was ~ 45 g/l. The sample was then slowly crystallized in a desiccator with ethylene glycol desiccant. Crystals formed within one week. All NMR data was collected on this 10 % sample, unless noted otherwise. Natural abundance APG was recrystallized following the same protocol. Both crystalline samples were then grounded and center-packed into 4 mm Revolution NMR zirconia rotors using Kel-F spacers. One of the spacers contained a KBr filled cavity for magic angle adjustments following the approach of Thurber et. al. [63]. Additionally, both drive tips and end caps were cryosealed with low-temperature epoxy for cryogenic experiments as described elsewhere [17].

3.2.2. Instrumentation

Solid State NMR spectra were recorded using a custom designed triple resonance (^1H , ^{13}C , ^{15}N) cryogenic magic angle spinning (MAS) NMR probe equipped with a cryogenic sample exchange system [64] on a custom built solid state NMR (SSNMR) spectrometer operating at 380 MHz ^1H frequency (courtesy of D. J. Ruben).

Liquid nitrogen boil-off gas was used for both bearing and drive gas streams, and the spinning frequency of 4.83 kHz for all experiments was controlled by a Bruker MAS controller (Billerica, MA). Both bearing and drive streams were cooled using a custom-built heat exchanger [64], and the temperature was subsequently controlled using heating elements inside vacuum jacketed transfer lines two PID controllers (Lakeshore, Westerville, OH). The temperature inside the MAS stator was monitored using a fiber optic temperature sensor (Neoptix, Quebec, Canada).

A precision automatic adiabatic calorimeter (BCT-3) was used to measure heat capacity over the temperature range of $6\text{ K} \leq T \leq 350\text{ K}$. The design and operation of an adiabatic calorimeter and experimental protocols are described in detail elsewhere [1,65-66].

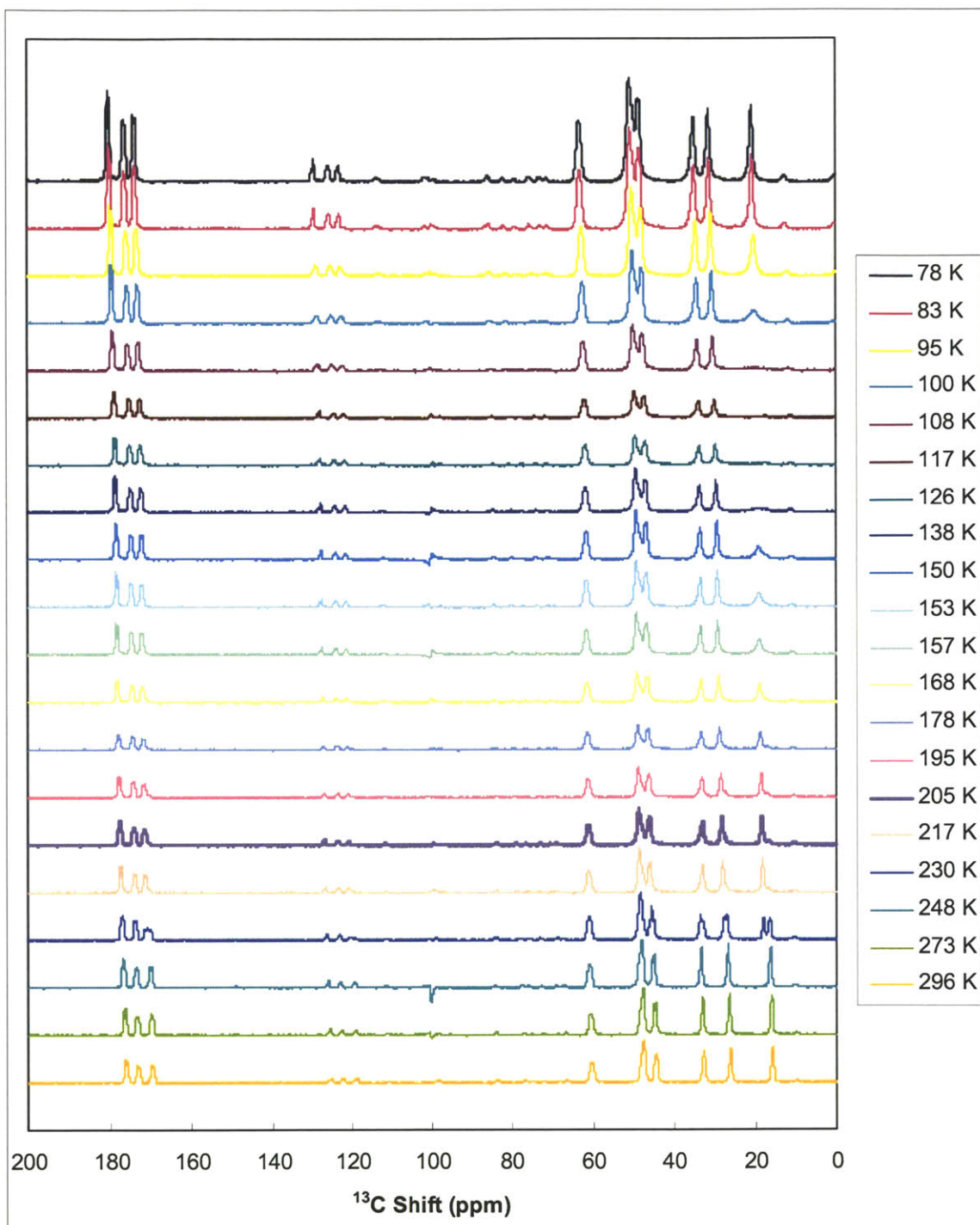


Figure 12. Temperature dependent ^{13}C CP MAS NMR spectra of 10%-U- ^{13}C , ^{15}N -APG.

This series was acquired starting from the lowest temperature and moving in the heating direction. Acquisition parameters: appropriate recycle delay, 30 μs dwell time, 2048 points, 32 scans, and two-pulse phase modulation (TPPM) ^1H decoupling ($\omega(^1\text{H})/2\pi = 83$ kHz).

X-ray data was collected using a Siemens three-circle Platform diffractometer and PANalytical X'Pert Pro multipurpose diffractometer equipped with Oxford Cryosystems PheniX cryostat.

3.2.3. Data processing

All NMR data was processed using NMRPipe and NMRDraw software [67], Microsoft™ Excel®, CurveExpert Professional (<http://www.curveexpert.net/>), and a set of custom shell scripts.

3.3. Results and Discussion

Figure 13 shows a sample ^{13}C CP MAS NMR spectrum indicating previously published assignments [17,62]. Note that with properly adjusted magic angle and experimental parameters, J-splitting can be observed on two out of three carbonyl lines. Also the linewidth is in general reasonable compared to room temperature spectra [2].

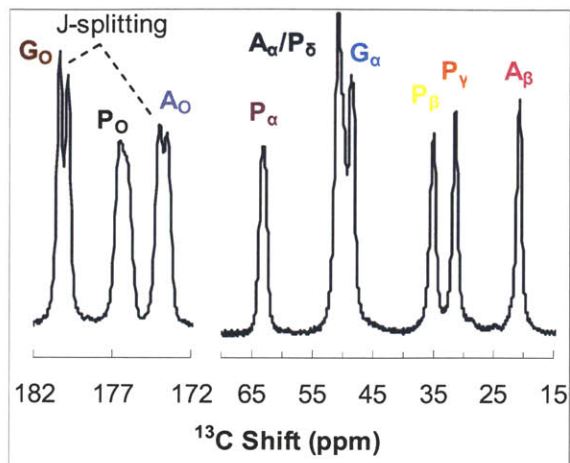


Figure 13. ^{13}C CP MAS NMR spectrum of 10%-U- ^{13}C , ^{15}N -APG at 78 K.

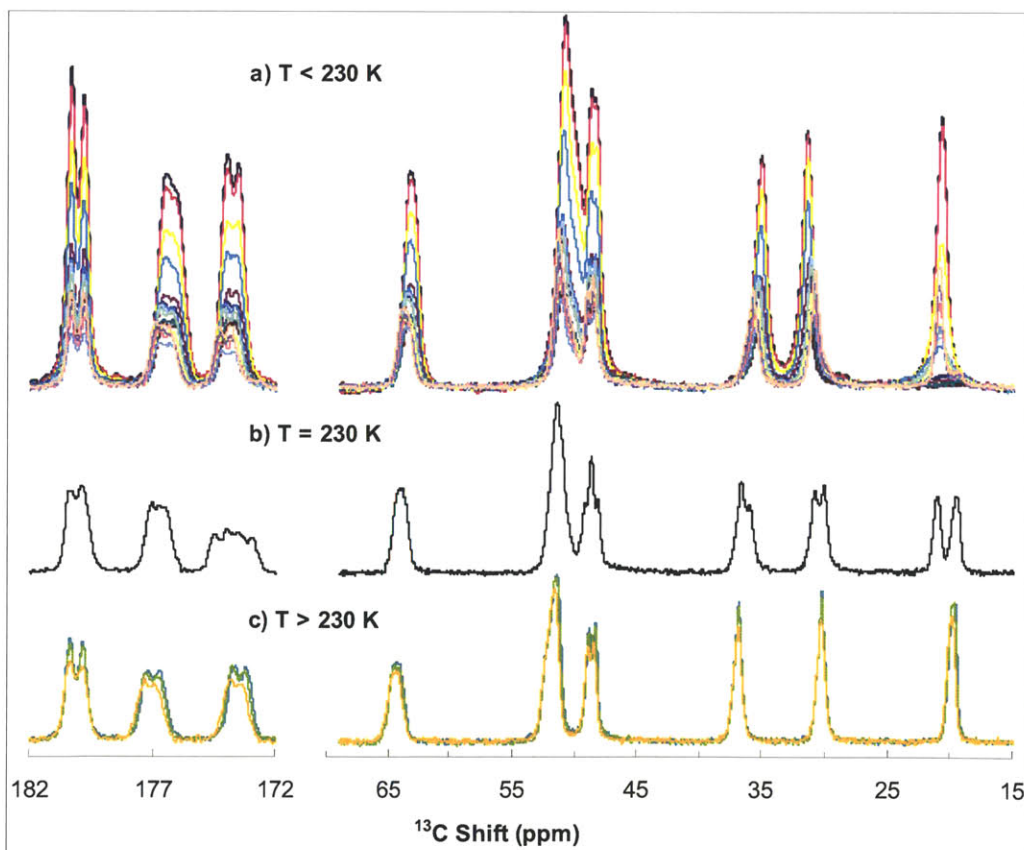


Figure 14. Aligned temperature dependent ^{13}C CP MAS NMR spectra of 10%-U- ^{13}C , ^{15}N -APG. All spectra are shifted according to Figure 15 relative to the spectrum at 78 K. The color code is the same as in Figure 12, except for the spectrum at 230 K, which is black (b). Color spectra at the top (a) and bottom (c) correspond to $T < 230$ K and $T > 230$ K, respectively.

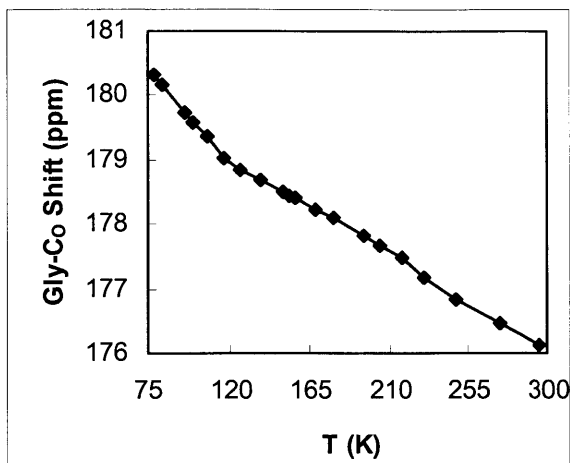


Figure 15. Temperature dependence of Gly-C_O isotropic chemical shift in APG.

change in spectral features observed between 217 K and 248 K, with pronounced changes in the chemical shift of several peaks. This observation suggests possible existence of a first-order phase transition in this temperature range. Third, the overall spectral intensity does not follow expected $\propto 1/T$ law; rather, at intermediate temperatures, it is lower than that above 248 K and goes through two local minima, one around 117 K and another one around 178 K. This behavior is attributed to inefficient CP and decoupling caused by short $T_{1\rho}$ of methyl (CH₃) and ammonium (NH₃⁺) protons due to interference between the spin-lock field and three-fold hopping of these groups. Finally, there is a gradual change of chemical shifts of all peaks with temperature. These features are discussed in detail in the following sections.

3.3.1. Temperature dependent shift

Gradual drift of chemical shift with temperature is not associated with any specific structural change, and it is convenient to remove it by aligning the spectra, so that other effects are easier to observe. Aligned stack plot of variable temperature ¹³C CP MAS NMR spectra is shown in Figure 14. All spectra were shifted, so that the Gly-C_O lines are aligned to its position at 78 K, according to Figure 15. The rest of the lines are aligned well too, indicating that the temperature dependent shift is virtually the same for all sites.

Figure 12, showing a stack plot of variable temperature ¹³C CP MAS NMR spectra collected starting from the lowest temperature up, reveals several temperature related spectral changes. First, the linewidth of the Ala-C_β peak ($\sigma \approx 18$ ppm) shows a strong dependence on sample temperature. Between 108 K and 138 K it is broadened beyond detection limit, while at lower temperatures it starts to narrow again to approach a linewidth of 84 Hz (0.88 ppm) FWHM at 78 K being relatively close to the room temperature value of 68 Hz (including ¹³C-¹³C *J*-coupling). This broadening is attributed to interference between the decoupling field and the three-fold methyl group reorientation, rendering decoupling ineffective in that certain temperature regime. Second, there is an abrupt

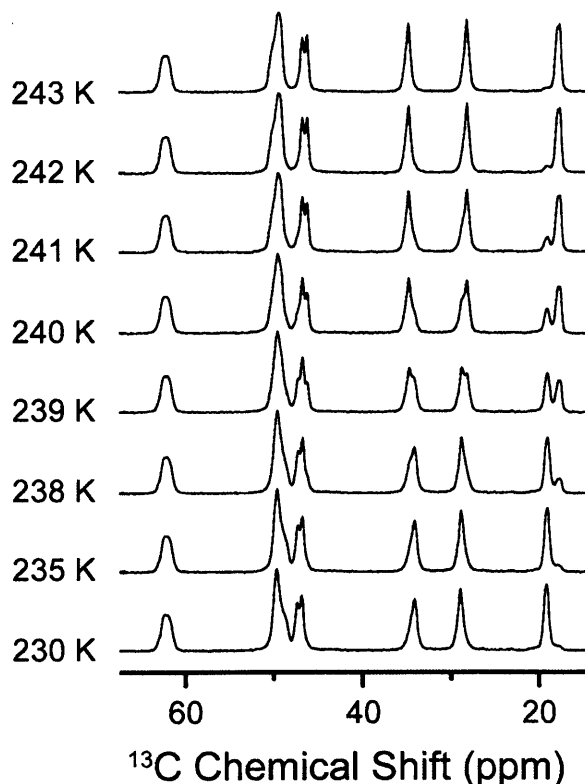


Figure 16. Aliphatic region of ¹³C CP MAS NMR spectra of 10%-U-¹³C, ¹⁵N-APG around the polymorphic phase transition region collected in the heating direction.

All spectra in Figure 14 are further grouped in to three temperature ranges corresponding to $T = 230$ K, $T > 230$ K, and $T < 230$ K.

3.3.2. Polymorphic phase transition

In Figure 14b, several peaks are doubled, and the spectrum appears to be a superposition of Figure 14a and 14c, indicating a structural transformation between two forms. In a separate series of experiments, additional spectra were collected around this transition region (Figure 16), revealing concomitant peak intensity decrease in one set and increase in the other set. Note, that while intensities of the two sets are comparable at 230 K in Figure 14, this point is shifted to about 239 K in Figure 16. Furthermore, in additional series of spectra, collected by going in the opposite direction from the highest temperature down (data not shown), the transition point was observed at substantially lower temperature below 200 K, thus indicating strong thermal hysteresis. Interestingly, Figure 14b indicates that while some sites are strongly affected by the transition, others are barely affected, as illustrated with black (largest effect), gray (medium effect), and green (smallest effect) balls in Figure 17.

To further investigate the nature of this transformation, the sample was studied using precision adiabatic calorimetry in the range of 6 K – 300 K, with all experiments conducted in the heating direction. While no anomalies in heat capacity were observed below 200 K (data not shown), a strong first order phase transition was observed between 254 K and 262 K (solid red trace in Figure 18). Additionally, to verify the supercooling phenomenon, the sample was cooled from room temperature to 220 K, and heat capacity was measured again in the range of 220 K – 290 K (dashed blue trace in Figure

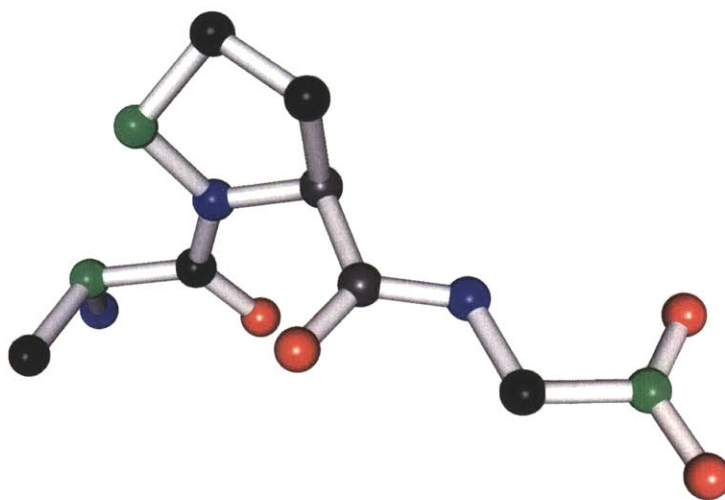


Figure 17. Crystal structure of APG. Black, gray, and green balls indicate carbons strongly, moderately and lightly affected, respectively, as evidenced by Figure 14b [17].

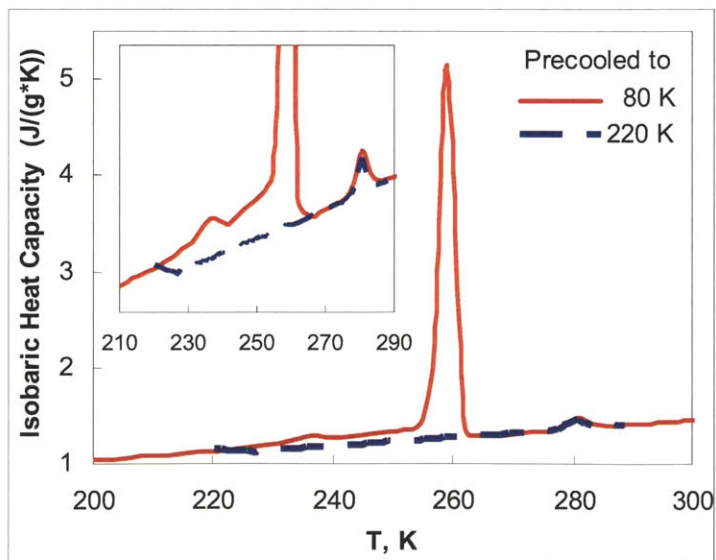


Figure 18. Isobaric heat capacity of APG. Solid red line and dashed blue line represent data obtained after cooling the sample down to 80 K and 220 K, respectively. The latter indicates supercooling of the high temperature phase.

18). The figure clearly indicates no phase transition in the latter experiment.

Although the temperatures of the phase transition determined by NMR and calorimetry are slightly different, we attribute the same physical effect to account for both observations, with several factors may be responsible for the observed discrepancy. On the one hand, in the case of MAS NMR, sample temperature cannot be measured directly due to fast mechanical spinning of the sample. Instead, temperature of the surrounding environment in as close proximity to the sample as possible is monitored. This measurement may be slightly inaccurate due to frictional and RF induced heating. Furthermore, temperature measurement approach used in precision calorimetry is substantially more precise compared to regular NMR experiments. On the other hand, the two physical methods employ different sample environments, when probing for the phase transition, involving, for example, different temperature ramping speeds or additional pressure induced by high frequency spinning. Such experimental parameters may significantly alter observed phase transition temperature, particularly in the case of nonequilibrium process.

In order to determine temperature dependent changes in the crystal structure, X-ray diffraction (XRD) studies were conducted using single crystal and powdered samples. Both single crystal and powder measurement confirmed $P2_12_12_1$ space group for the high temperature crystal phase and unit cell with parameters $a = 6.801 \text{ \AA}$, $b = 11.830 \text{ \AA}$, and $c = 16.080 \text{ \AA}$ [17]. Single crystal studies of the low temperature phase were not possible, as crystals shattered below 210 K as illustrate in Figure 19. Thus, supercooling of the high temperature phase was observed in XRD too.

Only powder XRD could be applied to the low temperature phase, which also confirmed that high temperature phase could be supercooled down to 210 K, whereas both phases coexisted down to 190 K. It is noteworthy that during the first cooling-heating cycle, the powder diffractogram showed significant peak broadening and the initial linewidth obtained from the freshly crystallized sample could not be recovered. This observation is attributed to microfracturing of powder crystallites induced by lattice parameter change occurring at the phase transition. During following temperature cycling through the phase transition no significant change in linewidth was observed, and the obtained diffractogram was consisted with a $Pnam$ space group with unit cell parameters $a = 14.681 \text{ \AA}$, $b = 12.058 \text{ \AA}$, and $c = 6.977 \text{ \AA}$. However, later we realized that $Pnam$ space group implies 8 molecules per unit cell as opposed to $P2_12_12_1$, which has 4 molecules per unit cell. Since the volume of the new unit cell is smaller than the volume of the high temperature cell, the findings of XRD for the low temperature phase appear questionable and additional investigation is necessary to resolve this problem.

3.3.3. *Low temperature dynamics*

Solid state NMR intimately relies on the ability to coherently average and recouple strong dipolar interactions. Partial loss of coherent control over spin dynamics due to local motion is a common source of attenuated or completely lost peaks in the NMR spectrum. Figure 22 shows temperature dependence of integrated intensity of $Ala-C\beta$. The overall intensity decrease with

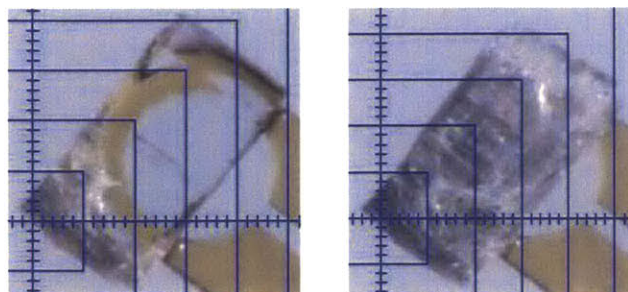


Figure 19. Photographs showing a single crystal of APG at 208 K (left) and 207 K (right).

temperature due to decrease of Boltzmann polarization. At the same time, the peak cannot be observed between 110 K and 140 K, and there is apparently a second region, in which the peak is attenuated at higher temperatures around 180 K.

It is convenient to remove the contribution to signal loss that is due to loss of Boltzmann polarization by multiplying the intensity of each peak with the corresponding temperature, as shown in Figure 23 for Ala-C β , Pro-C α , and Gly-C O . Clearly, there are two temperature regions, in which all peaks are strongly attenuated, while Ala-C β is unobservable in the middle of the first region. Disappearance of methyl carbon from ^{13}C MAS NMR spectrum is often caused by interference between ^1H decoupling and three-fold hops of the methyl protons about the C $_3$ symmetry axis of the methyl group [47,68-72]. To verify that inefficient decoupling in fact takes place, we also collected a series of directly excited ^{13}C MAS NMR spectra similar to those in Figure 12 (not shown).

Figure 24 shows temperature dependence of integrated intensities of Ala-C β , Pro-C α , and Gly-C O in directly excited ^{13}C MAS NMR spectra corrected for loss of Boltzmann polarization. Ala-C β is still unobservable in the first region, strongly supporting the hypothesis of inefficient ^1H decoupling. The other sites are still attenuated in the first region too, although to a smaller extent. These observations can be explained as follows. CP MAS experiment involves transfer of polarization via coherent recoupling of heteronuclear ^1H - ^{13}C dipolar interaction, followed by detection of ^{13}C signal in the presence of "coherent" heteronuclear decoupling. When a local motion renders dipolar decoupling inefficient, it interferes with coherent control of the ^1H spins and, therefore, should also affect recoupling process. When ^1H spins are spin-locked during the CP stage, spin-lock fails for protons of the methyl group, causing short longitudinal relaxation time in the rotating frame. Methyl protons, thus, become an efficient polarization sink for the entire molecule thanks to rapid proton spin diffusion and the combination of intra- and inter-molecular contacts (Figure 20). In the case of direct ^{13}C excitation, the transfer stage is removed. The fact that other carbon sites are still attenuated means that they are also affected by methyl protons, though to a smaller extent due to the larger distance. Therefore, signal attenuation observed in the CP MAS

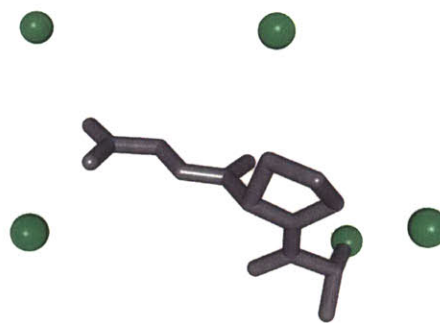


Figure 20. Fragment of crystal structure of APG showing five methyl groups (green balls) located within 4 Å of the molecule.

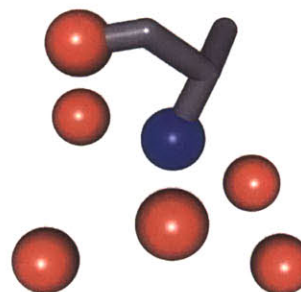


Figure 21. Fragment of crystal structure of APG showing six oxygen nuclei (red balls) located within 3.5 Å of Ala-N (blue ball).

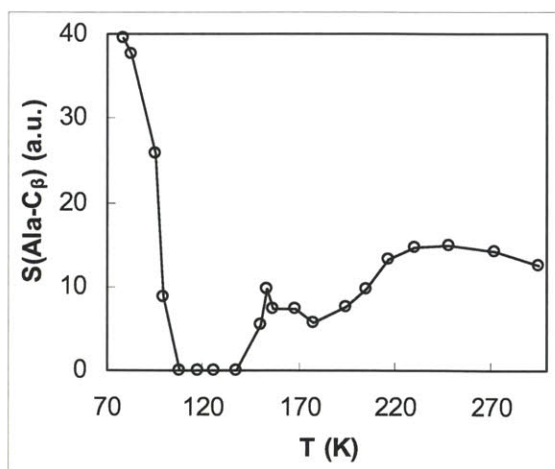


Figure 22. Temperature dependence of integrated intensity of Ala-C β .

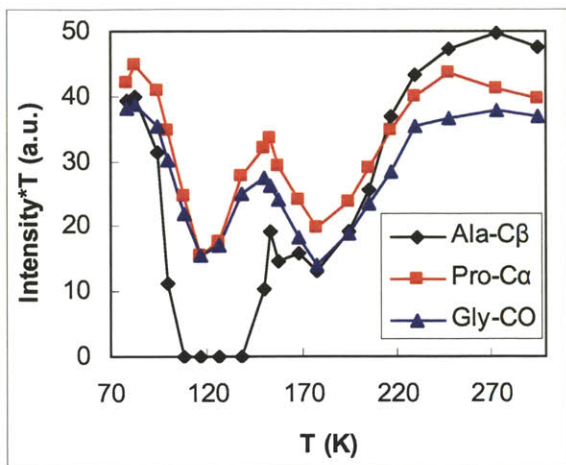


Figure 23. Temperature dependence of integrated intensity of select lines in CP MAS NMR spectra of APG corrected for loss of Boltzmann polarization.

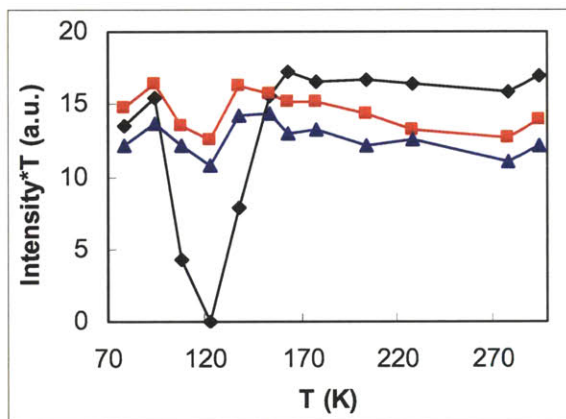


Figure 24. Same as Figure 23, except direct ^{13}C .

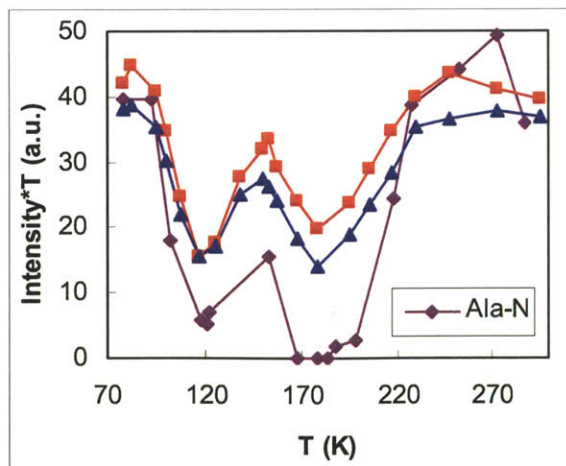


Figure 25. Same as Figure 23, with ^{15}N CP MAS NMR trace for Ala-N.

experiments should be due to both less efficient transfer stage and inefficient decoupling. It is noteworthy that the second signal depression is essentially absent from the direct excitation spectrum, indicating that it should be dominated by the inefficient CP transfer stage.

We should also note that signal intensity in Figure 24 gradually decrease with temperature after the first deep is passed. This decrease can be attributed to the fact that in our experiments the entire sample chamber was cooled, including the sample coil. As the coil becomes colder, its resistance decreases and the quality factor of the circuit increases, leading to correspondent increase in the detected signal amplitude.

Additionally, the low temperature intensity in Figure 23 is slightly lower than the high temperature intensity. This difference is attributed to incomplete recovery of Zeeman magnetization at low temperatures due to relatively shorter recycle delay.

While methyl group hopping causes the first (low temperature) signal depression, the second one may be caused by similar phenomenon involving the ammonium group. Indeed, ^{15}N CP MAS NMR experiments confirmed this hypothesis as shown in Figure 25, in which Ala-N trace is overlaid on ^{13}C traces.

It worth pointing out that ammonium group reaches NMR relevant hopping rates at higher temperatures. This order should be expected: while methyl is a neutral apolar group, ammonium group is charged, polar, and can readily form hydrogen bonds. Ala-N site also has six neighboring

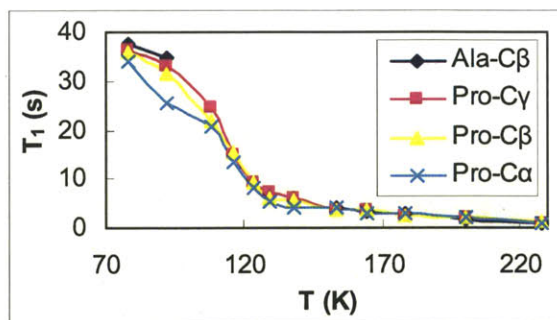


Figure 26. ^1H spin-lattice relaxation times measured via indirect detection of ^{13}C signal after CP transfer.

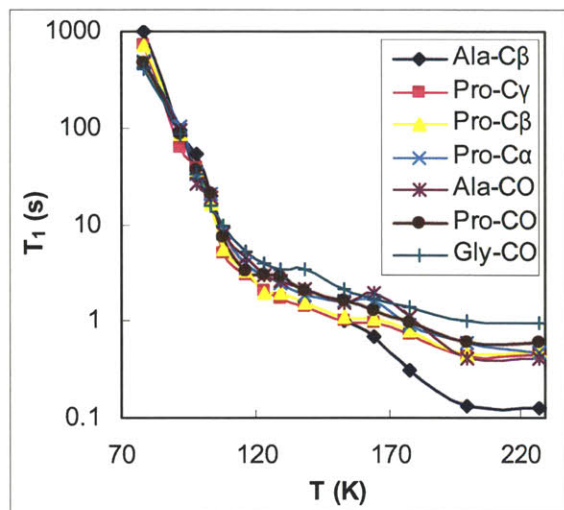


Figure 27. ^{13}C spin-lattice relaxation times.

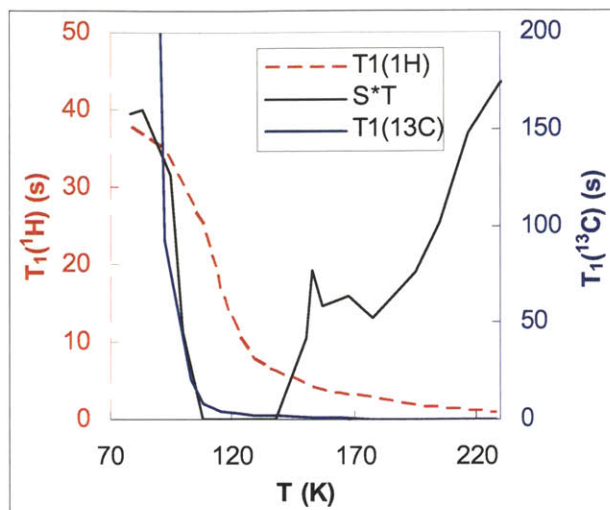


Figure 28. ^{13}C and ^1H spin-lattice relaxation times for Ala- C_β overlaid on top of its intensity trace. See details in text.

oxygen atoms (Figure 21), of which four are partially charged sites from terminal carboxyl groups. Thus, the hopping barrier for the ammonium group should be higher and more complex than the hopping barrier for the methyl group.

Another interesting observation is that spin-lattice relaxation times of ^1H (Figure 26) and ^{13}C (Figure 27) rapidly drop in the vicinity of the low temperature signal depression as illustrated in Figure 28, in which ^1H and ^{13}C spin-lattice relaxation times for Ala- C_β are overlaid on top of its intensity trace (missing T_1 points around 120 K were obtained by correlating the data on either side of the region with the average for the rest of sites following by interpolation).

3.3.4. Activation energy of methyl group reorientation

The threefold methyl hopping resembles a temperature activated process and, thus, usually obeys the Arrhenius's law. Furthermore, following a simple spectral density approach to couple the correlation time of the reorientation process to the typical timescale of the interference causing the relaxation the following relation can be derived [43]:

$$\Delta\omega_{\text{hom}} \propto \frac{\tau_c}{1 + \omega_c^2 \tau_c^2} = \frac{\tau_0 \exp\left(\frac{E_a}{k_B T}\right)}{1 + \omega_c^2 \tau_0^2 \exp\left(\frac{2E_a}{k_B T}\right)} \propto \frac{\exp\left(\frac{E_a}{k_B T}\right)}{1 + C \exp\left(\frac{2E_a}{k_B T}\right)},$$

ω_c can be linked in first order to the rate of the interfering motion. However, since oscillating interactions due to MAS couple to the ^1H decoupling field the exact magnitude of ω_c is unknown. Nevertheless an accurate value for the energy barrier of the hopping process can be obtained, since ω_c only affects τ_c and the absolute amplitude but not the temperature dependence directly.

Analysis based on this equation, involves investigation of temperature dependent homogeneous broadening of the affected spin, in this case Ala- C_β . However, the half width at half maxi-

mum (HWHM) of the Ala-C β line contains not only homogeneous contribution, but also contributions from site inhomogeneity and J -coupling. Therefore the spin relaxation time T_2 was determined by measuring the amplitude of Hahn echo as a function of refocusing period, while a selective Gaussian pulse was used to refocus J -coupling. At temperatures between 95 and 140 K no spin echo could be recorded even with the shortest possible rotor-synchronized evolution period, and the inverse of HWHM of the Ala-C β was used as T_2 , where the signal could be detected. The resulting full width at half maximum (FWHM) of the Ala-C β line as a function of temperature is shown in Figure 29. The fit, also shown in the figure, yielded activation energy of 10.9 kJ/mol, which is in excellent agreement with experimentally obtained reorientation barriers in Ala-Ala dipeptides.

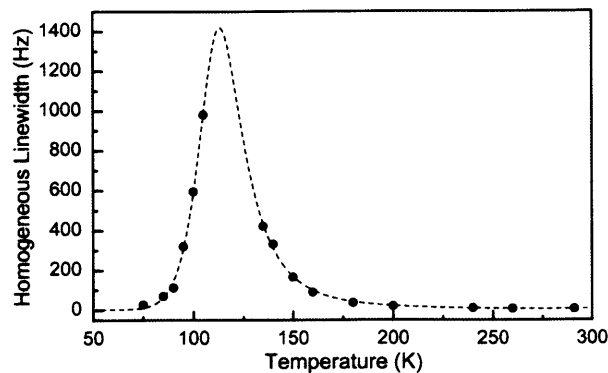


Figure 29. Homogeneous linewidth (FWHM) of the Ala-C β resonance in uniformly ^{13}C , ^{15}N -labeled APG. The dashed line represents a fit using a spectral density approach to transverse relaxation caused by interference of the temperature-activated three-fold methyl group hopping with the ^1H decoupling.

References

- [1] Markin, A. V.; Markhasin, E.; Sologubov, S. S.; Smirnova, N. N.; Griffin, R. G. Standard Thermodynamic Functions of Tripeptides N-formyl-Met-Pro-Phe-OH and N-formyl-Met-Pro-Phe-OMe.
- [2] Ni, Q. Z.; Corzilius, B.; Markhasin, E.; Barnes, A. B.; Ong, T.-C.; Andreas, L. B.; Markin, A. V.; Smirnova, N. N.; Griffin, R. G. Structural Dynamics and Transformations of Alanyl-prolyl-glycine investigated by low-temperature MAS NMR.
- [3] Ni, Q. Z.; Daviso, E.; Can, T. V.; Markhasin, E.; Jawla, S. K.; Swager, T. M.; Temkin, R. J.; Herzfeld, J.; Griffin, R. G. High Frequency Dynamic Nuclear Polarization. *Acc. Chem. Res.*, Ahead of Print. DOI: 10.1021/ar300348n
- [4] Renault, M.; Cukkemane, A.; Baldus, M. Solid-State NMR Spectroscopy on Complex Biomolecules. *Angew. Chem., Int. Ed.* **2010**, *49*, 8346. DOI: 10.1002/anie.201002823
- [5] Lesage, A. Recent advances in solid-state NMR spectroscopy of spin $I = 1/2$ nuclei. *Phys. Chem. Chem. Phys.* **2009**, *11*, 6876. DOI: 10.1039/b907733m
- [6] Andronesi, O. C.; von Bergen, M.; Biernat, J.; Seidel, K.; Griesinger, C.; Mandelkow, E.; Baldus, M. Characterization of Alzheimer's-like Paired Helical Filaments from the Core Domain of Tau Protein Using Solid-State NMR Spectroscopy. *J. Am. Chem. Soc.* **2008**, *130*, 5922. DOI: 10.1021/ja7100517
- [7] Etzkorn, M.; Boeckmann, A.; Lange, A.; Baldus, M. Probing Molecular Interfaces Using 2D Magic-Angle-Spinning NMR on Protein Mixtures with Different Uniform Labeling. *J. Am. Chem. Soc.* **2004**, *126*, 14746. DOI: 10.1021/ja0479181
- [8] Lange, A.; Becker, S.; Seidel, K.; Giller, K.; Pongs, O.; Baldus, M. A concept for rapid protein-structure determination by solid-state NMR spectroscopy. *Angew. Chem., Int. Ed.* **2005**, *44*, 2089. DOI: 10.1002/anie.200462516
- [9] Cady, S. D.; Schmidt-Rohr, K.; Wang, J.; Soto, C. S.; De Grado, W. F.; Hong, M. Structure of the amantadine binding site of influenza M2 proton channels in lipid bilayers. *Nature* **2010**, *463*, 689. DOI: 10.1038/nature08722
- [10] Griffin, R. G. Dipolar recoupling in MAS spectra of biological solids. *Nat. Struct. Biol.* **1998**, *5*, 508. DOI: 10.1038/749
- [11] Mak-Jurkauskas, M. L.; Bajaj, V. S.; Hornstein, M. K.; Belenky, M.; Griffin, R. G.; Herzfeld, J. Energy transformations early in the bacteriorhodopsin photocycle revealed by DNP-enhanced solid-state NMR. *Proc. Natl. Acad. Sci. U.S.A.* **2008**, *105*, 883. DOI: 10.1073/pnas.0706156105
- [12] Castellani, F.; van Rossum, B.-J.; Diehl, A.; Rehbein, K.; Oschkinat, H. Determination of solid-state NMR structures of proteins by means of three-dimensional ^{15}N - ^{13}C - ^{13}C dipolar correlation spectroscopy and chemical shift analysis. *Biochemistry* **2003**, *42*, 11476. DOI: 10.1021/bi034903r S0006-2960(03)04903-1
- [13] Hong, M.; Su, Y. Structure and dynamics of cationic membrane peptides and proteins: insights from solid-state NMR. *Protein Sci.* **2011**, *20*, 641. DOI: 10.1002/pro.600

- [14] Brown, S. P.; Spiess, H. W. Advanced solid-state NMR methods for the elucidation of structure and dynamics of molecular, macromolecular, and supramolecular systems. *Chem. Rev.* **2001**, *101*, 4125. DOI: 10.1021/cr990132e
- [15] Ladizhansky, V. Dipolar-Based Torsion Angle Measurements for Protein Structure Determination. In *Encyclopedia of Magnetic Resonance*; John Wiley & Sons, Ltd: 2007. DOI: 10.1002/9780470034590.emrstml153
- [16] De Paepe, G.; Lewandowski, J. R.; Loquet, A.; Boeckmann, A.; Griffin, R. G. Proton assisted recoupling and protein structure determination. *J. Chem. Phys.* **2008**, *129*, 245101/1. DOI: 10.1063/1.3036928
- [17] Barnes, A. B.; Andreas, L. B.; Huber, M.; Ramachandran, R.; van der Wel, P. C. A.; Veshtort, M.; Griffin, R. G.; Mehta, M. A. High-resolution solid-state NMR structure of Alanine-Prolyl-Glycine. *J. Magn. Reson.* **2009**, *200*, 95. DOI: 10.1016/j.jmr.2009.06.009
- [18] Van der Wel, P. C. A.; Lewandowski, J. R.; Griffin, R. G. Solid-State NMR Study of Amyloid Nanocrystals and Fibrils Formed by the Peptide GNNQQNY from Yeast Prion Protein Sup35p. *J. Am. Chem. Soc.* **2007**, *129*, 5117. DOI: 10.1021/ja068633m
- [19] Brinkmann, A. Dipolar recoupling in magic-angle-spinning nuclear magnetic resonance. Ph.D. Thesis, Stockholms Universitet, 2001. <http://search.proquest.com/docview/304780453/>
- [20] De Paepe, G. Dipolar recoupling in magic angle spinning solid-state nuclear magnetic resonance. *Annu. Rev. Phys. Chem.* **2012**, *63*, 661. DOI: 10.1146/annurev-physchem-032511-143726
- [21] Rienstra, C. M. Magic-angle spinning recoupling techniques for distance determinations among spin-1/2 nuclei in solid peptides and proteins. *NMR Spectrosc. Biol. Solids* **2006**, *1*. DOI: 10.1201/9781420027617.ch1
- [22] Schnell, I. Dipolar recoupling in fast-MAS solid-state NMR spectroscopy. *Prog. Nucl. Magn. Reson. Spectrosc.* **2004**, *45*, 145. DOI: 10.1016/j.pnmrs.2004.06.003
- [23] Ernst, M.; Meier, B. H. Adiabatic Polarization-Transfer Methods in MAS Spectroscopy. In *Encyclopedia of Magnetic Resonance*; John Wiley & Sons, Ltd: 2007. DOI: 10.1002/9780470034590.emrstm0004.pub2
- [24] Bjerring, M.; Rasmussen, J. T.; Krogshave, R. S.; Nielsen, N. C. Heteronuclear coherence transfer in solid-state nuclear magnetic resonance using a gamma -encoded transferred echo experiment. *J. Chem. Phys.* **2003**, *119*, 8916. DOI: 10.1063/1.1613933
- [25] Ernst, M. Heteronuclear spin decoupling in solid-state NMR under magic-angle sample spinning. *J. Magn. Reson.* **2003**, *162*, 1. DOI: 10.1016/S1090-7807(03)00074-0
- [26] Mithu, V. S.; Pratihari, S.; Paul, S.; Madhu, P. K. Efficiency of heteronuclear dipolar decoupling schemes in solid-state NMR: Investigation of effective transverse relaxation times. *J. Magn. Reson.* **2012**, *220*, 8. DOI: 10.1016/j.jmr.2012.04.005
- [27] Mithu, V. S.; Paul, S.; Kurur, N. D.; Madhu, P. K. Heteronuclear dipolar decoupling in solid-state nuclear magnetic resonance under ultra-high magic-angle spinning. *J. Magn. Reson.* **2011**, *209*, 359. DOI: 10.1016/j.jmr.2011.01.028

- [28] Brinkmann, A.; Levitt, M. H. Symmetry principles in the nuclear magnetic resonance of spinning solids. Heteronuclear recoupling by generalized Hartmann-Hahn sequences. *J. Chem. Phys.* **2001**, *115*, 357. DOI: 10.1063/1.1377031
- [29] Carravetta, M.; Eden, M.; Zhao, X.; Brinkmann, A.; Levitt, M. H. Symmetry principles for the design of radiofrequency pulse sequences in the nuclear magnetic resonance of rotating solids. *Chem. Phys. Lett.* **2000**, *321*, 205. DOI: 10.1016/s0009-2614(00)00340-7
- [30] Levitt, M. H. Symmetry-based pulse sequences in magic-angle spinning solid-state NMR. In *Encyclopedia of Magnetic Resonance*; Grant, D. M., Harris, R. K., Eds.; Wiley: 2002; Vol. 9, p 165. DOI: 10.1002/9780470034590.emrstm0551
- [31] van Beek, J. D.; Carravetta, M.; Antonioli, G. C.; Levitt, M. H. Spherical tensor analysis of nuclear magnetic resonance signals. *J. Chem. Phys.* **2005**, *122*, 244510/1. DOI: 10.1063/1.1943947
- [32] Zhao, X.; Hoffbauer, W.; Schmedt auf der Gunne, J.; Levitt, M. H. Heteronuclear polarization transfer by symmetry-based recoupling sequences in solid-state NMR. *Solid State Nucl. Magn. Reson.* **2004**, *26*, 57. DOI: 10.1016/j.ssnmr.2003.11.001
- [33] Drobny, G. P.; Long, J. R.; Karlsson, T.; Shaw, W.; Popham, J.; Oyler, N.; Bower, P.; Stringer, J.; Gregory, D.; Mehta, M.; Stayton, P. S. Structural studies of biomaterials using double-quantum solid-state NMR spectroscopy. *Annu. Rev. Phys. Chem.* **2003**, *54*, 531. DOI: 10.1146/annurev.physchem.54.011002.103903
- [34] LeMaster, D. M.; Kushlan, D. M. Dynamical Mapping of E. coli Thioredoxin via ¹³C NMR Relaxation Analysis. *J. Am. Chem. Soc.* **1996**, *118*, 9255. DOI: 10.1021/ja960877r
- [35] Hong, M. Determination of Multiple ϕ -Torsion Angles in Proteins by Selective and Extensive ¹³C Labeling and Two-Dimensional Solid-State NMR. *J. Magn. Reson.* **1999**, *139*, 389. DOI: 10.1006/jmre.1999.1805
- [36] Castellani, F.; van Rossum, B.; Diehl, A.; Schubert, M.; Rehbein, K.; Oschkinat, H. Structure of a protein determined by solid-state magic-angle-spinning NMR spectroscopy. *Nature* **2002**, *420*, 98. DOI: 10.1038/nature01070
- [37] Ellman, J. A.; Volkman, B. F.; Mendel, D.; Schulz, P. G.; Wemmer, D. E. Site-specific isotopic labeling of proteins for NMR studies. *J. Am. Chem. Soc.* **1992**, *114*, 7959. DOI: 10.1021/ja00046a080
- [38] Samuel-Landtiser, M.; Zachariah, C.; Williams, C. R.; Edison, A. S.; Long, J. R. Incorporation of Isotopically Enriched Amino Acids. In *Current Protocols in Protein Science*; John Wiley & Sons, Inc.: 2001. DOI: 10.1002/0471140864.ps2603s47
- [39] Jones, D. H.; Cellitti, S. E.; Hao, X.; Zhang, Q.; Jahnz, M.; Summerer, D.; Schultz, P. G.; Uno, T.; Geierstanger, B. H. Site-specific labeling of proteins with NMR-active unnatural amino acids. *J. Biomol. NMR* **2010**, *46*, 89. DOI: 10.1007/s10858-009-9365-4
- [40] Davis, L.; Chin, J. W. Designer proteins: applications of genetic code expansion in cell biology. *Nat. Rev. Mol. Cell Biol.* **2012**, *13*, 168. DOI: 10.1038/nrm3286
- [41] Loquet, A.; Habenstein, B.; Lange, A. Structural Investigations of Molecular Machines by Solid-State NMR. *Acc. Chem. Res.*, Ahead of Print. DOI: 10.1021/ar300320p

- [42] Abragam, A. *The principles of nuclear magnetism*; Clarendon Press: Oxford, 1961.
- [43] Concistre, M.; Johannessen, O. G.; Carignani, E.; Geppi, M.; Levitt, M. H. Magic-Angle Spinning NMR of Cold Samples. *Acc. Chem. Res.*, Ahead of Print. DOI: 10.1021/ar300323c
- [44] Griffin, R. G.; Prisner, T. F. High field dynamic nuclear polarization-the renaissance. *Phys. Chem. Chem. Phys.* **2010**, *12*, 5737. DOI: 10.1039/c0cp90019b
- [45] Bajaj, V. S.; van der Wel, P. C. A.; Griffin, R. G. Observation of a Low-Temperature, Dynamically Driven Structural Transition in a Polypeptide by Solid-State NMR Spectroscopy. *J. Am. Chem. Soc.* **2009**, *131*, 118. DOI: 10.1021/ja8045926
- [46] Carignani, E.; Borsacchi, S.; Geppi, M. Dynamics by Solid-State NMR: Detailed Study of Ibuprofen Na Salt and Comparison with Ibuprofen. *J. Phys. Chem. A* **2011**, *115*, 8783. DOI: 10.1021/jp202650n
- [47] Godoy-Ruiz, R.; Guo, C.; Tugarinov, V. Alanine Methyl Groups as NMR Probes of Molecular Structure and Dynamics in High-Molecular-Weight Proteins. *J. Am. Chem. Soc.* **2010**, *132*, 18340. DOI: 10.1021/ja1083656
- [48] Reif, B. Deuterated Peptides and Proteins: Structure and Dynamics Studies by MAS Solid-state NMR. In *Encyclopedia of Magnetic Resonance*; John Wiley & Sons, Ltd: 2007. DOI: 10.1002/9780470034590.emrstm1080
- [49] Torchia, D. A. Dynamics of biomolecules from picoseconds to seconds at atomic resolution. *J. Magn. Reson.* **2011**, *212*, 1. DOI: 10.1016/j.jmr.2011.07.010
- [50] Vugmeyster, L.; Ostrovsky, D.; Ford, J. J.; Burton, S. D.; Lipton, A. S.; Hoatson, G. L.; Vold, R. L. Probing the Dynamics of a Protein Hydrophobic Core by Deuteron Solid-State Nuclear Magnetic Resonance Spectroscopy. *J. Am. Chem. Soc.* **2009**, *131*, 13651. DOI: 10.1021/ja902977u
- [51] Vugmeyster, L.; Ostrovsky, D.; Khadjinova, A.; Ellden, J.; Hoatson, G. L.; Vold, R. L. Slow Motions in the Hydrophobic Core of Chicken Villin Headpiece Subdomain and Their Contributions to Configurational Entropy and Heat Capacity from Solid-State Deuteron NMR Measurements. *Biochemistry* **2011**, *50*, 10637. DOI: 10.1021/bi201515b
- [52] Vugmeyster, L.; Ostrovsky, D.; Penland, K.; Hoatson, G. L.; Vold, R. L. Glassy Dynamics of Protein Methyl Groups Revealed by Deuteron NMR. *J. Phys. Chem. B* **2013**, *117*, 1051. DOI: 10.1021/jp311112j
- [53] Xue, Y.; Pavlova, M. S.; Ryabov, Y. E.; Reif, B.; Skrynnikov, N. R. Methyl Rotation Barriers in Proteins from ²H Relaxation Data. Implications for Protein Structure. *J. Am. Chem. Soc.* **2007**, *129*, 6827. DOI: 10.1021/ja0702061
- [54] Latanowicz, L. NMR relaxation study of methyl groups in solids from low to high temperatures. *Concepts Magn. Reson., Part A* **2005**, *27A*, 38. DOI: 10.1002/cmr.a.20040
- [55] Bajaj, V. S.; Mak-Jurkauskas, M. L.; Belenky, M.; Herzfeld, J.; Griffin, R. G. Functional and shunt states of bacteriorhodopsin resolved by 250 GHz dynamic nuclear polarization-enhanced solid-state NMR. *Proc. Natl. Acad. Sci. U.S.A.* **2009**, *106*, 9244. DOI: 10.1073/pnas.0900908106

- [56] Schmidt, A.; Kababya, S.; Appel, M.; Khatib, S.; Botoshansky, M.; Eichen, Y. Measuring the Temperature Width of a First-Order Single Crystal to Single Crystal Phase Transition Using Solid-State NMR: Application to the Polymorphism of 2-(2,4-Dinitrobenzyl)-3-methylpyridine. *J. Am. Chem. Soc.* **1999**, *121*, 11291. DOI: 10.1021/ja991204m
- [57] Odin, C. NMR studies of phase transitions. *Annu. Rep. NMR Spectrosc.* **2006**, *59*, 117. DOI: 10.1016/s0066-4103(06)59003-9
- [58] Plohr, J. N.; Clements, B. E.; Addessio, F. L. Dynamically driven phase transformations in heterogeneous materials. II. Applications including damage. *J. Appl. Phys.* **2006**, *100*, 123521/1. DOI: 10.1063/1.2398327
- [59] Clements, B. E.; Plohr, J. N.; Addessio, F. L. Dynamically driven phase transformations in heterogeneous materials. I. Theory and microstructure considerations. *J. Appl. Phys.* **2006**, *100*, 123520/1. DOI: 10.1063/1.2398284
- [60] Plohr, J. N.; Clements, B. E.; Addessio, F. L. Dynamically driven phase transformations in damaged composite materials. *AIP Conf. Proc.* **2006**, *845*, 266
- [61] Bastea, M.; Bastea, S.; Emig, J. A.; Springer, P. T.; Reisman, D. B. Kinetics of propagating phase transformation in compressed bismuth. *Phys. Rev. B: Condens. Matter Mater. Phys.* **2005**, *71*, 180101/1. DOI: 10.1103/PhysRevB.71.180101
- [62] Barnes, A. B.; Corzilius, B.; Mak-Jurkauskas, M. L.; Andreas, L. B.; Bajaj, V. S.; Matsuki, Y.; Belenky, M. L.; Lugtenburg, J.; Sirigiri, J. R.; Temkin, R. J.; Herzfeld, J.; Griffin, R. G. Resolution and polarization distribution in cryogenic DNP/MAS experiments. *Phys. Chem. Chem. Phys.* **2010**, *12*, 5861. DOI: 10.1039/c003763j
- [63] Thurber, K. R.; Tycko, R. Measurement of sample temperatures under magic-angle spinning from the chemical shift and spin-lattice relaxation rate of ⁷⁹Br in KBr powder. *J. Magn. Reson.* **2009**, *196*, 84. DOI: 10.1016/j.jmr.2008.09.019
- [64] Barnes, A. B.; Mak-Jurkauskas, M. L.; Matsuki, Y.; Bajaj, V. S.; van der Wel, P. C. A.; De Rocher, R.; Bryant, J.; Sirigiri, J. R.; Temkin, R. J.; Lugtenburg, J.; Herzfeld, J.; Griffin, R. G. Cryogenic sample exchange NMR probe for magic angle spinning dynamic nuclear polarization. *J. Magn. Reson.* **2009**, *198*, 261. DOI: 10.1016/j.jmr.2009.03.003
- [65] Varushchenko, R. M.; Druzhinina, A. I.; Sorokin, E. L. Low-temperature heat capacity of 1-bromoperfluorooctane. *J. Chem. Thermodyn.* **1997**, *29*, 623. DOI: 10.1006/jcht.1996.0173
- [66] Malyshev, V. M.; Mil'ner, G. A.; Sorokin, E. L.; Shibakin, V. F. Automatic low-temperature calorimeter. *Instrum. Exp. Technol.* **1985**, 195
- [67] Delaglio, F.; Grzesiek, S.; Vuister, G. W.; Zhu, G.; Pfeifer, J.; Bax, A. NMRPipe: a multidimensional spectral processing system based on UNIX pipes. *J. Biomol. NMR* **1995**, *6*, 277. DOI: 10.1007/bf00197809
- [68] Gabrys, B.; Horii, F.; Kitamaru, R. Carbon-13 NMR study of the α -methyl group rotation in solid poly(methyl methacrylate): detection of the ¹³C T1 minimum. *Macromolecules* **1987**, *20*, 175. DOI: 10.1021/ma00167a029
- [69] Beshah, K.; Olejniczak, E. T.; Griffin, R. G. Deuterium NMR study of methyl group dynamics in L-alanine. *J. Chem. Phys.* **1987**, *86*, 4730. DOI: 10.1063/1.452693

- [70] Beshah, K.; Griffin, R. G. Deuterium quadrupole echo NMR study of methyl group dynamics in N-acetyl-DL-(γ -d₆)-valine. *J. Magn. Reson.* **1989**, *84*, 268. DOI: 10.1016/0022-2364(89)90370-3
- [71] Copie, V.; McDermott, A. E.; Beshah, K.; Williams, J. C.; Spijker-Assink, M.; Gebhard, R.; Lugtenburg, J.; Herzfeld, J.; Griffin, R. G. Deuterium Solid-State Nuclear Magnetic Resonance Studies of Methyl Group Dynamics in Bacteriorhodopsin and Retinal Model Compounds: Evidence for a 6-s-Trans Chromophore in the Protein. *Biochemistry* **1994**, *33*, 3280. DOI: 10.1021/bi00177a019
- [72] Maus, D. C.; Copie, V.; Sun, B.; Griffiths, J. M.; Griffin, R. G.; Luo, S.; Grohmann, A.; Liu, A. H.; Seidel, S. W.; Davis, W. M. A Solid-State NMR Study of Tungsten Methyl Group Dynamics in W(h₅-C₅Me₅)Me₄ PF₆. *J. Am. Chem. Soc.* **1996**, *118*, 5665. DOI: 10.1021/ja960248h
- [73] Noggle, J. H. Hindered rotation of methyl groups using nuclear magnetic resonance. *J. Phys. Chem.* **1968**, *72*, 1324. DOI: 10.1021/j100850a044
- [74] Stejskal, E. O.; Gutowsky, H. S. Proton magnetic resonance of the CH₃ group. IV. Calculation of the tunneling frequency and of T₁ in solids. *J. Chem. Phys.* **1958**, *28*, 388. DOI: 10.1063/1.1744143
- [75] Hilt, R. L.; Hubbard, P. S. Nuclear Magnetic Relaxation of Three Spin Systems Undergoing Hindered Rotations. *Phys. Rev.* **1964**, *134*, A392. DOI: 10.1103/PhysRev.134.A392
- [76] Long, J. R.; Sun, B. Q.; Bowen, A.; Griffin, R. G. Molecular Dynamics and Magic Angle Spinning NMR. *J. Am. Chem. Soc.* **1994**, *116*, 11950. DOI: 10.1021/ja00105a039

Program 1. PyMOL Script Generating Figure 17

```
set sphere_mode, -1
viewport 640,480

load APG.pdb
preset.ball_and_stick("all")
hide ribbon, all
set stick_radius, 0.1
alter all, vdw=1.1
show spheres, all
rebuild

select hydrogens
hide everything, sele
select water, resn HOH
hide everything, water

select conf_a, `2/*`A
hide everything, conf_a

select affected1, ALA/CB OR PRO/CB OR PRO/CG OR ALA/C OR GLY/CA
deselect
select affected2, PRO/C OR PRO/CA
deselect
color black, affected1
color gray30, affected2

set_view (\
  -0.043212805,  -0.994902670,  -0.091085687,\
    0.888710082,  -0.079930313,   0.451444417,\
  -0.456425816,  -0.061443478,   0.887637854,\
  -0.000019448,   0.000016478, -19.671785355,\
    3.987711906,   3.660412312,   2.335891485,\
    9.546894073,  29.797830582, -20.000000000 )

util.performance(0)
bg_color white
set opaque_background = 0
set show_alpha_checker = 1
set depth_cue = 0
set ray_trace_fog = 0
set orthoscopic = 0
set antialias = 1
set line_smooth = 1
set specular = 1
set surface_quality = 1
set stick_quality = 25
set sphere_quality = 2
set cartoon_sampling = 14
set ribbon_sampling = 10

ray 1200,900
png APG_2D_tr.png, dpi=300
```

Program 2. PyMOL Script Generating Figure 20

```
run supercell.py
set sphere_mode, -1
viewport 640,480

load APG.pdb
select hydrogens OR resn HOH OR `2/*`A
remove sele

supercell 2, 2, 2, APG, orange
delete apg
set_name m110_3, apg
select methyls, ((apg around 4) AND ALA/CB) OR apg///ALA/CB
deselect
select NOT (methyls OR apg)
remove sele
delete supercell

alter methyls, vdw=0.5
hide lines, all
hide spheres, all
set stick_color, gray
show sticks, all
show spheres, methyls
rebuild

set_view (\
  -0.190764621,  -0.129164681,  -0.973100543,\
   0.813758433,  -0.575220346,  -0.083174966,\
  -0.549003959,  -0.807735980,   0.214841053,\
  -0.000000480,   0.000015110, -27.587652206,\
   5.897864819,  14.065895081,  14.308712006,\
  16.065103531,  39.112632751, -20.000000000 )

util.performance(0)
bg_color white
set opaque_background = 0
set show_alpha_checker = 1
set depth_cue = 0
set ray_trace_fog = 0
set orthoscopic = 0
set antialias = 1
set line_smooth = 1
set specular = 1
set surface_quality = 1
set stick_quality = 25
set sphere_quality = 2
set cartoon_sampling = 14
set ribbon_sampling = 10

ray 1200,900
png methyls.png, dpi=300
```

Program 3. PyMOL Script Generating Figure 21

```
run supercell.py
set sphere_mode, -1

load APG.pdb
select hydrogens OR `2/*`A OR `101/O`D
remove sele

supercell 2, 2, 2, APG, orange
delete apg
set_name m011_1, apg
select os, (apg///ALA/N around 3.5) AND element O
deselect
select (NOT (os OR apg)) OR (resn HOH AND NOT os) OR (apg AND NOT (resn ALA))
remove sele
delete supercell

alter os OR ALA/N, vdw=0.6
hide lines, all
hide spheres, all
set stick_color, gray
show sticks, all
show spheres, os OR ALA/N
rebuild

set_view (\
  -0.447382748, 0.118891574, -0.886404693,\
  -0.620101213, 0.672958732, 0.403237164,\
  0.644455194, 0.730062246, -0.227344945,\
  -0.000007731, -0.000009283, -19.103395462,\
  5.673255920, 9.637927055, 16.646339417,\
  -0.412308693, 38.618892670, -20.000000000 )

util.performance(0)
bg_color white
set opaque_background = 0
set show_alpha_checker = 1
set depth_cue = 0
set ray_trace_fog = 0
set orthoscopic = 0
set antialias = 1
set line_smooth = 1
set specular = 1
set surface_quality = 1
set stick_quality = 25
set sphere_quality = 2
set cartoon_sampling = 14
set ribbon_sampling = 10

ray 1200,900
png os.png, dpi=300
```

4. Dynamic Nuclear Polarization Enhanced SSNMR of Oxygen-17

Adapted from references [1-2].

Abstract

Oxygen-17 detected DNP NMR of a water/glycerol glass enabled an 80-fold enhancement of signal intensities at 82 K, using the biradical TOTAPOL. The >6,000-fold savings in acquisition time enables ^{17}O - ^1H distance measurements and heteronuclear correlation experiments. These experiments are the initial demonstration of the feasibility of DNP NMR on quadrupolar ^{17}O .

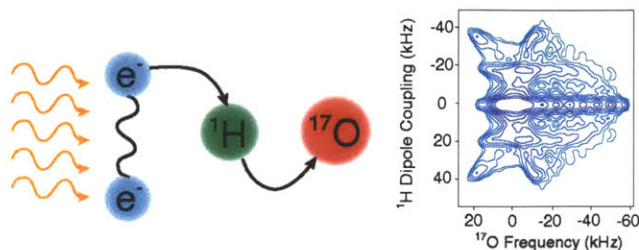


Figure 30. DNP enhanced NMR of oxygen-17.

4.1. Introduction

Recent years have seen an avalanche of new magic angle spinning (MAS) NMR methods developed to determine structures of macromolecular systems that are not amenable to study by either solution NMR or diffraction techniques, the two principle tools of structural chemistry. In particular, with MAS NMR there are now established methods to assign spectra and to perform distance and torsion angle measurements for the $I=1/2$ species ^1H , ^{13}C , ^{15}N and ^{31}P . [3-4] These tools, in turn, have enabled studies of protein and nucleic structures and dynamics. Largely missing from the biomolecular NMR repertoire is oxygen, a key element of water and a variety of chemically and biologically important functional groups. The difficulty is that the only NMR active natural oxygen isotope, ^{17}O , has a quadrupolar nucleus ($I=5/2$), with attendant spectral complications. Additionally, ^{17}O has low natural abundance of 0.037 %. On the other hand, ^{17}O chemical shifts span ~ 1000 ppm with the potential for chemically significant spectral resolution. Two recent examples showed that the ^{17}O shifts of carboxyl groups are dispersed over 60 ppm [5] and that the $-\text{C}^{17}\text{O}_2$ shift tensor elements are sensitive to H-bonding and span ~ 550 -600 ppm [6].

Progress in ^{17}O NMR has been stymied primarily by the low sensitivity resulting from the broad 2nd order powder patterns and low resolution of the spectra. This problem is further exacerbated by the low efficiency of the techniques used to observe ^{17}O . In more detail, ^{17}O MAS spectra display residual 2nd order broadening characteristic of a 4th rank tensor that is not averaged to zero by MAS [7-8]. To observe isotropic chemical shifts in the presence of and convolved with the 2nd order interaction requires either special instrumentation, as in case of double rotation (DOR) and dynamic-angle spinning (DAS) [9-10], or special spectroscopic techniques, as in case of multiple-quantum magic angle spinning (MQMAS) [11] and satellite-transition magic angle spinning (STMAS) [12]. However, when the quadrupole coupling is large (> 5 MHz) the excitation efficiency of these approaches drops dramatically; in the case of MQMAS spectra, to about $\sim 5\%$ [13-14]. Thus, although there are a number of exciting MQMAS studies of ^{17}O labeled biological samples, the experimental results are clearly limited by signal-to-noise [5,15-22]. In order to enable ^{17}O NMR as an important spectroscopic technique, a dramatic increase in sensitivity is required.

Being developed over the last two decades, gyrotron based high frequency dynamic nuclear polarization (DNP) has provided immense gains in NMR sensitivity via microwave-induced transfer of polarization from paramagnetic centers to nuclei [23-24]. In general, ^1H 's are polarized directly and then cross-polarization is used to transfer the enhanced polarization to other nuclei (e.g., ^{13}C , ^{15}N , etc.) at cryogenic temperatures (~ 85 K). [24-30] This approach has been successfully applied to membrane proteins [31-33], peptides [34-35], amyloid fibrils [36] as well as surfaces [37-38]. Most of these studies focus on $I=1/2$ nuclei (e.g., ^{13}C , ^{31}P , ^{29}Si , etc.) and a few on the $I=1$ and $5/2$ quadrupolar species [39-41]. The magnetization transfer yields enhancements $\epsilon = 30$ -250, and the low temperature yields another gain of ~ 3.5 in Boltzmann polarization relative to ambient temperature. In combination, $\epsilon^\dagger \sim 105$ -875 could dramatically improve the prospects of performing ^{17}O experiments in biological systems.

4.2. CPMG Experiment. Sensitivity Enhancement

NMR Hamiltonian of quadrupolar nuclei often contains a strong contribution, which is due to quadrupolar coupling [11]. In the solid state, this term usually results in a severe broadening of NMR spectrum, which is only partially attenuated by the MAS [12]. This broadening also corresponds to very fast transverse relaxation (Figure 31). At the same time, since the quadrupolar interaction is inhomogeneous [13], it can be refocused producing an echo [14] or a series of successive echoes (Figure 32) [15]. In the latter case, the overall decay of echo amplitude is typically dominated by the homogenous contribution to the transverse relaxation time (T_2), which in the case of quadrupolar nuclei is often 2-3 orders of magnitude longer than the overall transverse relaxation time (T_2^*), dominated by

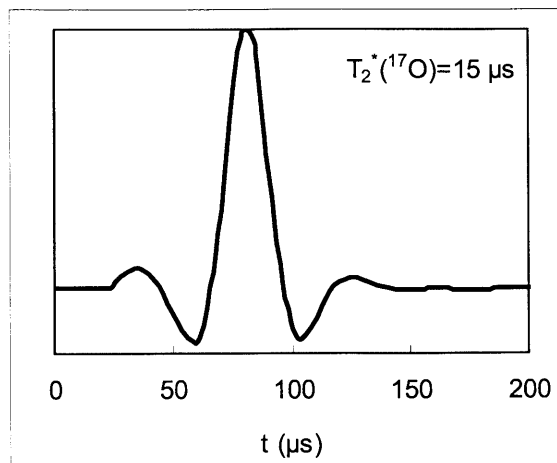


Figure 31. ^{17}O echo in a frozen water-glycerol matrix.

inhomogeneous contribution. As a result, a large number of echoes ($\sim T_2 / T_2^*$) can often be collected. These echoes can be added together to produce a significant S/N increase. Interestingly, utilization of an echo train for low sensitivity samples may result in a substantially increased rate of growth of S/N with the number of transient, as can be seen from the following analysis, making the CPMG experiment [15-19] a powerful technique.

We will start with the assumption

$$T_2^* \ll T_2 \ll T_{1\rho}, \quad (16)$$

where T_2^* is overall transverse relaxation time of FID, T_2 is the homogenous contribution to transverse relaxation time and $T_{1\rho}$ is the longitudinal relaxation time in the rotating frame. This

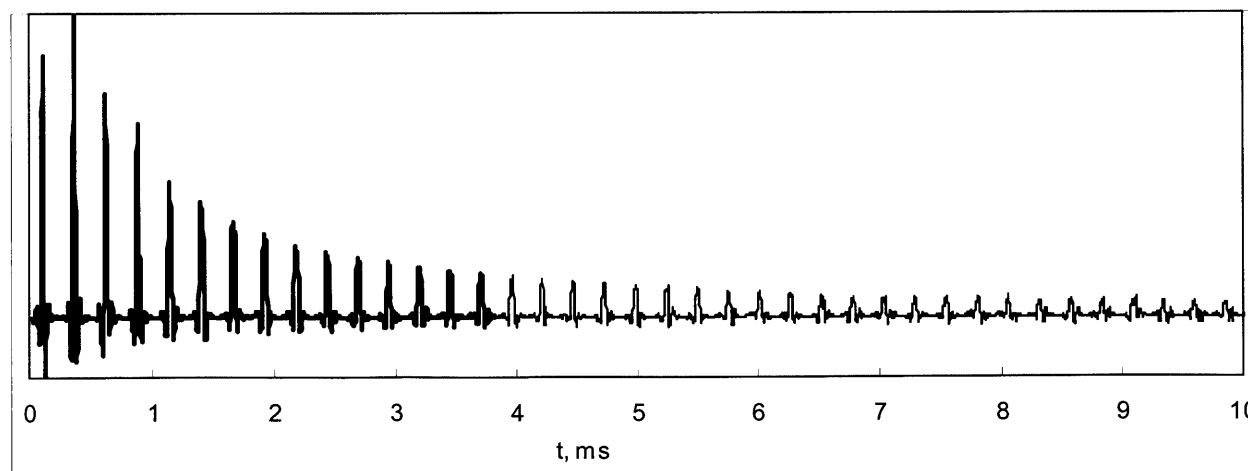


Figure 32. ^{17}O echo train in a frozen water-glycerol matrix. The bold part of the signal spans $1.26 \cdot T_2$.

assumption is often well satisfied for quadrupolar nuclei and describes the most favorable situation, allowing one to take full advantage of this technique.

In the limit of negligible relaxation, we can immediately determine that

$$f_{CPMG} = \sqrt{2}\sqrt{n},$$

where f_{CPMG} is the gain in S/N due to CPMG, n is the number of echoes and an additional $\sqrt{2}$ in S/N is achieved when compared to an FID, rather than a full echo.

When condition (16) is fulfilled, transverse relaxation can be represented as a superposition of relaxation of a signal within individual echoes and a slow relaxation of the overall echo envelope. We first consider the effect of signal relaxation within individual echoes:

$$S(T) = S_o(T) e^{-\frac{T}{T_2}} \approx S_o(T) - S_o(T) \frac{T}{T_2},$$

where $S_o(\tau)$ is the signal in the absence of homogenous contribution (T_2) to relaxation and T is a signed offset time with respect to the echo maximum (the middle point). To zeroth order, the second term can be neglected, because $T \leq 10T_2^*$. Furthermore, assuming that the first term is a symmetric function of τ and the second is antisymmetric, the folded signal

$$S'(T) = S(T) + S(-T) = 2S_o(T),$$

is the same as in the case of infinitely long T_2 .

Let us define CPMG period $\tilde{\tau} = \tau / T_2$, frequency $\tilde{\nu} = 1 / \tilde{\tau}$, and duration $\tilde{t} = n\tau / T_2$ in natural units of T_2 . The intensity S_{n-1} of the n^{th} echo in a CPMG train (Figure 33)

$$S_{n-1} = S_o \left(e^{-\frac{\tau}{T_2}} \right)^{n-1} = S_o e^{-\tilde{\tau}(n-1)},$$

the total signal of n folded echoes

$$S(n) = \sum_{i=0}^{n-1} S_i = \frac{1 - e^{-\tilde{\tau}}}{1 - e^{-\tilde{\tau}}} S_o,$$

and CPMG gain in S/N

$$f_{CPMG} = \sqrt{\frac{2}{n} \frac{1 - e^{-\tilde{\tau}}}{1 - e^{-\tilde{\tau}}}} \approx \sqrt{\frac{2}{\tilde{\tau}\tilde{\nu}} \tilde{\nu} (1 - e^{-\tilde{\tau}})} = \sqrt{\frac{2\tilde{\nu}}{\tilde{t}}} (1 - e^{-\tilde{\tau}}) = \sqrt{\frac{2}{\tilde{t}}} (1 - e^{-\tilde{\tau}}) \sqrt{\tilde{\nu}} = f(\tilde{t}) \sqrt{\tilde{\nu}}. \quad (17)$$

The first factor in the right hand side of Equation (17) only depends on the total length \tilde{t} of the echo train, and its functional dependence is shown in Figure 34. It has a maximum, when $\frac{\partial f_{CPMG}}{\partial \tilde{t}} = 0$, which is fulfilled when $\tilde{t} \approx 1.26$ corresponding to the last echo attenuated down to $e^{-1.26} \approx 28\%$. For example, for optimal S/N only the highlighted part in Figure 32 should be collected and used for further processing. The maximum gain in S/N provided by CPMG

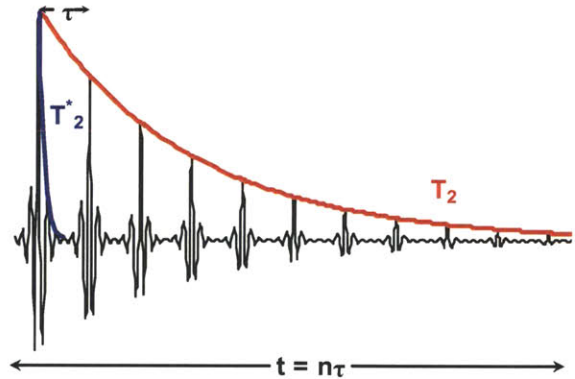


Figure 33. Model CPMG echo train. The homogenous relaxation time is exaggerated for the purpose of demonstration.

$$f_{CPMG}^{\max} \approx f_{CPMG}(\tilde{t} = 1.26) \approx 0.9\sqrt{\nu}. \quad (18)$$

Thus, maximum S/N gain that is due to CPMG is proportional to the square root of the number of echoes per T_2 , and the larger T_2/T_2^* , the larger potential advantage provided by CPMG.

4.3. NMR Experiments

Here we demonstrate the feasibility of this approach in the simple case of $H_2^{17}O$. We observe for the first time an enhancement of $\epsilon \sim 80$ or $\epsilon^\dagger \sim 280$ for ^{17}O using high field DNP NMR and the polarizing agent TOTAPOL in a glassy glycerol/ D_2O/H_2O matrix and an enhancement of $\epsilon \sim 100$ with polarizing agent Trityl OX063. In particular we are able to polarize ^{17}O for both via protons and directly and use the enhanced ^{17}O polarization to perform echo (Figure 35a) and Carr-Purcell-Meiboom-Gill (CPMG, Figure 35b,d) [42-46] experiments and to use spin-echo double resonance (SEDOR, Figure 35c)[47-48] experiments to measure $^1H-^{17}O$ distances. Finally, we use a heteronuclear correlation (HETCOR, Figure 35b) [49-50] experiment to record a simple 2D correlation spectrum. The dramatic savings in acquisition time demonstrates a potentially important approach to ^{17}O spectroscopy that can be extended to studies of $H_2^{17}O$ in other chemical systems and of ^{17}O in oxygen containing functional groups.

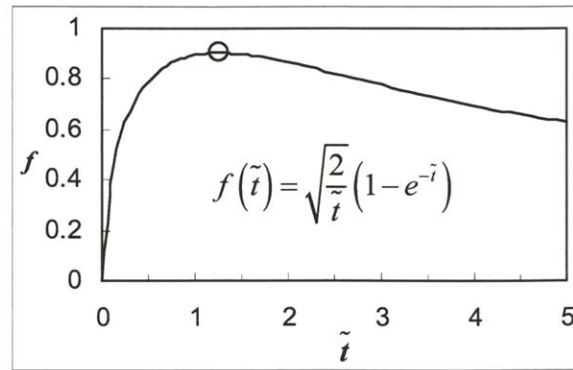


Figure 34. Dependence of the f_p gain factor on the length of echo train. The circle indicates the optimal signal to noise gain.

4.3.1. 1H Mediated and Direct Polarization. Sensitivity Limit

Figure 36a shows central transition ($1/2 \rightarrow -1/2$) 1D spectra demonstrating DNP enhancements of ^{17}O , and Figure 36b shows a DNP enhanced CPMG spectrum of the same sample. Figure 36 yields $\epsilon \sim 60$, which is close to the number observed using a different sample size and probe (data not shown). When the proton bath was diluted with deuterons using the commonly used composition, D_8 -glycerol/ $D_2O/H_2^{17}O$ (60:30:10 v/v), a higher enhancement of 80 was ob-

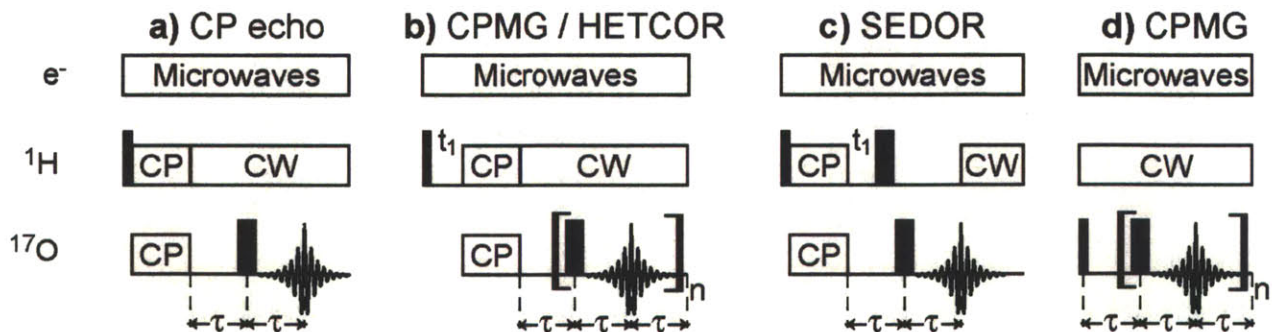


Figure 35. Pulse sequences of ^{17}O DNP/NMR experiments. **a)** $^1H-^{17}O$ cross polarization from polarized protons followed by echo on ^{17}O . **b)** Same as (a) with echo replaced by CPMG [42] train and optional t_1 evolution on 1H for HETCOR experiment [49-50]. **c)** Same as (a) with echo replaced by SEDOR sequence [47-48]. **d)** Direct polarization of ^{17}O followed by CPMG.

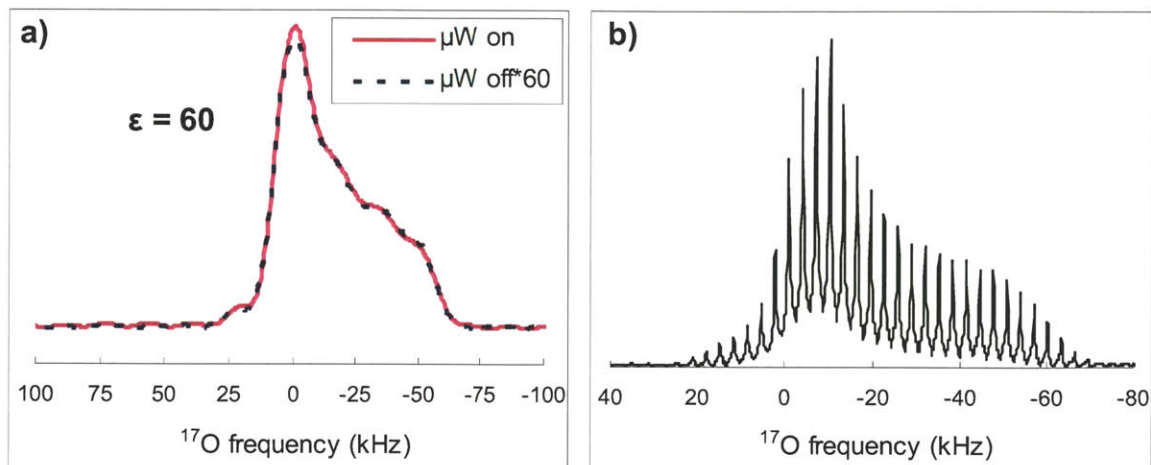


Figure 36. Static solid state NMR spectra of ^{17}O labeled water (^1H mediated polarization). **a)** On (128 scans) and off (10240 scans) echo spectra (Figure 35a) recorded using 5 s recycle delay. **b)** On (128 scans) CPMG spectrum (12 echoes) recorded using 16 s recycle delay. All experiments recorded at 88 K using 50 kHz CW ^1H decoupling and 8 W of μ wave power on 4 mm sapphire rotors containing ~ 76 mg of frozen D_8 -Glycerol/ $(^{17}\text{O}, 75\%)/\text{H}_2\text{O}$ (60:40 v) and 20 mM TOTAPOL.

served (data not shown).

The shapes of the static powder patterns shown in Figure 36 are characteristic of a second-order quadrupolar coupling pattern [51-53]. Chemical shielding anisotropy can also influence the lineshape, although, for water at 5 T, this effect is negligible compared to that of the quadrupolar interaction. The quadrupolar coupling constant, $C_Q = 6.8 \pm 0.2$ MHz, the asymmetry parameter, $\eta = 0.95 \pm 0.05$ and the isotropic chemical shift, $\delta_{\text{iso}} = 0 \pm 50$ ppm were determined by simulating the non-spinning powder pattern using SIMPSON [54] software. The sizeable quadrupolar coupling is reasonable for a frozen water environment. [55] The ~ 85 kHz breadth of the central transition limits the ability to use magic-angle spinning (MAS). In particular, the water/glycerol oxygen site at 5 T would require $\omega_r/2\pi > 30$ kHz to isolate the central transition from a series of rotational sidebands. Current spinning frequencies with 4 mm rotors at cryogenic temperatures are limited to ~ 7 kHz due to the density of the N_2 drive and bearing gases being near the liquefaction point ($T = 77$ K). As DNP NMR instruments are developed for higher fields, lower spinning frequencies could suffice due to the inverse relationship between the breadth of the second-order quadrupolar interaction and B_0 . For example, at 14 T, $\omega_r/2\pi = 10$ kHz would be sufficient for ^{17}O MAS DNP experiments.

Figure 37 shows central transition folded

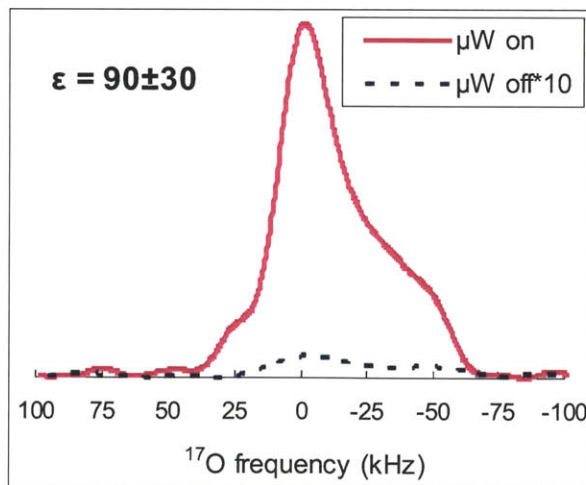


Figure 37. Static solid state NMR spectra of ^{17}O labeled water (direct polarization). On (32 scans) and off (2460 scans) CPMG (20 folded echoes in Figure 35d) spectra recorded at 77 K with 32 s recycle delay and 8 W of μ wave power on a 4 mm sapphire rotor packed with D_8 -Glycerol/ $(^{17}\text{O}, 75\%)\text{H}_2^{17}\text{O}$ (60:40 v/v), 40 mM Trityl OX063.

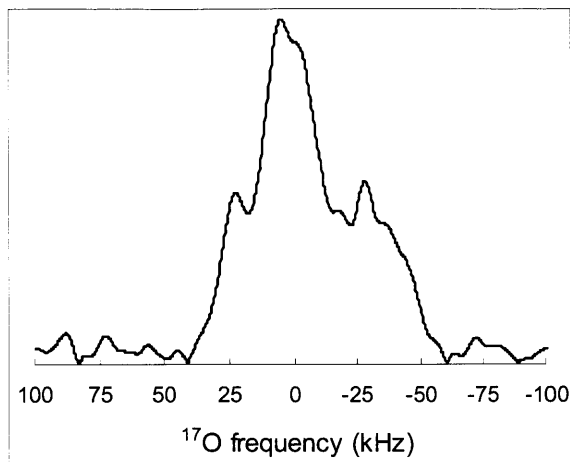


Figure 38. DNP enhanced MAS NMR spectrum of ^{17}O labeled water.

On (120 scans) echo spectrum recorded at 4 kHz MAS and 90 K with 20 s recycle delay and 8 W of μ wave power on a 2.5 mm sapphire rotor packed with $\text{D}_8\text{-Glycerol}/(^{17}\text{O}, 75\%)\text{H}_2^{17}\text{O}$ (60:40 v/v), 40 mM Trityl OX063.

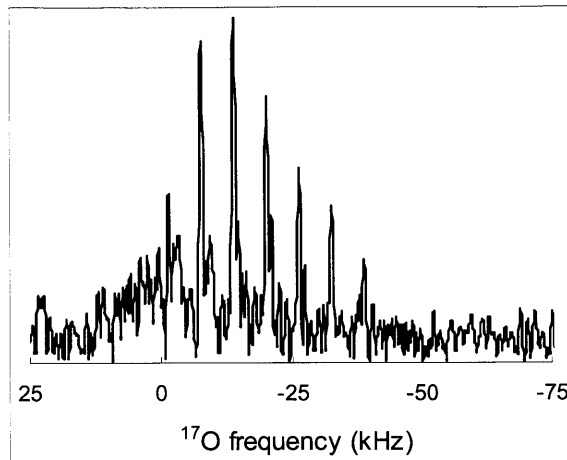


Figure 39. DNP enhanced static ssNMR spectrum of natural abundance ^{17}O sample.

Central transition CPMG spectrum recorded at 86 K, with 8 W of μ wave power using 5 s recycle delay and 21504 scans on a 4 mm sapphire rotor packed with frozen $\text{D}_8\text{-Glycerol}/\text{D}_2\text{O}/\text{H}_2\text{O}$ (60:30:10 v/v) and 20 mM TOTAPOL. Overall amount of ^{17}O spins $\approx 1\ \mu\text{mol}$.

CPMG spectra demonstrating DNP enhancements of ^{17}O that is due to direct polarization and yields an enhancement of $\epsilon \sim 100$. Figure 38 shows an on spectrum obtained at 4 kHz MAS. The breadth of the MAS spectrum is not reduced by MAS.

Finally, in order to evaluate the sensitivity limit of the instrument and of the technique, we recorded a CPMG spectrum shown in Figure 39 on a natural abundance sample. We estimated that this sample contains approximately $1\ \mu\text{mol}$ of ^{17}O spins, which is comparable to the amount of spins per site of a labeled moderate size protein in a 4 mm rotor. After two days of acquisition, we successfully detected the signal, though the signal to noise is still very low. However, we anticipate that further development and optimization of experimental condition should further increase the sensitivity.

Finally, in order to evaluate the sensitivity limit of the instrument and of the technique, we recorded a CPMG spectrum shown in Figure 39 on a natural abundance sample. We estimated that this sample contains approximately $1\ \mu\text{mol}$ of ^{17}O spins, which is comparable to the amount of spins per site of a labeled moderate size protein in a 4 mm rotor. After two days of acquisition, we successfully detected the signal, though the signal to noise is still very low. However, we anticipate that further development and optimization of experimental condition should further increase the sensitivity.

4.3.2. *Effect of ^1H Decoupling on ^{17}O NMR Spectra*

^1H heteronuclear decoupling is usually essential for obtaining high resolution NMR spectra in protonated solids [56]. Although certain recoupling experiments can be performed without ^1H decoupling during the mixing period [57-58], decoupling still must be used during acquisition. In the case of quadrupolar nuclei, however, the effect of heteronuclear decoupling may be obscured by the presence of strong quadrupolar interaction, which usually results in large inhomogeneous

broadening of the observed signal due to the second order quadrupolar terms, which is not averaged by MAS [59]. Figure 40a shows a sample FID of ^{17}O signal from a sample containing H_2^{17}O . The envelope of the FID decays with $T_2^* \approx 15 \mu\text{s}$. At the same time, the envelope of a decoupled CPMG train decays with a $T_2 \approx 3 \text{ ms}$ (Figure 40b). Even though the width of the lineshape in this case is not reduced by ^1H decoupling, there is a substantial loss of signal intensity and part of structural information encoded in the shape of the line is lost (Figure 40c). Comparison of CPMG FID's (Figure 40b) also clearly indicates the importance of heteronuclear ^1H decoupling to minimize the homogeneous contribution to transverse relaxation rate and associated loss of signal intensity.

4.3.3. ^{17}O Correlation Spectra

Multidimensional experiments also enable the extraction of structural information by corre-

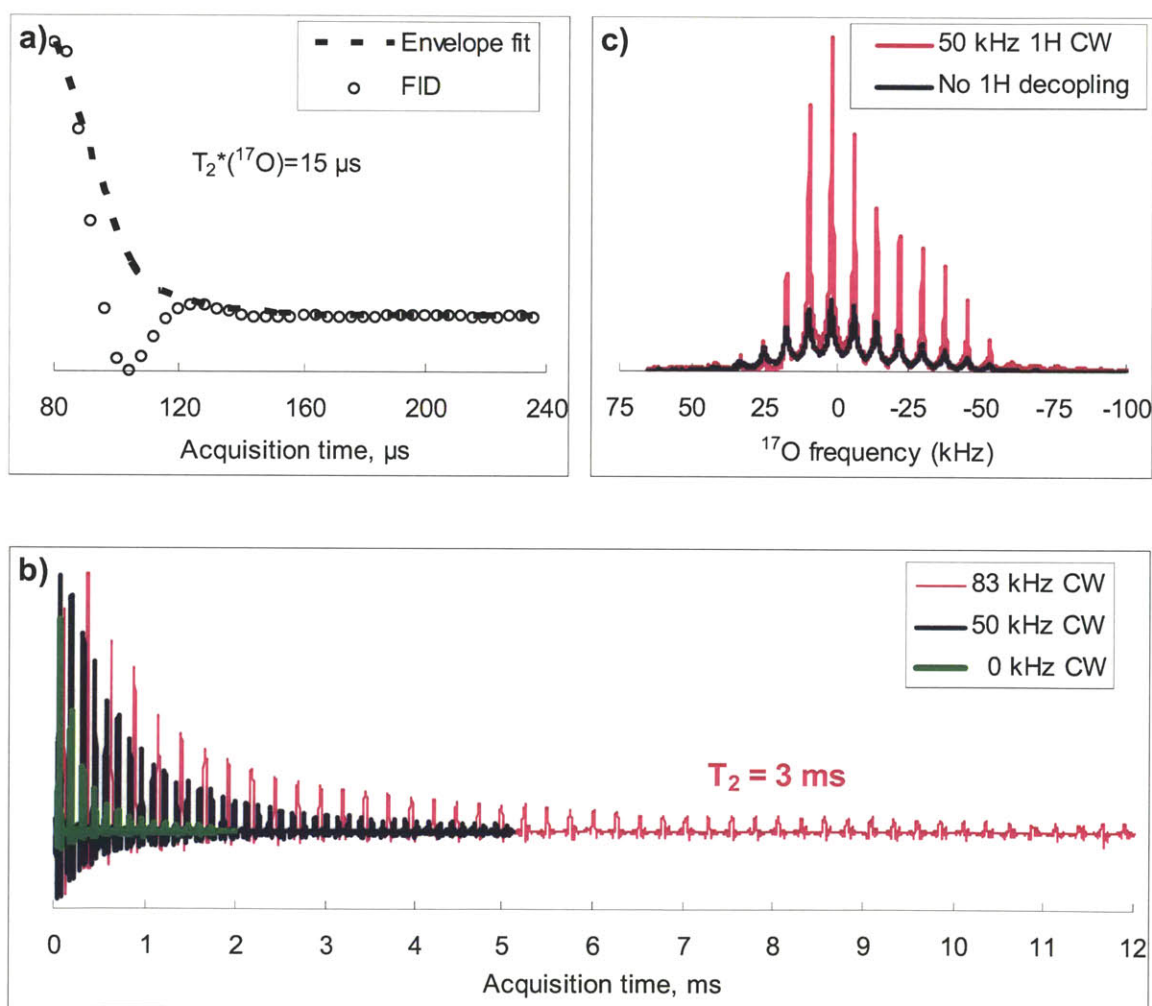


Figure 40. Effect of ^1H decoupling on T_2 , signal intensity and lineshape in ^{17}O SSNMR.

a) Echo decay (Figure 35a) collected using 128 scans and 5 s recycle delay and T_2^* envelope fit. b) CPMG echo trains (Figure 35b) collected using 16 scans and 16 s recycle delay employing varying level of ^1H decoupling. c) CPMG spectra corresponding to FID's in (b). All experiments recorded at 88 K using 8 W of μ wave power on a 4 mm sapphire rotors containing $\sim 76 \text{ mg}$ of $\text{D}_8\text{-Glycerol}/(^{17}\text{O}, 75\%)/\text{H}_2\text{O}$ (60:40 v) and 20 mM TOTAPOL.

lating resonance(s) from one NMR nucleus to another, through either the dipolar or J-coupling interactions. Figure 41 shows a ^{17}O - ^1H heteronuclear correlation spectrum (HETCOR) [49-50] combined with CPMG train for a water/glycerol glass. A projection along the ^{17}O dimension yields the quadrupolar spikelet pattern similar to Figure 36b. The indirect dimension (^1H) exhibits a broad resonance dominated by ^1H - ^1H homonuclear dipolar coupling. ^1H chemical shielding and heteronuclear dipolar coupling are also present, although they contribute minimally to the observed lineshape.

For quadrupolar NMR, a 16-phase cycle is often used during acquisition of one- and two-dimensional data often leading to improved quadrupolar lineshapes. With the sensitivity boost from DNP and CPMG, a HETCOR-CPMG spectrum of the water/glycerol glass was also acquired using an 8 scan, 8-phase cycle acquisition scheme (not shown). The reduced phase cycle (versus 16) provided similar results, with only minor variations within the discontinuities. With the use of hard pulses, increased field (B_0) strength and studying systems with lineshapes below 80 kHz, reduced phase cycle could provide an alternative for multidimensional experiments, further reducing acquisition time for broad resonances and low sensitivity.

The low sensitivity of ^{17}O NMR often requires weeks of acquisition time, rendering multidimensional structural experiments impractical. In consequence, most distances measured between ^{17}O and either ^1H or ^{13}C by NMR are indirect, applying a dephasing pulse on ^{17}O and observing ^1H or ^{13}C . [54,60-61] In Figure 42, we show the results of a SEDOR experiment used to measure the average ^1H - ^{17}O distance in the glycerol/water glass. A 1D stepped-SEDOR experiment was used to acquire a ^{17}O S/S₀ curve characteristic of the dipolar coupling (Figure 42a).

The SEDOR curve was simulated using SIMPSON [54] software and is compared with the experimental curve determined from the peak areas (Figure 42a). Various spin models included a single oxygen site with 2-5 ^1H 's between 0.8 and 1.2 Å and <HOH angles between 100° to 110° (values were chosen based on upper and lower limits of the experimental data). These inputs were adjusted until a reasonable model of the glass was obtained. A three-spin model (one O and two H's) indicated an average H-O bond distance of 1.1 ± 0.1 Å, a value that agrees well with X-ray and neutron diffraction data from various crystalline ice structures where H-O distances are found between 0.86 and 1.15 Å [62-64].

We found it to be difficult to achieve acceptable agreement between the experimental and simulated spectra. This difficulty can be attributed to the following two reasons. First, the samples used for all experiments were in the glassy state. Therefore, there must be a certain degree of structural disorder present (e.g., distance, angle and possibly coordination). Second, mobile protons were significantly diluted with deuterons, which come from deuterated glycerol used for sample preparation. Therefore, the observed 1D and 2D experiments have contributions from ^{17}O sites with varying number of neighboring protons.

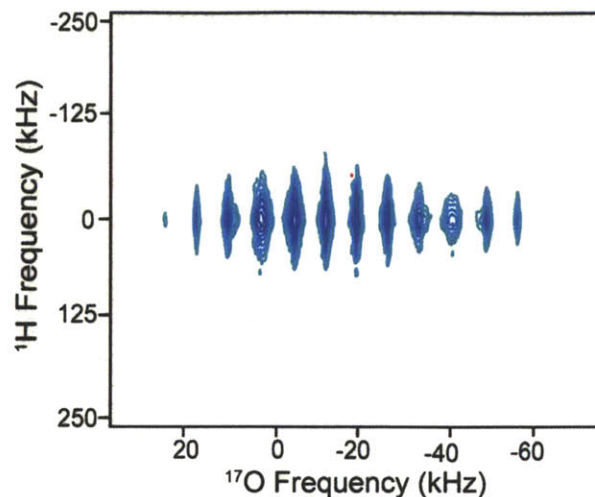


Figure 41. Central transition ^{17}O - ^1H HETCOR-CPMG spectrum of H_2^{17}O with DNP.

The sample is the same as in Figure 36.

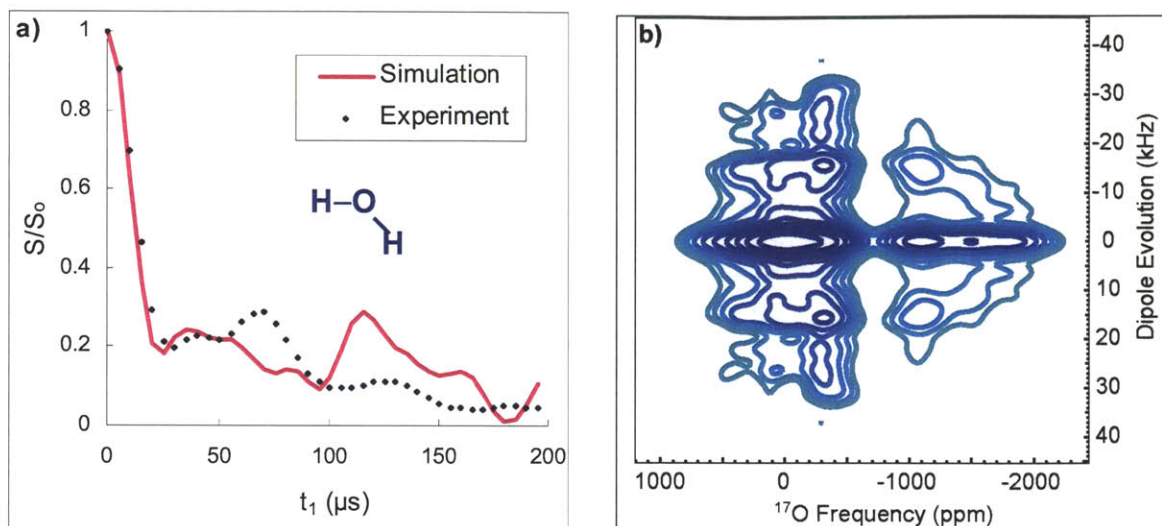


Figure 42. Central transition ^{17}O - ^1H SEDOR experiment.

a) SEDOR curve with SIMPSON simulation and b) 2D SEDOR spectrum recorded at 88 K with 8 W of μ wave power using $t_1 = 5$ μs , 40 t_1 points, 225 μs fixed echo period, 2 μs dwell time, 256 points in the direct dimension, and 5 s recycle delay. The sample is the same as in Figure 36.

A second Fourier transformation of the evolution dimension of the same SEDOR experiment yields a 2D dipole-quadrupolar correlation spectrum (Figure 42b) similar to those reported previously [65-66]. This spectrum is sensitive to the relative orientation of the dipole and quadrupolar tensors, and this information, in principle, can be extracted by fitting the experimental data [65].

DNP NMR enables SEDOR experiments to measure single ^{17}O bond lengths within hours. This could be extended to ^{17}O - ^{13}C or ^{17}O - ^{15}N bond distances with appropriate hardware and to other sequences, such as rotational echo double resonance (REDOR) and transferred echo double resonance (TEDOR), with higher field DNP. Experimental times for the identical experiments without DNP are projected to require >1.4 years.

4.4. Conclusions and Outlook

In summary, DNP in the simple case of H_2^{17}O provided an enhancement of 80. Water is of great importance in both biological and chemical processes, but is challenging to study using conventional ^{17}O solid state NMR. The ability to polarize protons by microwave irradiation followed by cross-polarization to oxygen has enabled a suite of multi-dimensional NMR experiments of this low-gamma, quadrupolar nucleus within hours. ^{17}O -detected multidimensional spectra were acquired between three and 10 hours using DNP NMR. By enhancing the signal-to-noise ratio, DNP provides a $\sim 6,000$ -fold gain in time at cryogenic temperatures, and, in the absence of relaxation, a $>18,000$ -fold gain in time compared to room temperature (298 K). These gains should be transferable to other difficult quadrupolar nuclei, providing a savings in acquisition time. The significant gain in sensitivity and reduction of experimental time from months to hours is extremely beneficial and provides new possibilities for further exploration of heteronuclear correlations and distances in multidimensional experiments. Extensions to MAS experiments for site assignments are currently in progress.

Acknowledgments

This research was supported by the National Institute of Biomedical Imaging and Bioengineering of the National Institute of Health under award numbers EB-001960, EB-002804, EB-001035, and EB-002026. VKM is grateful to the Natural Sciences and Engineering Research Council of Canada for a Postdoctoral Fellowship. We thank our colleagues Dr. G. Debelouchina, Dr. B. Corzilius, Dr. A. Smith, T.C. Ong and J. Bryant for their assistance and stimulating conversations during the course of this research.

References

- [1] Markhasin, E.; Michaelis, V. K.; Daviso, E.; Corzilius, B.; Herzfeld, J.; Griffin, R. G. In *Dynamic Nuclear Polarization of 17O at 212 MHz / 140 GHz*. VIII International Voevodsky Conference "Physics and Chemistry of Elementary Chemical Processes", Novosibirsk Akademgorodok, Russia, July 15-19, 2012. (poster)
- [2] Michaelis, V. K.; Markhasin, E.; Daviso, E.; Herzfeld, J.; Griffin, R. G. Dynamic Nuclear Polarization of Oxygen-17. *J. Phys. Chem. Lett.* **2012**, *3*, 2030. DOI: 10.1021/jz300742w
- [3] Rienstra, C. M.; Hohwy, M.; Hong, M.; Griffin, R. G. 2D and 3D 15N-13C-13C NMR Chemical Shift Correlation Spectroscopy of Solids: Assignment of MAS Spectra of Peptides. *J. Am. Chem. Soc.* **2000**, *122*, 10979. DOI: 10.1021/ja001092v
- [4] Reif, B.; Jaroniec, C. P.; Rienstra, C. M.; Hohwy, M.; Griffin, R. G. 1H-1H MAS correlation spectroscopy and distance measurements in a deuterated peptide. *J. Magn. Reson.* **2001**, *151*, 320. DOI: 10.1006/jmre.2001.2354
- [5] Wong, A.; Howes, A. P.; Yates, J. R.; Watts, A.; Anupold, T.; Past, J.; Samoson, A.; Dupree, R.; Smith, M. E. Ultra-high resolution 17O solid-state NMR spectroscopy of biomolecules: A comprehensive spectral analysis of monosodium L-glutamate monohydrate. *Phys. Chem. Chem. Phys.* **2011**, *13*, 12213. DOI: 10.1039/c1cp20629j
- [6] Waddell, K. W.; Chekmenev, E. Y.; Wittebort, R. J. Peptide 17O chemical shielding and electric field gradient tensors. *J. Phys. Chem. B* **2006**, *110*, 22935. DOI: 10.1021/jp060617o
- [7] Grandinetti, P. J. In *High Resolution Solid-State NMR of Quadrupolar Nuclei*. 48th ENC, Daytona Beach, 2007.
- [8] Grandinetti, P. J.; Ash, J. T.; Trease, N. M. Symmetry pathways in solid-state NMR. *Prog. Nucl. Magn. Reson. Spectrosc.* **2011**, *59*, 121. DOI: 10.1016/j.pnmrs.2010.11.003
- [9] Chmelka, B. F.; Mueller, K. T.; Pines, A.; Stebbins, J.; Wu, Y.; Zwanziger, J. W. Oxygen-17 NMR in solids by dynamic-angle spinning and double rotation. *Nature* **1989**, *339*, 42. DOI: 10.1038/339042a0
- [10] Baltisberger, J. H.; Gann, S. L.; Grandinetti, P. J.; Pines, A. Cross-polarization dynamic-angle spinning nuclear magnetic resonance of quadrupolar nuclei. *Mol. Phys.* **1994**, *81*, 1109. DOI: 10.1080/00268979400100741

- [11] Frydman, L.; Harwood, J. S. Isotropic Spectra of Half-Integer Quadrupolar Spins from Bidimensional Magic-Angle Spinning NMR. *J. Am. Chem. Soc.* **1995**, *117*, 5367. DOI: 10.1021/ja00124a023
- [12] Gan, Z. Isotropic NMR spectra of half-integer quadrupolar nuclei using satellite transitions and magic-angle spinning. *J. Am. Chem. Soc.* **2000**, *122*, 3242. DOI: 10.1021/ja9939791
- [13] Wu, G.; Rovnyak, D.; Griffin, R. G. Quantitative Multiple-Quantum Magic-Angle-Spinning NMR Spectroscopy of Quadrupolar Nuclei in Solids. *J. Am. Chem. Soc.* **1996**, *118*, 9326. DOI: 10.1021/ja9614676
- [14] Wu, G.; Rovnyak, D.; Huang, P. C.; Griffin, R. G. High-resolution oxygen-17 NMR spectroscopy of solids by multiple-quantum magic-angle-spinning. *Chem. Phys. Lett.* **1997**, *277*, 79. DOI: 10.1016/s0009-2614(97)00873-7
- [15] Brinkmann, A.; Kentgens, A. P. M. Proton-Selective ^{17}O - ^1H Distance Measurements in Fast Magic-Angle-Spinning Solid-State NMR Spectroscopy for the Determination of Hydrogen Bond Lengths. *J. Am. Chem. Soc.* **2006**, *128*, 14758. DOI: 10.1021/ja065415k
- [16] Gullion, T.; Yamauchi, K.; Okonogi, M.; Asakura, T. ^{13}C - ^{17}O REAPDOR NMR as a Tool for Determining Secondary Structure in Polyamides. *Macromolecules* **2007**, *40*, 1363. DOI: 10.1021/ma062835l
- [17] Hung, I.; Uldry, A.-C.; Becker-Baldus, J.; Webber, A. L.; Wong, A.; Smith, M. E.; Joyce, S. A.; Yates, J. R.; Pickard, C. J.; Dupree, R.; Brown, S. P. Probing Heteronuclear ^{15}N - ^{17}O and ^{13}C - ^{17}O Connectivities and Proximities by Solid-State NMR Spectroscopy. *J. Am. Chem. Soc.* **2009**, *131*, 1820. DOI: 10.1021/ja805898d
- [18] Sefzik, T. H.; Houseknecht, J. B.; Clark, T. M.; Prasad, S.; Lowary, T. L.; Gan, Z.; Grandinetti, P. J. Solid-state ^{17}O NMR in carbohydrates. *Chem. Phys. Lett.* **2007**, *434*, 312. DOI: 10.1016/j.cplett.2006.12.008
- [19] Wong, A.; Beevers, A. J.; Kukol, A.; Dupree, R.; Smith, M. E. Solid-state ^{17}O NMR spectroscopy of a phospholemman transmembrane domain protein: Implications for the limits of detecting dilute ^{17}O sites in biomaterials. *Solid State Nucl. Magn. Reson.* **2008**, *33*, 72. DOI: 10.1016/j.ssnmr.2008.04.003
- [20] Wu, G.; Dong, S.; Ida, R.; Reen, N. A solid-state ^{17}O nuclear magnetic resonance study of nucleic acid bases. *J. Am. Chem. Soc.* **2002**, *124*, 1768. DOI: 10.1021/ja011625f
- [21] Yamauchi, K.; Okonogi, M.; Kurosu, H.; Tansho, M.; Shimizu, T.; Gullion, T.; Asakura, T. High Field ^{17}O Solid-State NMR Study of Alanine Tripeptides. *J. Magn. Reson.* **2008**, *190*, 327. DOI: 10.1016/j.jmr.2007.11.006
- [22] Zhu, J.; Ye, E.; Terskikh, V.; Wu, G. Solid-State ^{17}O NMR Spectroscopy of Large Protein-Ligand Complexes. *Angew. Chem., Int. Ed.* **2010**, *49*, 8399. DOI: 10.1002/anie.201002041
- [23] Carver, T. R.; Slichter, C. P. Polarization of nuclear spins in metals. *Phys. Rev.* **1953**, *92*, 212. DOI: 10.1103/PhysRev.92.212.2
- [24] Bajaj, V. S.; Farrar, C. T.; Hornstein, M. K.; Mastovsky, I.; Vieregg, J.; Bryant, J.; Elena, B.; Kreisler, K. E.; Temkin, R. J.; Griffin, R. G. Dynamic nuclear polarization at 9 T us-

- ing a novel 250 GHz gyrotron microwave source. *J. Magn. Reson.* **2003**, *160*, 85. DOI: 10.1016/s1090-7807(02)00192-1
- [25] Becerra, L. R.; Gerfen, G. J.; Temkin, R. J.; Singel, D. J.; Griffin, R. G. Dynamic nuclear polarization with a cyclotron resonance maser at 5 T. *Phys. Rev. Lett.* **1993**, *71*, 3561. DOI: 10.1103/PhysRevLett.71.3561
- [26] Gerfen, G. J.; Becerra, L. R.; Hall, D. A.; Griffin, R. G.; Temkin, R. J.; Singel, D. J. High frequency (140 GHz) dynamic nuclear polarization: polarization transfer to a solute in frozen aqueous solution. *J. Chem. Phys.* **1995**, *102*, 9494. DOI: 10.1063/1.468818
- [27] Hall, D. A.; Maus, D. C.; Gerfen, G. J.; Inati, S.; Becerra, L. R.; Dahlquist, F. W.; Griffin, R. G. Polarization-enhanced NMR spectroscopy of biomolecules in frozen solution. *Science* **1997**, *276*, 930. DOI: 10.1126/science.276.5314.930
- [28] Rosay, M.; Lansing, J. C.; Haddad, K. C.; Bachovchin, W. W.; Herzfeld, J.; Temkin, R. J.; Griffin, R. G. High-frequency dynamic nuclear polarization in MAS spectra of membrane and soluble proteins. *J. Am. Chem. Soc.* **2003**, *125*, 13626. DOI: 10.1021/ja036898k
- [29] Rosay, M.; Tometich, L.; Pawsey, S.; Bader, R.; Schauwecker, R.; Blank, M.; Borchard, P. M.; Cauffman, S. R.; Felch, K. L.; Weber, R. T.; Temkin, R. J.; Griffin, R. G.; Maas, W. E. Solid-state dynamic nuclear polarization at 263 GHz: spectrometer design and experimental results. *Phys. Chem. Chem. Phys.* **2010**, *12*, 5850. DOI: 10.1039/c003685b
- [30] Rosay, M.; Weis, V.; Kreisler, K. E.; Temkin, R. J.; Griffin, R. G. Two-Dimensional ¹³C-¹³C Correlation Spectroscopy with Magic Angle Spinning and Dynamic Nuclear Polarization. *J. Am. Chem. Soc.* **2002**, *124*, 3214. DOI: 10.1021/ja0176752
- [31] Akbey, U.; Franks, W. T.; Linden, A.; Lange, S.; Griffin, R. G.; van Rossum, B.-J.; Oschkinat, H. Dynamic Nuclear Polarization of deuterated proteins. *Angew. Chem., Int. Ed.* **2010**, *49*, 7803. DOI: 10.1002/anie.201002044
- [32] Bajaj, V. S.; Mak-Jurkauskas, M. L.; Belenky, M.; Herzfeld, J.; Griffin, R. G. Functional and shunt states of bacteriorhodopsin resolved by 250 GHz dynamic nuclear polarization-enhanced solid-state NMR. *Proc. Natl. Acad. Sci. U.S.A.* **2009**, *106*, 9244. DOI: 10.1073/pnas.0900908106
- [33] Mak-Jurkauskas, M. L.; Bajaj, V. S.; Hornstein, M. K.; Belenky, M.; Griffin, R. G.; Herzfeld, J. Energy transformations early in the bacteriorhodopsin photocycle revealed by DNP-enhanced solid-state NMR. *Proc. Natl. Acad. Sci. U.S.A.* **2008**, *105*, 883. DOI: 10.1073/pnas.0706156105
- [34] Debelouchina, G. T.; Bayro, M. J.; van der Wel, P. C. A.; Caporini, M. A.; Barnes, A. B.; Rosay, M.; Maas, W. E.; Griffin, R. G. Dynamic nuclear polarization-enhanced solid-state NMR spectroscopy of GNNQQNY nanocrystals and amyloid fibrils. *Phys. Chem. Chem. Phys.* **2010**, *12*, 5911. DOI: 10.1039/c003661g
- [35] Van der Wel, P. C. A.; Hu, K.-N.; Lewandowski, J.; Griffin, R. G. Dynamic Nuclear Polarization of Amyloidogenic Peptide Nanocrystals: GNNQQNY, a Core Segment of the Yeast Prion Protein Sup35p. *J. Am. Chem. Soc.* **2006**, *128*, 10840. DOI: 10.1021/ja0626685

- [36] Bayro, M. J.; Debelouchina, G. T.; Eddy, M. T.; Birkett, N. R.; MacPhee, C. E.; Rosay, M.; Maas, W. E.; Dobson, C. M.; Griffin, R. G. Intermolecular Structure Determination of Amyloid Fibrils with Magic-Angle Spinning and Dynamic Nuclear Polarization NMR. *J. Am. Chem. Soc.* **2011**, *133*, 13967. DOI: 10.1021/ja203756x
- [37] Lelli, M.; Gajan, D.; Lesage, A.; Caporini, M. A.; Vitzthum, V.; Mieville, P.; Heroguel, F.; Rascon, F.; Roussey, A.; Thieuleux, C.; Boualleg, M.; Veyre, L.; Bodenhausen, G.; Coperet, C.; Emsley, L. Fast Characterization of Functionalized Silica Materials by Silicon-29 Surface-Enhanced NMR Spectroscopy Using Dynamic Nuclear Polarization. *J. Am. Chem. Soc.* **2011**, *133*, 2104. DOI: 10.1021/ja110791d
- [38] Lesage, A.; Lelli, M.; Gajan, D.; Caporini, M. A.; Vitzthum, V.; Mieville, P.; Alauzun, J.; Roussey, A.; Thieuleux, C.; Mehdi, A.; Bodenhausen, G.; Coperet, C.; Emsley, L. Surface Enhanced NMR Spectroscopy by Dynamic Nuclear Polarization. *J. Am. Chem. Soc.* **2010**, *132*, 15459. DOI: 10.1021/ja104771z
- [39] Maly, T.; Andreas, L. B.; Smith, A. A.; Griffin, R. G. 2H-DNP-enhanced 2H-13C solid-state NMR correlation spectroscopy. *Phys. Chem. Chem. Phys.* **2010**, *12*, 5872. DOI: 10.1039/c003705b
- [40] Vitzthum, V.; Caporini, M. A.; Bodenhausen, G. Solid-state nitrogen-14 nuclear magnetic resonance enhanced by dynamic nuclear polarization using a gyrotron. *J. Magn. Reson.* **2010**, *205*, 177. DOI: 10.1016/j.jmr.2010.04.014
- [41] Vitzthum, V.; Mieville, P.; Carnevale, D.; Caporini, M. A.; Gajan, D.; Coperet, C.; Lelli, M.; Zagdoun, A.; Rossini, A. J.; Lesage, A.; Emsley, L.; Bodenhausen, G. Dynamic nuclear polarization of quadrupolar nuclei using cross polarization from protons: surface-enhanced aluminium-27 NMR. *Chem. Commun.* **2012**, *48*, 1988. DOI: 10.1039/c2cc15905h
- [42] Larsen, F. H.; Jakobsen, H. J.; Ellis, P. D.; Nielsen, N. C. Sensitivity-Enhanced Quadrupolar-Echo NMR of Half-Integer Quadrupolar Nuclei. Magnitudes and Relative Orientation of Chemical Shielding and Quadrupolar Coupling Tensors. *J. Phys. Chem. A* **1997**, *101*, 8597. DOI: 10.1021/jp971547b
- [43] Larsen, F. H.; Jakobsen, H. J.; Ellis, P. D.; Nielsen, N. C. QCPMG-MAS NMR of half-integer quadrupolar nuclei. *J. Magn. Reson.* **1998**, *131*, 144. DOI: 10.1006/jmre.1997.1341
- [44] Larsen, F. H.; Jakobsen, H. J.; Ellis, P. D.; Nielsen, N. C. High-field QCPMG-MAS NMR of half-integer quadrupolar nuclei with large quadrupole couplings. *Mol. Phys.* **1998**, *95*, 1185. DOI: 10.1080/00268979809483250
- [45] Meiboom, S.; Gill, D. Modified spin-echo method for measuring nuclear relaxation times. *Rev. Sci. Instrum.* **1958**, *29*, 688. DOI: 10.1063/1.1716296
- [46] Carr, H. Y.; Purcell, E. M. Effects of diffusion on free precession in nuclear magnetic resonance experiments. *Phys. Rev.* **1954**, *94*, 630. DOI: 10.1103/PhysRev.94.630
- [47] Kaplan, D. E.; Hahn, E. L. Double irradiation experiments in magnetic resonance by the impulse method. *J. Phys. Radium* **1958**, *19*, 821. DOI: 10.1051/jphysrad:019580019011082100

- [48] Lang, D. V.; Boyce, J. B.; Lo, D. C.; Slichter, C. P. Measurement of electron spin density near cobalt atoms in copper. *Phys. Rev. Lett.* **1972**, *29*, 776. DOI: 10.1103/PhysRevLett.29.776
- [49] Caravatti, P.; Bodenhausen, G.; Ernst, R. R. Heteronuclear solid-state correlation spectroscopy. *Chem. Phys. Lett.* **1982**, *89*, 363. DOI: 10.1016/0009-2614(82)80001-8
- [50] Caravatti, P.; Braunschweiler, L.; Ernst, R. R. Heteronuclear correlation spectroscopy in rotating solids. *Chem. Phys. Lett.* **1983**, *100*, 305. DOI: 10.1016/0009-2614(83)80276-0
- [51] Abragam, A. *The principles of nuclear magnetism*; Clarendon Press: Oxford, 1961.
- [52] Slichter, C. P.; Fulde, P. *Principles of Magnetic Resonance*; Originally published by Harper and Row Publishers, New York, 1963, 3rd enlarged and updated 1990. Corr. 3rd printing ed.; Springer, 1996; Vol. 1.
- [53] Wasylishen, R. E.; Ashbrook, S. E.; Wimperis, S. *NMR of quadrupolar nuclei in solid materials*; Wiley: Chichester, West Sussex, 2012.
- [54] Bak, M.; Rasmussen, J. T.; Nielsen, N. C. SIMPSON. A general simulation program for solid-state NMR spectroscopy. *J. Magn. Reson.* **2000**, *147*, 296. DOI: 10.1006/jmre.2000.2179
- [55] Spiess, H. W.; Garrett, B. B.; Sheline, R. K.; Rabideau, S. W. Oxygen-17 quadrupole coupling parameters for water in its various phases. *J. Chem. Phys.* **1969**, *51*, 1201. DOI: 10.1063/1.1672122
- [56] Ernst, M. Heteronuclear spin decoupling in solid-state NMR under magic-angle sample spinning. *J. Magn. Reson.* **2003**, *162*, 1. DOI: 10.1016/S1090-7807(03)00074-0
- [57] Bayro, M. J.; Ramachandran, R.; Caporini, M. A.; Eddy, M. T.; Griffin, R. G. Radio frequency-driven recoupling at high magic-angle spinning frequencies: Homonuclear recoupling sans heteronuclear decoupling. *J. Chem. Phys.* **2008**, *128*, 052321/1. DOI: 10.1063/1.2834736
- [58] De Paepe, G.; Lewandowski, J. R.; Griffin, R. G. Spin dynamics in the modulation frame: Application to homonuclear recoupling in magic angle spinning solid-state NMR. *J. Chem. Phys.* **2008**, *128*, 124503. DOI: 10.1063/1.2834732
- [59] Jerschow, A. From nuclear structure to the quadrupolar NMR interaction and high-resolution spectroscopy. *Prog. Nucl. Magn. Reson. Spectrosc.* **2005**, *46*, 63. DOI: 10.1016/j.pnmrs.2004.12.001
- [60] Sachleben, J. R.; Frydman, V.; Frydman, L. Dipolar Determinations in Solids by Relaxation-Assisted NMR Recoupling. *J. Am. Chem. Soc.* **1996**, *118*, 9786. DOI: 10.1021/ja961636m
- [61] Widdifield, C. M.; Bryce, D. L. Solid-State ⁷⁹/⁸¹Br NMR and Gauge-Including Projector-Augmented Wave Study of Structure, Symmetry, and Hydration State in Alkaline Earth Metal Bromides. *J. Phys. Chem. A* **2010**, *114*, 2102. DOI: 10.1021/jp909106j
- [62] Bilalbegovic, G. Nuclear Magnetic Resonance Parameters of Water Hexamers. *J. Phys. Chem. A* **2010**, *114*, 715. DOI: 10.1021/jp9075614

- [63] Fortes, A. D.; Wood, I. G.; Grigoriev, D.; Alfredsson, M.; Kipfstuhl, S.; Knight, K. S.; Smith, R. I. No evidence for large-scale proton ordering in Antarctic ice from powder neutron diffraction. *J. Chem. Phys.* **2004**, *120*, 11376. DOI: 10.1063/1.1765099
- [64] Kuhs, W. F.; Lehmann, M. S. Bond-lengths, bond angles and transition barrier in ice Ih by neutron scattering. *Nature* **1981**, *294*, 432. DOI: 10.1038/294432a0
- [65] van Beek, J. D.; Dupree, R.; Levitt, M. H. Symmetry-based recoupling of ^{17}O - ^1H spin pairs in magic-angle spinning NMR. *J. Magn. Reson.* **2006**, *179*, 38. DOI: 10.1016/j.jmr.2005.11.003
- [66] van Eck, E. R. H.; Smith, M. E. Orientation of the quadrupole and dipole tensors of hydroxyl groups by ^{17}O quadrupole separated local field NMR. *J. Chem. Phys.* **1998**, *108*, 5904. DOI: 10.1063/1.476001

Program 4. SIMMOL Setup File Water.mol for Water.spinsys

```
set machine0 1e-8
set eye {{1 0 0} {0 1 0} {0 0 1}}
set bondshort 0.5
set spinsyssize 3
set Ai 0
set Bi 1
set Ci 2

set filename "water"
set buf1 1
set buf2 2
set m [mload $filename.pdb]

msetooglfile $m "$filename.oogl"
msetspinsysfile $m ${filename}.spinsys -numbered

set atoms [mselect $m $buf1 atom *]
mselect $m $buf1 atom {1..3}
mdipole $m $buf1 $buf1 OAA 400Hz

set atoms_O [mselect $m $buf2 atom O*]

mclosespinsysfile $m -keep
mclosespinsysfile $m

mselect $m $buf2 atom {1..5}
set pos [mposition $m [list $buf2]]
puts $pos

#define 3-atom basis for the local coordinate system
set basis [list [lindex $pos $Ai] [lindex $pos $Bi] [lindex $pos $Ci]]
puts $basis

#translate the coordinate system and place the first atom at the origin
set dxyz [lindex $basis 0]
mtranslate $m $dxyz
set pos [mposition $m [list $buf2]]
set basis [list [lindex $pos $Ai] [lindex $pos $Bi] [lindex $pos $Ci]]

#calculate the matrix for a z rotation and place the second atom in xz plane
set v2 [lindex $basis 1]
set x2 [lindex $v2 0]
set y2 [lindex $v2 1]
set z2 [lindex $v2 2]
set r2xy [expr sqrt($x2*$x2+$y2*$y2)]
set r2 [expr sqrt($r2xy*$r2xy+$z2*$z2)]

if { $r2xy < $machine0 } {
  set r2xy 0
  set v22xz $eye
} else {
  set v22xz [list [list [expr $x2/$r2xy] [expr $y2/$r2xy] 0] \
```

```

                [list [expr  $-\$y2/\$r2xy$ ] [expr  $\$x2/\$r2xy$ ] 0] \
                [list 0 0 1] \
            ]
        }

#calculate the matrix for a y rotation and
#place the second atom on the positive x axis
if {  $\$r2 < \$machine0$  } {
    puts "The bond between the atom 1 and atom 2 is too short."
    exit
} else {
    set v22x [list [list [expr  $\$r2xy/\$r2$ ] 0 [expr  $\$z2/\$r2$ ]] \
                 [list 0 1 0] \
                 [list [expr  $-\$z2/\$r2$ ] 0 [expr  $\$r2xy/\$r2$ ]] \
            ]
}

#calculate the matrix for a x rotation and
#place the third atom on positive y-x plane
set v3 [mmath  $\$v22x * [mmath \$v22xz * [lindex \$basis 2]]]$ 
set y3 [lindex  $\$v3 1$ ]
set z3 [lindex  $\$v3 2$ ]
set r3yz [expr sqrt( $\$y3*\$y3+\$z3*\$z3$ )]

if {  $\$r3yz < \$machine0$  } {
    set r3yz 0
    set v32xy  $\$eye$ 
} else {
    set v32xy [list [list 1 0 0] \
                   [list 0 [expr  $\$y3/\$r3yz$ ] [expr  $\$z3/\$r3yz$ ]] \
                   [list 0 [expr  $-\$z3/\$r3yz$ ] [expr  $\$y3/\$r3yz$ ]] \
            ]
}

set coordsys [mmath  $\$v32xy * [mmath \$v22x * \$v22xz]$ ]
puts  $\$coordsys$ 

for {set i 0} { $\$i < \$spinsysize$ } {incr i} {
    set spincoords( $\$i$ ) [mmath  $\$coordsys * [lindex \$pos \$i]$ ]
    puts  $\$spincoords(\$i)$ 
}

munload  $\$m$ 

#Add initial parameters to the spinsysfile
set spinsysfile [open " $\${filename}.spinsys$ " r+]
set atom_i [lindex [lindex  $\$atoms_0 0$ ] 0]

seek  $\$spinsysfile -1 end$ 
puts  $\$spinsysfile " quadrupole \$atom_i 2 6.5e6 0.97 0 0 0"$ 
puts  $\$spinsysfile " shift 1 0 0p 1 0 0 0"$ 
puts  $\$spinsysfile " shift 2 0 0p 1 0 0 0"$ 
puts  $\$spinsysfile " shift 3 0 0p 1 0 0 0"$ 
puts  $\$spinsysfile "}"$  nonewline

puts  $\$spinsysfile "\n"$ 

```

```

puts $spinsysfile "proc siminit {} {"
puts $spinsysfile "  global spincoords\n"
for {set i 0} {$i < $spinsysfile} {incr i} {
  puts $spinsysfile \x20\x20[list set spincoords($i) $spincoords($i)]
}
puts $spinsysfile "}"
puts $spinsysfile "siminit"

flush $spinsysfile
close $spinsysfile

```

Program 5. Water.spinsys

```

spinsys {
#      1      2      3
#      101    2H1    3H2
#
  channels 170 1H
  nuclei   170 1H 1H
  dipole 1 2 16289.8 0 180 -90
  dipole 1 3 15986 0 70.917 -90
  dipole 2 3 -27523 0 35.587 -90
  quadrupole 1 2 6.7e6 0.97 0 0 0
  shift 1 0 0p 1 0 0 0
  shift 2 0 0p 1 0 0 0
  shift 3 0 0p 1 0 0 0
}

proc siminit {} {
  global spincoords

  set spincoords(0) {0 0 0}
  set spincoords(1) {1 0 0}
  set spincoords(2) {-0.329 0.951 0}
}
siminit

```


5. Efficient, Balanced, Transmission Line RF Circuits by Back Propagation of Common Impedance Nodes

Adapted from references [1-2].

Abstract

We present a new, efficient strategy for designing fully balanced transmission line RF circuits for MAS NMR probes based on back propagation of a common impedance node (BPCIN). In this approach, the impedance node phenomenon is the sole means of achieving mutual RF isolation and balance in all RF channels. BPCIN is illustrated using a custom double resonance 3.2 mm MAS probe operating at 500 MHz (^1H) and 125 MHz (^{13}C). When fully optimized, the probe is capable of producing high homogeneity ($810^\circ/90^\circ$ ratios of 86% and 89% for ^1H and ^{13}C , respectively) and high efficiency ($\gamma B_1 = 100$ kHz for ^1H and ^{13}C at 70 W and 180 W of RF input, respectively; up to 360 kHz for ^1H). The probe's performance is illustrated by 2D MAS correlation spectra of microcrystals of the tripeptide N-f-MLF-OH and hydrated amyloid fibrils of the protein PI3-SH3.

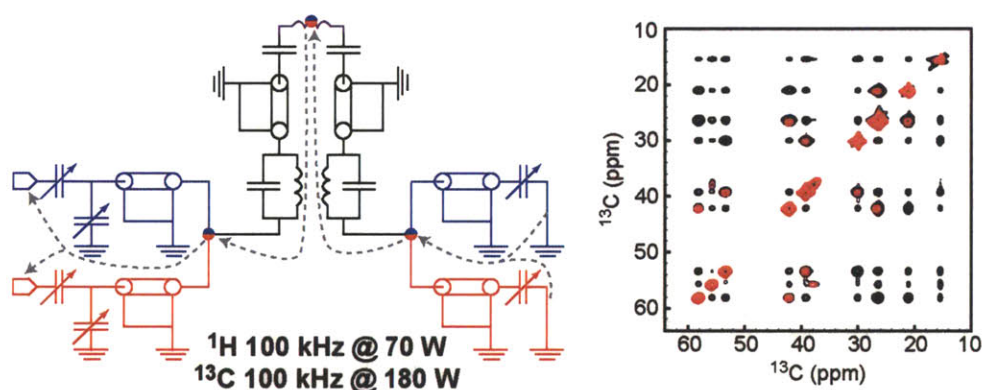


Figure 43. Back propagation of a common impedance node.

5.1. Introduction

Due to multiple advances in magic angle spinning (MAS) NMR in the last two decades, it is rapidly becoming accepted as a powerful and versatile tool for many fields and particularly structural biology [3-17]. These advances are the result of progress in both MAS methodology [3,9,18-19] and instrumentation [20-23].

Contemporary biological MAS applications set stringent, often contradictory, requirements for NMR probes, with the most important subsystem being the radio-frequency (RF) circuit. Critical features include RF efficiency, RF field homogeneity, and RF heating at high (^1H) and low (^{13}C and ^{15}N) frequencies, as well as the robustness and stability. In addition, advanced applications, such as cryogenic MAS and dynamic nuclear polarization (DNP) enhanced NMR, require that the probe RF circuit function over a wide range of temperatures [24-33].

A NMR probe circuit comprises a resonator, which houses the sample, and a tuning / matching network. Different types of commonly used NMR resonators, each having certain strengths and weaknesses, are reviewed elsewhere [20]. A suitable tuning / matching network not only tunes the resonator, but can also compensate for certain weaknesses.

Tuning / matching circuits may provide *common mode* (Figure 44a) or *balanced* (Figure 44b) input, with a balanced design providing a number of advantages over common mode design [34-37]. These include improved RF field homogeneity [34] and power efficiency [38]. While the former is generally important for multiple pulse and recoupling experiments [34], the latter is particularly crucial for experiments on biological samples, which are often sensitive to RF heating caused by ^1H decoupling. We have recently introduced a novel balanced transmission line RF circuit design [35-36,39]. Here we present results from a fully balanced $^{13}\text{C}/^1\text{H}$ transmission line probe and discuss the underlying theory of the circuit design.

5.2. RF circuit design and implementation

5.2.1. Circuit overview

The schematic in Figure 45a illustrates a double resonance, balanced RF circuit design, and Figure 45b shows a block diagram of the same circuit. The circuit can be divided into two parts connected to opposite ends of the solenoid resonator. The combination of the left “tuning / matching” side and the right “balun” side results in a completely balanced output to the sample coil (Figure 45b). On each side, individual RF channels are connected at common impedance nodes (green dots in Figure 45), which assure mutual isolation without insertion of lossy RF traps (as discussed below).

5.2.2. Circuit design based on impedance nodes

A key role of the tuning / matching network in a multi-channel RF circuit is to maximize channel independence and limit RF losses by means of isolation. Traditional isolation elements have included lumped RF traps [40], transmission line based RF traps [41-42] and their lumped analogs [43]. Sometime ago McKay et al. [44] used a ^1H im-

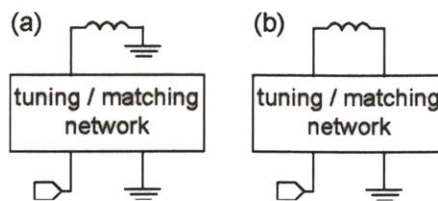


Figure 44. Schematic of a RF circuit with a common mode input (a) and balanced input (b).

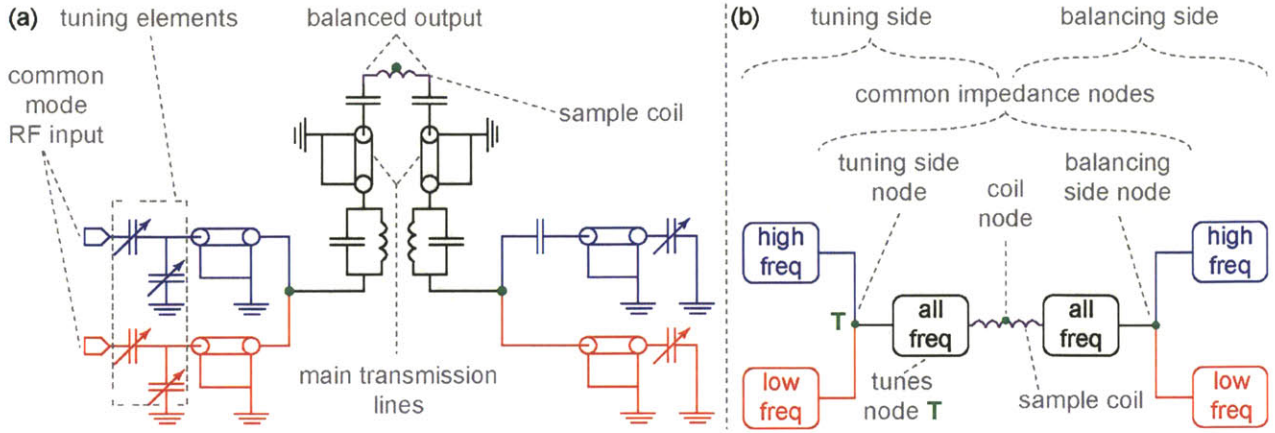


Figure 45. Simplified schematic (a) and block diagram (b) of a balanced double resonance RF circuit. Red and blue colors indicate two different working frequencies. Green dots indicate positions of common impedance nodes. Each impedance node is tuned by a circuit section that is further along the electrical pathway (on the right) and propagates the signal through that section [36,39].

pedance node as an isolation element in a transmission line probe. Here we demonstrate that complete and efficient isolation between the RF channels can be achieved using impedance nodes as the only isolation elements.

Figure 46a shows a parallel combination of two impedance elements with impedance Z_p at the junction point

$$Z_p = \frac{Z_1 \cdot Z_2}{Z_1 + Z_2}, \quad (19)$$

The incoming signal (gray arrows in Figure 46a) will split at the junction point in proportion to the electrical admittance of the individual branches. If one of the elements in a parallel combination is a short (Figure 46b), the impedance at the junction point will also be zero and the incoming signal will flow exclusively through the shorted branch. Similarly, if one impedance element in a parallel combination is much smaller than the others (Figure 46c), then Equation (19) can be simplified as

$$Z_p = \frac{Z_1 \cdot Z_2}{Z_1 + Z_2} \approx \frac{Z_1 \cdot Z_2}{Z_1} = Z_2. \quad (20)$$

Although the incoming signal will split at the junction point, most of the signal will flow through the branch that has the smallest impedance.

If the incoming signal is an RF signal, it is possible to adjust (tune) the impedance of a branch such that the condition in Figure 46c is only fulfilled in a narrow frequency band (Figure 46d). In that case, the circuit will have an *impedance node* at the junction point at that frequency, i.e. a point at which impedance with respect to ground is very small at that frequency. For incoming signals within that band, the behavior of the circuit will be similar to that in Figure 46c, while for other frequencies it will be similar to that in Figure 46a. If the incoming signal is a superposition of several components with different frequencies, the circuit will behave with respect to each component as if it was the only component.

A branch that tunes an impedance node at a given frequency behaves like ground at that frequency. It is, thus, convenient to say that an *impedance node pulls the signal* (in the band to

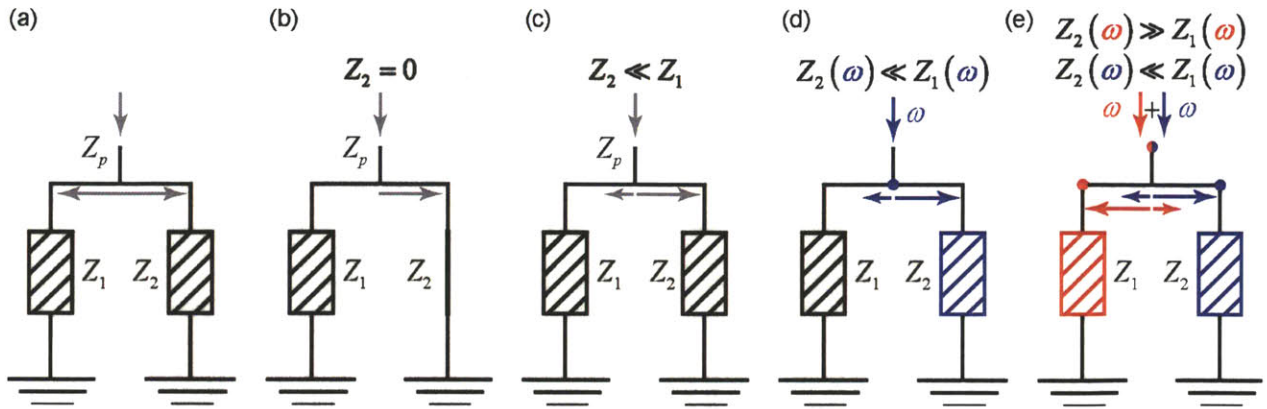


Figure 46. Mutual isolation of multiple RF channels by means of a common impedance node. The locations of impedance nodes are indicated with colored dots.

which the node is tuned) *through the corresponding tuned branch*. It is also possible to tune different branches to different frequencies. In that case, the junction point will have a *common impedance node*, i.e. a point where an impedance node occurs simultaneously at several different frequencies, and a composite signal will split at the junction point so that each component will predominantly flow through the branch tuned to that component (Figure 46e). Therefore, mutual isolation between the RF channels is achieved using impedance nodes only.

Isolation using impedance nodes has two major advantages over the schemes based on RF traps. First, a trap is typically designed to block entrance of a particular frequency into another channel. Since mutual isolation for each pair of channels must be achieved, for n channels $n(n-1)$ unwanted pathways must be blocked. For example, for a triple resonance probe, there exist at least $3 \times (3-1) = 6$ unwanted electrical pathways. Furthermore, the fact that traps usually affect tuning of all the channels makes it difficult to tune the circuit and establish isolation between the channels at the same time. In contrast, an impedance node prevents leakage of a particular frequency from its own channel to any other channels connected near that node. Thus, the number of unwanted pathways to be blocked is equal to the number of channels and is substantially fewer than in the trap-based design.

The second advantage is related to circuit performance. Due to its lossy nature as a resonator, a trap usually reduces the performance of the channel to which it is tuned, compared to a single resonance circuit. It also affects performance of any other signal flowing through it, although this penalty may be smaller than that for the blocked channel. Even though impedance nodes may not provide ideal isolation, the isolation is passive in the sense that it does not rely on additional lossy resonators. Therefore, the performance penalty for a circuit utilizing impedance nodes is smaller than the penalty for a trap-based circuit.

5.2.3. Back propagation of common impedance node

The overall strategy for building the circuit shown in Figure 45 involves “back propagation of the common impedance node” with several priorities.

First, we would like to balance the sample coil on all channels. It is known [36,38] that a balanced coil has an impedance node in the middle and vice versa. Therefore, if a common impedance node is set in the middle of the coil, the coil will be simultaneously balanced at all frequencies. In the present case, we balance the circuit by partially symmetrizing it as shown in Figure 2

Second, we would like to use another common impedance node for RF isolation, as discussed above. Thus, if we connect all channels to a common junction point and tune a simultaneous impedance node at that junction such that the node points towards the sample coil, electrical isolation between the channels will be achieved.

Finally, it follows from Figure 46 and Equation (20), that any branches connected to a circuit near an impedance node have only a small effect on the behavior of the circuit at the frequency to which the impedance node is tuned. In other words, in accordance with Equation (20), the impedance at the junction point is Z_2 and is independent of Z_1 . Accordingly, if a blue impedance node is set at the junction point in the circuit, the blue branch can be tuned with the red branch disconnected. Once the blue branch is tuned and the blue impedance node is set, the red branch can be connected to the blue impedance node with little effect on the node. This modularity is conveniently exploited in the “back propagation of common impedance node” procedure, as illustrated in Figure 47.

The RF signals enter the circuit through the RF ports (Figure 45a). The desired electrical path then goes through the sample coil and eventually ends at a corresponding ground point on the right. These target paths can be selected using the previously mentioned property of an impedance node. In order to achieve this goal, each of the three common impedance nodes in Figure 45 should be tuned by sections of the circuit that are further along the path. Therefore, we shall start tuning the circuit going from the end, i.e. from the ground points where the RF signals leave the circuit (Figure 47a), and traverse backward towards the RF input ports, while serially adjusting the intervening circuit sections.

Figure 47a shows the initial state of the circuit before tuning (in gray). The two rightmost sections can be tuned individually (as discussed above) until each presents an impedance node at its respective frequency. Then the two tuned sections can be connected together to form the first common impedance node on the balancing side (Figure 47b).

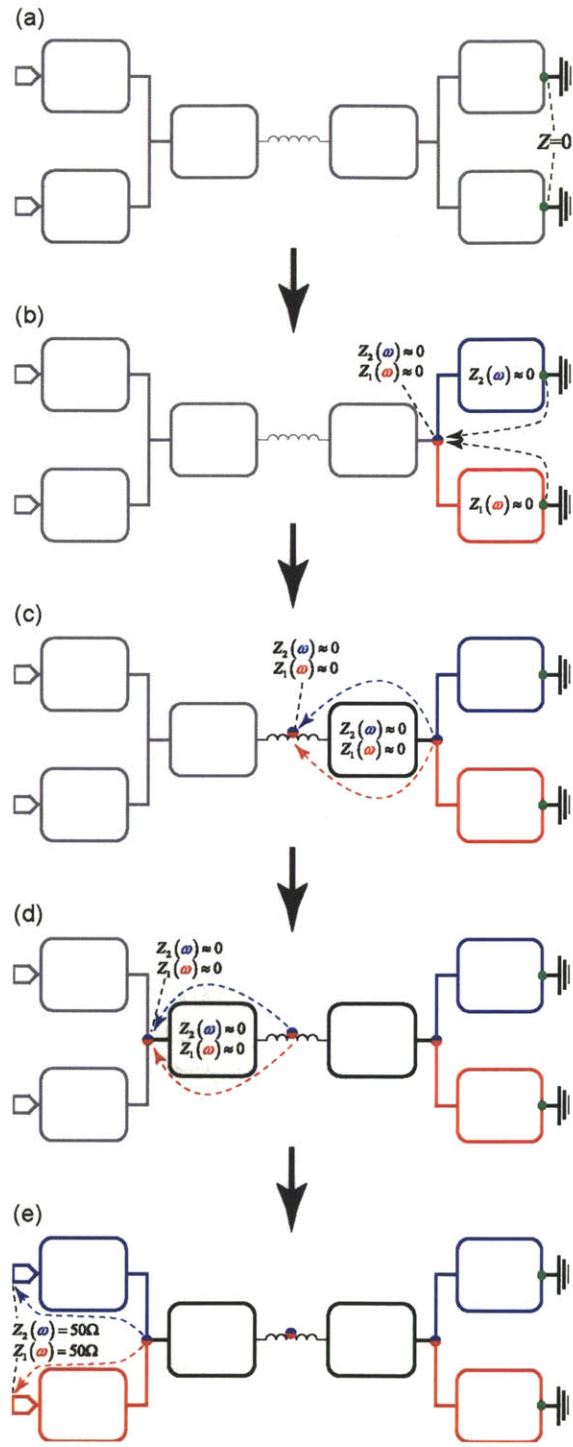


Figure 47. Stepwise propagation of common impedance nodes along the circuit. Gray color indicates circuit blocks that have not yet been tuned. Dots indicate locations of common impedance nodes for two frequencies (red and blue) and the ends of RF paths (green).

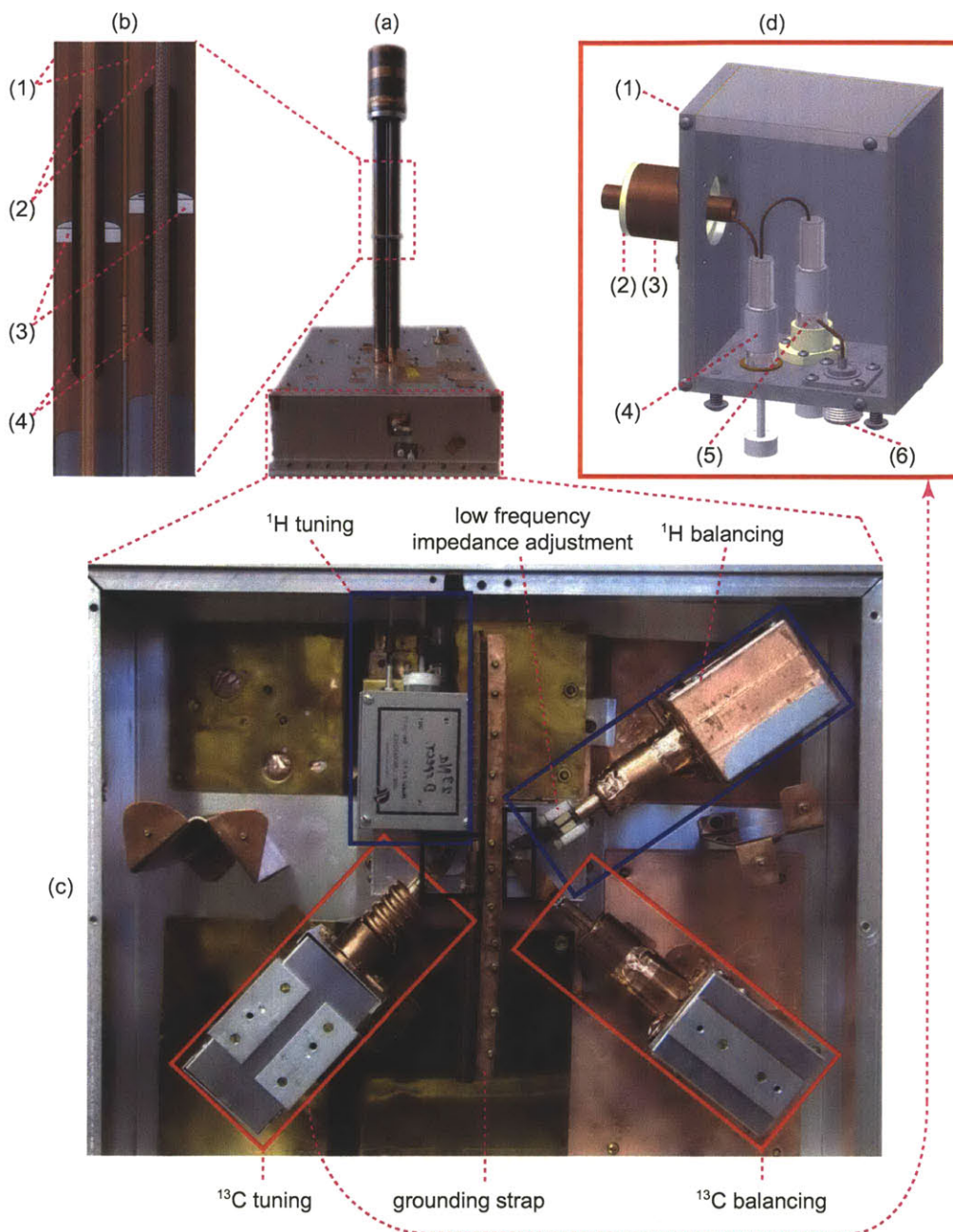


Figure 48. Implementation of ^1H (500 MHz), ^{13}C (125 MHz) fully balanced, transmission line probe. **a)** Photograph of the probe. **b)** 3D CAD cutaway view of a section of main coaxial transmission lines with (1) outer conductors, Cu tube, 2.858 cm (1.125”) O.D., (2) inner conductors, Cu, 0.953 cm (0.375”) O.D. and OFHC Cu, 0.635 cm (0.25”) O.D., (3) PTFE spacer, (4) large O.D. inner conductor (“sausage”), Cu, O.D. and length to be adjusted. **c)** Photograph of probe box with colored rectangles identifying parts corresponding to the colored blocks in Figure 45b. **d)** 3D CAD view of a tuning / matching module showing (1) aluminum casing, (2) PTFE spacer, (3) short coaxial transmission line, Cu tubes, 2.858 cm (1.125”) O.D. and 0.953 cm (0.375”) O.D., (4) variable tuning capacitor (Polyflon), (5) variable matching capacitor (Polyflon), (6) RF port. Original design and construction by Jianping Hu [36,39].

The next section (i.e., the preceding section along the RF pathway) is then connected to the previously tuned sections and can be adjusted until the next common impedance node, at the midpoint of the sample coil, is tuned (Figure 47c). This process is repeated to yield the state in Figure 47d. Finally, the remaining sections are connected and adjusted until the circuit can be tuned and matched to standard impedance (50 Ω) as shown in Figure 47e.

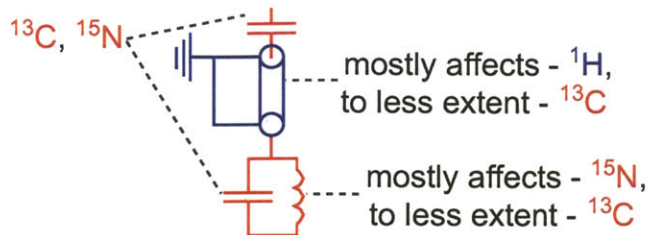


Figure 49. Schematic indicating the function of the tuning elements that form the common (black) blocks in Figure 45b.

The same elements are used in both double and triple resonance configurations.

5.2.4. Tuning elements

Each of the blocks in Figure 45b comprises several tuning elements. The symmetry of the overall circuit is such that the two common blocks (black rectangles in Figure 45b) are structurally identical (comprising the elements in Figure 49) and the four frequency specific blocks (colored rectangles in Figure 45b) are structurally similar (comprising the elements in Figure 48d).

Starting on the balancing side, the first blocks are balancing modules similar to the ones shown in Figure 48d, except that these balancing modules have a single variable capacitor connected to ground. These blocks tune the first common impedance node. The nodes are first roughly tuned by adjusting the length of the short transmission lines, and then fine-tuned by adjusting variable capacitors. As discussed below, short sections of transmission line may not transform the ^{13}C impedance efficiently. For this reason, the impedance of the ^1H module may not be sufficiently high at low frequencies and may need to be adjusted by adding chip capacitors.

The second section (black right rectangle in Figure 45b) consists of a coaxial transmission line, a parallel combination of an inductor and ATC chip capacitor in the probe box, and another chip capacitor at the probe top. This section tunes the second common impedance node in the middle of the coil ensuring that the coil is balanced. Since the impedance of this section must be adjusted at multiple frequencies (here, ^1H and ^{13}C), multiple tuning elements are generally necessary.

Commonly used tuning elements include lumped components, (i.e., capacitors and inductors) and distributed components, such as transmission lines. The effectiveness of these components is frequency dependent. Lumped elements are most efficient at low to medium frequencies, for which the impedance of inductors is not too high and the impedance of capacitors is not too small. At the same time, transmission lines are optimal impedance transformers when the wavelength of the signal approaches the length of the line. As a result, the behaviors of lumped and distributed circuit elements are largely complementary with respect to frequency, and their combination can be used to control all the frequencies as indicated in Figure 49. Specifically, a variable impedance transmission line is used to transform the ^1H impedance (Figure 48b). At the same time, the impedance Z of a parallel combination of an inductor L and a capacitor C is

$$Z = j \frac{1}{C} \frac{\omega}{\omega_0^2 - \omega^2},$$

where ω_0 is the resonant frequency. When frequency (ω) is lower than the resonant frequency (ω_0), Z is positive, i.e. inductive, and when frequency is above the resonant frequency, Z is nega-

tive, i.e. capacitive. Therefore, as long as ω_0 is lower than the ^{13}C frequency and higher than the ^{15}N frequency (in case of triple resonance circuit), the ^{13}C channel will be more affected by the capacitor while the ^{15}N channel will be more affected by the inductor.

Finally, tuning modules (Figure 48d and colored blocks on the left in Figure 45b), incorporating short sections of coaxial transmission lines and variable capacitors, transform the small node impedance to the standard $50\ \Omega$ real impedance. Further technical details are out of the scope of this communication and can be found elsewhere [36].

5.3. Experimental verification

The experimental implementation of the procedures outlined above was divided into several stages. The first stage was the fabrication of a double resonance ^1H and ^{13}C static NMR probe, with careful optimization of its circuit and static performance tests. The second stage was conversion of the static probe into a MAS probe with tests under MAS conditions. At this point we did not perform a full circuit optimization, since additional modifications of the probe will be necessary for future cryogenic experiments. Here we report results from the fully optimized static probe and initial MAS results.

5.3.1. Static optimized circuit

A custom double resonance ^1H (500 MHz) and ^{13}C (125 MHz) NMR probe using a 6-turn 3.2 mm solenoid coil and the novel electrical circuit [36,39] schematically represented in Figure 45 was designed, fabricated and tested on a custom 500 MHz (^1H) NMR spectrometer (courtesy Dr. David J. Ruben). An ETFE tube (3.2 mm O.D.) was center packed (20 μL) with $\text{U-}^{13}\text{C}$ -glycerol (100% ^{13}C). Figure 50 shows the results of nutation experiments and yields $810^\circ/90^\circ$ ratios of 86% for ^1H and 89% for ^{13}C , indicating ex-

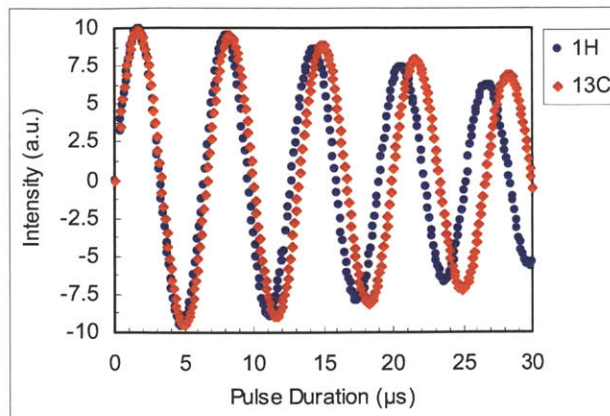


Figure 50. ^1H and ^{13}C nutation curves.

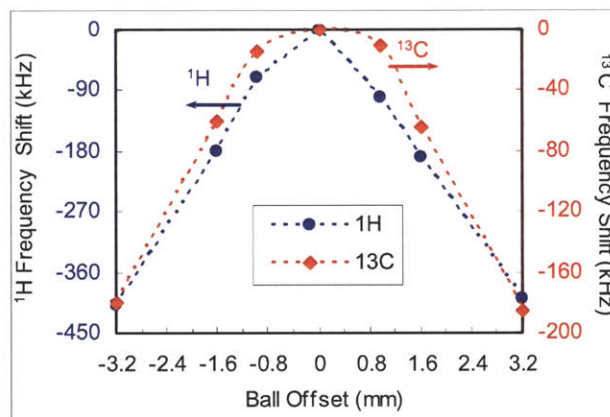


Figure 51. ^1H and ^{13}C balance ball shift test.

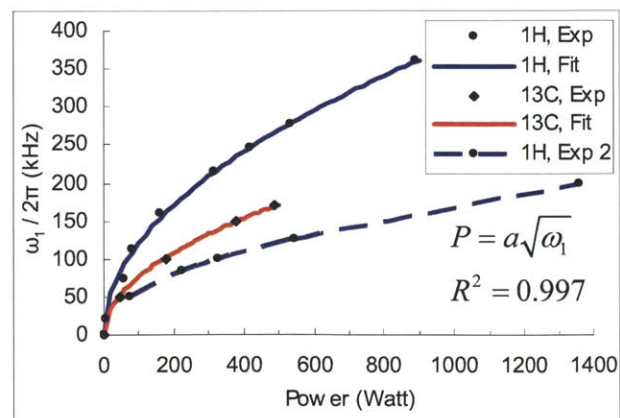


Figure 52. ^1H and ^{13}C γB_1 dependence on input RF power [36].

cellent homogeneity on both channels. The high quality of balance on both channels was also verified in profiles of the RF fields (Figure 51) obtained via a “ball shift test” [34,36,45-46]. This test was performed by accurately positioning a small brass ball (1.6 mm (0.0625”)) at different positions along the coil axis and recording resonant frequency shifts. Figure 51 confirms that both profiles are symmetric with a maximum at the center of the coil.

The probe demonstrated outstanding power performance. It generated $\gamma B_1 = 100$ kHz for ^1H and ^{13}C with just 70 W and 180 W of RF input, respectively. The probe also generated $\gamma B_1(^1\text{H}) = 360$ kHz at 890 W and handled prolonged irradiation on both channels simultaneously without arcing [36]. Figure 52 shows γB_1 vs. RF power dependences for both channels (the top two traces). The data conform well to the theoretical dependence [47].

Figure 52 also illustrates the results of two RF tests. The top blue trace corresponds to the best RF performance of the ^1H channel obtained after carefully optimizing the circuit for good balance (Figure 51) and ensuring that all components and connections had high mechanical and electrical quality. The bottom blue trace shows the result of an intermediate test. While the latter is comparable to performance of a commercial probe, the optimized circuit generates the same $\gamma B_1(^1\text{H})$ using 4-fold less RF power. Although the efficiency of the ^{13}C channel (data not shown) was also better for the optimized circuit, the improvement was substantially smaller than for ^1H channel.

5.3.2. MAS tests

The initial performance of the probe equipped with a MAS stator was found to be comparable to that of the static probe. The power levels decreased slightly, due to the fact that the sample coil in the MAS stator is inclined at the magic angle with respect to the static field, as opposed to 90° in the case of a static probe. In order to evaluate the robustness and long-term stability of the probe, we acquired 2D correlation spectra for a model microcrystalline peptide and a hydrated protein.

The peptide, N-formyl-[U- ^{13}C , ^{15}N]-Met-Leu-Phe-OH (N-f-MLF-OH) was prepared as described previously [48] and used for testing MAS stability and the performance of multi-pulse ^1H decoupling and ^{13}C dipolar recoupling. Stable spinning at 12.5 kHz (± 5 Hz) was maintained throughout the experiments (six days). Figure 53a shows 2D ^{13}C - ^{13}C correlation spectra of N-f-MLF-OH using RFDR recoupling in a broadband fashion [49-52]. Recoupling times of 1.3 ms and 9.3 ms were used for one-bond (red) and multi-bond (black) correlations, respectively. The 1D cross polarization (CP) spectrum of MLF (data not shown) indicates a ^{13}C linewidth of 24 Hz for the methyl carbon of Met C δ at 14.0 ppm (referenced to TMS), suggesting efficient ^1H TPPM decoupling [53]. The one-bond correlation spectrum contains well-resolved cross peaks of directly bonded carbon spins, indicating the high efficiency of the RFDR mixing scheme. At a longer mixing time of 9.3 ms, multi-bond intra- and inter-residue correlations appear, indicating consistently efficient ^1H decoupling.

To further test the probe performance for hydrated protein samples, a 2D one-bond RFDR experiment (Fig. 53b) was carried out using a PI3-SH3 fibril sample. 50% hydration (w/w) was achieved by using a 60/40 (w/w) mixture of *d5*-glycerol and buffer (pH = 2.0). The line width is 0.5-0.8 ppm (62.5-100 Hz). The single set of chemical shifts and excellent linewidth reveal the high degree of sample homogeneity. Overall, the spectrum compares favorably with our previous studies of PI3-SH3 [54], in terms of the number of cross peaks, resolution, intensities and linewidths, suggesting efficient recoupling and strong circuit performance.

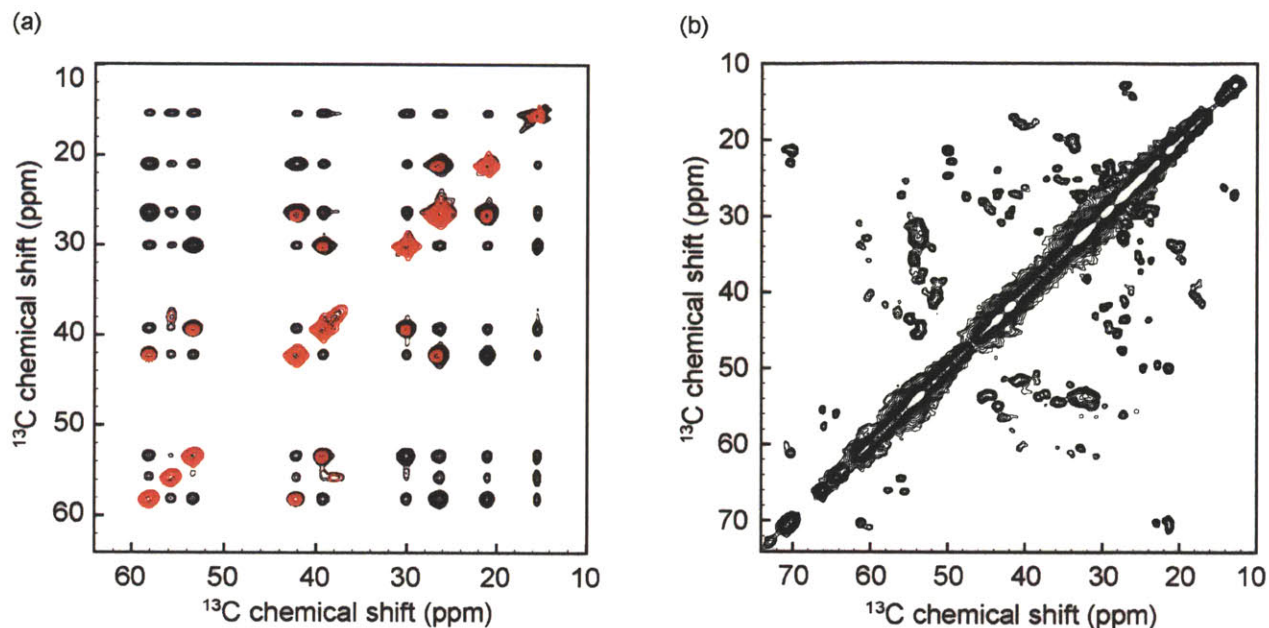


Figure 53. Broadband RFDR spectra of uniformly ^{13}C and ^{15}N labeled peptide and protein samples. **a)** N-f-MLF and **b)** PI3-SH3 fibrils. All spectra were acquired at $\omega_r/2\pi = 12.5$ kHz MAS frequency and at room temperature. A rotor-synchronized 33 kHz ^{13}C π -pulses were used during the RFDR [49-52] mixing period in all experiments. The ^1H TPPM [53] decoupling field of 100 kHz was applied during mixing and acquisition periods.

5.4. Conclusions and Outlook

We presented an efficient new strategy for designing fully balanced transmission line RF circuits for MAS probes based on back propagation of common impedance nodes. This strategy was illustrated using a custom double resonance (^1H , ^{13}C) 3.2 mm NMR probe. With high quality implementation, BPCIN yielded a RF circuit that demonstrated outstanding RF field characteristics (810°/90° ratios of 86% for ^1H and 89% for ^{13}C ; $\gamma B_1 = 100$ kHz for ^1H and ^{13}C at 70 W and 180 W of RF input, respectively, and up to 360 kHz for ^1H). 2D MAS correlation spectra confirmed the robust performance of the probe, which is critical for long-term signal averaging in studies of biological samples. A triple resonance probe based on the same design is under construction. Some additional theoretical aspects pertaining to the observed performance of the circuit will be discussed forthcoming publication (Markhasin et al., manuscript in preparation).

Acknowledgments

This research was supported by the National Institutes of Health through grants EB003151, EB002026, EB001960, and EB001035. We thank Michael Mullins and Ajay Thakkar, for crucial assistance with construction of the probe.

References

- [1] Markhasin, E.; Hu, J.; Su, Y.; Herzfeld, J.; Griffin, R. G. Efficient balanced transmission line RF circuits by back propagation of common impedance nodes. *Submitted manuscript*
- [2] Markhasin, E.; Barnes, A. B.; Hu, J.; Herzfeld, J.; Griffin, R. G. In *Balanced Triple Resonance Probe for Cryogenic MAS NMR and Dynamic Nuclear Polarization at 700 MHz*. WWMR2010. Joint EUROMAR 2010 and 17th ISMAR Conference, Florence, Italy, July 4-9, 2010. (oral presentation and poster)
- [3] Renault, M.; Cukkemane, A.; Baldus, M. Solid-State NMR Spectroscopy on Complex Biomolecules. *Angew. Chem., Int. Ed.* **2010**, *49*, 8346. DOI: 10.1002/anie.201002823
- [4] Lesage, A. Recent advances in solid-state NMR spectroscopy of spin $I = 1/2$ nuclei. *Phys. Chem. Chem. Phys.* **2009**, *11*, 6876. DOI: 10.1039/b907733m
- [5] Andronesi, O. C.; von Bergen, M.; Biernat, J.; Seidel, K.; Griesinger, C.; Mandelkow, E.; Baldus, M. Characterization of Alzheimer's-like Paired Helical Filaments from the Core Domain of Tau Protein Using Solid-State NMR Spectroscopy. *J. Am. Chem. Soc.* **2008**, *130*, 5922. DOI: 10.1021/ja7100517
- [6] Etzkorn, M.; Boeckmann, A.; Lange, A.; Baldus, M. Probing Molecular Interfaces Using 2D Magic-Angle-Spinning NMR on Protein Mixtures with Different Uniform Labeling. *J. Am. Chem. Soc.* **2004**, *126*, 14746. DOI: 10.1021/ja0479181
- [7] Lange, A.; Becker, S.; Seidel, K.; Giller, K.; Pongs, O.; Baldus, M. A concept for rapid protein-structure determination by solid-state NMR spectroscopy. *Angew. Chem., Int. Ed.* **2005**, *44*, 2089. DOI: 10.1002/anie.200462516
- [8] Cady, S. D.; Schmidt-Rohr, K.; Wang, J.; Soto, C. S.; De Grado, W. F.; Hong, M. Structure of the amantadine binding site of influenza M2 proton channels in lipid bilayers. *Nature* **2010**, *463*, 689. DOI: 10.1038/nature08722
- [9] Griffin, R. G. Dipolar recoupling in MAS spectra of biological solids. *Nat. Struct. Biol.* **1998**, *5*, 508. DOI: 10.1038/749
- [10] Mak-Jurkauskas, M. L.; Bajaj, V. S.; Hornstein, M. K.; Belenky, M.; Griffin, R. G.; Herzfeld, J. Energy transformations early in the bacteriorhodopsin photocycle revealed by DNP-enhanced solid-state NMR. *Proc. Natl. Acad. Sci. U.S.A.* **2008**, *105*, 883. DOI: 10.1073/pnas.0706156105
- [11] Castellani, F.; van Rossum, B.-J.; Diehl, A.; Rehbein, K.; Oschkinat, H. Determination of solid-state NMR structures of proteins by means of three-dimensional ^{15}N - ^{13}C - ^{13}C dipolar correlation spectroscopy and chemical shift analysis. *Biochemistry* **2003**, *42*, 11476. DOI: 10.1021/bi034903r S0006-2960(03)04903-1
- [12] Hong, M.; Su, Y. Structure and dynamics of cationic membrane peptides and proteins: insights from solid-state NMR. *Protein Sci.* **2011**, *20*, 641. DOI: 10.1002/pro.600
- [13] Brown, S. P.; Spiess, H. W. Advanced solid-state NMR methods for the elucidation of structure and dynamics of molecular, macromolecular, and supramolecular systems. *Chem. Rev.* **2001**, *101*, 4125. DOI: 10.1021/cr990132e

- [14] Ladizhansky, V. Dipolar-Based Torsion Angle Measurements for Protein Structure Determination. In *Encyclopedia of Magnetic Resonance*; John Wiley & Sons, Ltd: 2007. DOI: 10.1002/9780470034590.emrstml153
- [15] De Paepe, G.; Lewandowski, J. R.; Loquet, A.; Boeckmann, A.; Griffin, R. G. Proton assisted recoupling and protein structure determination. *J. Chem. Phys.* **2008**, *129*, 245101/1. DOI: 10.1063/1.3036928
- [16] Barnes, A. B.; Andreas, L. B.; Huber, M.; Ramachandran, R.; van der Wel, P. C. A.; Veshkort, M.; Griffin, R. G.; Mehta, M. A. High-resolution solid-state NMR structure of Alanyl-Prolyl-Glycine. *J. Magn. Reson.* **2009**, *200*, 95. DOI: 10.1016/j.jmr.2009.06.009
- [17] Van der Wel, P. C. A.; Lewandowski, J. R.; Griffin, R. G. Solid-State NMR Study of Amyloid Nanocrystals and Fibrils Formed by the Peptide GNNQQNY from Yeast Prion Protein Sup35p. *J. Am. Chem. Soc.* **2007**, *129*, 5117. DOI: 10.1021/ja068633m
- [18] Tycko, R. Biomolecular solid state NMR: advances in structural methodology and applications to peptide and protein fibrils. *Annu. Rev. Phys. Chem.* **2001**, *52*, 575. DOI: 10.1146/annurev.physchem.52.1.575
- [19] Frydman, L. Spin-1/2 and beyond. A perspective in solid state NMR spectroscopy. *Annu. Rev. Phys. Chem.* **2001**, *52*, 463. DOI: 10.1146/annurev.physchem.52.1.463
- [20] Grant Christopher, V.; Wu Chin, H.; Opella Stanley, J. Probes for high field solid-state NMR of lossy biological samples. *J. Magn. Reson.* **2010**, *204*, 180. DOI: 10.1016/j.jmr.2010.03.011
- [21] McKay, R. A. Probes for Special Purposes. In *Encyclopedia of Magnetic Resonance*; John Wiley & Sons, Ltd: 2007. DOI: 10.1002/9780470034590.emrstm0416
- [22] Schaefer, J.; McKay, R. A. Multi-tuned single coil transmission line probe for nuclear magnetic resonance spectrometer. Patent #5861748, 1999.
- [23] Gor'kov, P. L.; Brey, W. W.; Long, J. R. Probe Development for Biosolids NMR Spectroscopy. In *Encyclopedia of Magnetic Resonance*; John Wiley & Sons, Ltd: 2007. DOI: 10.1002/9780470034590.emrstm1149
- [24] Barnes, A. B.; Mak-Jurkauskas, M. L.; Markhasin, E.; Hu, J.; Matsuki, Y.; Lugtenburg, J.; Herzfeld, J.; Griffin, R. G. In *Instrumentation for Cryogenic MAS and High-Field Dynamic Nuclear Polarization*. Magnetic Resonance Gordon Research Conference, University of New England, Biddeford, ME, June 14-19, 2009.
- [25] Barnes, A. B.; Markhasin, E.; Daviso, E.; Michaelis, V. K.; Nanni, E. A.; Jawla, S. K.; Mena, E. L.; DeRocher, R.; Thakkar, A.; Woskov, P. P.; Herzfeld, J.; Temkin, R. J.; Griffin, R. G. Dynamic Nuclear Polarization at 700 MHz / 460 GHz. *J. Magn. Reson.* **2012**, *224*, 1. DOI: 10.1016/j.jmr.2012.08.002
- [26] Barnes, A. B.; Mak-Jurkauskas, M. L.; Matsuki, Y.; Bajaj, V. S.; van der Wel, P. C. A.; De Rocher, R.; Bryant, J.; Sirigiri, J. R.; Temkin, R. J.; Lugtenburg, J.; Herzfeld, J.; Griffin, R. G. Cryogenic sample exchange NMR probe for magic angle spinning dynamic nuclear polarization. *J. Magn. Reson.* **2009**, *198*, 261. DOI: 10.1016/j.jmr.2009.03.003
- [27] Barnes, A. B.; De Paepe, G.; van der Wel, P. C. A.; Hu, K. N.; Joo, C. G.; Bajaj, V. S.; Mak-Jurkauskas, M. L.; Sirigiri, J. R.; Herzfeld, J.; Temkin, R. J.; Griffin, R. G. High-

- field dynamic nuclear polarization for solid and solution biological NMR. *Appl. Magn. Reson.* **2008**, *34*, 237. DOI: 10.1007/s00723-008-0129-1
- [28] Van der Wel, P. C. A.; Hu, K.-N.; Lewandowski, J.; Griffin, R. G. Dynamic Nuclear Polarization of Amyloidogenic Peptide Nanocrystals: GNNQQNY, a Core Segment of the Yeast Prion Protein Sup35p. *J. Am. Chem. Soc.* **2006**, *128*, 10840. DOI: 10.1021/ja0626685
- [29] Maly, T.; Debelouchina, G. T.; Bajaj, V. S.; Hu, K.-N.; Joo, C.-G.; Mak-Jurkauskas, M. L.; Sirigiri, J. R.; van der Wel, P. C. A.; Herzfeld, J.; Temkin, R. J.; Griffin, R. G. Dynamic nuclear polarization at high magnetic fields. *J. Chem. Phys.* **2008**, *128*, 052211/1. DOI: 10.1063/1.2833582
- [30] Debelouchina, G. T.; Bayro, M. J.; van der Wel, P. C. A.; Caporini, M. A.; Barnes, A. B.; Rosay, M.; Maas, W. E.; Griffin, R. G. Dynamic nuclear polarization-enhanced solid-state NMR spectroscopy of GNNQQNY nanocrystals and amyloid fibrils. *Phys. Chem. Chem. Phys.* **2010**, *12*, 5911. DOI: 10.1039/c003661g
- [31] Bajaj, V. S.; van der Wel, P. C. A.; Griffin, R. G. Observation of a Low-Temperature, Dynamically Driven Structural Transition in a Polypeptide by Solid-State NMR Spectroscopy. *J. Am. Chem. Soc.* **2009**, *131*, 118. DOI: 10.1021/ja8045926
- [32] Lesage, A.; Lelli, M.; Gajan, D.; Caporini, M. A.; Vitzthum, V.; Mieville, P.; Alauzun, J.; Roussey, A.; Thieuleux, C.; Mehdi, A.; Bodenhausen, G.; Coperet, C.; Emsley, L. Surface Enhanced NMR Spectroscopy by Dynamic Nuclear Polarization. *J. Am. Chem. Soc.* **2010**, *132*, 15459. DOI: 10.1021/ja104771z
- [33] Vitzthum, V.; Mieville, P.; Carnevale, D.; Caporini, M. A.; Gajan, D.; Coperet, C.; Lelli, M.; Zagdoun, A.; Rossini, A. J.; Lesage, A.; Emsley, L.; Bodenhausen, G. Dynamic nuclear polarization of quadrupolar nuclei using cross polarization from protons: surface-enhanced aluminium-27 NMR. *Chem. Commun.* **2012**, *48*, 1988. DOI: 10.1039/c2cc15905h
- [34] Paulson, E. K.; Martin, R. W.; Zilm, K. W. Cross polarization, radio frequency field homogeneity, and circuit balancing in high field solid state NMR probes. *J. Magn. Reson.* **2004**, *171*, 314. DOI: 10.1016/j.jmr.2004.09.009
- [35] Hu, J.; Bielecki, A.; Griffin, R. G.; Herzfeld, J. In *A Totally Balanced, Fully Transmission Line, Triple Resonance NMR Probe for High Frequencies*. 49th ENC, Pacific Grove, California, 2008.
- [36] Hu, J. Balanced multi-resonant transmission line nuclear magnetic resonance probes. Ph.D. Thesis, Brandeis University, 2010. <http://search.proquest.com/docview/305185343>
- [37] Mispelter, J.; Lupu, M.; Briguet, A. *NMR probeheads for biophysical and biomedical experiments: theoretical principles & practical guidelines*; Imperial College Press; Distributed by World Scientific: London, Hackensack, NJ, 2006.
- [38] Engelke, F. Electromagnetic wave compression and radio frequency homogeneity in NMR solenoidal coils: Computational approach. *Concepts Magn. Reson.* **2002**, *15*, 129. DOI: 10.1002/cmr.10029

- [39] Hu, J.; Herzfeld, J. Baluns, a fine balance and impedance adjustment module, a multi-layer transmission line, and transmission line NMR probes using same. Patent #7936171, 2011.
- [40] Schnall, M. D.; Subramanian, V. H.; Leigh, J. S., Jr.; Chance, B. A new double-tuned probe for concurrent proton and phosphorus-31 NMR. *J. Magn. Reson.* **1985**, *65*, 122. DOI: 10.1016/0022-2364(85)90380-4
- [41] Stoll, M. E.; Vega, A. J.; Vaughn, R. W. Simple single-coil double resonance NMR probe for solid state studies. *Rev. Sci. Instrum.* **1977**, *48*, 800. DOI: 10.1063/1.1135159
- [42] Cross, V. R.; Hester, R. K.; Waugh, J. S. Single coil probe with transmission-line tuning for nuclear magnetic double resonance. *Rev. Sci. Instrum.* **1976**, *47*, 1486. DOI: 10.1063/1.1134560
- [43] Doty, F. D.; Inners, R. R.; Ellis, P. D. A multinuclear double-tuned probe for applications with solids or liquids utilizing lumped tuning elements. *J. Magn. Reson.* **1981**, *43*, 399. DOI: 10.1016/0022-2364(81)90051-2
- [44] McKay, R. A. Double-tuned single coil probe for nuclear magnetic resonance spectrometer. Patent #4446431, 1984.
- [45] Maier, J. L. C.; Slater, J. C. Field Strength Measurements in Resonant Cavities. *J. Appl. Phys.* **1952**, *23*, 68. DOI: 10.1063/1.1701980
- [46] Maier, J. L. C.; Slater, J. C. Determination of Field Strength in a Linear Accelerator Cavity. *J. Appl. Phys.* **1952**, *23*, 78. DOI: 10.1063/1.1701982
- [47] Doty, F. D. Probe Design and Construction. In *Encyclopedia of Magnetic Resonance*; John Wiley & Sons, Ltd: 2007. DOI: 10.1002/9780470034590.emrstm1000
- [48] Rienstra, C. M.; Tucker-Kellogg, L.; Jaroniec, C. P.; Hohwy, M.; Reif, B.; McMahon, M. T.; Tidor, B.; Lozano-Perez, T.; Griffin, R. G. De novo determination of peptide structure with solid-state magic-angle spinning NMR spectroscopy. *Proc. Natl. Acad. Sci. U.S.A.* **2002**, *99*, 10260. DOI: 10.1073/pnas.152346599
- [49] Bennett, A. E.; Ok, J. H.; Griffin, R. G.; Vega, S. Chemical shift correlation spectroscopy in rotating solids: radio frequency-driven dipolar recoupling and longitudinal exchange. *J. Chem. Phys.* **1992**, *96*, 8624. DOI: 10.1063/1.462267
- [50] Bayro, M. J.; Ramachandran, R.; Caporini, M. A.; Eddy, M. T.; Griffin, R. G. Radio frequency-driven recoupling at high magic-angle spinning frequencies: Homonuclear recoupling sans heteronuclear decoupling. *J. Chem. Phys.* **2008**, *128*, 052321/1. DOI: 10.1063/1.2834736
- [51] Bennett, A. E.; Rienstra, C. M.; Griffiths, J. M.; Zhen, W.; Lansbury, P. T., Jr.; Griffin, R. G. Homonuclear radio frequency-driven recoupling in rotating solids. *J. Chem. Phys.* **1998**, *108*, 9463. DOI: 10.1063/1.476420
- [52] Boender, G. J.; Vega, S.; de Groot, H. J. M. Quantized field description of rotor frequency-driven dipolar recoupling. *J. Chem. Phys.* **2000**, *112*, 1096. DOI: 10.1063/1.480664

- [53] Bennett, A. E.; Rienstra, C. M.; Auger, M.; Lakshmi, K. V.; Griffin, R. G. Heteronuclear decoupling in rotating solids. *J. Chem. Phys.* **1995**, *103*, 6951. DOI: 10.1063/1.470372
- [54] Bayro, M. J.; Debelouchina, G. T.; Eddy, M. T.; Birkett, N. R.; MacPhee, C. E.; Rosay, M.; Maas, W. E.; Dobson, C. M.; Griffin, R. G. Intermolecular Structure Determination of Amyloid Fibrils with Magic-Angle Spinning and Dynamic Nuclear Polarization NMR. *J. Am. Chem. Soc.* **2011**, *133*, 13967. DOI: 10.1021/ja203756x

6. Analysis of Probe RF Circuitry Using Analytical Expressions and SPICE-like Simulators

Adapted from references [1].

Abstract

We revisit the basics of phasor approach to alternating current (AC) circuit analysis. Particular attention is given to the phenomenon of impedance waves and nodes in phasor domain, which is distinct from the time domain voltage / current waves. We discuss probe circuitry and derive analytical expressions useful for SPICE-like circuit simulations. Finally, several phenomena, including coil leads effect, circuit efficiency limitation due to resistive power losses and efficiency of transmission lines are illustrated using a combination of analytical relations and numerical simulations.

6.1. Introduction

Development of custom instrumentation for NMR has been one of the key research areas over the last four decades [2-23]. Continuous progress in superconducting magnet technology, electronics, and NMR probe technology combined with methodological advances made NMR a versatile tool for a variety of systems and areas, such as structural biology [24-40]. As the field of NMR expands and, therefore, demand increases, NMR instrumentation development gradually moves from academic to industrial and commercial laboratories, while the focus of academic research shifts towards NMR methodology and applications. Nowadays, most of the research is conducted using commercial instrumentation, which also progressively replaces old custom instruments.

Different components, however, have been developed at different pace. For example, the state-of-the-art cryogenic magnet technology approaches its theoretical limits, because there are only a few application specific parameters, such as sample size, important in production of complex and expensive cryogenic magnets. At the same time, less expensive NMR probes are much more diverse, as their design is usually tailored to specific classes of systems and applications [7,12,20,41-63]. Certain areas, including solid state NMR (ssNMR) on both static and spinning samples, biomolecular NMR [24,56], as well as experiments requiring harsh conditions, such as cryogenic temperatures [19,64-72], are particularly demanding and impose stringent and frequently conflicting requirements on probes. In such areas, probe technology is often one of the major limiting factors. Although commercial vendors develop probes for demanding applications, academic research still makes important contribution in this area [19,21,58-59,65,73-77]. With few laboratories actively developing instrumentation, it is still instructive to become familiar with the basics of instrumentation, in general, and probes, in particular. This knowledge is useful for safe operation of complex instrumentation; for planning, setting and conducting advanced experiments; and as a part of general NMR training.

The focus of this article is on probe RF circuitry, arguably the most important subsystem of a NMR probe, which is ultimately responsible for the overall probe performance. More specifically, we will revisit the basics of AC circuit analysis in a manner targeted at NMR spectroscopists, discuss *impedance node* phenomenon, which is particularly important at high magnetic fields (high frequencies). We will also discuss certain aspects of SPICE-like [78] software and its application to simulations of probe RF circuits. Finally, we will demonstrate utility of such simulators as a learning tool and will use one such simulator, AWR APLAC® [79], in combination with analytical expressions to illustrate several phenomena affecting performance of the RF circuit.

6.2. Basics of RF Circuits

Nuclear magnetic resonance phenomenon involves resonant transitions between nuclear magnetic energy levels. The frequencies of these transitions, which correspond to static magnetic fields of modern NMR spectrometers, belong in the radio frequency range of the electromagnetic spectrum. Thus, conventional excitation and detection of NMR spectra requires instrumentation equipped with electrical AC circuits operating at those frequencies. Furthermore, most of the modern NMR spectrometers operate in the pulsed mode employing short RF energy bursts, with RF energy being distributed over certain spectral bands. In order to provide sufficient amount of

energy in such short pulses to achieve efficient excitation, large RF powers provided by resonant AC circuits are required.

Designing and fabricating circuits capable of efficient operation at several different frequencies simultaneously for multiple resonance experiments is a challenging task, particularly at high magnetic fields employed by contemporary NMR. Apparatus provided by AC circuit analysis and circuit simulators is a useful tool, which help better understand these difficulties and provide valuable guidance.

6.2.1. AC Circuit Analysis. Phasor Domain

Extensive literature on AC circuits in various forms and for various audiences is readily available, including general electronics textbooks [80-89], textbooks for NMR spectroscopists [90-91], articles in peer reviewed journals [13,20,92-96], encyclopedic articles [54,56,97], Ph.D. dissertations [22] and introductory [98-99] and advanced [100] online sources. Here, we briefly review one of the common approaches used to analyze electrical AC circuit, the method of complex impedances in the phasor domain.

The goal of circuit analysis is to find potential differences across different elements and at the output ports, as well as to find currents flowing through different elements. In the case of an electrical DC circuit, the analysis largely relies on Kirchhoff's voltage law (Equation (21)), Kirchhoff's current law (Equation (22)), Ohm's law (Equation (23)), and the linearity assumption (Equation (24)):

$$\sum_n v_n = 0, \quad (21)$$

$$\sum_n i_n = 0, \quad (22)$$

$$i_R = \frac{1}{R} v_R, \quad (23)$$

$$i(C_1 v_1 + C_2 v_2) = C_1 i(v_1) + C_2 i(v_2), \quad (24)$$

where $\{v_n\}$ is a set of potential differences and electromotive forces (EMF) along a closed loop in the circuit, $\{i_n\}$ is a set of currents flowing into a particular circuit node, v_R is voltage that induces current i_R across resistor R , and C_1 and C_2 are constant numbers. According to Equation (24), a circuit response to a composite driving signal can be represented as a linear combination of circuit responses to the individual components with appropriate coefficients.

In the case of electrical AC circuits, currents and voltages become time dependent, and Equation (21)-(24) are still applicable to resistive networks, if all quantities are replaced by the corresponding instantaneous values. For example, Equation (23) should be replaced with Equation (25)

$$i_R(t) = \frac{1}{R} v_R(t). \quad (25)$$

In contrast, reactive elements have the following well-known ideal volt-ampere characteristics (Equation (26) and (27) for inductor and capacitor, respectively):

$$v_L(t) = L \frac{\partial i_L(t)}{\partial t}, \quad (26)$$

$$i_C(t) = C \frac{\partial v_C(t)}{\partial t}, \quad (27)$$

where L and C are electrical inductance and capacitance, respectively, and, in general, do not obey Equation (23).

A common AC driving function is a sinusoid

$$v(t) = v^{\max} \cos(\omega t + \varphi_0), \quad (28)$$

where ω , φ_0 and v^{\max} are angular frequency, initial phase and amplitude of the sinusoid, respectively. It follows from Equation (25)-(28) that a response to a sinusoidal driving force is a sinusoid for both resistive and reactive elements with different phase and amplitude, but the same frequency. Therefore, if all $\{v^{\max}, \varphi\}$ and $\{i^{\max}, \varphi\}$ (where φ is the full or relative phase) are known, behavior of the circuit is completely described.

Since reactive elements do not obey the Ohm's law (compare Equation (25) with Equation (26) and (27)), DC analysis cannot be directly extended to AC circuits. However, in the special case, when

$$\frac{\partial i_L(t)}{\partial t} \sim i_L(t) \text{ and } \frac{\partial v_C(t)}{\partial t} \sim v_C(t), \quad (29)$$

the Ohm's law may also become applicable to reactive elements, thus, allowing extension of DC analysis to AC circuits. The solution to the first order ordinary differential equations (29) is an exponential. At the same time, the Euler's identity relates a linear combination of two sinusoids to complex exponential

$$\cos(\varphi) + j \sin(\varphi) = e^{j\varphi}, \quad (30)$$

where $j^2 \equiv -1$. If equation (28) is replaced with equation (31)

$$\mathbf{V}(t) = v^{\max} e^{j(\omega t + \varphi_0)} = v^{\max} e^{j\varphi_0} e^{j\omega t}, \quad (31)$$

and equations (25)-(27) are replaced with equations (32)

$$\begin{aligned} \mathbf{I}_R(t) &= \frac{1}{R} v^{\max} e^{j\varphi_0} e^{j\omega t}, \\ \mathbf{I}_L(t) &= \frac{1}{j\omega L} v^{\max} e^{j\varphi_0} e^{j\omega t}, \\ \mathbf{I}_C(t) &= j\omega C v^{\max} e^{j\varphi_0} e^{j\omega t}, \end{aligned} \quad (32)$$

the new set of equations (31)-(32) representing sinusoidal functions with complex amplitudes

$$\mathbf{V}^{\max} = v^{\max},$$

$$\mathbf{I}_R^{\max} = \frac{1}{\mathbf{Z}_R} \mathbf{V}_R^{\max}, \quad (33)$$

$$\mathbf{I}_C^{\max} = \frac{1}{\mathbf{Z}_C} \mathbf{V}_C^{\max},$$

$$\mathbf{I}_L^{\max} = \frac{1}{\mathbf{Z}_L} \mathbf{V}_L^{\max},$$

and complex impedances

$$\mathbf{Z}_R = R,$$

$$\mathbf{Z}_C = \frac{1}{j\omega C} = j\left(-\frac{1}{\omega C}\right), \quad (34)$$

$$\mathbf{Z}_L = j\omega L,$$

obeys the Ohm's Law. As long as linearity assumption (Equation (24)) is valid, the phase factor $e^{j\omega t}$ common to all quantities in Equation (31)-(32) can be dropped, and a set of time independent equations (33)-(34) can be used instead. The transformation from Equation (25)-(27) to Equation (33)-(34) does not affect phases or amplitudes. Therefore, a set of $\{v^{\max}, \varphi\}$ and $\{i^{\max}, \varphi\}$ found using Equation (33)-(34) is also a solution to the original problem. Note that this transformation is valid for stationary conditions only. During transient periods, amplitudes are time dependent and more general solutions to Equation (29) must be used.

Both the time dependent quantities in Equation (31)-(32) and the time independent complex amplitudes in Equation (33)-(34) can be referred to as *phasors* [101]. Here we will use "phasor" term to refer to quantities in Equation (33)-(34). These set of quantities is said to belong in the *phasor domain* as opposed to time dependent expressions containing real trigonometric functions from the time domain.

In practice, the resulted system of equations in phasor domain is solved numerically using, for example, SPICE-like simulators. The basic output of such simulations is a set of unknown $\{v^{\max}, \varphi\}$ and $\{i^{\max}, \varphi\}$, as well as values for the tuning elements. This information is then used to analyze the circuit.

In order to simplify further expressions, we will drop superscript "max" and assume that all capitalized symbols for voltages, currents, impedances and admittances denote phasor quantities. We will use subscripts to differentiate between different symbols and superscripts "r" and "i" to denote real and imaginary parts, as in I_r^i .

6.2.2. Waves in Time and Phasor Domains. Impedance Waves and Nodes

There are three major contributions to the phase factor of voltages and currents. The first contribution ultimately comes from the *temporal modulation* of the driving force, is common for

the entire circuit and can be isolated by transforming expressions from the time domain (Equation (25)-(27)) to phasor domain (Equation (33)-(34)) as discussed above. The two other contributions are responsible for *spatial modulation* of the phase factor, give rise to wave-like phenomena in the time and phasor domains, and are discussed below.

Time domain. For simplicity, let us consider a circuit consisting of ideal conductors. When a point driving force described by a sinusoid (Equation (28)) is applied to such a circuit, the oscillating signal propagates through the circuit at the speed of light. Voltages at different points in the circuit change in the same fashion with phase of the sinusoid varying along the electrical path due to finiteness of the speed of light and resulting electrical delay t_d

$$v(t, t_d) = v \cos\left(2\pi \frac{t}{\tau} - 2\pi \frac{t_d}{\tau}\right), \quad (35)$$

where we expressed angular frequency ω from Equation (28) in terms of the period of oscillations τ

$$\omega = \frac{2\pi}{\tau}.$$

If electrical delay term in Equation (35) is negligible $t_d \ll \tau$, Equation (28) and (35) are equivalent. Equation (35) describes a traveling wave [102]. An important characteristic of this wave is its wavelength λ

$$\lambda = \frac{2\pi c}{\omega}, \quad (36)$$

where c is the speed of light. Switching to complex exponential form as before and dropping the common phase factor containing t , we obtain

$$\mathbf{V}(t_d) = v e^{-j2\pi \frac{t_d}{\tau}}. \quad (37)$$

Since $t_d = x/c$, where x is distance from the source and c is the speed of light, and $\tau c = \lambda$, Equation (37) can also be written in terms of the distance and the wavelength

$$\mathbf{V}(x) = v e^{-j2\pi \frac{x}{\lambda}}. \quad (38)$$

If the size of the circuit, x_{\max} , is much smaller than the wavelength λ of the operating signal (which is equivalent to inequality $t_d \ll \tau$ above), the phase factor in Equation (38) becomes practically constant for the entire circuit

$$x_{\max} \ll \lambda \Rightarrow e^{-j2\pi \frac{x}{\lambda}} \approx 1, \quad (39)$$

and the wave collapses, that is wave-like behavior in the time domain becomes insignificant. Similarly, if Equation (39) only holds for some circuit components, those components behave like *lumped* (discrete) elements, i.e. elements whose properties do not depend on their size. Otherwise, *distributed* properties / wave-like behavior should be taken into account, as further discussed below.

Phasor domain. In addition to spatial modulation of voltages / currents caused by temporal modulation of the source and electrical delays in time domain, there exists a different type of

wave-like behavior in the phasor domain, which is caused by electrical impedance. Impedance is in general a complex quantity, which can be represented in either the real-imaginary form as in Equation (34) or in the magnitude-phase form, $Z^{\max}(\omega)e^{j\phi(\omega)}$. The real part of impedance is of resistive nature and can only be positive for a passive circuit. For an ideal resistor, impedance is purely real. The imaginary part of impedance is of reactive nature. For an ideal inductor or capacitor, impedance is purely imaginary. It follows from Equation (34) that the reactive part of impedance can be both positive, as in case of an inductor, and negative, as in case of a capacitor. Impedance phase factor, $e^{j\phi(\omega)}$, directly reflects the sign of the imaginary part and is the ultimate source of wave-like behavior in the phasor domain introduced through Equation (32)-(34). The imaginary part of impedance can vanish at certain frequencies, when frequency dependent contributions from inductors and capacitors compensate each other, as illustrated below. This phenomenon is the electrical resonance.

Consider a string of ideal capacitors and inductors shown in Figure 54(a). Black dots in the figure denote circuit *nodes* (any point in a circuit), with circuit being open at node Q. Figure

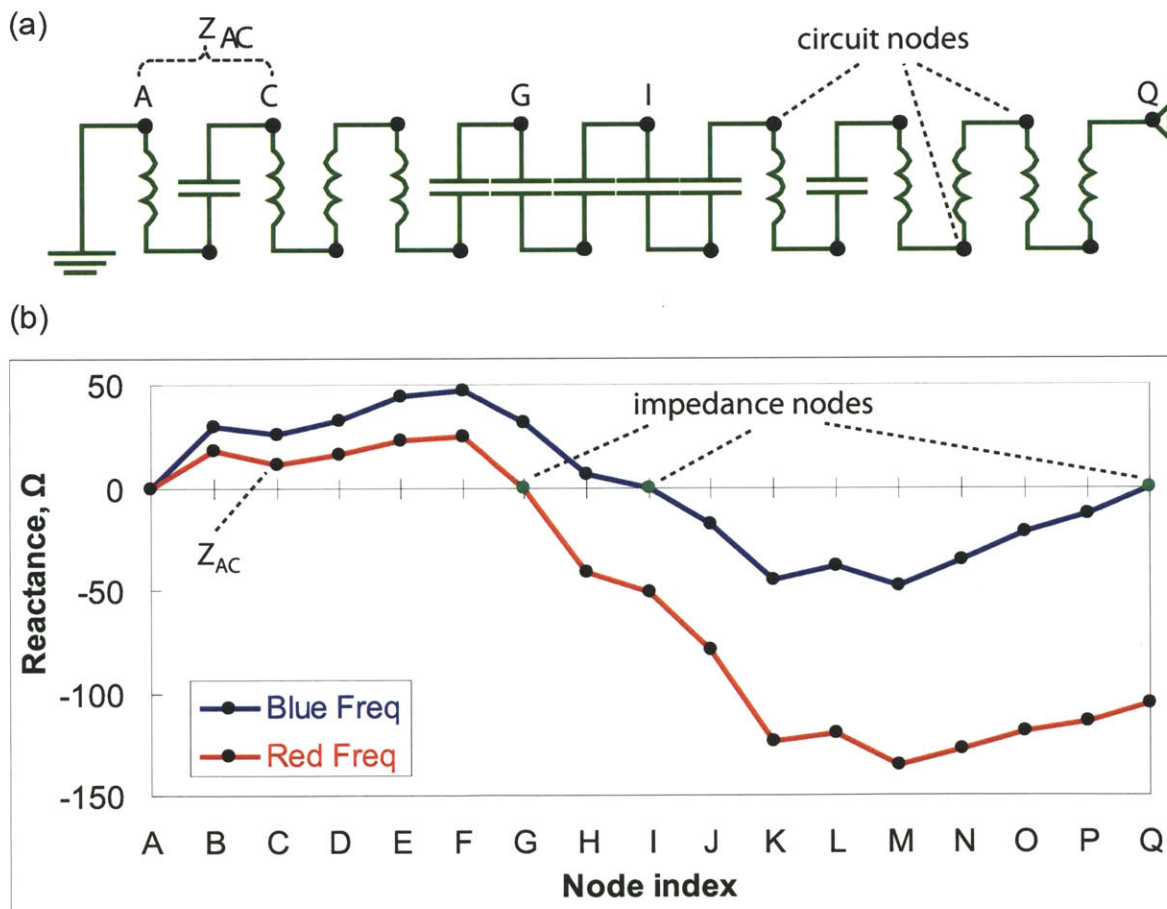


Figure 54. Illustration of impedance waves in the phasor domain.

a) Fragment of an AC circuit consisting of a series of inductors and capacitors. Circuit nodes (black dots) are labeled with Latin letters, and components are assigned values of inductance and capacitance (not shown). b) Diagram showing reactance of circuit sections between the grounded node A and other nodes at two suitably selected frequencies. Impedance nodes are indicated with green dots. See also Question 1 about this figure.

54(b) shows a diagram indicating reactance between ground node A and other circuit nodes (values of reactances and frequencies have been suitably chosen for this illustration). Since all the elements are connected in series, reactance between the node A and any other node X is a sum of reactances of all elements that belong in the section AX. The ground node A has impedance and reactance of 0Ω irrespective of frequency. Non-ground nodes G, I, and Q in Figure 54(a) have 0Ω reactance at the chosen frequencies and are called *impedance nodes*.

In practice, all components are non-ideal. For example, inductors and conductors have finite resistance, which affects performance of the circuit and should be taken into account. If small resistance is assigned to each inductor in the circuit shown in Figure 54(a), impedance at different nodes will be affected as illustrated in Figure 55. In specific, the real part of impedance cannot be negative for passive components; therefore, it can never become 0Ω . This relation is illustrated in Figure 55, where solid black dots indicate impedance magnitude incorporating real (violet dashed trace) and imaginary (solid blue trace) components. In tuned circuits used for NMR, the real part of impedance must be kept small compared to overall impedance (this requirement is further discussed below). The consequence of this requirement is that the real part of impedance does not make significant contribution to overall impedance, except at resonance, as illustrated by the top trace in Figure 55. When resonance condition is fulfilled, large imaginary part of impedance becomes negligible, and impedance is dominated by the real component.

Importantly, an impedance node resembles a grounding strip at and near the corresponding frequency having a vanishing impedance (ideally, green dots in Figure 54(b)) or small real im-

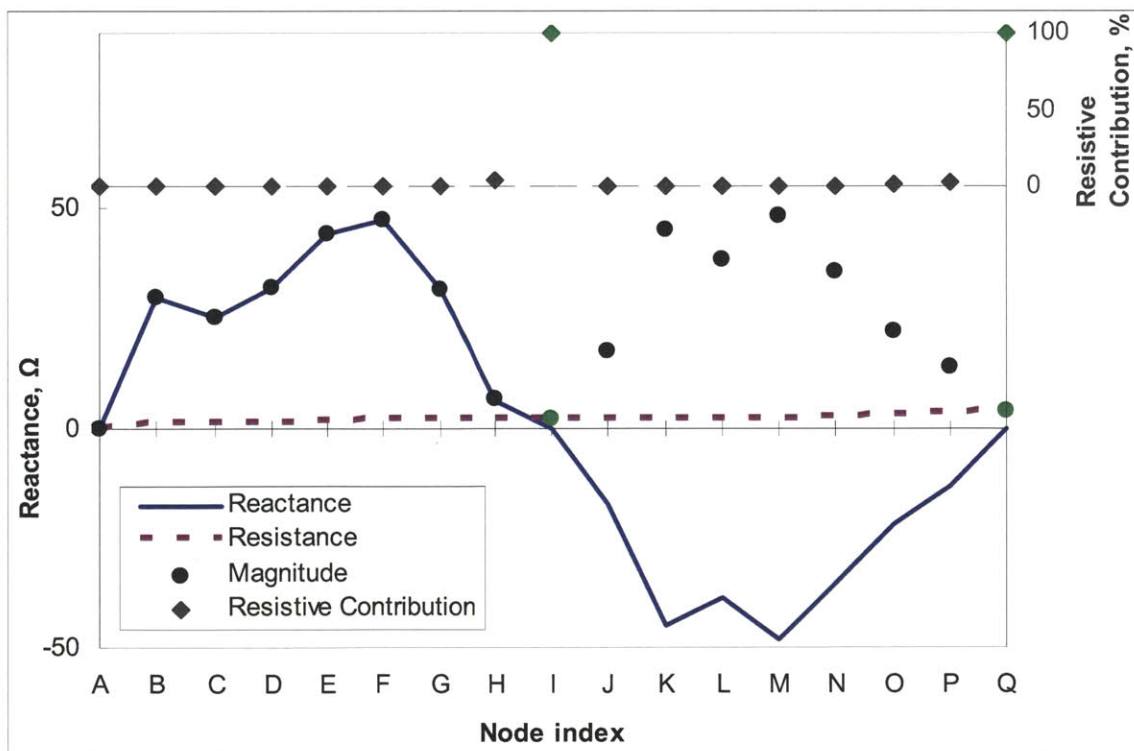


Figure 55. Typical contributions of the real and imaginary parts to impedance of high Q components used in resonant circuits.

“Real” impedance nodes are indicated with green dots, and node index refers to Figure 54(a).

pedance (for real circuits, green dots in Figure 55) at and near that frequency, and large mostly reactive impedance away from it. The concept of impedance nodes (both ideal and real) plays a central role in the recently introduced novel probe RF circuit design [103].

6.3. RF Circuit Simulations

Designing RF circuit is an essential part of NMR probe development. Ideally, this process involves a transformation starting from a desired goal, such as “triple resonance, triple port RF circuit”, to an actual detailed description of a specific circuit that can be readily implemented based on this description. The core part of this transformation is modeling and simulation of the electrical circuit with the purpose of finding accurate model of the physical design. If the behavior of the model meets certain specifications, such as electrical isolation between the channels, the model is accepted; otherwise, it is modified to improve the match between the model and actual circuit. In reality due to certain complications, some of which are briefly discussed below, it may be difficult to achieve this ideal goal, particularly at high magnetic fields (RF frequencies). Under such circumstances, additional circuit optimization at the fabrication stage may be required.

Even when accurate circuit model is attainable, it may not be economically viable. Academic laboratories that develop instrumentation typically have limited oftentimes old electronic equipment at their disposal. At the same time, usually one - two copies of the same probe are constructed. In contrast, commercial users of circuit simulation software, such as IC chip manufactures, have modern expensive equipment; they can also afford to invest substantial resources into refining their simulations, because serial manufacturing of simulated devices will justify the investments. For these reasons, attempts to obtain very accurate circuit model, especially in the case of complex devices, such MAS DNP probes, may be impractical in the academic environment. At the same time, certain important electrical phenomena, such as a coil leads effect illustrated below, can be readily reproduced even in a rough simulation, helping anticipate and diagnose potential issues, as well as making the simulation software a useful learning tool.

Simulation workflow varies depending on particular goal, and in general, involves several stages. Initially, it is necessary to

- 1) choose appropriate simulation approach and environment (software) for AC circuit simulations;
- 2) create circuit model, including tuning elements;
- 3) perform initial simulation with the goal to determine the values of the tuning elements that fulfill resonant condition.

We will limit our discussion to steps 1) and 3).

6.3.1. *Simulation Approaches*

An important criterion that largely dictates the choice of circuit simulation software is the ratio of typical size of circuit components (D) to signal wavelength (λ).

$\lambda \gg D$. **Discrete regime.** SPICE-like [78] simulators, such as AWR APLAC® simulator [79] used in our laboratory, can be used. In this regime, the circuit is modeled as a collection of individual circuit components, which do not interact or interfere with each other except where these interactions are explicitly modeled. Each modeled component is represented by a predefined or user-defined mathematical model, and electrical delays are generally not taken into account.

The SPICE-like simulation approach is the most efficient one. At the same time, it has certain limitations. First of all, this approach relies on mathematical models, which must be provided for all components. Furthermore, those models are only valid within a certain range of its parameters. If a component does not have a library model or its model is expected to be inaccurate, the *mixed mode* simulation approach can be used.

More serious limitations arise as the operating frequency increases. Ideally, the size of lumped elements (e.g., the sample coil) should not matter. In practice, validity of this assumption is frequency dependent. Specifically, for components having electrical path length l , lumped models are generally applicable as long as the wavelength λ of the operating frequency fulfills inequality [104]

$$l \leq 0.1\lambda. \quad (40)$$

See Question 2 for an example of application of this empirical rule.

Additionally, certain phenomena, such as the skin and proximity effects [81,105-106] or parasitic admittances increase with frequency contributing to non-ideal behavior of standard components. Some of these effects can be taken into account by more sophisticated models, which may or may not be implemented in particular simulator; other effects are system specific, depend on environment and may not be generalized for isolated components, thus, limiting the applicability of predefined models.

$\lambda \ll D$. **Distributed regime.** 3D full-wave simulators, such as Ansys HFSS™ [107], naturally accounts for non-ideal behavior of different components. This type of simulators takes a physical description of the circuit, including geometry and materials of different parts, as well as basic electromagnetic properties of materials (or obtains those properties from an internal database). Then the simulator solves Maxwell's equations for electromagnetic waves propagation. This added flexibility comes at the expense of substantially increased computational time and power limits.

Intermediate regime and mixed mode simulation. The two types of simulators can also be used together in a mixed mode simulation, taking flexibility from one approach and computational efficiency from the other one. For example, when built-in models are not available or inaccurate for some components, 3D full-wave simulator can be used to analyze such components and produce numerical models, such as S-parameters [100] based description. Then, these numerical models are used alongside built-in models available for standard components in a SPICE-like simulator to analyze the entire circuit.

6.3.2. SPICE-like Circuit Simulations

A simplified model of a single resonance transmission line circuit is shown in Figure 56(a). Usually, the first simulation step is to find the values of tuning (C_t) and matching (C_m) capacitors, such that port impedance $\mathbf{Z} = 50 \Omega$ (admittance $\mathbf{Y} = 0.02 \text{ S}$). Although it is possible to directly simulate the tuning process, the same goal can be achieved much more efficiently using analytical expressions.

In order to derive these expressions, it is convenient to consider a “black-box” model shown in Figure 56(b), which is applicable to a multiple resonance circuit as well. If we know impedance \mathbf{Z}_p of the black-box, we can set up a system of two equations in two variables, C_m and C_t . In order to determine \mathbf{Z}_p , AC circuit analysis needs to be performed once with arbitrarily chosen values for C_m and C_t . Then expressions derived below can be used to calculate values of C_m and C_t corresponding to $\mathbf{Z} = \mathbf{Z}_o$.

There are two approaches that can be used to solve this system for C_m and C_t . The first approach involves straightforward but tedious derivations and is left as an exercise (see Question 4). The second approach involves careful control of intermediate steps, thus making the expressions substantially simpler.

To simplify derivations, it is convenient to use shortcut vector notation for complex numbers, with superscripts denoting real (r) and imaginary (i) parts,

$$\mathbf{A} = A^r + jA^i \equiv (A^r, A^i), \tag{41}$$

magnitude of a complex number,

$$|\mathbf{A}| = \sqrt{(A^r)^2 + (A^i)^2} \equiv A,$$

and basic algebraic operations (addition, multiplication and inversion) involving complex numbers (see Question 3).

When a circuit is tuned and matched to Z_o , it means that

$$\mathbf{Z} = \mathbf{Z}_o, \tag{42}$$

where \mathbf{Z} is the port impedance. To simplify the derivations, we should also switch from impedances \mathbf{Z} to admittances \mathbf{Y} ,

$$\mathbf{Y} = \frac{1}{\mathbf{Z}}. \tag{43}$$

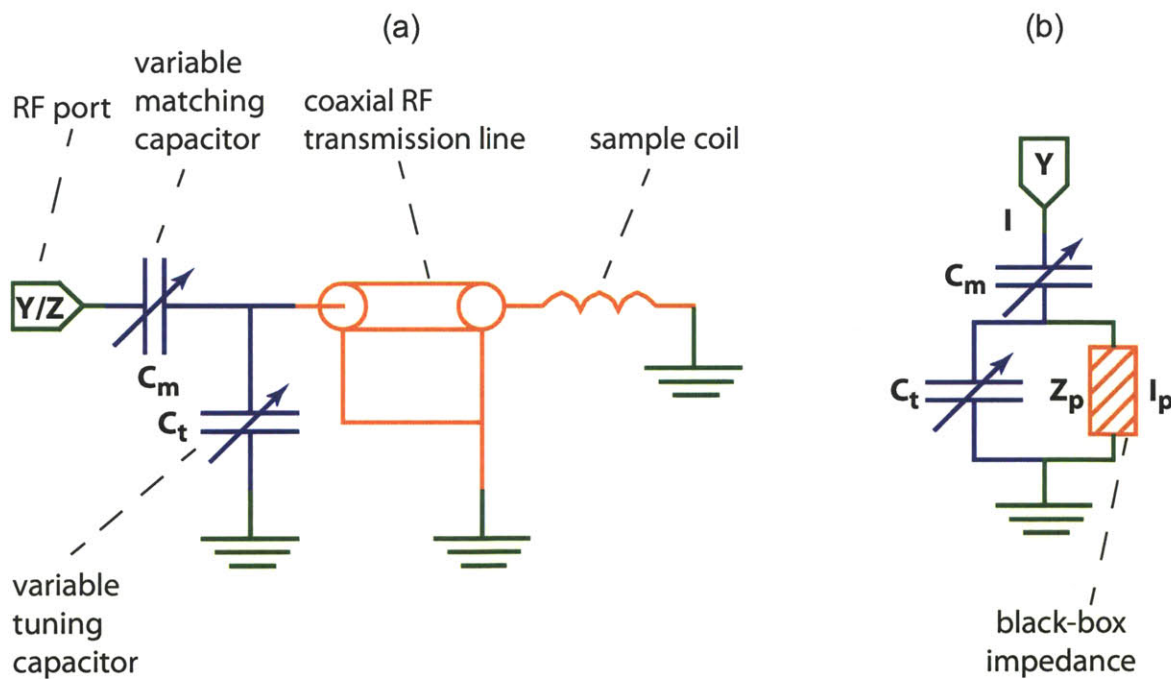


Figure 56. Single resonance transmission line circuit model.

a) Simplified representations. b) Black-box model. Tuning / matching network is highlighted with blue color, RF ports and ground symbols – with green color, and the rest of the circuit – with light brown color.

The standard admittance Y_o and admittances for the three circuit components in Figure 56(b) are denoted as follows:

$$\begin{aligned}
 \mathbf{Y}_o &= (Y_o^r, Y_o^i) = (Y_o^r, 0), \\
 \mathbf{Y}_p &= (Y_p^r, Y_p^i), \\
 \mathbf{Y}_m &= (Y_m^r, Y_m^i) = (0, Y_m^i), \\
 \mathbf{Y}_t &= (Y_t^r, Y_t^i) = (0, Y_t^i),
 \end{aligned} \tag{44}$$

where we used the fact that the standard admittance is purely real, while that of an ideal capacitor is purely imaginary. Using the rules for parallel and series combination of multiple impedances, equation (42) can be expanded in terms of impedances of individual components,

$$\mathbf{Z}_m + \mathbf{Z}_t \parallel \mathbf{Z}_p = \mathbf{Z}_o, \tag{45}$$

where the second term denotes a parallel combination of elements. Equation (45) is a vector equation equivalent to the following system of two scalar equations:

$$\begin{cases} \operatorname{Re}(\mathbf{Z}_m + \mathbf{Z}_t \parallel \mathbf{Z}_p) = \operatorname{Re}(\mathbf{Z}_o), \\ \operatorname{Im}(\mathbf{Z}_m + \mathbf{Z}_t \parallel \mathbf{Z}_p) = \operatorname{Im}(\mathbf{Z}_o). \end{cases} \tag{46}$$

Equation (46) can now be transformed using Equation (43) and (44)

$$\begin{cases} \operatorname{Re}\left(\frac{1}{\mathbf{Y}_p + \mathbf{Y}_t}\right) = \frac{1}{Y_o^r}, \\ \operatorname{Im}\left(\frac{1}{\mathbf{Y}_p + \mathbf{Y}_t}\right) = \frac{1}{Y_m^i}. \end{cases}$$

$$\begin{cases} \operatorname{Re}\left(\frac{1}{\mathbf{Y}_p + \mathbf{Y}_t}\right) = \frac{Y_p^r}{|\mathbf{Y}_p + \mathbf{Y}_t|^2} = \frac{1}{Y_o^r}, \\ \operatorname{Im}\left(\frac{1}{\mathbf{Y}_p + \mathbf{Y}_t}\right) = -\frac{Y_p^i + Y_t^i}{|\mathbf{Y}_p + \mathbf{Y}_t|^2} = \frac{1}{Y_m^i}. \end{cases}$$

$$\begin{cases} |\mathbf{Y}_p + \mathbf{Y}_t|^2 = Y_p^r Y_o^r, \\ Y_m^i = -\frac{|\mathbf{Y}_p + \mathbf{Y}_t|^2}{Y_p^i + Y_t^i}. \end{cases}$$

$$\begin{cases} (Y_p^r)^2 + (Y_p^i + Y_t^i)^2 = Y_p^r Y_o^r, \\ Y_m^i = -\frac{Y_p^r Y_o^r}{Y_p^i + Y_t^i}. \end{cases}$$

$$\begin{cases} (Y_p^i + Y_t^i)^2 = Y_p^r (Y_o^r - Y_p^r), \\ Y_m^i = -\frac{Y_p^r Y_o^r}{Y_p^i + Y_t^i}. \end{cases}$$

Denominator in the second equation must be negative (verify it), therefore,

$$\begin{cases} Y_p^i + Y_t^i = -\sqrt{Y_p^r (Y_o^r - Y_p^r)}, \\ Y_m^i = -\frac{Y_p^r Y_o^r}{Y_p^i + Y_t^i}. \end{cases}$$

$$\begin{cases} Y_t^i = -Y_p^i - \sqrt{Y_p^r (Y_o^r - Y_p^r)}, \\ Y_m^i = Y_o^r \sqrt{\frac{Y_p^r}{Y_o^r - Y_p^r}}. \end{cases} \quad (47)$$

Finally,

$$\begin{cases} C_t = \frac{1}{\omega} \left(-Y_p^i - \sqrt{Y_p^r (Y_o^r - Y_p^r)} \right), \\ C_m = \frac{1}{\omega} Y_o^r \sqrt{\frac{Y_p^r}{Y_o^r - Y_p^r}}. \end{cases} \quad (48)$$

It follows from Equation (48) that tuning is only possible, if all of the following conditions are fulfilled:

$$Y_p^r < Y_o^r.$$

Conductance of the black-box must be smaller than that of the standard admittance.

$$C_t > 0 \Rightarrow Y_p^i < 0.$$

The black-box must be inductive.

$$|Y_p^i| > \sqrt{Y_p^r (Y_o^r - Y_p^r)}.$$

Susceptance of the black-box must be sufficiently large; conversely, assuming that reactance of the black box is the dominating part of its impedance, the black box must not be too inductive.

6.4. Resonant Phenomena and Circuit Efficiency

We will now use RF circuit simulations as well as analytical expressions to discuss several phenomena that may affect circuit efficiency.

6.4.1. Coil Leads Effect

While building custom probes in our laboratory, we have noticed that coil leads had a significant effect on the RF circuit. Tuning of the high frequency channel was particularly affected. Here we use SPICE-like simulations to verify this observation and demonstrate that by changing the length of the coil leads within a range of 2.5 cm (1") shifts the tuning range at 700 MHz (which is the ^1H Larmor frequency, for which one of the probes has been designed) by as much as 13 MHz, thus possibly making it necessary to adjust other components of the circuit to compensate for this shift.

Figure 57 shows a model circuit used to investigate the sensitivity of the circuit with respect to the length of coil leads. In order to investigate this effect, we modeled the leads as a two-wire transmission line in air [108, pp. 5297, 5310]. The simulator that we use does not have a built-in model for a two-wire transmission line, so a mixed mode simulation was used. In specific, we used a built-in generic transmission line element, whose properties are defined in terms of linear resistance (R), conductance, capacitance (C), and inductance (L). For a two-wire transmission line this properties can be readily evaluated using formulas found elsewhere [86,108, pp. 5297, 5310]:

$$\delta = \sqrt{\frac{2\rho}{\mu_o\mu_r\omega}},$$

$$R = \frac{\rho}{\pi a\delta} = \frac{1}{a} \sqrt{\frac{\mu_o}{\pi}} \mu_r \nu \rho,$$

$$L = \frac{\mu_o\mu_r}{\pi} \ln\left(\frac{d}{a}\right),$$

$$C = \frac{\pi\epsilon_o\epsilon_r}{\ln(d/a)},$$
(49)

where δ is skin depth for the conductor material at cyclic frequency ν , ω is angular frequency, ρ is specific electrical resistance of the conductor material, a is wire radius, $\mu_r\mu_o$ and $\epsilon_r\epsilon_o$ are magnetic permeability and electric permittivity of the conductor material.

Behavior of the circuit in Figure 57 was investigated as a function of coil leads length (l). Specifically, simulations with the goal to find whether this circuit can be tuned at 700 MHz, that is whether all the requirements outlined in the previous section are fulfilled, was performed for

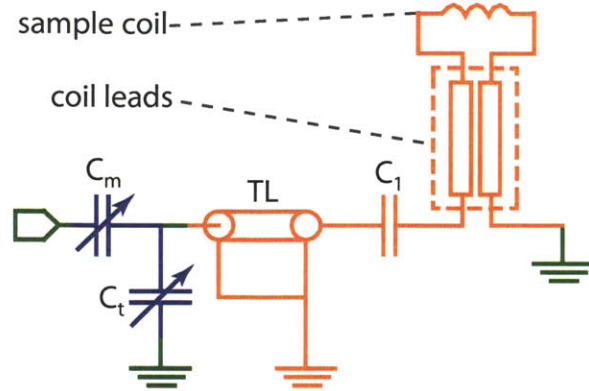


Figure 57. Tuned circuit for coil leads effect modeling. Circuit components: matching, tuning and fixed capacitors C_m , C_t , $C_1 = 33$ pF, coaxial transmission line TL (copper conductors, O.D. = 2.68 cm / 1.055", I.D. = 6.35 mm / 0.25" and length = 65 cm / 25.6") sample coil (copper wire, 6 turns, wire O.D. = 0.635 mm / 0.025", coil diameter = 4.45 mm / 0.175", and pitch = 1.27 mm / 0.05"), and coil leads (modeled as a two-wire transmission line [108, pp. 5297, 5310], spacing = 7.6 mm / 0.3", length = 5.1 mm / 0.2" – 25.4 mm / 1").

coil leads lengths in the range of $0.5 \text{ cm} < l < 2.5 \text{ cm}$. It has been found that for $l = 0.5 \text{ cm}$ the circuit could be tuned, that is there exist a meaningful solution for Equation (48). At the other end, $l = 2.5 \text{ cm}$, the circuit could no longer be tuned due to a shift of the tuning range by 13 MHz.

6.4.2. Efficiency Limit due to Power Dissipation

The law of conservation of energy oftentimes leads to elegant solutions to problems and highlights their essential features. Here, we apply this method to illustration of the relationship between circuit efficiency and resistive losses. Consider the circuit in Figure 58. When the circuit is tuned, the input impedance $\mathbf{Z} = \mathbf{Z}_o$ is purely real irrespective of details of the black-box impedance \mathbf{Z}_p , as illustrated in Figure 55. Therefore, given the input voltage $\mathbf{V} = \mathbf{V}_o$, the input current $\mathbf{I} = \mathbf{I}_o = \mathbf{V}_o / \mathbf{Z}_o$ does not depend on the details of the black-box impedance \mathbf{Z}_p . Assuming that the input voltage \mathbf{V}_o is purely real and taking into account that the standard impedance \mathbf{Z}_o is also purely real, the input power phasor defined as [84]

$$\mathbf{S}_o = \frac{\mathbf{V}_o \mathbf{I}_o^\dagger}{2} = P_o + jQ_o,$$

where dagger symbol denotes complex conjugation, P is the average (ohmic) power, and Q is reactive power (associated with stored energy), is purely real. In other words, $Q = 0$ and all energy supplied to the circuit at the resonant frequency in a steady state is completely dissipated in the form of ohmic heating (radiation losses are neglected here). Ohmic power is proportional to electrical resistivity and the square of current magnitude

$$P_o = \frac{|\mathbf{I}_o|^2 Z_o^r}{2} = \frac{I_o^2 Z_o^r}{2}.$$

Neglecting power losses in capacitors, we conclude that

$$P_o = P_p = \frac{|\mathbf{I}_p|^2 Z_p^r}{2} = \frac{I_p^2 Z_p^r}{2}.$$

Therefore,

$$\frac{|\mathbf{I}_p|^2 Z_p^r}{2} = \frac{I_o^2 Z_o^r}{2},$$

$$|\mathbf{I}_p| = I_o \sqrt{\frac{Z_o^r}{Z_p^r}} = I_o \sqrt{\frac{Z_o^r}{R}}. \quad (50)$$

Equation (50) has three consequences. First, since the RF magnetic field in the coil is proportional to current, $B_1 \sim |\mathbf{I}_p|$, and Q -factor of the circuit in Figure 58, is proportional to the Q -factor of the coil,

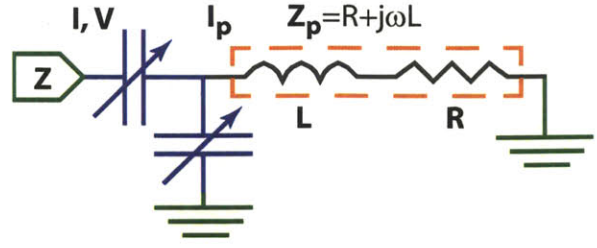


Figure 58. Simplified model of a lossy single resonance circuit.

Model includes ideal tuning / matching network and solenoidal resonator \mathbf{L} with finite resistance \mathbf{R} .

$$Q \sim Q_L = \frac{\omega L}{R},$$

the well-known dependence $B_1 \sim \sqrt{Q}$ follows from Equation (50).

The second consequence can be illustrated by calculating electrical resistance of the coil and transmission line in the circuit in Figure 57. Using Equation (49) and parameters from the caption of Figure 57, we find that

$$\begin{aligned} R_{coax} &= 0.11 \, \Omega, \\ R_L &= 0.29 \, \Omega \, (1.11 \, \Omega), \end{aligned} \tag{51}$$

where the first value for R_L is underestimated due to the proximity effect [81,105-106], while the value in parentheses was obtained using APLAC simulator [79] based on a more detailed model [109]. These numbers are small, and even small additional resistance coming, for example, from electrical connections in the circuit of insufficient quality may produce significant contribution to overall circuit resistance, lowering circuit efficiency.

Finally, it also follows from Equation (50) that an additional inductor does not necessarily take energy away from the sample coil or lower overall performance of the circuit. If resistive losses in that inductor are much smaller than losses in other elements of the circuit, such an inductor will not affect circuit performance.

At the same time, resistive losses in an inductor can be substantial. For example, consider a RF trap consisting of a parallel combination of inductor and capacitor. A trap is designed to resonate at the target frequency, which means that large current develops in the inductor, and, thus, substantial RF energy may be lost.

6.4.3. Power Transfer Efficiency in Transmission Line RF Circuit

We have recently reported a new balanced transmission line probe design [22,103,110-111] that demonstrated outstanding performance. One factor, which contributed to this result, is the overall high circuit quality (in the sense described in the previous section and illustrated by Equation (50) and (51)). The other factor, which is relevant for transmission line probes, is discussed below.

The primary functions of the electric circuit of a NMR probe are matching the coil impedance to that of transmitter and receiver at several RF frequencies, as well as ensuring efficient performance of the circuit at those frequencies. As discussed earlier, the circuit may incorporate lumped (such as inductors and chip capacitors) and distributed (transmission lines) elements.

Coaxial transmission lines have been commonly used in design of multiple resonance NMR probes [10,15,55] and provide several advantages. They are often times less lossy compared to lumped elements (Equation (51)), more robust and permit *remote tuning*, such that most of the tuning elements can be moved away from the sample and, possibly, placed outside of the magnet bore. The latter is important, for example, for cryogenic applications, where the sample chamber is kept at cryogenic temperatures, while sensitive electronic components stay at ambient conditions.

Transmission line is also an impedance transformer device that delivers power from the “source” connected at one end of the line to the “load” connected at the other end [13,83,89]. A fundamental characteristic of a transmission line is its power transfer efficiency, which depends on impedances of source and load and characteristic impedance of the line. The optimum effi-

ciency is achieved when impedances of both source and load match the characteristic impedance of the line (Z_o), to which they are connected. Whenever these impedances do not match, a fraction of power is reflected back away from the load towards the source in accordance with the complex reflection coefficient ρ [89]

$$\rho = \frac{Z_L - Z_o}{Z_L + Z_o}, \quad (52)$$

where Z_L is load (source) impedance and Z_o . Full transmission (no reflection) takes place when $Z_L = Z_o$. When the phase of the load phasor is fixed, minimum reflection occurs when $|Z_L| = |Z_o|$ [89]; the larger mismatch the larger reflection.

Consider the circuit in Figure 56(a). During the excitation period, the coil acts as a load connected to the transmission line. Using parameter from Figure 57, we find that reactance of the coil at 700 MHz is 380 Ω (calculated using APLAC simulator [79] based on the model described elsewhere [109]) and the characteristic impedance of the coaxial transmission line can be calculated as follows (46)

$$Z_o = \frac{\ln(R/r)}{2\pi} \sqrt{\frac{\mu}{\epsilon}},$$

where R and r are the inner radius of the outer conductor and the outer radius of the inner conductor, respectively, and equals to 45 Ω . Therefore, substantial reflection at this frequency should occur. One way to reduce impedance mismatch would be by adding a capacitor in series with the coil. However, this approach requires small capacitors, which present high impedance at lower frequencies, such as ^{13}C and ^{15}N .

A more robust approach involves balancing the coil using additional transmission line as described previously [22,103,110-111]. In this case, an impedance node is tuned at the middle of the coil, reducing load reactance by a factor of two at the expense of slight increase of the resistive part of the load impedance. Overall, load impedance, which is mostly reactive, is, in turn, decreased nearly by a factor of two, thereby reducing the amount of reflected power.

6.5. Conclusions

We reviewed the basics of phasor approach to AC circuit analysis and discussed the origins of waves in time and phasor domain. While some oversimplified circuits can be treated analytically, usually it is necessary to use AC circuit simulators. SPICE-like simulators are efficient and easily provide detailed information about all parts of the circuit; however, at high frequencies, it becomes increasingly difficult to achieve a good match between a model and the real circuit. At the same time, a combination of SPICE-like simulations with partial analytical analysis can be beneficial for understanding underlying electrical phenomena.

6.6. Questions and Answers

Question 1. Which frequency in Figure 54(b) is higher?

Question 2. Determine whether lumped model is applicable to a 5-turn coil having I.D. of 3.2 mm and 1 cm long leads at 700 MHz.

Question 3. Using shortcut in Equation (41) basic algebraic operations (addition, multiplication and inversion) involving complex numbers.

Question 4. Derive values of C_t and C_m starting from admittance analog of equation (42) (“brute-force” derivation).

Answer 1. Observe that if $\omega_1 > \omega_2$, $Z^i(\omega_1) > Z^i(\omega_2)$ for both inductor ($Z_L = j\omega L$) and capacitor ($Z_C = -j/(\omega C)$) and vice versa. Therefore, the blue trace corresponds to the high frequency, and the red trace to the low one.

Answer 2. Electrical path length and signal wavelength

$$0.1\lambda = 0.1 \frac{c}{v} \approx \frac{3 \cdot 10^8 \text{ m} \cdot \text{s}^{-1}}{700 \text{ MHz} \cdot 10} \approx 4.3 \text{ cm},$$

$$l \approx \pi \cdot \text{I.D.} \cdot N + \text{lead} \cdot 2 \approx 3.14 \cdot 3.2 \text{ mm} \cdot 5 + 1 \text{ cm} \cdot 2 \approx 7 \text{ cm}$$

violate inequality (40), and lumped models for such a coil at this frequency may no longer be accurate.

Answer 3.

$$\mathbf{A} + \mathbf{B} = (A^r, A^i) + (B^r, B^i) = (A^r + B^r, A^i + B^i),$$

$$\mathbf{A} \bullet \mathbf{B} = (A^r, A^i)(B^r, B^i) = (A^r B^r - A^i B^i + j(A^r B^i + A^i B^r)) = (A^r B^r - A^i B^i, A^r B^i + A^i B^r),$$

$$\frac{1}{\mathbf{A}} = \frac{1}{A^r + jA^i} = \frac{A^r - jA^i}{(A^r + jA^i)(A^r - jA^i)} = \frac{A^r - jA^i}{(A^r)^2 + (A^i)^2} = \frac{A^r}{|A|^2} - j \frac{A^i}{|A|^2} = \left(\frac{A^r}{|A|^2}, -\frac{A^i}{|A|^2} \right).$$

Answer 4.

$$\mathbf{Y} = \mathbf{Y}_o,$$

which can be expanded similarly to Equation (45)

$$\mathbf{Y}_m + \mathbf{Y}_t \parallel \mathbf{Y}_p = \mathbf{Y}_o, \quad (53)$$

which can be replaced by a system of scalar equations similarly to Equation (46)

$$\begin{cases} \text{Re}(\mathbf{Y}_m + \mathbf{Y}_t \parallel \mathbf{Y}_p) = Y_o^r, \\ \text{Im}(\mathbf{Y}_m + \mathbf{Y}_t \parallel \mathbf{Y}_p) = 0. \end{cases} \quad (54)$$

We can now expand admittance \mathbf{Y} in terms of individual circuit components (Figure 56(b))

$$\begin{aligned} \mathbf{Y}_m + \mathbf{Y}_t \parallel \mathbf{Y}_p &= \frac{(\mathbf{Y}_p + \mathbf{Y}_t) \mathbf{Y}_m}{\mathbf{Y}_p + \mathbf{Y}_t + \mathbf{Y}_m} = \frac{(Y_p^r, Y_p^i + Y_t^i)(0, Y_m^i)}{(Y_p^r, Y_p^i + Y_t^i + Y_m^i)} = \frac{Y_m^i (-(Y_p^i + Y_t^i), Y_p^r)}{(Y_p^r, Y_p^i + Y_t^i + Y_m^i)}, \\ \mathbf{Y}_m + \mathbf{Y}_t \parallel \mathbf{Y}_p &= \frac{Y_m^i (Y_p^r Y_m^i, (Y_p^i + Y_t^i)(Y_p^i + Y_t^i + Y_m^i) + (Y_p^r)^2)}{(Y_p^r)^2 + (Y_p^i + Y_t^i + Y_m^i)^2}, \end{aligned} \quad (55)$$

where all quantities in the denominator must be non-zero and, thus, the whole denominator must be positive for Equation (53) to have a solution and for the circuit in Figure 56(b) to be tunable. Substituting Equation (55) into the second Equation (54) we obtain

$$(Y_p^i + Y_t^i)(Y_p^i + Y_t^i + Y_m^i) + (Y_p^r)^2 = 0,$$

which can be further rearranged as follows

$$\frac{Y_p^r}{Y_p^i + Y_t^i} + \frac{Y_p^i + Y_t^i}{Y_p^r} = -\frac{Y_m^i}{Y_p^r}, \quad (56)$$

where we took into account that all factors in the previous expression must be non-zero. Substituting Equation (55) and then (56) into the first Equation (54) we obtain

$$\frac{\left(\frac{Y_m^i}{Y_p^r}\right)^2}{1 + \left(\frac{Y_p^r}{Y_p^i + Y_t^i}\right)^2} = \frac{Y_p^r}{Y_p^r}, \quad (57)$$

and Equation (54) can now be replaced with

$$\begin{cases} \frac{\left(\frac{Y_m^i}{Y_p^r}\right)^2}{1 + \left(\frac{Y_p^r}{Y_p^i + Y_t^i}\right)^2} = \frac{Y_p^r}{Y_p^r}, \\ \frac{Y_p^r}{Y_p^i + Y_t^i} + \frac{Y_p^i + Y_t^i}{Y_p^r} = -\frac{Y_m^i}{Y_p^r}. \end{cases},$$

which can be rewritten as follows

$$\begin{cases} \frac{m^2}{1+t^2} = \frac{Y_p^r}{Y_p^r}, \\ \frac{1}{t} + t = -m, \end{cases} \quad (58)$$

in terms of new variables

$$\begin{cases} t = \frac{Y_p^r}{Y_p^i + Y_t^i}, \\ m = \frac{Y_m^i}{Y_p^r}. \end{cases} \quad (59)$$

It follows from the second Equation (58) and (59) that

$$\begin{aligned} m &> 0, \\ t &< 0. \end{aligned} \quad (60)$$

Multiplying equations (58) and substituting the result into the first equation (58), we obtain

$$\begin{cases} \frac{t^2 + 1}{t^2} = \frac{Y_o^r}{Y_p^r}, \\ t \frac{Y_o^r}{Y_p^r} = -m. \end{cases}$$

Taking into account Equation (60), we obtain

$$\begin{cases} Y_t^i = -Y_p^i - \sqrt{Y_p^r (Y_o^r - Y_p^r)}, \\ Y_m^i = Y_o^r \sqrt{\frac{Y_p^r}{Y_o^r - Y_p^r}}. \end{cases} ,$$

which is identical to the expressions derived in the main text.

Acknowledgments

This research was supported by the National Institutes of Health through grants EB003151, EB002026. We thank Dr. Anthony Bielecki for assistance with APLAC software.

References

- [1] Markhasin, E.; Griffin, R. G. Analysis of Probe RF Circuitry Using Analytical Expressions and SPICE-like Simulators. *Manuscript in preparation*
- [2] Meiboom, S.; Hewitt, R. C. High-resolution N.M.R. (nuclear magnetic resonance) probe suitable for use in a superconducting solenoid. *Rev. Sci. Instrum.* **1965**, *36*, 1509. DOI: 10.1063/1.1719377
- [3] Jefferts, K. B.; Jones, E. D. Ultrahigh-frequency nuclear magnetic resonance spectrometer. *Rev. Sci. Instrum.* **1965**, *36*, 983. DOI: 10.1063/1.1719801
- [4] Cross, V. R.; Hester, R. K.; Waugh, J. S. Single coil probe with transmission-line tuning for nuclear magnetic double resonance. *Rev. Sci. Instrum.* **1976**, *47*, 1486. DOI: 10.1063/1.1134560
- [5] Stoll, M. E.; Vega, A. J.; Vaughn, R. W. Simple single-coil double resonance NMR probe for solid state studies. *Rev. Sci. Instrum.* **1977**, *48*, 800. DOI: 10.1063/1.1135159
- [6] Doty, F. D.; Inners, R. R.; Ellis, P. D. A multinuclear double-tuned probe for applications with solids or liquids utilizing lumped tuning elements. *J. Magn. Reson.* **1981**, *43*, 399. DOI: 10.1016/0022-2364(81)90051-2
- [7] Idziak, S.; Haeberlen, U. Design and construction of a high homogeneity rf coil for solid-state multiple-pulse NMR. *J. Magn. Reson.* **1982**, *50*, 281. DOI: 10.1016/0022-2364(82)90058-0
- [8] Chingas, G. C. Overcoupling NMR probes to improve transient response. *J. Magn. Reson.* **1983**, *54*, 153. DOI: 10.1016/0022-2364(83)90156-7
- [9] Sullivan, N. S.; Deschamps, P.; Neel, P.; Vaissiere, J. M. Efficient fast-recovery scheme for NMR pulse spectrometers. *Revue de Physique Appliquee* **1983**, *18*, 253. DOI: 10.1051/rphysap:01983001804025300
- [10] McKay, R. A. Double-tuned single coil probe for nuclear magnetic resonance spectrometer. Patent #4446431, 1984.
- [11] Schnall, M. D.; Subramanian, V. H.; Leigh, J. S., Jr.; Chance, B. A new double-tuned probe for concurrent proton and phosphorus-31 NMR. *J. Magn. Reson.* **1985**, *65*, 122. DOI: 10.1016/0022-2364(85)90380-4
- [12] Eastman, M. A.; Grandinetti, P. J.; Lee, Y. K.; Pines, A. Double-tuned hopping-coil probe for dynamic-angle-spinning NMR. *J. Magn. Reson.* **1992**, *98*, 333. DOI: 10.1016/0022-2364(92)90136-U
- [13] Traficante, D. D. Introduction to Transmission Lines Basic Principles and Applications of Quarter-wavelength Cables and Impedance Matching. *Concepts Magn. Reson.* **1993**, *5*, 57. DOI: 10.1002/cmr.1820050105
- [14] Doty, D. F. Doubly broadband triple resonance or quad resonance NMR probe circuit. Patent #5424645, 1995.

- [15] Schaefer, J.; McKay, R. A. Multi-tuned single coil transmission line probe for nuclear magnetic resonance spectrometer. Patent #5861748, 1999.
- [16] Zeiger, H. Probehead for nuclear magnetic resonance measurements. Patent #6307371, 2001.
- [17] Marek, D. Cooled NMR probe head with thermal insulation of the sample. Patent #6441617, 2002.
- [18] Stringer, J.; Bronnimann, C. E. Balanced mode operation of a high frequency NMR probe. Patent #6380742, 2002.
- [19] Barnes, A. B.; Mak-Jurkauskas, M. L.; Matsuki, Y.; Bajaj, V. S.; van der Wel, P. C. A.; De Rocher, R.; Bryant, J.; Sirigiri, J. R.; Temkin, R. J.; Lugtenburg, J.; Herzfeld, J.; Griffin, R. G. Cryogenic sample exchange NMR probe for magic angle spinning dynamic nuclear polarization. *J. Magn. Reson.* **2009**, *198*, 261. DOI: 10.1016/j.jmr.2009.03.003
- [20] Martin, R. W.; Paulson, E. K.; Zilm, K. W. Design of a triple resonance magic angle sample spinning probe for high field solid state nuclear magnetic resonance. *Rev. Sci. Instrum.* **2003**, *74*, 3045. DOI: 10.1063/1.1571951
- [21] Paulson, E. K.; Martin, R. W.; Zilm, K. W. Cross polarization, radio frequency field homogeneity, and circuit balancing in high field solid state NMR probes. *J. Magn. Reson.* **2004**, *171*, 314. DOI: 10.1016/j.jmr.2004.09.009
- [22] Hu, J. Balanced multi-resonant transmission line nuclear magnetic resonance probes. Ph.D. Thesis, Brandeis University, 2010. <http://search.proquest.com/docview/305185343>
- [23] Frydel, J. A.; Krzystyniak, M.; Pienkowski, D.; Pietrzak, M.; Amadeu, N. d. S.; Ratajczyk, T.; Idzik, K.; Gutmann, T.; Tietze, D.; Voigt, S.; Fenn, A.; Limbach, H. H.; Buntkowsky, G. Efficient design of multituned transmission line NMR probes: The electrical engineering approach. *Solid State Nucl. Magn. Reson.* **2011**, *39*, 72. DOI: 10.1016/j.ssnmr.2011.01.001
- [24] Renault, M.; Cukkemane, A.; Baldus, M. Solid-State NMR Spectroscopy on Complex Biomolecules. *Angew. Chem., Int. Ed.* **2010**, *49*, 8346. DOI: 10.1002/anie.201002823
- [25] Lesage, A. Recent advances in solid-state NMR spectroscopy of spin $I = 1/2$ nuclei. *Phys. Chem. Chem. Phys.* **2009**, *11*, 6876. DOI: 10.1039/b907733m
- [26] Andronesi, O. C.; von Bergen, M.; Biernat, J.; Seidel, K.; Griesinger, C.; Mandelkow, E.; Baldus, M. Characterization of Alzheimer's-like Paired Helical Filaments from the Core Domain of Tau Protein Using Solid-State NMR Spectroscopy. *J. Am. Chem. Soc.* **2008**, *130*, 5922. DOI: 10.1021/ja7100517
- [27] Etkorn, M.; Boeckmann, A.; Lange, A.; Baldus, M. Probing Molecular Interfaces Using 2D Magic-Angle-Spinning NMR on Protein Mixtures with Different Uniform Labeling. *J. Am. Chem. Soc.* **2004**, *126*, 14746. DOI: 10.1021/ja0479181
- [28] Lange, A.; Becker, S.; Seidel, K.; Giller, K.; Pongs, O.; Baldus, M. A concept for rapid protein-structure determination by solid-state NMR spectroscopy. *Angew. Chem., Int. Ed.* **2005**, *44*, 2089. DOI: 10.1002/anie.200462516

- [29] Cady, S. D.; Schmidt-Rohr, K.; Wang, J.; Soto, C. S.; De Grado, W. F.; Hong, M. Structure of the amantadine binding site of influenza M2 proton channels in lipid bilayers. *Nature* **2010**, *463*, 689. DOI: 10.1038/nature08722
- [30] Griffin, R. G. Dipolar recoupling in MAS spectra of biological solids. *Nat. Struct. Biol.* **1998**, *5*, 508. DOI: 10.1038/749
- [31] Mak-Jurkauskas, M. L.; Bajaj, V. S.; Hornstein, M. K.; Belenky, M.; Griffin, R. G.; Herzfeld, J. Energy transformations early in the bacteriorhodopsin photocycle revealed by DNP-enhanced solid-state NMR. *Proc. Natl. Acad. Sci. U.S.A.* **2008**, *105*, 883. DOI: 10.1073/pnas.0706156105
- [32] Castellani, F.; van Rossum, B.-J.; Diehl, A.; Rehbein, K.; Oschkinat, H. Determination of solid-state NMR structures of proteins by means of three-dimensional ¹⁵N-¹³C-¹³C dipolar correlation spectroscopy and chemical shift analysis. *Biochemistry* **2003**, *42*, 11476. DOI: 10.1021/bi034903r S0006-2960(03)04903-1
- [33] Hong, M.; Su, Y. Structure and dynamics of cationic membrane peptides and proteins: insights from solid-state NMR. *Protein Sci.* **2011**, *20*, 641. DOI: 10.1002/pro.600
- [34] Brown, S. P.; Spiess, H. W. Advanced solid-state NMR methods for the elucidation of structure and dynamics of molecular, macromolecular, and supramolecular systems. *Chem. Rev.* **2001**, *101*, 4125. DOI: 10.1021/cr990132e
- [35] Ladizhansky, V. Dipolar-Based Torsion Angle Measurements for Protein Structure Determination. In *Encyclopedia of Magnetic Resonance*; John Wiley & Sons, Ltd: 2007. DOI: 10.1002/9780470034590.emrstml153
- [36] Zhou, D. H. Fast Magic Angle Spinning for Protein Solid-State NMR Spectroscopy. In *Encyclopedia of Magnetic Resonance*; John Wiley & Sons, Ltd: 2007. DOI: 10.1002/9780470034590.emrstml150
- [37] De Paepe, G.; Lewandowski, J. R.; Loquet, A.; Boeckmann, A.; Griffin, R. G. Proton assisted recoupling and protein structure determination. *J. Chem. Phys.* **2008**, *129*, 245101/1. DOI: 10.1063/1.3036928
- [38] Ishii, Y. ¹³C-¹³C dipolar recoupling under very fast magic angle spinning in solid-state nuclear magnetic resonance: Applications to distance measurements, spectral assignments, and high-throughput secondary-structure determination. *J. Chem. Phys.* **2001**, *114*, 8473. DOI: 10.1063/1.1359445
- [39] Barnes, A. B.; Andreas, L. B.; Huber, M.; Ramachandran, R.; van der Wel, P. C. A.; Veshtort, M.; Griffin, R. G.; Mehta, M. A. High-resolution solid-state NMR structure of Alanyl-Prolyl-Glycine. *J. Magn. Reson.* **2009**, *200*, 95. DOI: 10.1016/j.jmr.2009.06.009
- [40] Van der Wel, P. C. A.; Lewandowski, J. R.; Griffin, R. G. Solid-State NMR Study of Amyloid Nanocrystals and Fibrils Formed by the Peptide GNNQQNY from Yeast Prion Protein Sup35p. *J. Am. Chem. Soc.* **2007**, *129*, 5117. DOI: 10.1021/ja068633m
- [41] Grant Christopher, V.; Wu Chin, H.; Opella Stanley, J. Probes for high field solid-state NMR of lossy biological samples. *J. Magn. Reson.* **2010**, *204*, 180. DOI: 10.1016/j.jmr.2010.03.011

- [42] Carduner, K.; Villa, M.; White, D. Variable-temperature solid-state nuclear-magnetic-resonance probe for superconducting magnets operating in the range 3-350 K. *Rev. Sci. Instrum.* **1984**, *55*, 68. DOI: 10.1063/1.1137592
- [43] Dillmann, B.; Elbayed, K.; Zeiger, H.; Weingertner, M.-C.; Piotta, M.; Engelke, F. A novel low-E field coil to minimize heating of biological samples in solid-state multinuclear NMR experiments. *J. Magn. Reson.* **2007**, *187*, 10. DOI: 10.1016/j.jmr.2007.02.018
- [44] Gor'kov, P. L.; Chekmenev, E. Y.; Fu, R.; Hu, J.; Cross, T. A.; Cotten, M.; Brey, W. W. A large volume flat coil probe for oriented membrane proteins. *J. Magn. Reson.* **2006**, *181*, 9. DOI: 10.1016/j.jmr.2006.03.008
- [45] Gor'kov, P. L.; Chekmenev, E. Y.; Li, C.; Cotten, M.; Buffy, J. J.; Traaseth, N. J.; Veglia, G.; Brey, W. Using low-E resonators to reduce RF heating in biological samples for static solid-state NMR up to 900 MHz. *J. Magn. Reson.* **2007**, *185*, 77. DOI: 10.1016/j.jmr.2006.11.008
- [46] Li, Y.; Logan, T. M.; Edison, A. S.; Webb, A. Design of small volume HX and triple-resonance probes for improved limits of detection in protein NMR experiments. *J. Magn. Reson.* **2003**, *164*, 128. DOI: 10.1016/s1090-7807(03)00184-8
- [47] Peshkovsky, A. S.; Forguez, J.; Cerioni, L.; Pusiol, D. J. RF probe recovery time reduction with a novel active ringing suppression circuit. *J. Magn. Reson.* **2005**, *177*, 67. DOI: 10.1016/j.jmr.2005.07.004
- [48] Privalov, A. F.; Dvinskikh, S. V.; Vieth, H. M. Coil Design for Large-Volume High-B1 Homogeneity for Solid-State NMR Applications. *J. Magn. Reson. A* **1996**, *123*, 157. DOI: 10.1006/jmra.1996.0229
- [49] Stringer, J. A.; Bronnimann, C. E.; Mullen, C. G.; Zhou, D. H.; Stellfox, S. A.; Li, Y.; Williams, E. H.; Rienstra, C. M. Reduction of RF-induced sample heating with a scroll coil resonator structure for solid-state NMR probes. *J. Magn. Reson.* **2005**, *173*, 40. DOI: 10.1016/j.jmr.2004.11.015
- [50] Kubo, A.; Ichikawa, S. Ultra-broadband NMR probe: numerical and experimental study of transmission line NMR probe. *J. Magn. Reson.* **2003**, *162*, 284. DOI: 10.1016/s1090-7807(03)00014-4
- [51] Krahn, A.; Priller, U.; Emsley, L.; Engelke, F. Resonator with reduced sample heating and increased homogeneity for solid-state NMR. *J. Magn. Reson.* **2008**, *191*, 78. DOI: 10.1016/j.jmr.2007.12.004
- [52] Rainey, J. K.; DeVries, J. S.; Sykes, B. D. Estimation and measurement of flat or solenoidal coil inductance for radiofrequency NMR coil design. *J. Magn. Reson.* **2007**, *187*, 27. DOI: 10.1016/j.jmr.2007.03.016
- [53] Haase, J.; Curro, N. J.; Slichter, C. P. Double resonance probes for close frequencies. *J. Magn. Reson.* **1998**, *135*, 273. DOI: 10.1006/jmre.1998.1579
- [54] Hill, H. D. W. Probes for High Resolution. In *Encyclopedia of Magnetic Resonance*; John Wiley & Sons, Ltd: 2007. DOI: 10.1002/9780470034590.emrstm0415
- [55] McKay, R. A. Probes for Special Purposes. In *Encyclopedia of Magnetic Resonance*; John Wiley & Sons, Ltd: 2007. DOI: 10.1002/9780470034590.emrstm0416

- [56] Gor'kov, P. L.; Brey, W. W.; Long, J. R. Probe Development for Biosolids NMR Spectroscopy. In *Encyclopedia of Magnetic Resonance*; John Wiley & Sons, Ltd: 2007. DOI: 10.1002/9780470034590.emrstml149
- [57] Qian, C.; Masad, I. S.; Rosenberg, J. T.; Elumalai, M.; Brey, W. W.; Grant, S. C.; Gor'kov, P. L. A volume birdcage coil with an adjustable sliding tuner ring for neuroimaging in high field vertical magnets: Ex and in vivo applications at 21.1 T. *J. Magn. Reson.* **2012**, *221*, 110. DOI: 10.1016/j.jmr.2012.05.016
- [58] Litvak, I. M.; Espinosa, C. A.; Shapiro, R. A.; Oldham, A. N.; Duong, V. V.; Martin, R. W. Pneumatic switched angle spinning NMR probe with capacitively coupled double saddle coil. *J. Magn. Reson.* **2010**, *206*, 183. DOI: 10.1016/j.jmr.2010.07.001
- [59] Gor'kov, P. L.; Witter, R.; Chekmenev, E. Y.; Nozirov, F.; Fu, R.; Brey, W. W. Low-E probe for ¹⁹F-¹H NMR of dilute biological solids. *J. Magn. Reson.* **2007**, *189*, 182. DOI: 10.1016/j.jmr.2007.09.008
- [60] Hagaman, E. W.; Jiao, J.; Moore, T. The generation of intense radiofrequency fields in μ coils. *J. Magn. Reson.* **2008**, *193*, 150. DOI: 10.1016/j.jmr.2008.04.022
- [61] Janssen, H.; Brinkmann, A.; Van Eck, E. R. H.; Van Bentum, P. J. M.; Kentgens, A. P. M. Microcoil High-Resolution Magic Angle Spinning NMR Spectroscopy. *J. Am. Chem. Soc.* **2006**, *128*, 8722. DOI: 10.1021/ja061350+
- [62] Seeber, D. A.; Cooper, R. L.; Ciobanu, L.; Pennington, C. H. Design and testing of high sensitivity microreceiver coil apparatus for nuclear magnetic resonance and imaging. *Rev. Sci. Instrum.* **2001**, *72*, 2171. DOI: 10.1063/1.1359190
- [63] Peck, T. L.; Magin, R. L.; Lauterbur, P. C. Design and analysis of microcoils for NMR microscopy. *J. Magn. Reson. B* **1995**, *108*, 114. DOI: 10.1006/jmrb.1995.1112
- [64] Barnes, A. B.; Mak-Jurkauskas, M. L.; Markhasin, E.; Hu, J.; Matsuki, Y.; Lugtenburg, J.; Herzfeld, J.; Griffin, R. G. In *Instrumentation for Cryogenic MAS and High-Field Dynamic Nuclear Polarization*. Magnetic Resonance Gordon Research Conference, University of New England, Biddeford, ME, June 14-19, 2009.
- [65] Barnes, A. B.; Markhasin, E.; Daviso, E.; Michaelis, V. K.; Nanni, E. A.; Jawla, S. K.; Mena, E. L.; DeRocher, R.; Thakkar, A.; Woskov, P. P.; Herzfeld, J.; Temkin, R. J.; Griffin, R. G. Dynamic Nuclear Polarization at 700 MHz / 460 GHz. *J. Magn. Reson.* **2012**, *224*, 1. DOI: 10.1016/j.jmr.2012.08.002
- [66] Barnes, A. B.; De Paepe, G.; van der Wel, P. C. A.; Hu, K. N.; Joo, C. G.; Bajaj, V. S.; Mak-Jurkauskas, M. L.; Sirigiri, J. R.; Herzfeld, J.; Temkin, R. J.; Griffin, R. G. High-field dynamic nuclear polarization for solid and solution biological NMR. *Appl. Magn. Reson.* **2008**, *34*, 237. DOI: 10.1007/s00723-008-0129-1
- [67] Van der Wel, P. C. A.; Hu, K.-N.; Lewandowski, J.; Griffin, R. G. Dynamic Nuclear Polarization of Amyloidogenic Peptide Nanocrystals: GNNQQNY, a Core Segment of the Yeast Prion Protein Sup35p. *J. Am. Chem. Soc.* **2006**, *128*, 10840. DOI: 10.1021/ja0626685
- [68] Maly, T.; Debelouchina, G. T.; Bajaj, V. S.; Hu, K.-N.; Joo, C.-G.; Mak-Jurkauskas, M. L.; Sirigiri, J. R.; van der Wel, P. C. A.; Herzfeld, J.; Temkin, R. J.; Griffin, R. G. Dy-

- dynamic nuclear polarization at high magnetic fields. *J. Chem. Phys.* **2008**, *128*, 052211/1. DOI: 10.1063/1.2833582
- [69] Debelouchina, G. T.; Bayro, M. J.; van der Wel, P. C. A.; Caporini, M. A.; Barnes, A. B.; Rosay, M.; Maas, W. E.; Griffin, R. G. Dynamic nuclear polarization-enhanced solid-state NMR spectroscopy of GNNQQNY nanocrystals and amyloid fibrils. *Phys. Chem. Chem. Phys.* **2010**, *12*, 5911. DOI: 10.1039/c003661g
- [70] Bajaj, V. S.; van der Wel, P. C. A.; Griffin, R. G. Observation of a Low-Temperature, Dynamically Driven Structural Transition in a Polypeptide by Solid-State NMR Spectroscopy. *J. Am. Chem. Soc.* **2009**, *131*, 118. DOI: 10.1021/ja8045926
- [71] Lesage, A.; Lelli, M.; Gajan, D.; Caporini, M. A.; Vitzthum, V.; Mieville, P.; Alauzun, J.; Roussey, A.; Thieuleux, C.; Mehdi, A.; Bodenhausen, G.; Coperet, C.; Emsley, L. Surface Enhanced NMR Spectroscopy by Dynamic Nuclear Polarization. *J. Am. Chem. Soc.* **2010**, *132*, 15459. DOI: 10.1021/ja104771z
- [72] Vitzthum, V.; Mieville, P.; Carnevale, D.; Caporini, M. A.; Gajan, D.; Coperet, C.; Lelli, M.; Zagdoun, A.; Rossini, A. J.; Lesage, A.; Emsley, L.; Bodenhausen, G. Dynamic nuclear polarization of quadrupolar nuclei using cross polarization from protons: surface-enhanced aluminium-27 NMR. *Chem. Commun.* **2012**, *48*, 1988. DOI: 10.1039/c2cc15905h
- [73] Smith, A. A.; Corzilius, B.; Barnes, A. B.; Maly, T.; Griffin, R. G. Solid effect dynamic nuclear polarization and polarization pathways. *J. Chem. Phys.* **2012**, *136*, 015101/1. DOI: 10.1063/1.3670019
- [74] Denysenkov, V.; Prandolini, M. J.; Gafurov, M.; Sezer, D.; Endeward, B.; Prisner, T. F. Liquid state DNP using a 260 GHz high power gyrotron. *Phys. Chem. Chem. Phys.* **2010**, *12*, 5786. DOI: 10.1039/c003697h
- [75] Degen, C. L.; Poggio, M.; Mamin, H. J.; Rettner, C. T.; Rugar, D. Nanoscale magnetic resonance imaging. *Proc. Natl. Acad. Sci. U.S.A.* **2009**, *106*, 1313. DOI: 10.1073/pnas.0812068106
- [76] Krahn, A.; Lottmann, P.; Marquardsen, T.; Tavernier, A.; Tuerke, M.-T.; Reese, M.; Leonov, A.; Bennati, M.; Hofer, P.; Engelke, F.; Griesinger, C. Shuttle DNP spectrometer with a two-center magnet. *Phys. Chem. Chem. Phys.* **2010**, *12*, 5830. DOI: 10.1039/c003381b
- [77] Feintuch, A.; Shimon, D.; Hovav, Y.; Banerjee, D.; Kaminker, I.; Lipkin, Y.; Zibzener, K.; Epel, B.; Vega, S.; Goldfarb, D. A Dynamic Nuclear Polarization spectrometer at 95 GHz/144 MHz with EPR and NMR excitation and detection capabilities. *J. Magn. Reson.* **2011**, *209*, 136. DOI: 10.1016/j.jmr.2010.12.010
- [78] Nagel, L. W.; Pederson, D. O. *SPICE (Simulation Program with Integrated Circuit Emphasis)*, EECS Department, University of California, Berkeley, 1973.
- [79] APLAC. 9.0: AWR.
- [80] Horowitz, P.; Hill, W. *The art of electronics*; 2nd ed.; Cambridge University Press: Cambridge [England] ; New York, 1989.

- [81] Terman, F. E. *Radio engineer's handbook*; 1st ed.; McGraw-Hill Book Company, inc.: New York, London,, 1943.
- [82] Agarwal, A.; Lang, J. *Foundations of analog and digital electronic circuits*; Elsevier-Morgan Kaufmann: Amsterdam ; Boston, 2005.
- [83] Nilsson, J. W.; Riedel, S. A. *Electric circuits*; 9th ed.; Prentice Hall: Upper Saddle River, N.J., 2011.
- [84] Irwin, J. D.; Nelms, R. M. *Basic engineering circuit analysis*; 8th ed.; J. Wiley: Hoboken, NJ, 2005.
- [85] Boylestad, R. L. *Introductory circuit analysis*; 11th ed.; Pearson Prentice Hall: Upper Saddle River, N.J., 2007.
- [86] Orfanidis, S. J. Electromagnetic Waves and Antennas. Accessed online at <http://eceweb1.rutgers.edu/~orfanidi/ewa/> on 09/10/12.
- [87] Tcheslavski, G. V. ELEN-3441 Fundamentals of Power Engineering. Accessed online at <http://ee.lamar.edu/gleb/power/Index.htm> on 09/10/12.
- [88] Jordan, E. C.; Balmain, K. G. *Electromagnetic waves and radiating systems*; 2d ed.; Prentice-Hall: Englewood Cliffs, N.J., 1968.
- [89] Ramo, S.; Whinnery, J. R.; van Duzer, T. *Fields and waves in communication electronics*; 3rd ed.; Wiley: New York, 1994.
- [90] Fukushima, E.; Roeder, S. B. W. *Experimental pulse NMR : a nuts and bolts approach*; Addison-Wesley Pub. Co. Advanced Book Program: Reading, Mass., 1981.
- [91] Mispelter, J.; Lupu, M.; Briguët, A. *NMR probeheads for biophysical and biomedical experiments: theoretical principles & practical guidelines*; Imperial College Press; Distributed by World Scientific: London, Hackensack, NJ, 2006.
- [92] Traficante, D. D. Impedance: What It Is, and Why It Must Be Matched. *Concepts Magn. Reson.* **1989**, *1*, 73
- [93] Cho, S.-I.; Sullivan, N. S. Parameterized description of NMR signal reception systems part I: Impedance of transmission line and probe. *Concepts Magn. Reson.* **1992**, *4*, 227. DOI: 10.1002/cmr.1820040304
- [94] Hoult, D. I. The NMR receiver: A description and analysis of design. *Prog. Nucl. Magn. Reson. Spectrosc.* **1978**, *12*, 41. DOI: 10.1016/0079-6565(78)80002-8
- [95] Jacquinet, J.-F.; Sakellariou, D. NMR signal detection using inductive coupling: applications to rotating microcoils. *Concepts Magn. Reson. A* **2011**, *38A*, 33. DOI: 10.1002/cmr.a.20205
- [96] Hoult, D. I.; Ginsberg, N. S. The Quantum Origins of the Free Induction Decay Signal and Spin Noise. *J. Magn. Reson.* **2001**, *148*, 182. DOI: 10.1006/jmre.2000.2229
- [97] Doty, F. D. Probe Design and Construction. In *Encyclopedia of Magnetic Resonance*; John Wiley & Sons, Ltd: 2007. DOI: 10.1002/9780470034590.emrstml1000
- [98] Circuit Theory. Accessed online at

http://en.wikibooks.org/w/index.php?title=Circuit_Theory/All_Chapters&oldid=891664
on 06/09/07.

- [99] An introduction to electronics. Accessed online at http://en.wikipedia.org/wiki/Book:An_introduction_to_electronics on 04/12/12.
- [100] Anderson, D.; Smith, L.; Gruszynski, J. S-Parameter Techniques for Faster, More Accurate Network Design (Application Note 95-1). 1996.
- [101] Phasor. Accessed online at <http://en.wikipedia.org/wiki/Phasor> on 04/12/12.
- [102] Wave. Accessed online at <http://en.wikipedia.org/wiki/Wave> on 04/12/12.
- [103] Markhasin, E.; Hu, J.; Su, Y.; Herzfeld, J.; Griffin, R. G. Efficient, balanced, transmission line RF circuits by back propagation of common impedance nodes. *J. Magn. Reson.* **2013**, *231*, 32. DOI: 10.1016/j.jmr.2013.02.017
- [104] Tsai, C.-T. Package inductance characterization at high frequencies. *IEEE Trans. Compon. Packag. Manuf. Technol. B* **1994**, *17*, 175. DOI: 10.1109/96.330432
- [105] Skin effect. Accessed online at http://en.wikipedia.org/wiki/Skin_effect on 04/12/12.
- [106] Proximity effect (electromagnetism). Accessed online at [http://en.wikipedia.org/wiki/Proximity_effect_\(electromagnetism\)](http://en.wikipedia.org/wiki/Proximity_effect_(electromagnetism)) on 04/12/12.
- [107] HFSS, High Frequency Structure Simulator: Ansys.
- [108] Chang, K. *Encyclopedia of RF and microwave engineering*; John Wiley: Hoboken, N.J., 2005.
- [109] Lorenz, W. Dimensionierung einlagiger Zylinderluftspulen mit optimaler Güte. *Frequenz* **1970**, *24*, 20. DOI: 10.1515/freq.1970.24.1.20
- [110] Hu, J.; Herzfeld, J. Baluns, a fine balance and impedance adjustment module, a multi-layer transmission line, and transmission line NMR probes using same. Patent #7936171, 2011.
- [111] Hu, J.; Bielecki, A.; Griffin, R. G.; Herzfeld, J. In *A Totally Balanced, Fully Transmission Line, Triple Resonance NMR Probe for High Frequencies*. 49th ENC, Pacific Grove, California, 2008.

7. Precision Calorimetry of Tripeptides Ala-Pro-Gly•H₂O, N-formyl-Met-Leu-Phe-OH, and N-formyl-Met-Leu-Phe-OMe

Adapted from references [1].

Abstract

Heat capacity of tripeptides Ala-Pro-Gly•H₂O, N-formyl-Met-Leu-Phe-OH, and N-formyl-Met-Leu-Phe-OMe was measured by precision adiabatic vacuum calorimetry over the temperature range $T = (6 \text{ to } 350) \text{ K}$. The tripeptides were stable over this temperature range. The first tripeptide exhibited a first-order polymorphic phase transition, while no phase change, transformation, association, or thermal decomposition was observed for the other two tripeptides. The sensitivity of low temperature dynamic scanning calorimetry is evaluated, and the phase transition was well reproduced on a sample as small as 4.7 mg. Calorimetric data is compared to the information obtained from cryogenic magic angle spinning nuclear magnetic resonance and X-ray experiments. The standard thermodynamic functions, molar heat capacity $C_{p,m}^\circ$, enthalpy $H^\circ(T) - H^\circ(0)$, entropy $S^\circ(T)$, and Gibbs energy $G^\circ(T) - H^\circ(0)$, of peptides were calculated over the range $T = (0 \text{ to } 350) \text{ K}$. The low-temperature ($T < 50 \text{ K}$) heat capacity dependence was analyzed using the Debye's and multifractal theories. The standard entropies of formation of peptides at $T = 298.15 \text{ K}$ were calculated.

7.1. Introduction

Elucidating complete or, sometimes, partial atomic level structure of biological molecules, such as peptides and proteins, is essential for subsequent investigation of their function and dysfunction, as well as for understanding biological processes in which these molecules participate. Structural information at the atomic level is primarily provided by diffraction and magnetic resonance techniques. Since both techniques can benefit from low temperatures, these experiments are often performed at cryogenic temperatures. Furthermore, certain techniques, such as Dynamic Nuclear Polarization (DNP) in combination with cryogenic Magic Angle Spinning (MAS) Nuclear Magnetic Resonance (NMR), provide valuable data, which may not be unavailable otherwise. At the same time, it is the ambient temperature structure, which is of interest. Therefore, an important question that must be addressed is how relevant the structural data obtained at lowered temperatures, and whether these data can be used for studying the role and function of biological molecules at their normal operating temperatures.

Several strategies can be used to address this question. For example, spectroscopic techniques may be complemented by calorimetric experiment. Calorimetric techniques, such as Dynamic Scanning Calorimetry (DSC) or adiabatic calorimetry, are particularly suitable for probing temperature dependent changes in structure [2-4]. Additionally, thermodynamic properties can be used for analysis of processes and in thermodynamic databanks [5]. While thermodynamic properties are available for most of the canonical amino acids [2,6-23], in present work, we selected three tripeptides, exhibiting different temperature dependent behavior, that we use as model samples for MAS NMR experiments.

7.2. Experimental Section

7.2.1. Samples

Tripeptides Ala-Pro-Gly (APG, lot 0513046), *N*-formyl-Met-Leu-Phe-OH (MLF-OH, lot 2500845) and *N*-formyl-Met-Leu-Phe-OMe (MLF-OMe, lot 1016424) were purchased from Bachem (King of Prussia, PA). APG was recrystallized from water, while the other two were used without further purification.

The crystal structure of the sample (space group $P2_12_12_1$, $Z=4$ [24]) was confirmed by single-crystal X-ray diffraction (Siemens three-circle Platform diffractometer, results are included in the supporting information) and by powder X-ray diffraction (PANalytical X'Pert Pro multipurpose diffractometer equipped with Oxford Cryosystems PheniX cryostat).

7.2.2. Adiabatic Calorimeter

A precision automatic adiabatic calorimeter (BCT-3) was used to measure heat capacity over the temperature range of $6\text{ K} \leq T \leq 350\text{ K}$. The design and operation of an adiabatic calorimeter are described in detail elsewhere [25-26]. A calorimetric cell is a thin-walled cylindrical vessel made from titanium with a volume of $1.5 \cdot 10^{-6}\text{ m}^3$ and mass $(1.626 \pm 0.005)\text{ g}$. A miniature iron-rhodium resistance thermometer (nominal resistance $100\ \Omega$, calibrated on ITS-90 standard by the Russian Metrology Research Institute, Moscow region, Russia) was used to measure the temperature of the sample. Temperature difference between the ampule and an adiabatic shield

was controlled by a four-junction copper-iron-chromel thermocouple. The sensitivity of the thermometric circuit was $1 \cdot 10^{-3}$ K and that of the analog-to-digital converter was 0.1 μ V. The speed of the computer-controlled measuring system was 10 points per second. The accuracy of the calorimeter was verified using standard reference samples (K-2 benzoic acid and α -Al₂O₃) [27-28] prepared by the Institute of Metrology of the State Standard Committee of the Russian Federation. It was established that the measurement error of heat capacity did not exceed $\pm 2\%$, $\pm 0.5\%$, and $\pm 0.2\%$ within temperature ranges $T = (6 \text{ to } 15) \text{ K}$, $(15 \text{ and } 40) \text{ K}$, and $40 \leq (T/\text{K}) \leq 350$ respectively; and that measurement errors of phase transition temperature and its enthalpy did not exceed $\pm 0.01 \text{ K}$ and $\pm 0.2\%$ respectively.

7.2.3. Heat Capacity Measurements

0.2438 g of N-*f*-MLF-OH ($M = 437.56 \text{ g} \cdot \text{mol}^{-1}$, 0.557 mmol) or 0.2716 g of N-*f*-MLF-OMe ($M = 451.59 \text{ g} \cdot \text{mol}^{-1}$, 0.601 mmol) was placed in a calorimetric cell, and the ampule was then filled with dry helium gas (4 kPa, room temperature) to facilitate the heat exchanging process. Initially, the samples were cooled to the temperature of the measurement onset ($\sim 6 \text{ K}$) at a rate of 0.01 K s^{-1} . Then the samples were heated in $0.5 - 2 \text{ K}$ increments at a rate of 0.01 K s^{-1} . Sample temperature was recorded after an equilibration period (temperature drift $< 0.01 \text{ K} \cdot \text{s}^{-1}$, approximately 10 min per point).

The experimental values of $c_{p,m}^{\circ}$ (156 and 187 points for N-*f*-MLF-OH and N-*f*-MLF-OMe, respectively) were collected using liquid helium as a cryogen in the intervals $6 \text{ K} \leq T \leq 88 / 96 \text{ K}$ (Series 1) and using liquid nitrogen in the intervals $T = (83 \text{ to } 349) / (90 \text{ to } 343) \text{ K}$ (Series 2) for N-*f*-MLF-OH and N-*f*-MLF-OMe, respectively.

The heat capacity of the samples was between 55 % and 83 % of the overall heat capacity of the calorimetric ampule. The molar masses were calculated from the IUPAC table of atomic weights [29].

7.3. Results and Discussion

7.3.1. Heat Capacity Measurements

Experimental data for the isobaric heat capacity of N-*f*-MLF-OH, N-*f*-MLF-OMe, and APG over the range $T = (6 \text{ to } 350) \text{ K}$ are presented in Table 3, 4, and 5 and Figure 59 and 60. The heat capacity of the samples rises gradually with temperature. The tripeptides were stable over the studied temperature range. No phase change, transformation, association, or thermal decomposition was observed for N-*f*-MLF-OH and N-*f*-MLF-OMe, while APG exhibited a first-order polymorphic phase transition. The experimental data were smoothed using least squares polynomial fits as follows:

$$C_{p,m}^{\circ} = \begin{cases} \sum_{i=0}^7 A_i \ln\left(\frac{T}{30}\right)^i, & \delta = \pm 0.6\%, \quad 6\text{K} \leq T \leq 40\text{K} \\ \sum_{i=0}^6 B_i \left(\frac{T}{30}\right)^i, & \delta = \pm 0.3\%, \quad 40\text{K} \leq T \leq 350\text{K} \end{cases},$$

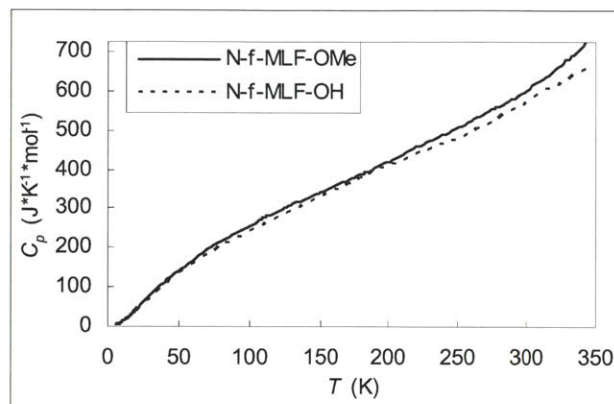


Figure 59. Experimental temperature dependence of heat capacity of N-*f*-MLF-OH and N-*f*-MLF-OMe.

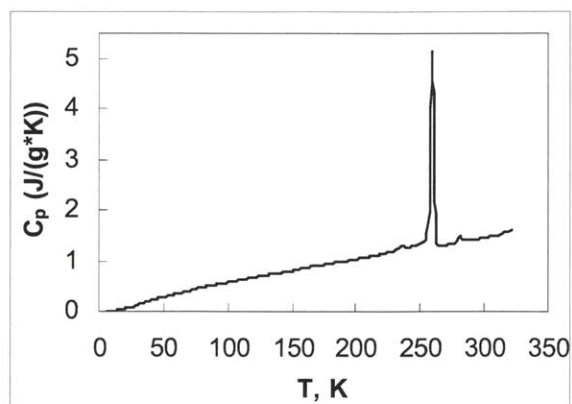


Figure 60. Experimental temperature dependence of heat capacity of APG.

where A_i and B_i are polynomial coefficients and δ is relative deviation of experimental data from the smoothing functions. The temperature dependencies of heat capacities of N-*f*-MLF-OH and N-*f*-MLF-OMe are similar below 50 K. This tendency can be expected, since skeletal vibrations provide the main contribution to heat capacity in this range.

Heat capacity of APG was also studied using dynamic scanning calorimetry to test the sensitivity of the technique Figure 61. The observed phase transition was well reproduced with samples as small as 4.7 mg.

Low-temperature heat capacity data were also analyzed using the Debye theory [30] and the fractal theory of heat capacity [31].

According to the fractal theory [31],

$$C_v = 3D(D+1)kN\gamma(D+1)\zeta(D+1)\frac{1}{\Theta_{\max}^D}T^D, \quad (61)$$

where D is the fractal dimension, N is the number of atoms in a molecular unit, k is the Boltzmann constant, γ is the γ -function, ζ is the Riemann ζ -function, and Θ_{\max} is the characteristic temperature. Equation (61) can be rewritten as follows:

$$\ln(C_v) = A + D \ln(T),$$

which can be used to obtain D and Θ_{\max} .

Since below 50 K $C_p \approx C_v$, experimental data in the range $20 \text{ K} \leq T \leq 50 \text{ K}$ were used and yielded $D = 1.6$ and 1.8 and $\Theta_{\max} = 202.8 \text{ K}$ and 183.0 K for N-*f*-MLF-OH and N-*f*-MLF-OMe, respectively. The obtained parameters and Equation (61) reproduced the experimental data in the same temperature range with a relative error of $\pm 0.8 \%$.

According to the multifractal theory of heat capacity [31], $D = 1$ corresponds to solids with a chain structure, $D = 2$ corresponds to solids with a layered structure, and $D = 3$ corresponds to solids

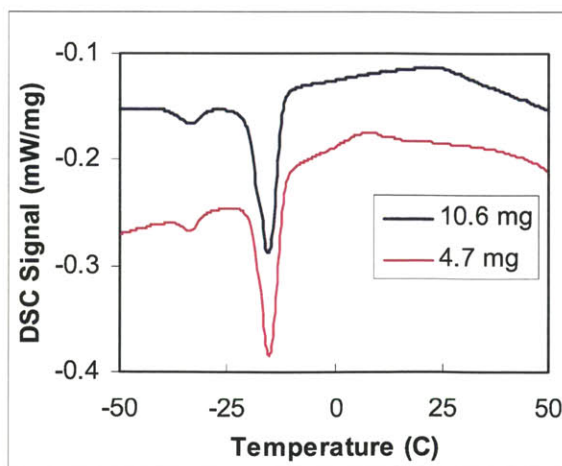


Figure 61. DSC curves for small samples of APG.

with a lattice characterized by comparable interactions in all three dimensions. Obtained values of D for both tripeptides are indicative of the chain-layer structure.

Debye theory was used to fit the experimental data in the range $6 \text{ K} \leq T \leq 12 \text{ K}$ and extrapolate it to 0 K [30]

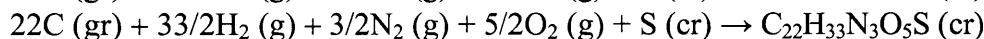
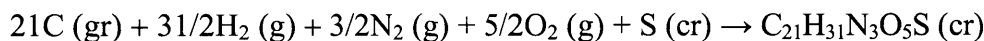
$$C_{p,m}^{\circ} = nD\left(\frac{\Theta_D}{T}\right), \quad (62)$$

where n is the number of degrees of freedom, D is the Debye function, and Θ_D is the Debye characteristic temperature. Using this equation, we obtained $n = 4$ and 6 and $\Theta_D = 56.7$ and 62.2 K for N-f-MLF-OH and N-f-MLF-OMe, respectively. The obtained parameters and eq. 3 reproduced the experimental data in the same temperature range with a relative error of ± 1.3 %. In subsequent calculations, we assumed that Equation (62) described heat capacity in the range $0 \text{ K} \leq T \leq 6 \text{ K}$ with the same relative error.

7.3.2. Standard Thermodynamic Functions of Tripeptides

The calculations of $H^{\circ}(T) - H^{\circ}(0)$ and $S^{\circ}(T)$ were made by numerical integration of heat capacity with respect to T and $\ln T$, respectively, as described in detail elsewhere [32]. Gibbs energy $G^{\circ}(T) - H^{\circ}(0)$ was calculated from enthalpy and entropy values. The zero entropy for all samples was assumed to be zero. Calculated functions are presented in Table 6, 7, and 8 and have relative errors ± 2 %, ± 0.6 %, and ± 0.3 % in ranges $T < 15 \text{ K}$, $15 \text{ K} \leq T \leq 40 \text{ K}$, and $40 \text{ K} \leq T \leq 350 \text{ K}$, respectively.

Using the values of absolute entropies of studied tripeptides and of elemental substances, including carbon,[33] hydrogen,[34] nitrogen,[33] oxygen,[34] and sulfur,[34] standard entropies of formation



where gr, cr and g are graphite, crystal, and gas respectively, were calculated:

$$\Delta_f S_m^{\circ}(298.15, \text{N-f-MLF-OH, cr}) = -2348 \pm 21 \text{ J} \cdot \text{K}^{-1} \cdot \text{mol}^{-1},$$

$$\Delta_f S_m^{\circ}(298.15, \text{N-f-MLF-OMe, cr}) = -2448 \pm 22 \text{ J} \cdot \text{K}^{-1} \cdot \text{mol}^{-1}$$

7.4. Conclusions

This work reports heat capacity of crystalline tripeptides N-formyl-Met-Leu-Phe-OH, N-formyl-Met-Leu-Phe-OMe, and Ala-Pro-Gly measured over the range $T = (6 \text{ to } 350) \text{ K}$ by precise adiabatic vacuum calorimetry. The standard thermodynamic functions of N-f-MLF-OH and N-f-MLF-OMe over the range $T = (0 \text{ to } 350) \text{ K}$ were calculated.

The low-temperature ($T < 50 \text{ K}$) heat capacity dependence was analyzed using the Debye's and multifractal theories, and the chain-layer structures topology was established.

Table 3. Experimental Molar Heat Capacity of Crystalline N-f-MLF-OH.

T (K)	$C_{p,m}$ (J* mol^{-1} *K $^{-1}$)						
Series 1							
6.07	3.03	9.27	8.3	16.23	26.48	44.97	118.8
6.2	3.36	9.44	9.17	16.73	28.13	47.45	124.6
6.39	3.61	9.62	9.38	17.24	29.68	49.34	129.9
6.58	3.95	9.8	9.82	17.76	31.41	50.8	134.7
6.77	4.09	9.98	10	18.29	32.48	54.2	143.5
6.95	4.46	10.26	10.5	18.81	34.25	56.9	149.6
7.13	4.64	10.67	11	19.34	36.24	59	154.9
7.31	5.02	11.08	11.5	19.87	38.47	61.1	159.7
7.49	5.4	11.52	12.5	21.37	44.43	64.2	166.3
7.66	5.64	11.95	13.4	23.57	51.73	67.25	173.7
7.84	5.84	12.39	15.2	25.84	59.41	69.89	180.6
8.02	6.22	12.85	16.5	28.14	67.29	72.43	186.4
8.19	6.56	13.31	17	30.47	75.15	75.35	193.1
8.37	6.65	13.78	18.1	32.83	82.65	77.93	197.9
8.55	7.15	14.29	19.5	35.21	90.33	80	202.2
8.72	7.42	14.76	21.3	37.62	97.96	83.2	207.8
8.92	7.63	15.24	23.4	40.05	105.2	85.77	213.1
9.1	7.8	15.73	24.77	42.5	112.5	87.5	215.7
Series 2							
83.9	210	162.34	345.7	218.3	433.6	285.29	546.2
86.84	216	165.75	352.2	220.18	434.9	288.58	552.1
90.2	221.9	169.1	358.5	223.47	439.6	293.3	564
93.7	228.4	171.03	363.2	226.98	445.4	297.8	569.2
96.85	234	174.39	366.7	230.48	451.2	301.54	577.7
100.96	240.6	176.01	369	238.8	464.7	304.73	584.4
104.77	248.7	177.95	374.1	242.45	469.1	307.89	590.6
110	259	179.11	375.4	244.9	472.6	311.05	596
114.57	267	181.51	379.4	246.3	474.8	313.2	599.5
118.1	273.3	182.44	381.6	247.7	474.8	316	602.2
121.64	279	185.9	388.3	250	478.6	318.33	605.8
128.71	291.7	188.64	393.2	253.99	484.7	321.4	610.8
132.24	297.1	192.2	399.6	257.43	489.4	326.18	619.5
135.78	305.4	195.77	405	260.84	494.6	329.7	626.6
139.31	312.3	199.33	410.4	267.6	507.4	331.99	630.9
142.85	318.5	200.73	412.6	270.95	513.7	334.86	638.4
146.39	323.5	204.09	416.6	273.8	518.1	337.66	643.6
149.76	327.1	207.65	420.2	277.59	524.9	340.47	648.2
156.66	336.9	211.2	423.3	280.88	532.5	342.7	653.7
158.99	340.4	214.75	427.8	282.23	537.3	346.02	662.6

Table 4. Experimental Molar Heat Capacity of Crystalline N-f-MLF-OMe.

T (K)	$C_{p,m}$ ($J \cdot mol^{-1} \cdot K^{-1}$)	T (K)	$C_{p,m}$ ($J \cdot mol^{-1} \cdot K^{-1}$)	T (K)	$C_{p,m}$ ($J \cdot mol^{-1} \cdot K^{-1}$)	T (K)	$C_{p,m}$ ($J \cdot mol^{-1} \cdot K^{-1}$)
Series 1							
6.02	2.6	8.98	9.89	15.6	26.78	44.78	127.7
6.13	2.71	9.13	10.3	15.99	28	47.26	134.1
6.28	2.91	9.3	10.7	16.64	29.85	49.75	139.9
6.43	3.21	9.45	11	17.1	31.58	52.01	145.9
6.59	3.52	9.62	11.5	17.62	33.24	54.78	153.1
6.73	3.88	9.78	11.8	18.1	34.79	57.3	161.2
6.88	4.29	9.95	12.3	18.78	37.21	59.87	167.1
7.04	4.56	10.27	13.2	19.22	38.75	62.41	174.3
7.19	4.97	10.63	14.1	19.72	40.59	64.96	180.2
7.35	5.42	11.04	15	21.41	47.32	66.9	186.5
7.52	5.83	11.45	16	23.4	55.2	70.06	193.1
7.66	6.28	11.88	17.1	25.67	63.45	72.6	201
7.84	6.73	12.29	18	27.96	71.89	75.15	207.1
7.98	7.23	12.79	19.2	30.29	80.5	77.73	212.1
8.17	7.72	13.24	20.4	32.65	88.71	80.1	216.1
8.33	8.13	13.71	21.7	35.04	96.64	82.93	221.7
8.5	8.58	14.18	22.7	37.44	105	85.5	226.2
8.7	9.08	14.65	24.1	39.87	112.9	88.2	231.2
8.84	9.48	15.12	25.3	42.32	120.6	90.85	237.1
Series 2							
90.6	238.4	163.28	361.6	210.28	436.5	252.78	509.6
93.51	243.4	296.39	591.6	212.77	442.5	254.83	514.5
96.19	248.8	298.4	596.2	215.23	446.4	257.07	518.7
98.88	253.3	300.24	601.4	217.6	450.8	259.3	523.3
101.58	258.9	302.09	606.6	220.02	455.6	261.5	528
104.28	264	304.77	614.7	222.4	463	263.68	532.6
106.98	269.4	307.42	624.6	224.71	467.6	265.84	537.8
109.69	274.9	309.83	631	227.02	471.4	267.99	543.3
112.38	279.5	312.19	630.9	229.33	476.7	270.16	546
115.08	284.3	314.41	635	231.66	479.9	272.34	549.8
117.78	289.3	165.92	365.7	234	481.3	274.5	552.1
120.47	293.3	168.56	368.7	316.68	638.7	276.67	557.8
123.16	297.5	171.19	373.7	318.91	645.4	277.1	557.8
125.85	302.5	174.6	377.8	321.09	652.2	279.97	561.2
128.53	306.7	176.09	381.9	323.22	661.1	282.11	564.9
131.22	310.6	179.5	385.9	325.19	665.5	284.23	568.8
133.99	316.2	182.11	390.6	327.12	669.6	286.34	571.5
136.67	319.1	184.71	394.8	329.13	677.2	288.8	578
139.35	323.5	187.31	400.2	330.96	681.9	290.49	581
142.02	328.1	189.9	403.2	332.75	688.8	292.53	584.6
144.68	332.5	192.49	408.7	236.36	484.2	294.54	587.8
147.35	336.5	195.07	410.5	238.72	488	334.5	691.9
150.01	340.6	197.64	414.8	241.09	490.9	335.18	698

T (K)	$C_{p,m}$ ($J \cdot mol^{-1} \cdot K^{-1}$)	T (K)	$C_{p,m}$ ($J \cdot mol^{-1} \cdot K^{-1}$)	T (K)	$C_{p,m}$ ($J \cdot mol^{-1} \cdot K^{-1}$)	T (K)	$C_{p,m}$ ($J \cdot mol^{-1} \cdot K^{-1}$)
152.68	344.7	200.2	420	243.46	493.2	336.88	700.5
155.33	348.5	202.74	423.8	245.83	495.6	338.54	704.4
157.99	352.7	205.27	428.2	248.18	499.9	340.17	710.6
160.64	357.1	207.77	433.6	250.5	504.2	341.74	717

Table 5. Experimental Molar Heat Capacity of Crystalline APG•H₂O.

T (K)	$C_{p,m}$ ($J \cdot mol^{-1} \cdot K^{-1}$)	T (K)	$C_{p,m}$ ($J \cdot mol^{-1} \cdot K^{-1}$)	T (K)	$C_{p,m}$ ($J \cdot mol^{-1} \cdot K^{-1}$)	T (K)	$C_{p,m}$ ($J \cdot mol^{-1} \cdot K^{-1}$)
Series 1							
6.0946	0.8123	9.6	1.62	17.941	10.51	57.296	83.68
6.2949	0.8653	9.8098	1.706	18.46	11.22	59.858	88.96
6.4893	0.9093	9.9758	1.805	19.037	12.05	62.026	92.76
6.6831	0.9328	10.242	1.912	19.564	12.9	64.602	97.2
6.8661	0.9955	10.626	2.207	20.502	14.19	67.203	101.6
7.0477	1.019	11.019	2.442	21.76	16.7	70.024	106.8
7.2287	1.056	11.449	2.753	23.732	20.38	73.322	110.5
7.4064	1.084	11.864	3.048	25.95	24.39	75.533	116.3
7.67	1.092	12.28	3.344	28.206	28.76	78.829	120
7.7512	1.165	12.65	3.703	30.492	33.35	81.427	122.6
7.9617	1.165	13.26	4.353	32.811	38.1	84.039	125.4
8.1321	1.188	13.64	4.799	35.164	42.85	86.667	127.4
8.3001	1.265	14.049	5.17	37.548	47.73	89.308	130.4
8.467	1.278	14.515	5.67	39.954	52.71	91.963	133.8
8.6355	1.331	14.979	6.22	42.38	57.57	94.625	138.7
8.803	1.351	15.453	6.923	44.826	62.33	97.303	142.3
8.9735	1.364	15.935	7.499	47.291	67.03	99.995	144.4
9.1381	1.42	16.426	8.295	49.772	71.33	102.7	151.9
9.3054	1.51	17.016	9.093	52.268	75.01	105.39	155.8
9.4743	1.607	17.428	9.735	54.777	79.95		
Series 2							
80.01	122.9	141.89	199.3	203.47	274.5	265.43	336.5
82.71	125.9	144.59	202.4	206.43	276.6	268	339.7
85.33	129.6	147.28	205.4	209.79	281.6	270.55	342.9
87.97	133.3	149.97	208.6	212.45	285.3	273.09	346
90.61	137	152.66	213	215.11	288.9	275.61	350.1
93.27	140.8	155.35	217.9	217.76	292.4	278.12	362.3
95.94	144.3	158.03	221.3	220.42	295.9	280.59	387.7
98.63	148.1	160.72	224.8	223.08	300	283.07	369.8
101.32	151.6	163.4	227.8	225.73	304.8	285.57	364.6
104.02	154.6	166.17	231.3	228.38	311.2	288.03	365.3
106.72	157.8	168.85	233.9	231.01	316.5	290.38	367.1
109.41	161.3	171.53	237.1	233.63	325.6	292.79	370.2
112.11	164.4	174.21	239.8	236.25	334.6	295.19	372.7

T (K)	$C_{p,m}$ (J* mol^{-1} *K $^{-1}$)						
114.81	167.7	176.88	243	238.87	333.3	297.56	375.8
117.51	171	179.56	245.9	241.5	330.2	299.89	379
120.2	174.7	182.22	249.2	244.12	336.1	302.43	381.5
123.01	178.1	184.89	252.2	246.72	341.7	305.53	386.2
125.71	180.9	187.55	255.5	249.35	348.5	308.63	393
128.41	184	190.21	258.3	251.95	355.5	309.48	392.8
131.11	187.2	192.87	261.6	254.53	370.5	313.26	401.3
133.8	190.3	195.52	264.4	256.94	593.5	316.03	407.6
136.5	193.5	198.17	267.4	258.95	1343	318.73	412.3
139.2	196.4	200.82	271	261.99	350.9	321.43	423.6

Table 6. Smoothed Molar Heat Capacity and Thermodynamic Functions of Crystalline N-f-MLF-OH ($M = 437.56$ g/mol, $p^\circ = 0.1$ MPa).

T (K)	$C_{p,m}$ ($J \cdot mol^{-1} \cdot K^{-1}$)	$H(T)-H(0)$ ($kJ \cdot mol^{-1}$)	$S(T)$ ($J \cdot mol^{-1} \cdot K^{-1}$)	$-(G(T)-H(0))$ ($kJ \cdot mol^{-1}$)
5	1.75	0.002	0.587	0.001
10	9.91	0.030	4.06	0.011
15	22.2	0.106	10.10	0.045
20	38.8	0.258	18.72	0.117
25	56.8	0.498	29.35	0.236
30	73.3	0.823	41.17	0.412
40	105.1	1.720	66.74	0.950
50	132.5	2.906	93.11	1.749
60	157.1	4.357	119.5	2.812
70	180.8	6.048	145.5	4.138
80	202.1	7.964	171.1	5.721
90	221.4	10.08	196.0	7.557
100	240.0	12.39	220.3	9.639
110	258.7	14.88	244.0	11.96
120	276.5	17.56	267.3	14.52
130	293.5	20.41	290.1	17.31
140	310.2	23.43	312.5	20.32
150	326.8	26.61	334.4	23.55
160	343.5	29.96	356.1	27.01
170	360.3	33.48	377.4	30.67
180	376.9	37.17	398.5	34.55
190	392.9	41.02	419.3	38.64
200	408.3	45.03	439.8	42.94
210	422.9	49.18	460.1	47.44
220	436.8	53.48	480.1	52.14
230	450.3	57.92	499.8	57.04
240	464.1	62.49	519.3	62.13
250	478.6	67.20	538.5	67.42
260	494.4	72.07	557.6	72.90
270	511.8	77.10	576.6	78.57
280	530.7	82.31	595.5	84.43
290	550.8	87.71	614.5	90.48
298.15	567.5	92.27	630.0	95.55
300	571.2	93.32	633.5	96.72
310	591.1	99.14	652.5	103.2
320	609.8	105.1	671.6	109.8
330	627.6	111.3	690.7	116.6
340	647.0	117.7	709.7	123.6
348	667.5	123.0	724.9	129.3

Table 7. Smoothed Molar Heat Capacity and Thermodynamic Functions of Crystalline N-f-MLF-OMe ($M = 451.59$ g/mol, $p^{\circ} = 0.1$ MPa).

T (K)	$C_{p,m}$ (J* mol^{-1} *K $^{-1}$)	$H(T)-H(0)$ (kJ* mol^{-1})	$S(T)$ (J* mol^{-1} *K $^{-1}$)	$-(G(T)-H(0))$ (kJ* mol^{-1})
5	1.99	0.002	0.664	0.001
10	12.50	0.034	4.630	0.012
15	25.10	0.130	12.00	0.053
20	41.76	0.292	21.37	0.135
25	61.13	0.550	32.77	0.270
30	79.28	0.902	45.54	0.465
40	113.3	1.867	73.10	1.057
50	140.8	3.146	101.5	1.930
60	167.6	4.683	129.5	3.086
70	194.3	6.496	157.4	4.520
80	216.1	8.558	184.8	6.231
90	236.3	10.81	211.4	8.213
100	256.4	13.27	237.3	10.46
110	275.6	15.94	262.7	12.96
120	292.9	18.78	287.4	15.71
130	309.1	21.79	311.5	18.70
140	324.7	24.96	335.0	21.94
150	340.1	28.29	357.9	25.40
160	355.6	31.77	380.4	29.09
170	371.3	35.40	402.4	33.01
180	387.3	39.19	424.1	37.14
190	403.7	43.15	445.5	41.49
200	420.3	47.27	466.6	46.05
210	437.2	51.6	487.5	50.82
220	454.3	56.03	508.2	55.79
230	471.6	60.64	528.8	60.98
240	489.0	65.41	549.2	66.37
250	506.5	70.42	569.6	71.97
260	524.3	75.61	589.8	77.76
270	542.4	80.9	609.9	83.76
280	561.1	86.43	630.0	89.96
290	580.7	92.13	650.0	96.36
298.15	597.6	96.94	666.3	101.7
300	601.6	98.05	670.0	103.0
310	624.4	104.2	690.1	109.8
320	649.7	110.5	710.3	116.8
330	678.4	117.2	730.8	123.9
340	711.3	124.1	751.5	131.4
344	726.0	127	759.9	134.4

Table 8. Smoothed Molar Heat Capacity and Thermodynamic Functions of Crystalline APG•H₂O (M = 261.28 g/mol, p^o = 0.1 MPa).

T (K)	C _{p,m} (J*mol ⁻¹ *K ⁻¹)	H(T)-H(0) (kJ*mol ⁻¹)	S(T) (J*mol ⁻¹ *K ⁻¹)	-(G(T)-H(0)) (kJ*mol ⁻¹)
Crystal II				
5	0.235	0.0003	0.078	0.0001
10	1.792	0.005	0.627	0.002
15	6.259	0.023	2.082	0.008
20	13.50	0.073	4.868	0.025
25	22.66	0.163	8.848	0.058
30	32.37	0.300	13.83	0.115
40	52.79	0.726	25.93	0.312
50	71.54	1.350	39.79	0.639
60	89.18	2.154	54.39	1.110
70	106.6	3.133	69.45	1.729
80	122.9	4.281	84.76	2.500
90	137.5	5.585	100.1	3.424
100	150.2	7.025	115.3	4.501
110	162.1	8.587	130.1	5.728
120	174.1	10.27	144.8	7.103
130	186.1	12.07	159.2	8.623
140	197.2	13.99	173.4	10.29
150	208.8	16.01	187.3	12.09
160	222.5	18.17	201.3	14.03
170	235.1	20.46	215.1	16.11
180	246.6	22.87	228.9	18.34
190	258.0	25.39	242.5	20.69
200	269.8	28.03	256.1	23.19
210	282.2	30.79	269.5	25.81
220	292.6	33.67	282.9	28.58
230	302.3	36.64	296.1	31.47
240	312.0	39.71	309.2	34.50
250	321.7	42.88	322.2	37.65
260	331.4	46.15	335.0	40.94
265	336.3	47.82	341.3	42.63
Crystal I				
265	336.3	50.76	352.4	42.63
270	341.9	52.46	358.8	44.41
280	354.7	55.94	371.4	48.06
290	367.0	59.55	384.1	51.84
298.15	376.6	62.58	394.4	55.01
300	378.8	63.28	396.7	55.74
310	393.2	67.13	409.4	59.77
320	418.1	71.17	422.2	63.93
321	421.6	71.59	423.5	64.35

References

- [1] Markin, A. V.; Markhasin, E.; Sologubov, S. S.; Smirnova, N. N.; Griffin, R. G. Standard Thermodynamic Functions of Tripeptides N-formyl-Met-Pro-Phe-OH and N-formyl-Met-Pro-Phe-OMe.
- [2] Mrevlishvili, G. M. Low-temperature calorimetry of biological macromolecules. *Soviet Physics Uspekhi* 1979, 22, 433. DOI: 10.1070/PU1979v022n06ABEH005573
- [3] Pometun, M. S.; Gundusharma, U. M.; Richardson, J. F.; Wittebort, R. J. Solid-State NMR and Calorimetry of Structural Waters in Helical Peptides. *J. Am. Chem. Soc.* 2002, 124, 2345. DOI: 10.1021/ja017364r
- [4] Bordallo, H. N.; Boldyreva, E. V.; Fischer, J.; Koza, M. M.; Seydel, T.; Minkov, V. S.; Drebushchak, V. A.; Kyriakopoulos, A. Observation of subtle dynamic transitions by a combination of neutron scattering, X-ray diffraction and DSC: A case study of the monoclinic -cysteine. *Biophys. Chem.* 2010, 148, 34. DOI: 10.1016/j.bpc.2010.02.003
- [5] Kutysin, A. M.; Markhasin, E. M.; Karyakin, N. V. Processing and approximation of calorimetric data by the generalized Debye functions. *Russian J. Phys. Chem.* 2004, 78, 571
- [6] Cole, A. G.; Hutchens, J. O.; Stout, J. W. Heat capacities from 11 to 305°K. and entropies of L-arginine-HCl, L-histidine-HCl, and L-lysine-HCl. *J. Phys. Chem.* 1963, 67, 2245. DOI: 10.1021/j100805a001
- [7] Hutchens, J. O.; Cole, A. G.; Stout, J. W. Heat capacities from 11 to 305°K., entropies, and free energies of formation of L-valine, L-isoleucine, and L-leucine. *J. Phys. Chem.* 1963, 67, 1128. DOI: 10.1021/j100799a047
- [8] Hutchens, J. O.; Cole, A. G.; Stout, J. W. Heat capacities from 11 to 305°K. and entropies of L-alanine and glycine. *J. Am. Chem. Soc.* 1960, 82, 4813. DOI: 10.1021/ja01503a014
- [9] Cole, A. G.; Hutchens, J. O.; Stout, J. W. Heat capacities from 11 to 305°K. and entropies of L-phenylalanine, L-proline, L-tryptophan, and L-tyrosine. Some free energies of formation. *J. Phys. Chem.* 1963, 67, 1852. DOI: 10.1021/j100803a027
- [10] Hutchens, J. O.; Cole, A. G.; Robie, R. A.; Stout, J. W. Heat Capacities from 11 to 305°K, Entropies and Free Energies of Formation of l-Asparagine Monohydrate, l-Aspartic Acid, l-Glutamic Acid, and l-Glutamine. *J. Bio. Chem.* 1963, 238, 2407
- [11] Hutchens, J. O.; Cole, A. G.; Stout, J. W. Heat Capacities and Entropies of l-Cystine and l-Methionine. *J. Bio. Chem.* 1964, 239, 591
- [12] Paukov, I. E.; Kovalevskaya, Y. A.; Drebushchak, V. A.; Drebushchak, T. N.; Boldyreva, E. V. An Extended Phase Transition in Crystalline L-Cysteine near 70 K. *J. Phys. Chem. B* 2007, 111, 9186. DOI: 10.1021/jp073655w
- [13] Drebushchak, V. A.; Kovalevskaya, Y. A.; Paukov, I. E.; Boldyreva, E. V. Heat capacity of α -glycylglycine in a temperature range of 6 to 440 K. Comparison with glycines. *J. Therm. Anal. Calorim.* 2006, 85, 485. DOI: 10.1007/s10973-006-7680-5

- [14] Drebuschak, V. A.; Kovalevskaya, Y. A.; Paukov, I. E.; Boldyreva, E. V. Heat capacity of D- and DL-serine in a temperature range of 5.5 to 300 K. *J. Therm. Anal. Calorim.* 2007, 89, 649. DOI: 10.1007/s10973-006-7668-1
- [15] Drebuschak, V.; Kovalevskaya, Y.; Paukov, I.; Boldyreva, E. Low-temperature heat capacity of α and β polymorphs of glycine. *J. Therm. Anal. Calorim.* 2003, 74, 109. DOI: 10.1023/a:1026377703260
- [16] Drebuschak, V. A.; Boldyreva, E. V.; Kovalevskaya, Y. A.; Paukov, I. E.; Drebuschak, T. N. Low-temperature heat capacity of β -glycine and a phase transition at 252 K. *J. Therm. Anal. Calorim.* 2005, 79, 65. DOI: 10.1007/s10973-004-0563-8
- [17] Drebuschak, V.; Kovalevskaya, Y.; Paukov, I.; Boldyreva, E. Low-temperature heat capacity of diglycylglycine. *J. Therm. Anal. Calorim.* 2008, 93, 865. DOI: 10.1007/s10973-007-8891-0
- [18] Paukov, I.; Kovalevskaya, Y.; Boldyreva, E. Low-temperature heat capacity of L- and DL-phenylglycines. *J. Therm. Anal. Calorim.* 2010, 1. DOI: 10.1007/s10973-009-0665-4
- [19] Paukov, I.; Kovalevskaya, Y.; Boldyreva, E. Low-temperature thermodynamic properties of dl-cysteine. *J. Therm. Anal. Calorim.* 2010, 100, 295. DOI: 10.1007/s10973-009-0457-x
- [20] Paukov, I. E.; Kovalevskaya, Y. A.; Boldyreva, E. V. Low-temperature thermodynamic properties of L-cysteine. *J. Therm. Anal. Calorim.* 2008, 93, 423. DOI: 10.1007/s10973-007-8697-0
- [21] Boldyreva, E. V.; Chesalov, Y. A.; Drebuschak, T. N.; Kolesnik, E. N.; Kovalevskaya, Y. A.; Paukov, I. E.; Drebuschak, V. A.; Kolesov, B. A. Phase transition at 204-250 K in the crystals of β -alanine: kinetically irreproducible, or an artefact? *Phase Transitions* 2009, 82, 497. DOI: 10.1080/01411590903114198
- [22] Kolesov, B. A.; Minkov, V. S.; Boldyreva, E. V.; Drebuschak, T. N. Phase Transitions in the Crystals of L- and DL-Cysteine on Cooling: Intermolecular Hydrogen Bonds Distortions and the Side-Chain Motions of Thiol-Groups. 1. L-Cysteine. *J. Phys. Chem. B* 2008, 112, 12827. DOI: 10.1021/jp804142c
- [23] Minkov, V. S.; Tumanov, N. A.; Kolesov, B. A.; Boldyreva, E. V.; Bizyaev, S. N. Phase Transitions in the Crystals of L- and DL-Cysteine on Cooling: The Role of the Hydrogen-Bond Distortions and the Side-Chain Motions. 2. DL-Cysteine. *J. Phys. Chem. B* 2009, 113, 5262. DOI: 10.1021/jp810355a
- [24] Barnes, A. B.; Andreas, L. B.; Huber, M.; Ramachandran, R.; van der Wel, P. C. A.; Veshtort, M.; Griffin, R. G.; Mehta, M. A. High-resolution solid-state NMR structure of Alanine-Prolyl-Glycine. *J. Magn. Reson.* 2009, 200, 95. DOI: 10.1016/j.jmr.2009.06.009
- [25] Varushchenko, R. M.; Druzhinina, A. I.; Sorokin, E. L. Low-temperature heat capacity of 1-bromoperfluorooctane. *J. Chem. Thermodyn.* 1997, 29, 623. DOI: 10.1006/jcht.1996.0173
- [26] Malyshev, V. M.; Mil'ner, G. A.; Sorokin, E. L.; Shibakin, V. F. Automatic low-temperature calorimeter. *Instrum. Exp. Technol.* 1985, 195

- [27] Ginnings, D. C.; Furukawa, G. T. Heat-capacity standards for the range 14 to 1200K. *J. Am. Chem. Soc.* 1953, 75, 522. DOI: 10.1021/ja01099a004
- [28] Gatta, G. D.; Richardson, M. J.; Sarge, S. M.; Stolen, S. Standards, calibration, and guidelines in microcalorimetry. Part 2. Calibration standards for differential scanning calorimetry. *Pure Appl. Chem.* 2006, 78, 1455. DOI: 10.1351/pac200678071455
- [29] Coplen, T. B. Atomic weights of the elements 1999. *Pure Appl. Chem.* 2001, 73, 667. DOI: 10.1351/pac200173040667
- [30] Rabinovich, I. B.; Nistratov, V. P.; Telnoy, V. I.; Sheiman, M. S. Thermochemical and thermodynamic properties of organometallic compounds; Begell House: New York, 1999.
- [31] Lazarev, V. B.; Izotov, A. D.; Gavrichev, K. S.; Shebershneva, O. V. Fractal model of heat capacity for substances with diamond-like structures. *Thermochim. Acta* 1995, 269/270, 109. DOI: 10.1016/0040-6031(95)02529-4
- [32] McCullough, J. P.; Scott, D. W. *Calorimetry of Non-reacting Systems*; Butterworth: London, 1968.
- [33] Chase, M. W. J. NIST-JANAF Thermochemical Tables. *J. Phys. Chem. Ref. Data* 1998, 9, 1
- [34] Cox, J. D.; Wagman, D. D.; Medvedev, V. A. *CODATA Key Values for Thermodynamics*; Hemisphere: New York, 1984.